How Open Ocean Dynamics Affects Coastal Sea Level, an Investigation of the Influence of the Continental Shelf and Slope

Thesis submitted in accordance with the requirements of the University of Liverpool for the degree of Doctor of Philosophy

by

Anthony Wise

University of Liverpool

April 2020

Declaration of Authorship

I declare that this thesis titled, *How Open Ocean Dynamics Affects Coastal Sea Level, an Investigation of the Influence of the Continental Shelf and Slope* and the work presented in it are my own work. The material contained in the thesis has not been presented, nor is currently being presented, either wholly or in part, for any other degree or qualification.

Date: 24th April, 2020

How open ocean dynamics affects coastal sea level, an investigation of the influence of the continental shelf and slope

Anthony Wise

Abstract

Large scale, annual to decadal period motions in the deep ocean drive large scale gradients in dynamic sea level that are important as baseline levels with the potential to amplify short term sea level fluctuations from extreme events such as storm surges. Model projections assessing flood risk therefore depend on accurately simulating both short and long term variability. The decreasing depth of the bathymetry from the deep ocean to the shallow coastal zone tends to produce an insulating effect between the deep ocean and the coast. Nevertheless, studies show coherence between signals on- and off-shore over vast distances, implying that remote driving of the coastal sea level by deep ocean forcing is important. Western boundaries of ocean basins are of particular interest as the rotation and curvature of the Earth result in the intensification of currents and sea level gradients adjacent to the coastal zone. This thesis seeks to develop an improved physical understanding of how coastal sea level along a western boundary is related to the open ocean and to what extent this relationship depends on bottom topography h, the effects of the Coriolis parameter f, and friction. To investigate these questions, a hierarchy of idealized models is developed. Analytic and numerical solutions are sought for the linearised problem, while an idealized configuration of the NEMO General Ocean Circulation Model is developed to probe more

realistic scenarios in the North Atlantic. For a homogeneous ocean layer above sloping topography that is uniform alongshore, the β-effect and bottom topography result in the mean dynamic sea level tending to follow h/f contours. The inclusion of friction allows sea level to cross these contours, with steeper topography and a larger friction parameter promoting penetration to the coast. This leads to the equatorward displaced and attenuated coastal sea level (relative to the open ocean) that is seen in observations. Fluctuations in the open ocean are shown to generate a new type of leaky Slope wave that transmits energy equatorward and dissipates locally on the slope and via the radiation of short Rossby waves into the interior ocean. Coastal sea level is explicitly related to poleward and open ocean sea level in terms of coastally trapped boundary waves and it is shown how the β-effect and friction result in enhanced wave decay that promotes signal penetration from ocean to coast. Steeper topography "kills-off" the boundary waves and also promotes penetration, tending towards the vertical sidewall solution in the steep limit. The inclusion of realistic bathymetry and non-linearity, which allows for the advection of potential vorticity, is not found to significantly alter the character of the solution. In particular, hot spots of off-slope sea level variability are found to excite waves that exert control over equatorward coastal latitudes, demonstrating the poleward control of coastal sea level along western boundaries. It is concluded that shelf seas are vulnerable to on and off-shelf variability originating many degrees of latitude further poleward, and that the representation of friction and bottom topography are important for numerical simulations to faithfully capture the effect of the open ocean on the coastal sea level.

Contents

Acknowledgements

The funding for this Ph.D has been provided by the Natural Environment Research Council as part of the Earth, Oceans and Atmosphere doctoral training partnership provided by the National Oceanography Centre, University of Liverpool and University of Manchester (grant number NE/L002469/1). Thank you for supporting this research.

While I quickly realised getting a Ph.D was going to involve a lot of hard work, I've benefited from a good dose of fortune throughout my time in Liverpool by having incredible support from others.

A big thank you to my supervisors: Jeff Polton, Chris Hughes, John Huthnance, Jason Holt and James Harle, for providing their time, energy and wisdom. In particular, I am not sure where this thesis might have ended up without the guidance and patience of Jeff and Chris, who have been incredibly knowledgeable, easy to talk with, and pragmatic throughout - even when they probably had better things to be doing. Thank you again. A word of thanks must also go to the anonymous reviewers of my work for introducing me to peer review with thoughtful and constructive comments, and for not living up to the horror stories that circle Ph.D offices. I would also like to thank my examiners Prof. Ted Johnson and Dr. David Lewis for their comments and critique, which has improved the quality of the final thesis.

The biggest acknowledgement must go to my wife Kelly, who actually suggested that I apply for a Ph.D, for being superhumanly empathetic and kind - as well as keeping me in the life I'd grown accustomed to. Teamed with our delinquent dog Bruce, you made this possible, thank you. I would also like to thank my parents-in-law, Colin and Gerri, for keeping me well stocked with biscuits and Marmite (long may that continue) and to my parents Arnold and Elaine, for never truly understanding what I have been doing all day for four years but cheering me on nonetheless. A big thank you also to family and friends who have been supportive and excited for me.

Finally, I would like to thank the people of the National Oceanography Centre in Liv-

erpool for creating such a great atmosphere and institution, in addition to providing an endless supply of free caffeine.

Chapter 1

Introduction

1.1 An Overview

The central theme of this thesis is to develop a better understanding of how the continental shelf and slope influence the connection between coastal sea level and ocean dynamics.

There are at least two pressing reasons for developing a better understanding of the relationship between the coast and the deep ocean. Firstly, while variability in sea level affects all regions, deep or shallow, it is at the coast where people live and businesses operate, and therefore where society is most vulnerable to changes in sea level. To what extent therefore does coastal sea level reflect open ocean sea level?

Secondly, oceanic signals travel rapidly along coastlines, connecting ocean basins and distributing changes in the state of the ocean over large distances. As a consequence, these coastal boundary signals not only provide information about the large scale ocean circulation, but can also provide a means for variability in one location to drive change in another far away location. Ultimately, because the state of the open ocean is driven via interaction with other Earth systems, which are susceptible to variability and change over time, it is desirable to understand how this might drive change in coastal sea level and how this can be understood in terms of the signals that propagate along the coastal boundaries. To give a concrete example: how and why might a change in wind stress patterns over the North Atlantic, which increases dynamic sea level in the subtropical open ocean, affect coastal sea level along the US south east coast?

In the open ocean, surface currents establish gradients in sea level; to first order, currents and elevation gradient are in geostrophic balance and perpendicular to each other. This balance supports an approximately 1 m difference in sea level across the subtropical

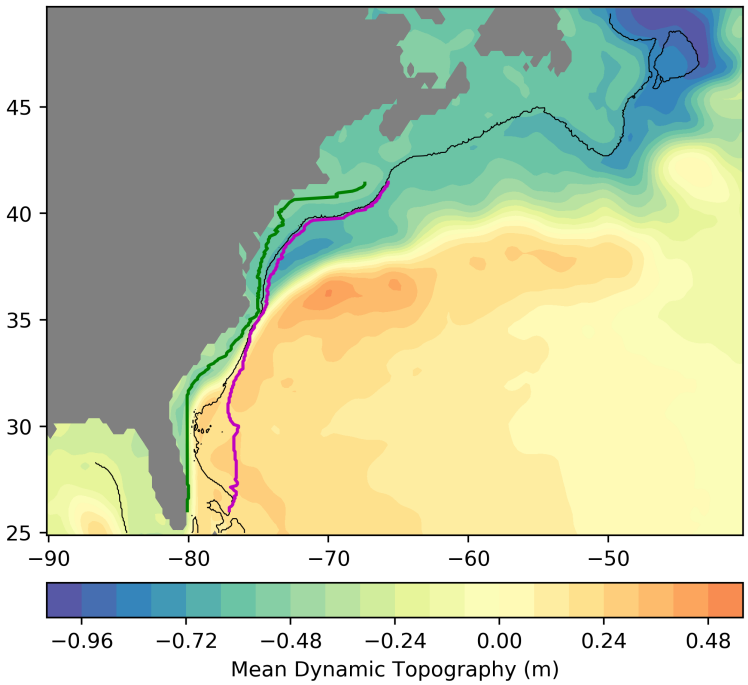

Figure 1.1: *AVISO altimeter-derived 22-year mean dynamic sea level (MDSL) (1993-2014 inclusive) (This is the sea level relative to the geoid - the Ssalto/Duacs, delayed mode, gridded absolute dynamic topography product using all available satellites). The pink and green lines denote the 2000 m and 40 m depth contours respectively. The black line denotes the 500 m depth contour. The Ssalto/Duacs altimeter products were produced and distributed by the Copernicus Marine and Environment Monitoring Service (CMEMS) (http://www.marine.copernicus.eu).*

and subpolar bands of the North Atlantic - Fig. 1.1 shows the altimeter derived 22-year mean dynamic sea level (sea level resulting from ocean currents) (1993-2014 inclusive) in the deep ocean and on the continental shelf in the North Atlantic. The Ssalto/Duacs altimeter products were produced and distributed by the Copernicus Marine and Environment Monitoring Service (CMEMS) (http://www.marine.copernicus.eu). Geostrophic balance implies that at the coast, an alongshore sea level gradient is consistent with a flow towards or away from the coast. The coast is, however, a boundary of the ocean basin and acts like a wall, imposing no normal flow as the coast is approached. As a consequence, the dynamical balance governing flow and sea level gradients at the coast is different to that in the open ocean. Typically this can result in an insulating effect, where sea level gradients at the coast are smaller than the comparable gradients in the open ocean (Wang, 1982; Csanady

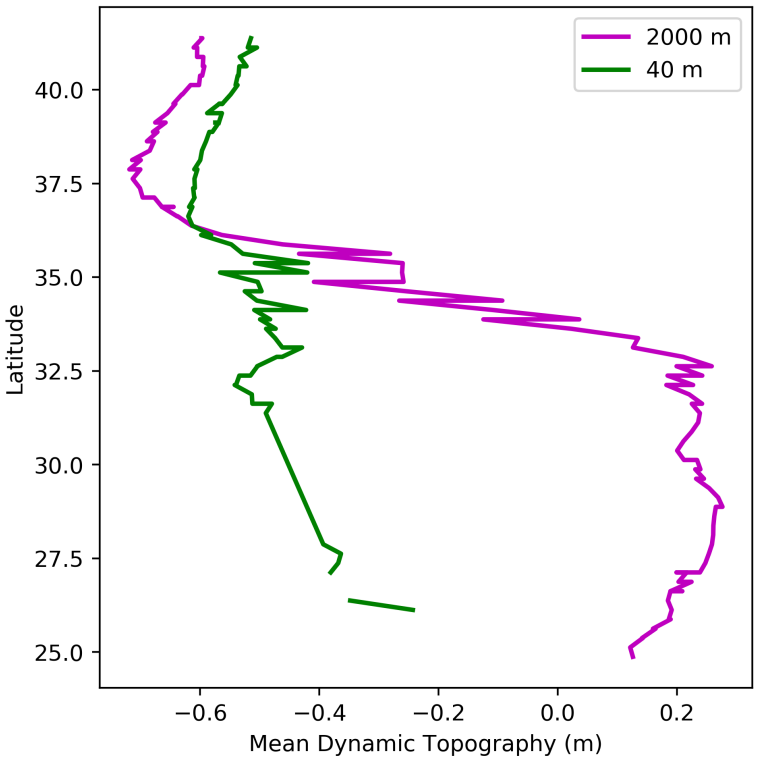

Figure 1.2: *The 22-year mean dynamic sea level (1993-2014 inclusive, AVISO Ssalto/Duacs altimeter-derived as in Fig. 1.1) along the 2000 m and 40 m depth contours denoted in Fig. 1.1.*

and Shaw, 1983). Suggestions are that bottom topography modifies this insulating effect (e.g., Huthnance, 2004; Higginson et al., 2015), and this is the problem addressed here. In demonstration of this insulating effect, Fig. 1.2 picks out the mean dynamic sea level from Fig. 1.1 along the 2000 m and 40 m depth contours (denoted in Fig. 1.1) and highlights the difference between the deep ocean and the coastal zone.

Fluctuations in the forcing that drive open ocean currents, for example surface wind stress or surface heat fluxes, generate anomalies in the state of the ocean. As discussed in many text books (e.g., Von Schwind, 1980, p.287), for large scale fluctuations that occur over periods longer than the inertial period, $2\pi/f$, where f is the Coriolis parameter, long Rossby waves propagate the anomaly westward towards a western boundary of the ocean basin. On reaching the boundary, the incident anomaly generates Coastally Trapped Waves (CTW) (referred to also as boundary waves) that propagate the anomaly cyclonically along the continental shelf and slope (Huthnance, 1987b). In this manner, fluctuations in forcing are transmitted around the oceans.

The variation of the Coriolis parameter with latitude, approximately represented by $df/dy = \beta$, where the y-axis is oriented meridionally and increasing with latitude, results in the westward propagation of energy at the group velocity of long Rossby waves. This β-effect, together with the need to dissipate energy (or balance the vorticity) results in an asymmetry in the basin circulation, known as western intensification (Stommel, 1948), whereby the currents are stronger, and the alongshore sea level gradients steeper, at the western boundary relative to the eastern boundary. The larger open ocean sea level gradients and the importance of a mechanism for dissipation (with friction being an important sink) at western boundaries, makes them particularly relevant regions to investigate the ocean-to-coast relationship.

The interest in sea level along western boundaries has increased in recent years, particularly in regions such as the North Atlantic where there has been an identification of hotspots of accelerated rates of sea level rise along stretches of the North American east coast (Sallenger Jr et al., 2012; Boon, 2012). Debate regarding the sources of these hotspots is active and ongoing. Observational studies have compared time series of dynamic sea level from tide gauges and satellite altimetry to describe variability and demonstrate correlations (e.g., Kenigson et al., 2018), however while CTW theory is sometimes invoked as an important mechanism, detailed studies into sea level and CTWs have tended to evolve separately. Can theory help provide better physical explanations of sea level variability?

In terms of dynamic adjustment at western boundaries, the β-effect and dissipation appear to be important (Marshall and Johnson, 2013), however it is the sloping bottom topography, together with the necessary divergence of the flow due to the depth tending to zero at the coast, that makes boundaries special. In idealized conceptual models, the boundary has been modelled as a vertical sidewall, as a uniform slope, and as a more realistic shelf and slope combination. It has been shown that different geometries of bottom topography can constrain the types of CTWs permitted, with classes of wave having distinct properties - see reviews (e.g. Mysak, 1980b; Huthnance et al., 1986). How exactly does the modification of CTWs affect coastal sea level and coastal variability? Much of the literature also considers CTWs on an f-plane, where the Coriolis parameter is held constant $df/dy = 0$, and a source of dissipation is not always considered. Both have the potential to modify wave behaviour and therefore the coastal response.

More sophisticated numerical models (or Ocean General Circulation Models as they are referred to) are powerful in their ability to complement observations and examine processes difficult to isolate in simpler models. Often, however, these models are limited in horizontal resolution due to computational expense. Coarse resolution can result in a failure to properly

represent the coastal bottom topography, potentially distorting the representation of sea level and propagating anomalies on the shelf and slope - for example, a 1/4 ° horizontal resolution ($\sim$ 25 km) model may have only 1 or 2 grid points on a narrow stretch of shelf and slope. While finer resolutions are becoming increasingly accessible, the sophistication of these models can also make the output difficult to interpret, expensive to explore, and potentially susceptible to configuration sensitivities. Despite these difficulties, numerical models are invaluable tools for exploring more complex aspects of the relationship between ocean and coast involving nonlinearity, stratification and realistic bathymetry. Are results from numerical models consistent with idealized theory?

Observations provide the ultimate description of change in coastal sea level, but the constraint of having to use past data means that modelling studies are important for predicting future change. The desire here is to be able to better explain the results of observations using a hierarchy of models.

Ultimately it will be found that the CTW theoretical framework gives insight into the spatial structure and variability of dynamic sea level along western boundaries. The equatorward displacement and attenuation of coastal sea level relative to the open ocean results from the equatorward propagation of long boundary waves, which exert control (from poleward) over lower latitudes, i.e. information is transmitted in the pole-to-equator direction. In the barotropic case, the evolution of these waves is affected by the geometry of the bottom topography, representation of friction and the latitude dependence of the Coriolis parameter. The extent to which ocean dynamics influences coastal sea level depends in part, as a consequence, on how these elements are represented. The control of sea level from poleward latitudes is not found to be significantly modified by the inclusion of realistic bathymetry and nonlinear effects in the barotropic case. The results progress the theoretical understanding of western boundary sea level and are useful for interpreting observations of mean dynamic sea level as well as variability. Furthermore the results highlight potential sensitivities in complex numerical models which may bias future projections.

1.2 Thesis Aim, Objectives and Structure

Aim: To increase our understanding of how the continental shelf and slope affects the relationship between coastal sea level and ocean dynamics along western boundaries.

One of the challenges associated with this research aim is the need to draw together ideas

and results from sub-disciplines of Physical Oceanography with typically quite different focuses. The objective of Chapter 2 is, therefore, to review the relevant background material and literature from within the Sea Level Science, CTW Theory and Ocean Dynamics research fields, and to create a coherent narrative. Chapters 3, 4 and 5, which address the central questions of the project, have been written in journal article format, with independent introductions and conclusions (chapters 3 and 4 published in the Journal of Physical Oceanography). The objectives of these chapters are as follows:

Chapter 3:

i. To create an idealized model of the relationship between long period open ocean and coastal sea level along a western boundary that includes a continental shelf and slope.

ii. To indicate the roles of the β-effect and friction in this relationship.

iii. To investigate the sensitivity of the coastal sea level response to the geometry of the shelf and slope.

Chapter 4:

i. To model the relationship between low frequency open ocean sea level fluctuations and barotropic CTWs.

ii. To investigate the effect of friction, bottom topography and the β-effect on the CTWs.

iii. To relate the behaviour of the CTWs to coastal sea level.

Chapter 5:

i. To include nonlinear effects and realistic bottom topography in the barotropic coastal response to open ocean forcing using the NEMO General Ocean Circulation Model configured for the North Atlantic western boundary.

ii. To examine the amplitude and propagation of variability on the shelf and slope in response to offshore forcing.

iii. To contrast modelled variation with theory and with observational studies of sea level rise hotspots.

In chapter 6 results from the proceeding chapters are reflected upon and conclusions are drawn with respect to the overall project aim. Appendix A includes an article (co-authored Hughes et al. (2019)) published in Surveys in Geophysics reviewing the role of CTW on sea level and is particularity useful as background for Chapter 4.

Chapter 2

Background and Literature

2.1 What is sea level?

The definition of *sea level* depends upon what the sea surface is being measured in relation to. Three important references that sea level can be measured against are the Earth's crust, the Geoid, and the reference ellipsoid. While the Earth's crust is simply the ocean floor, the Geoid can be considered as the surface of the ocean when in equilibrium, i.e. when it is not in motion. While a detailed discussion of the Geoid is beyond the scope of this thesis, the Geoid is more specifically the geopotential surface that results from a sum of the gravitational potential and the centrifugal potential that most closely matches the sea surface - see Woodworth et al. (2012) for discussion on representing the Geoid that is relevant to sea level. Finally, because the Geoid can be approximated by an ellipsoid, a reference ellipsoid is used as a reference surface, for example the NEMO ocean model makes the Spherical Earth approximation (Gurvan Madec and NEMO System Team, 2019).

Three important measures of sea level result from the different references: relative sea level, absolute sea level and dynamic sea level (note this is also referred to as dynamic topography by the satellite community, though we follow Gregory et al. (2019) in avoiding this terminology as it can lead to ambiguity with the term's other common usage regarding the depth integration of density anomalies.). Relative sea level refers to the ocean thickness, or the sea surface relative to the Earth's crust. Absolute sea level refers to the sea surface relative to the reference ellipsoid, and the dynamic sea level refers to the sea surface relative to the Geoid - see Figure 2.1 for reference.

The Earth's crust and Geoid can change locally due to solid earth dynamics, resulting in redistribution of the water in the ocean, similarly currents due to atmospheric winds

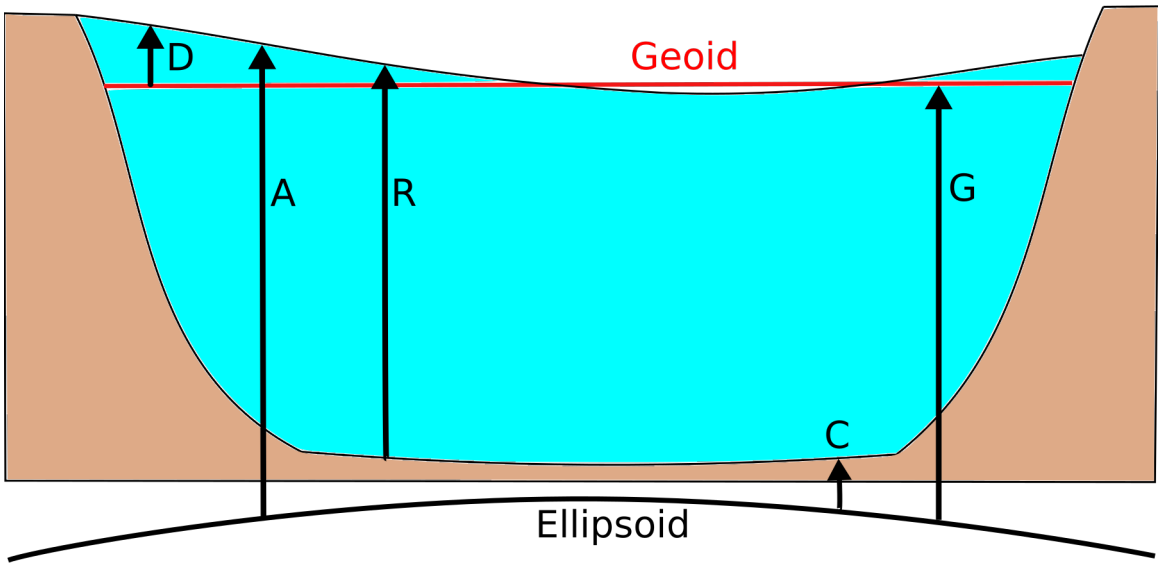

Figure 2.1: *Schematic showing the definitions of the different measures of sea level and relevant quantities, where D is Dynamic Sea Level, A is Absolute Sea Level, R is Relative Sea Level, C is Crustal height and G is Geoid.*

or density gradients can cause the water to spatially redistribute. In both cases, while global mean relative sea level has not changed, local stretches of coastline, for example, can experience increased relative sea level. On the other hand, global mean relative sea level can change when the total volume of water changes, this can result from expansion or contraction of the ocean or from changes in total ocean mass, for example from land ice-melt. The research presented here is solely concerned with dynamic sea level due to the distribution of ocean water that results from atmospheric and ocean dynamics, i.e. from phenomena such as atmospheric wind over the surface of the ocean that drive ocean currents. As a result, when comparing the spatial variation of sea level between observations and model output, the spatial average is unimportant, as it is the spatial variation of dynamic sea level that is of concern.

As will be discussed in section 2.3, historically there has been uncertainty regarding the observations of gradients in dynamic coastal sea level due to uncertainty in the geodetic levelling. In recent years however, satellite gravity missions such as the European Space Agency's Gravity field and steady-state Ocean Circulation Explorer (GOCE) mission, have brought improvements to geoid models with objectives to bring geoid accuracy to within 1-2 cm (Siemes, 2012) (note that estimates of the difference in sea level between 25°N and 40°N along the North American east coast are in the region of about 30 cm, see Fig 1.2

and (Woodworth et al., 2012; Higginson et al., 2015). As a result, gradients in dynamic coastal sea level along the western Atlantic derived from observations referenced against the geoid have been found to be consistent with those derived from ocean models (solving the equations governing ocean dynamics), for example see Figure 1 in Higginson et al. (2015). More specifically, Woodworth et al. (2012) found the standard deviation of the difference between one ocean model and one geoid model to be 9.5 cm along the western Atlantic coastline and Higginson et al. (2015) found that using the mean dynamic sea levels from an ensemble of geoid and ocean models brought the standard deviation of the differences to 2.3 cm. Throughout the proceeding chapters, gradients in sea level produced by ocean models of varying complexity will be discussed and compared against the sea level gradient established by recent numerical ocean models and geoid referenced observations. Given the aforementioned consistency between these approaches, it is felt that this comparison justifiably provides insight about the spatial distribution of coastal sea level along western boundaries.

2.2 Ocean dynamics

2.2.1 The interior ocean

An important theoretical concept in physical oceanography relates the horizontal circulation of the ocean to the mean atmospheric wind. Demonstrated by Sverdrup (1947), the theory of wind-driven currents in a baroclinic ocean is the starting point for understanding dynamic sea level along western boundaries of ocean basins.

The primitive equations are first written in the form

$$\frac{\partial u}{\partial t}+u\frac{\partial u}{\partial x}+v\frac{\partial u}{\partial y}+w\frac{\partial u}{\partial z}-fv=-\frac{1}{\rho_0}\frac{\partial p}{\partial x}+\left[\frac{\partial}{\partial x}\left(A_H\frac{\partial u}{\partial x}\right)+\frac{\partial}{\partial y}\left(A_H\frac{\partial u}{\partial y}\right)+\frac{\partial}{\partial z}\left(A_V\frac{\partial u}{\partial z}\right)\right], \tag{2.1}$$

$$\frac{\partial v}{\partial t}+u\frac{\partial v}{\partial x}+v\frac{\partial v}{\partial y}+w\frac{\partial v}{\partial z}+fu=-\frac{1}{\rho_0}\frac{\partial p}{\partial y}+\left[\frac{\partial}{\partial x}\left(A_H\frac{\partial v}{\partial x}\right)+\frac{\partial}{\partial y}\left(A_H\frac{\partial v}{\partial y}\right)+\frac{\partial}{\partial z}\left(A_V\frac{\partial v}{\partial z}\right)\right], \tag{2.2}$$

$$\frac{\partial p}{\partial z}=-\rho g, \tag{2.3}$$

$$\frac{\partial \rho}{\partial t}+\frac{\partial \rho u}{\partial x}+\frac{\partial \rho v}{\partial y}+\frac{\partial \rho w}{\partial z}=0, \tag{2.4}$$

where $\boldsymbol{u}=(u,v)$ is the velocity in the horizontal (x,y); w is the velocity in the vertical, z; t is time; f is the Coriolis parameter; ρ is the density perturbation; ρ_0 the constant reference density; p pressure; and A_H and A_V are the horizontal and vertical eddy viscosity

coefficients. Note that throughout subscripts are used to sub-label particular quantities, with the *exceptions* of subscripts x, y and t, which are used as short-hands for derivatives with respect to x, y and t, for example

$$u_{x \text{ or } y \text{ or } t} \text{ means } \frac{\partial u}{\partial x \text{ or } \partial y \text{ or } \partial t}. \tag{2.5}$$

In general, the density perturbation ρ and vertical velocity w are functions of 3-dimensional space and time, however in chapters 3, 4 and 5 we are concerned with homogeneous oceans, or homogeneous ocean layers, where the density is taken to be constant $\rho = 0$ and the velocities u and v independent of depth, with stresses at the surfaces included as 'body' forces. This particular idealisation is applied to simplify the analysis and has a rich history in oceanography, including its application by Stommel (1948) in his seminal work on western boundary currents, which will be discussed in section 2.2.2. The effects of relaxing this constraint are discussed further in sections 2.2.3, 2.2.4 and 2.5.2.

Considering now a box model with vertical side walls, then for a stationary flow of basin scale, the time derivatives are dropped and it is assumed that the nonlinear terms on the left hand side of (2.1) and (2.2) and the lateral friction terms

$$\left[\frac{\partial}{\partial x}\left(A_H \frac{\partial u}{\partial x}\right) + \frac{\partial}{\partial y}\left(A_H \frac{\partial u}{\partial y}\right)\right], \tag{2.6}$$

$$\left[\frac{\partial}{\partial x}\left(A_H \frac{\partial v}{\partial x}\right) + \frac{\partial}{\partial y}\left(A_H \frac{\partial v}{\partial y}\right)\right], \tag{2.7}$$

are small and can be neglected. Integrating over the vertical between $z = 0$ and $z = -h$, where h is a depth at which the horizontal velocity is zero, but not as deep as the ocean floor (so that there is no bottom friction), gives

$$\int_{-h}^{0} \boldsymbol{\nabla} p \, dz = -f \hat{\boldsymbol{k}} \times \boldsymbol{U} + \boldsymbol{\tau}^s, \tag{2.8}$$

where $\boldsymbol{\nabla}$ is the horizontal derivative operator, $\hat{\boldsymbol{k}}$ is the vertical unit vector, $\boldsymbol{\tau}^s = (\tau^x, \tau^y)$ is the lateral stress at the surface due to wind stress in the x and y directions

$$A_V \frac{\partial \boldsymbol{u}}{\partial z}\bigg|_{z=0} = \frac{1}{\rho_0}(\tau^x, \tau^y), \tag{2.9}$$

$\boldsymbol{U}$ gives the depth integrated mass transport

$$\boldsymbol{U} = (U, V) = \int_{-h}^{0} \rho_0 \boldsymbol{u} \, dz. \tag{2.10}$$

Vertically integrating the steady form of (2.4) gives $\boldsymbol{\nabla} \cdot \boldsymbol{U} = 0$ and using this in the vertical component of the curl of (2.8) gives Sverdrup's relation

$$\frac{df}{dy} V = \hat{\boldsymbol{k}} \cdot \boldsymbol{\nabla} \times \boldsymbol{\tau^s}, \tag{2.11}$$

expressing a balance between the vorticity added through the wind with the meridional mass transport (with a variable Coriolis parameter).

To see the effect of this relationship on dynamic sea level first consider that for the North Atlantic, for example, it is fair to represent the time mean wind field as being directed zonally and with strength that changes only with latitude, i.e. $\boldsymbol{\tau^s} = (\tau^x(y), 0)$. Then substituting (2.11) into the zonal component of (2.8) gives

$$\int_{-h}^{0} \frac{\partial p}{\partial x}\, dz = -\frac{f}{df/dy}\left(\frac{\partial \tau_x}{\partial y}\right) + \tau^x \tag{2.12}$$

$$= -\frac{f^2}{(df/dy)} \frac{\partial}{\partial y}\left(\frac{\tau^x}{f}\right). \tag{2.13}$$

Now assume the ocean can be represented by an upper layer of constant density ρ_0 above a motionless abyssal layer of density $\rho_0 + \Delta\rho$, where the pressure gradient in the upper layer is related to the free surface η by $\boldsymbol{\nabla} p = \rho_0 g \boldsymbol{\nabla} \eta$ and the free surface is related to the upper layer thickness h by $\boldsymbol{\nabla}\eta = (\Delta\rho/\rho_0)\boldsymbol{\nabla} h$. In this case

$$\int_{-h}^{0} \frac{\partial p}{\partial x}\, dz = \frac{\rho_0 g'}{2} \frac{\partial}{\partial x}\left(h^2\right), \tag{2.14}$$

where $g' = \Delta\rho g/\rho_0$ is the reduced gravity, and the depth integrated zonal pressure gradient in (2.12) can be eliminated to give an expression for the upper layer thickness

$$h_{in}^2 = h_e^2 + \frac{2f^2}{\rho_0 g'(df/dy)} \frac{\partial}{\partial y}\left(\frac{\tau^x}{f}\right)(x_e - x_{in}), \tag{2.15}$$

where subscript 'e' denotes the eastern boundary and subscript 'in' denotes some point in the interior open ocean, west of the eastern boundary. As characterised in Fig. 2.2, equation (2.15) describes a lowering of dynamic sea level relative to the eastern boundary at latitudes where the zonal wind stress is weakening as latitude increases. Conversely it describes a raising of dynamic sea level relative to the eastern boundary at latitudes where the zonal wind stress is increasing as latitude increases.

2.2.2 The western boundary with a vertical sidewall

In the Sverdrup model, vorticity added by wind-stress is balanced by a meridional flow, however in a whole ocean model, as much water must flow south as flows north on average,

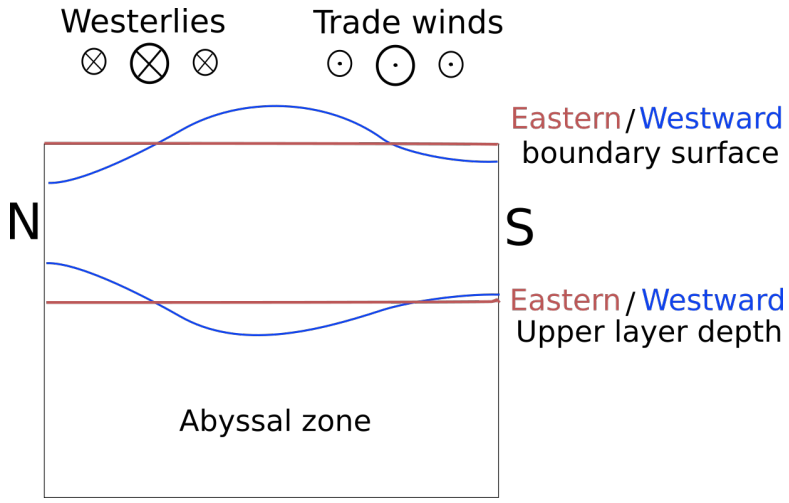

Figure 2.2: *Schematic characterising the sea surface and upper layer depth for 1.5 layer ocean along the eastern boundary and a longitude west of the eastern boundary (but not at the western boundary). Here N denotes north and S denotes south.*

and therefore no equilibrium can be reached. Stommel (1948) showed that to close the model, and extend the solution to the western boundary, a simple representation of friction could be used to act as a 'sink' for the vorticity. Starting from (2.8), the fluid can be considered homogeneous and a simple representation of friction can be included by dividing through by ρ_0 and assuming friction to be proportional to the fluid velocity, giving

$$(h/\rho_0)\boldsymbol{\nabla} p = -f\hat{\boldsymbol{k}} \times h\boldsymbol{u} + \boldsymbol{\tau}^s/\rho_0 - r\boldsymbol{u}, \tag{2.16}$$

where r is the friction coefficient (note that the $1/\rho_0$ factor has been absorbed into r). Now again taking the vertical component of the curl of (2.16) and substituting in the vertically integrated steady form of (2.4) gives

$$\beta h v = \hat{\boldsymbol{k}} \cdot \boldsymbol{\nabla} \times \left(\boldsymbol{\tau^s}/\rho_0 - r\boldsymbol{u}\right), \tag{2.17}$$

where the beta-plane approximation $df/dy = \beta$ is made. Stommel (1948) showed that an intensified western boundary current of increased velocity and shear, of width $\delta_s = r/(h\beta)$, enabled amplified frictional and planetary vorticity tendencies to balance on the western boundary, without altering the balance on the eastern boundary, and therefore create a whole basin circulation in steady state. Illustratively, within the western boundary layer, the equation (2.17) approximately reduces to

$$\beta h v = -r\frac{\partial v}{\partial x}, \tag{2.18}$$

and then integration across the western boundary layer allows the interior ocean to be related to the western boundary by

$$\psi + \delta_s \frac{\partial \psi}{\partial x} = \psi_{in} \tag{2.19}$$

where ψ is the streamfunction $\frac{\partial \psi}{\partial y} = -hu$, $\frac{\partial \psi}{\partial x} = hv$. While Munk (1950) later developed the theory further by using a baroclinic ocean with a more realistic representation of friction, the key aspects of asymmetry in the ocean circulation and dynamic sea level between the eastern and western boundaries remained.

Before moving on it is important to discuss the representation of dissipation employed by Munk and Stommel and to set the context for future chapters where the effect of dissipative processes on coastal sea level are investigated. For the equations (2.1) - (2.4), the horizontal boundary conditions for an ocean basin are no normal velocity and vanishing tangential velocity at each boundary.

Following Salmon (1998a) and introducing the horizontal velocity scale U, horizontal distance scale L, average ocean depth H, time scale T vertical velocity scale HU/L, representative Coriolis parameter f_0, reference density ρ_0 and pressure scale $f_0 U L \rho_0$ in to the momentum equations (2.1) and (2.2) gives the following scales (after dividing through by the Coriolis force scale $f_0 U$)

$$\frac{1}{f_0 T},\ \frac{U}{f_0 L},\ 1,\ 1,\ \frac{A_H}{f_0 L^2},\ \frac{A_V}{f_0 H^2}. \tag{2.20}$$

For the large spatial scales and long (sub-inertial) time periods considered throughout, the first two terms, commonly referred to as the temporal Rossby number and Rossby number respectively, are much less than unity. Ignoring these terms removes the non-linear advective terms from the problem, making it much simpler, albeit representative of large scale ocean behaviour in an averaged sense. As previously noted, in order to support a boundary condition at the western boundary, either or both the horizontal or vertical viscous terms must be retained. For the case of a steady state western boundary with a vertical sidewall and flat bottom basin, Stommel (1948) used a representation of vertical viscosity term (bottom friction) and Munk (1950) used a representation of the horizontal viscosity, to examine western boundary currents. Their results were qualitatively similar and in both cases a boundary layer forms to dissipate energy. Munk's approach of retaining the horizontal viscosity term has been considered more realistic (for the vertical side wall topography) and supports no normal depth integrated flow (as in Stommels model) and vanishing tangential depth integrated flow at the boundary due to being a higher order equation, it also complicates the problem when adding variable depth bottom topography. Note also that Marshall

and Johnson (2013) used both dissipation approaches when investigating western boundary waves for a vertical sidewall, flat bottomed ocean, and found qualitatively similar results, which is relevant to chapter 4.

Given the qualitative similarity of results between the two approaches for including dissipation, it makes sense to first use the simpler representation in chapters 3 and 4 before using a full non-linear model in chapter 5 which can support non-linear inertial, horizontal and vertical viscous boundary layers. In fact it will be found in chapter 5 that despite the inclusion of these addition processes, the results remain consistent with the simple models employing a simple representation of dissipation. If then

$$A_V \frac{\partial \boldsymbol{u}}{\partial z}\bigg|_{z=-H} = \frac{1}{\rho_0}\boldsymbol{\tau}_b, \tag{2.21}$$

is the bottom stress, then depth integrating the momentum equations introduces a bottom stress term $-\boldsymbol{\tau}_b/\rho_0$ to the right hand side of the momentum equations. This stress is regarded as a drag due to the bottom surface and is therefore a form of friction. To relate the stress to the current speed, it is common to use a form of Rayleigh dissipation function where for example

$$\tau_b^y = C_d \rho_0 v^2 \tag{2.22}$$

gives the alongshore bottom stress proportional to the square of the alongshore velocity, with C_d a drag coefficient. Note that here with a depth independent velocity the stress enters as a body force. The added complexity of employing a non-linear friction relation can be simplified for modeling purposes by the linear form

$$\tau_b^y = r \rho_0 v_g \tag{2.23}$$

where v_g is the geostrophic alongshore velocity and $r \approx 2C_d v_c$ is the linear friction parameter where v_c is a characteristic speed of alongshore bottom current (Gill, 1982). For a tidal current of 0.1 m/s and drag coefficient of 0.002 gives $r = 0.0004$, which is the standard value used in the NEMO model for this particular friction parameterisation. The linear representation is justifiable for capturing the character of dissipative effects on the large scale flows, clearly however the finer scale nuances of the non-linear relation are lost. Clearly then there are significant simplifications in deriving the form of the dissipation term and this underscores the importance of exploring the sensitivity of modelled coastal sea level in areas (western boundaries) where significant dissipation is thought to occur.

As a final note, while the simpler representation of friction supports only a single boundary condition at the coast (no normal depth integrated flow), when a bottom topography

that tends to zero at the coast is employed, the tangential velocity will also vanish at the coast as a result. Hence the distinction between the vertical sidewall models of Munk and Stommel is not the same when more realistic bathymetry is included.

2.2.3 The western boundary with sloping bottom topography

So far the boundaries have been considered as vertical sidewalls, however at real boundaries, while the continental slope is steep, it is not vertical, and the slope is separated from the coast by a shallow, relatively flat, shelf.

In the case of an ocean that is not uniform in depth, $h = h(x, y)$, multiplying equation (2.16) through by ρ_0/h and then taking the vertical component of the curl gives the potential vorticity equation

$$\boldsymbol{J}\left(\Psi, f/h\right) = \hat{\boldsymbol{k}} \cdot \boldsymbol{\nabla} \times \left(\frac{\boldsymbol{\tau}}{h}\right), \tag{2.24}$$

where the mass transport streamfunction $\boldsymbol{U} = \hat{\boldsymbol{k}} \times \boldsymbol{\nabla}\Psi$ has been introduced and $\boldsymbol{\tau}$ represents wind - bottom stress. Here $\boldsymbol{J}(a, b) \equiv \hat{\boldsymbol{k}} \cdot (\boldsymbol{\nabla}a \times \boldsymbol{\nabla}b)$ is the Jacobian operator. Unlike the flat bottom models of western boundaries (with boundary layers in a mathematical sense), equation (2.24) implies that within a western boundary region that has a sloping bottom, the flow tends to follow f/h contours, with modification due to bottom friction. Salmon (1998a) discusses the influence of topography on the depth averaged flow for both homogeneous and non-homogeneous oceans. In the latter case, allowing density to vary introduces a new term into (2.24), referred to as the joint effect of baroclinicity and relief (JEBAR) term.

When the density field is specified, in a diagnostic sense, the JEBAR term may be regarded as the forcing due to the baroclinicity of the flow, and equation (2.24) can be written

$$\boldsymbol{J}\left(\Psi, f/h\right) = \hat{\boldsymbol{k}} \cdot \boldsymbol{\nabla} \times \left(\frac{\boldsymbol{\tau} - \boldsymbol{\nabla}\chi}{h}\right), \tag{2.25}$$

where $\chi = \int_{-h}^{0} \rho g z \, dz$ (Huthnance, 1984; Mertz and Wright, 1992). The JEBAR term, more commonly written as $J(\chi, h^{-1})$, implies strong forcing over steeply sloping bottom topography (advection of the density field along the slope). Huthnance (1984) notes that the density gradients and longshore windstress behave similarly over changes in bottom depth, where depth variation causes vorticity input, resulting in a longshore current, and bottom friction matches the imbalance between the forcing and the pressure gradient that forms across the slope.

Another way to consider the JEBAR term for low frequencies is as a correction term. Mertz and Wright (1992) and Cane et al. (1998) note that JEBAR corrects for using the

depth-integrated velocity in the topographic vortex stretching calculation, rather than the bottom velocity. This implies that JEBAR is a measure of the departure of the true depth integrated motion from the depth-integrated motion of a homogeneous ocean. Cane et al. (1998) argues that considering the JEBAR as a forcing term can artificially imply a greater role for topography than is correct, because transport is largely confined to upper parts of water columns. Another issue that arises when considering stratification is whether the nonlinear advection of density can justifiably be ignored for planetary-scale flow and what effect this might have (Salmon, 1998a).

2.2.4 Layered models

Another approach used to examine the effects of stratification while avoiding this issue is through the use of layered models. Parsons (1969) used a model based on the assumption of an ocean with two layers differing discretely in density, where the lower layer was considered infinitely deep and motionless and the upper layer conserved mass. The circulation was again steady, the topography was flat with vertical sidewalls, and friction acted between the layers. In this case, for upper layer thickness h, the continuity equation $\boldsymbol{\nabla} \cdot (h\boldsymbol{u}) = 0$ effectively includes the advection of density. Qualitatively, solutions at the western boundary consisted of a thickening of the upper layer in the subtropical band (wind-stress curl negative) and a thinning of the upper layer in the subpolar band (wind-stress curl positive). With large enough forcing, '*outcropping*' occurs, whereby the upper layer disappears in the subpolar band, exposing the motionless layer below, simulating boundary current separation as in the case of the Gulf Stream.

The Parson type model has received various extensions, for example by Veronis (1973) and Veronis et al. (1976) to world ocean circulation and cooling effects along the separation boundary (Nurser and Williams, 1990). However, a clear issue with a single active layer model is the constraint of no flow in the lower layer, even in the outcropped region where the lower layer is exposed to surface stress. Huang (1984) generalised to the case of two moving layers and showed that while the upper layer closely resembled the upper layer of Parson-like models, the lower layer was in motion in the outcropped area, and also extended to lower latitudes as a distinct boundary current.

In general, the Parson model approach to representing stratification has been supported by special case solutions of models representing interior ocean flow beneath the surface layer with continuous stratification and non-linear density advection (thermocline equations), i.e. Welander (1971) - see also discussion by Salmon (1998a). While these layered models

typically neglect bottom topography, inverse reduced gravity models have also be used e.g., Speer et al. (1993). From the perspective of understanding the effects of bottom topography and friction at western boundaries, the dynamics of a grounded upper layer of the ocean are important. Indeed, as will be discussed further, barotropic dynamics appear to play an important role on the shelf and upper slope.

The theory of steady circulation has shown that latitudinal gradients in dynamic sea level along western boundaries due to wind driven gyres, amplified by gradients in heat and salinity, make western boundaries of ocean basins particularly interesting for investigating the influence of remote ocean dynamics on coastal sea level. Attention is now turned to observational and modelling studies of dynamic sea level along the western boundary of the North Atlantic.

2.3 The tilt in mean sea level

Measuring the mean sea level along the east coast of North America, and relating it to the ocean circulation, has a long and rich history e.g., Bowie (1927). Sturges (1974) estimated a downward trend of 2.0 ± 0.4 cm per degree of latitude from Florida to Cape Hatteras based on Gulf Stream surface flow measurements, the cross-stream flow gradient and geostrophic balance. It was argued that a tilt on the shoreward side of the Gulf Stream existed as a result of the latitude dependence of the Coriolis parameter and the estimated tilt (2.2×10^{-7}) was supported by estimates of the downward slope based on calculations using steric height (2.5 ± 0.5 cm/deg latitude). The estimated tilt offered by Sturges (1974) was, however, of the opposite sign to estimates from geodetic leveling, and highlighted the issue of large geodetic levelling errors relative to the magnitude of the sea level gradient (Sturges, 1977).

North of Cape Hatteras, in the Middle Atlantic Bight, estimations of the gradient suggest an upward tilt in sea level from south to north of 1.44×10^{-7} (Scott and Csanady, 1976) and 3.7×10^{-8} (Lentz, 2008). Whether this tilt originates from remote off-shore forcing or locally on the shelf has been a source of debate. Lentz (2008) noted that the along-shelf gradient in pressure did not vary across the shelf and was therefore consistent with models suggesting that an alongshelf pressure gradient formed as a result of large-scale circulation that would also not vary across the shelf (Csanady, 1978; Beardsley and Winant, 1979).

Csanady (1978) used an appealingly simple ***theoretical model*** of barotropic flow over the shelf, bounded by no normal transport at the coast and an imposed pressure at the shelf edge. For a steady, non-divergent flow, and by assuming geostrophic balance in the

zonal momentum equation and a linear ageostophic friction term in the meridional momentum equation, the pressure could be shown to behave analogously to one-dimensional heat conduction, where analogous diffusion was cross-shore and each latitude represented an analogous point in time, i.e.,

$$\frac{\partial^2 \eta}{\partial x^2} + \frac{f}{r}\frac{dh}{dx}\frac{\partial \eta}{\partial y} = 0. \tag{2.26}$$

In this picture, diffusion is analogous to the penetration of the along-shelf edge pressure gradient to the coast, where larger friction implies great penetration, and a balance exists between bottom stress rv and the longshore pressure gradient. While the heat conduction analogy is powerful for describing the effect of bottom stress on the shelf, the solution cannot be connected with the quasi-frictionless adjacent ocean, muddying the argument that the sea level tilt on the shelf is being remotely driven. Indeed this issue is a topic of discussion in Chapter 3.

Another issue not addressed was the role of the continental slope. Wang (1982) used the same model with a continental slope to show that an alongshore pressure gradient in the open ocean would drive a strong alongshore flow on the slope, but would not penetrate significantly onto the shelf. In terms of the heat conduction analogy, the steep continental slope has low conductivity. Csanady and Shaw (1983) showed a similar effect working in the opposite sense, from shelf to slope, and Chapman et al. (1986) used a similar model, with variable friction coefficient, to argue that the mean flow on the Middle Atlantic Bight was a downstream extension of the poleward mean flow on the Scotian shelf. Using a more sophisticated numerical model and observations Xu and Oey (2011) have argued that the mean upward tilt is primarily the combined result of freshwater discharge and Coastal Labrador Seawater transport, with offshore forcing producing a smaller sea level gradient.

There has been an improvement in the accuracy of ***geoid models*** in recent years as the Gravity and steady-state Ocean Circulation Explorer (GOCE) satellite mission improved on gravity field measurements (Bingham et al., 2011). Woodworth et al. (2012) compared ocean circulation model derived mean sea level tilts with tilts derived from tide gauge measurements referenced to the geoid and found convergence in the consistency of the two approaches. They noted a significant downward tilt (south to north) in mean sea level around the Florida Straits, where the Gulf Stream flows particularly closely to the coast, as well as a more erratic (in terms of estimates) tilt around Cape Hatteras. Higginson et al. (2015) extend this comparison to a suite of geoid and ocean models and ultimately show a mean tilt of 3.5×10^{-7} downward from Florida Keys to Cape Canaveral and a small to non-existent tilt at Cape Hatteras. They noted, however, considerable spread between

ocean model derived tilts at Cape Hatteras and suggested that different resolutions and approaches to data assimilation could be an underlying cause. They consequently noted caution should be taken when interpreting drivers of sea level variability in this region. In explaining the larger sea level tilt around Florida, Higginson et al. (2015) hypothesised that narrowing of the bottom topography around the Florida Straits could be responsible for increased frictional forcing, thus supporting a larger sea level gradient to balance it.

Dynamic sea level along the North American east coast has recently come into focus because of the identification of sea level rise hot spots north and south of Cape Hatteras that have been linked to a number of phenomena and increase the vulnerability of coastlines. In the following section, coastal sea level variability along this coastline is reviewed.

2.4 Sea level hotspots and variability

2.4.1 North of Cape Hatteras

"Hot spots" of accelerated sea level rise have been identified along different sections of the North American east coast in recent years and threaten to raise the background sea level, thus making nearby coastal communities vulnerable to flooding from extreme short term events such as storm surges (Little et al., 2015). Using observations, Sallenger Jr et al. (2012) identified rates of sea level rise 3-4 times larger than the global average during the 1980-2009 period along a 1000 km stretch of coastline north of Cape Hatteras. While the causes are debated, they argued that the hotspot was consistent with a slowdown in the Atlantic Meridional Overturning Current (AMOC) - the nature of AMOC variability, itself, is a hotly researched topic e.g., (Jackson et al., 2016; Smeed et al., 2018). The central idea is that sea levels are low north of Cape Hatteras due to strong geostrophic currents from the Gulf Stream and North Atlantic Current. Warming and freshening of surface water in the subpolar gyre reduces deep convection associated with the AMOC and therefore the AMOC weakens and pressure gradients decrease, raising sea level (Sallenger Jr et al., 2012).

Local forcing

In addition to AMOC variability, a number of other remote and local forcing phenomena have been linked to sea level rise north of the Cape. More generally, the complex nature of assigning causality has become clearer, with coupling between forcing mechanisms difficult to unpick. Kenigson et al. (2018) argue that changes in (particularly alongshore) wind stress patterns on the shelf, linked to the North Atlantic Oscillation (NAO), are strongly

connected with sea level anomalies north of Cape Hatteras. This supports conclusions by Piecuch et al. (2016) that annual coastal sea level changes north of the Cape are driven by local winds on the shelf and slope. They compared annual sea level records from tide gauges over the 1980-2010 period with data-assimilating ocean reanalysis products and a global barotropic model forced with wind stress and surface pressure. They found the barotropic model to have as much skill as the reanalyses products in explaining 50% of the variance in the annual tide gauge record in that region, thus highlighting the importance of barotropic dynamics on coastal sea level over interannual and longer time periods. The important role of alongshore winds, as well as air surface pressure (inverse barometer effect), in driving sea level rise variability north of the Cape was further demonstrated by Piecuch et al. (2019).

Remote forcing

Local on-shelf and on-slope forcing has been identified as an important driver along the northern coastline, however remote forcing has also been identified. Frederikse et al. (2017) highlighted a strong correlation between decadal steric variability in the subpolar gyre and coastal sea level north of Cape Hatteras. Over a 50 year period the signal showed an upward trend and acceleration, and they suggested this variability might originate in the Labrador sea and then propagate southward. While Andres et al. (2013) found that interannual changes in sea level north of the Cape appeared to be forced locally, they also found a correlation map resembling that in Frederikse et al. (2017), suggesting an additional source of variability from the open ocean. They also suggested that on-shelf variability might be influencing the Gulf stream downstream of Cape Hatteras. On the basis of correlation maps showing separation north and south of the Cape, they speculated that on shelf anomalies might be affecting potential vorticity at the Gulf Stream separation point, hence causing variability in the separation latitude of the Gulf Stream. This would be in contrast with studies suggesting the reverse, that variability in Gulf Stream separation position results in sea level variability on the shelf (Ezer et al., 2013). Specifically, Ezer et al. (2013) suggests that a strong Gulf Stream leads to lower coastal sea level in the Middle Atlantic Bight as a result of geostrophic balance.

The role of warm-core rings, offshoots of northward meanders of the Gulf Stream that propagate southwestward between the shelfbreak and Gulf Stream north of Cape Hatteras, have also been investigated as remote sources of on-shelf variability in the Middle Atlantic Bight (Xu and Oey, 2011; Zhang and Gawarkiewicz, 2015). Xu and Oey (2011) suggest that

warm core rings arriving at the shelf produce positive sea surface height anomalies over the shelf north of Cape Hatteras. They argue that the joint effect of baroclinicity and relief (the JEBAR term noted in subsection 2.2) is the dominant ageostrophic term accounting for the cross-isobath fluxes.

2.4.2 South of Cape Hatteras

South of the Cape, Park and Sweet (2015) showed that tide gauge data in Florida Bay and the straits recorded an accelerating mean sea level rise between 2004-2014 and that while this was consistent with a decline in transport by the Florida current from cable measurements, it was not verified by direct measurements from ship surveys. The sea level rise acceleration south of the Cape was supported by Valle-Levinson et al. (2017), who demonstrated that during the period 2011-2015, sea level rise decelerated north of Cape Hatteras while accelerating to 3 times the global mean south of Cape Hatteras. They used long term records to point out the existence of hotspots at different latitudes along the coast over the past century and link the occurrence of hotspots with cumulative effects of El Niño, modulating net transport into the western boundary, and the latitude of hotspots with the NAO.

Large scale remote forcing

The recent variability along the southeast coast of the US has also been attributed to a 0.2 °C per year warming of the Florida Current (Domingues et al., 2018). This interpretation is developed by Volkov et al. (2019) who suggest that large-scale meridional heat divergence has driven sea level rise along the southeast coast. They identify anomalously strong heat transport by the Florida Current as increasing off-slope thermosteric sea level, which is coherent with coastal sea level. They point to a large-scale (North Atlantic basin wide) tripole mode of variability in sea surface height, steric sea level, and thermosteric sea level, where tripole refers to the spatial pattern of the variability, which is separated into three bands: tropical, sub-tropical and sub-polar, with the tropical and sub-polar out of phase with the sub-tropical band. While they note that large scale wind stress forcing is connected to the meridional heat divergence, it seems likely that the NAO exerts a similar tripole mode of variability on the wind-stress curl, whereby positive and negative phases of the NAO oscillation act to shift the latitude of the zero wind-stress curl throughout the basin. The effect of the NAO on ocean circulation has been discussed by Marshall et al. (2001).

Remote forcing from the open ocean has also been demonstrated to have an effect on

the amplitude of the annual sea level cycle south of Cape Hatteras, all the way into the Gulf of Mexico. Calafat et al. (2018) point to westward propagating Rossby waves as sources of buoyancy anomaly that coherently modulate the coastal sea level when reaching the western boundary. They also point out the larger upper ocean transport that accompanies the larger annual cycle sea level amplitudes, and highlight the connection between western boundary sea level and the AMOC. Indeed Bingham and Hughes (2009) have suggested a 2 cm drop in sea level along the US east coast corresponds to a 1 Sv increase in the AMOC. More generally an understanding of the connection between coastal sea level and the AMOC, and the role of propagating buoyancy anomalies (Rossby waves and coastally trapped boundary waves) has seen significant development in the last decade (Johnson et al., 2019).

2.4.3 Idealized models of western boundary sea level

The various forcing phenomena cited as being connected to variability in coastal sea level suggest a number of modes of variability are present. Comparing model experiments with observations, Woodworth et al. (2014) show that while local wind forcing is important in driving on-shelf variability on interannual and longer timescales, smaller and lower frequency signals occur along different sections of coast due to large spatial scale processes in the interior ocean. To better understand the physics driving the variability, a number of studies have used simplified models to directly relate coastal sea level anomalies with open ocean and local sea level signals.

Using a vertical sidewall western boundary in a reduced gravity model, Minobe et al. (2017) derive an explicit relationship to describe the western boundary coastal sea level as consisting of a contribution from the open ocean and a contribution from poleward. While the model is in steady state, they explain the dynamical physical process as consisting of mass being added to the boundary by long Rossby waves (from the open ocean) and then redistributed equatorward by boundary waves. In doing so they connect the process of buoyancy anomaly propagation described by Marshall and Johnson (2013) to sea level. In an earlier study, Hong et al. (2000) derive a very similar relationship, and also include a tuning parameter to account for topographic effects. In both studies, despite the simple nature of the models, the explicit relationships are shown to give a good account of the character of coastal sea level along the US east coast when an open ocean sea level is supplied. In addition, Hong et al. (2000) showed the importance of the meridional variation in the wind-stress curl in driving coastal sea level variability along the US east coast, which has also been suggested by Thompson and Mitchum (2014). Thompson and Mitchum (2014)

identify variability in the divergence of Sverdrup transport in the open ocean as a driver of coherent time integrated variability along the entire coastline, though their approach of averaging over large areas obscures detail of the spatial structure along the coast.

While the simple analytic models of Hong et al. (2000) and Minobe et al. (2017) relate coastal sea level to open ocean sea level, and improve our understanding of the connection between the coast and interior ocean, the assumption of a vertical sidewall boundary has important implications for the representation of sea level and the propagation of variability along the boundary. As will be discussed in detail in the following chapters, the effects of bottom topography can be very important. This is best appreciated by first reviewing how the ocean adjusts at the boundary via the generation of coastally trapped boundary waves, an understanding of which provides physical insight into how remote anomalies are distributed along the coast.

2.5 Coastally Trapped Boundary Waves

The boundaries of ocean basins act like walls, and an ocean flow must diverge laterally as it approaches the boundary. This implies that circulation and sea level dynamics in the interior ocean are quite different from those at the boundary. In the ocean interior, variability in forcing generates long Rossby waves that arise due to the meridional gradient in the Coriolis parameter, and which propagate the resulting oceanic anomaly westward, towards the western boundary. The group velocity of the long Rossby waves is also westward, and therefore energy from the interior ocean is transmitted towards the western boundary. At the western boundary, these anomalies generate waves that are trapped by the boundary and, for sub-inertial frequencies, propagate the anomaly equatorward (with the coast on the right hand side). In this way, anomalies caused by remote forcing, are distributed along the western boundary.

Variability can also be advected by the current, though because this is a slower process, the focus here is on coastal adjustment via boundary waves. Note also that the focus here is relatively low frequency variability (monthly and longer period forcing) and so only subinertial frequency waves are considered. The literature on the theory of trapped waves using different idealisations is extensive and technical, in the following the key underlying ideas most relevant to sea level at the western boundary are introduced. For detailed reviews and derivations, the following are recommended (Huthnance, 1975, 1978; Huthnance et al., 1986; Mysak, 1980b; Allen, 1980; Brink, 1991; Hughes et al., 2019).

In the following, for a western boundary, the convention of a right handed coordinate sys-

tem with the x-axis oriented cross-shore (directed off-shore), the y-axis oriented alongshore (directed poleward in northern hemisphere) and the z-axis directed upward, is adopted.

2.5.1 Barotropic waves

Assuming a coast that is uniform in depth alongshore (y) but monotonically increasing in depth across shore (x), following Mysak (1980b) the equations (2.1, 2.2 and 2.4) for a homogeneous, uniformly rotating fluid with constant Coriolis parameter f (generally standard in CTW theory), sea floor $z = -H(x)$ and free surface elevation η above $z = 0$, can be approximately reduced to

$$\frac{\partial \boldsymbol{u}}{\partial t} + f\hat{\boldsymbol{k}} \times \boldsymbol{u} = -g\boldsymbol{\nabla}\eta, \tag{2.27}$$

$$\frac{\partial \eta}{\partial t} + \boldsymbol{\nabla} \cdot (H\boldsymbol{u}) = 0. \tag{2.28}$$

In the above equations, an inviscid, unforced fluid is assumed and the nonlinear momentum terms are neglected on the basis that the waves are long, such that the fluid particle speed is small compared to the phase speed. The small non-linear free surface terms are also neglected in (2.28). Equations (2.27) and (2.28) can be written in terms of η as a single equation

$$\Delta\frac{\partial \eta}{\partial t} + \frac{H'}{H}\frac{\partial^2 \eta}{\partial x \partial t} + \frac{fH'}{H}\frac{\partial \eta}{\partial y} - \frac{1}{gH}\left(\partial_{tt} + f^2\right)\frac{\partial \eta}{\partial t} = 0, \tag{2.29}$$

where $\Delta = \partial_{xx} + \partial_{yy}$ and prime denotes d/dx. The boundary conditions in x are $Hu = 0$ at the coast $x = 0$ and decay away from the coast (trapping) $\eta \to 0$ as $x \to \infty$. Huthnance (1975) showed that for solutions of the form

$$\eta = A(x)\exp\left(iky + i\omega t\right), \tag{2.30}$$

equation (2.29) permits an infinite set of low-frequency continental Shelf waves (Robinson, 1964) and a single Kelvin wave that decay away from the coast and propagate with the coast on the right hand side (in the northern hemisphere), with wave number k, frequency $\omega > 0$ and amplitude A. While much of the literature typically focuses on the characteristics of the free waves of the system, the importance of the waves in terms of the coastal adjustment to forcing is that the coastal response will consist of a weighted sum of these wave modes. The characteristics of the waves are therefore important in helping to explain the coastal boundary response - this point is the primary topic of Chapter 4.

Propagation and boundary-interior decoupling

For the barotropic Kelvin wave, the Rossby radius of deformation $L_d = \sqrt{gh}/f$ acts as an exponential decay scale away from the coastal boundary, and the wave propagation speed is of order 200 m/s. For a fixed along-shelf wavenumber, higher Shelf wave modes have an increasing number of nodes (where the amplitude is zero), lower frequency, and slower propagation. Importantly, Huthnance (1975) also showed that for low wave numbers, the phase and energy of Shelf waves propagate in the same direction (when H'/H is bounded for all x). Note that close to the equator, equatorial Kelvin waves are generated and carry signals back toward the east (unlike at the coast, here the equator acts as a trapping waveguide - see discussion in Gill (1982)). The ability of waves to transmit signals and energy along boundaries and the equator underpins theories of the global thermohaline circulation response to decadal time scale variability (Johnson and Marshall, 2002; Marshall and Johnson, 2013).

For the first Shelf wave mode (Mode 1), propagation speed is of order Lf, with L the shelf width, giving order 10 m/s propagation speed for $f = 10^{-4}$ s^{-1} and L = 100 km (Huthnance et al., 1986). Hence, the barotropic Kelvin wave and first few Shelf waves can propagate elevation (bottom pressure) variability along the boundary very quickly. Considering that the Mode 1 Rossby wave speed poleward of about 20° is less than 10 cm/s, there is significant decoupling between the open ocean and boundary in terms of adjustment to variability, as discussed by Hughes et al. (2019). The decoupling between ocean and coast has been identified in observations and ocean models, with a difference in the spectra of sea level between the coast and open ocean (Hughes et al., 2018; Hughes and Williams, 2010), for example in response to El Niño cycles (Enfield and Allen, 1980) and the NAO (Calafat et al., 2012). The role of coastal trapped waves in the boundary adjustment process is further highlighted by the coherence of global sea level signals extending 1000s of km around continental slopes (Hughes and Meredith, 2006; Roussenov et al., 2008). Using analysis of model output, Hughes et al. (2018) suggest that coherence on the shelf is to a large degree the result of suppression of mesoscale variability along the continental slope, enabling the large-scale barotropic mode of variability to be seen more clearly at boundaries. Investigating this largescale and low frequency barotropic boundary adjustment is a primary objective of this thesis.

2.5.2 Effects of stratification

When stratification effects are accounted for, considering first the case of a flat bottomed basin with vertical sidewall boundary, the coastal response is formed by a set of internal Kelvin waves (plus the external barotropic Kelvin wave) with cross-shore scale determined by the internal Rossby radius, typically of order 30 km. In this case, the nodes of zero amplitude are oriented horizontally, rather then vertically as in the case of Shelf waves (in the homogeneous ocean). In reality, both stratification and bottom topography are present, resulting in waves that take on characteristics from both internal Kelvin waves and Shelf waves. Typically these waves have been termed Coastally Trapped Waves (Gill and Clarke, 1974) and were discussed initially for discrete 2-layer models (Kajiura, 1974; Allen, 1975; Wang, 1975) as well as for continuous stratification (Wang and Mooers, 1976; Huthnance, 1978). Following Hughes et al. (2019), the response at the boundary to interaction with the open ocean at low frequencies is well represented to a first approximation by the long wave response with the linear, inviscid horizontal momentum and continuity equations

$$\rho_0 f \tilde{v} = \frac{\partial \tilde{p}}{\partial x}, \tag{2.31}$$

$$\rho_0 \frac{\partial \tilde{v}}{\partial t} + \rho_0 f \tilde{u} = -\frac{\partial \tilde{p}}{\partial y}, \tag{2.32}$$

$$\rho \frac{\partial \tilde{\rho}}{\partial t} + \rho_0 \frac{N^2}{g} \tilde{w} = 0, \tag{2.33}$$

where the $\tilde{\cdot}$ represents perturbation about a stably stratified state of rest. The solutions for the variables are then $(\tilde{u}, \tilde{v}, \tilde{w}, \tilde{\rho}, \tilde{p}) = (u, v, w, \rho, p) \exp(iky + i\omega t)$ and substitution into the momentum equations gives

$$\rho_0 f^2 (u, v) = \left(-ik \left[c \frac{\partial p}{\partial x} + fp \right], f \frac{\partial p}{\partial x} \right), \tag{2.34}$$

where $c = \omega/k$ is the phase speed of alongshore propagation. The alongshore flow v is therefore in phase with the pressure, whereas the cross-shore flow u lags by 90°. The pressure is determined by

$$\frac{\partial^2 p}{\partial x^2} + \frac{f^2}{N^2} \frac{\partial^2 p}{\partial z^2} = 0, \tag{2.35}$$

where N is the buoyancy frequency obeying $N^2 = -(g/\rho_0) d\hat{\rho}/dz$, and $\hat{\rho}(z)$ is the background potential density.

While the results can be complex, Huthnance (1978) showed that in the strong and weak stratification limits, the wave response tends between a baroclinic Kelvin wave and a barotropic Shelf wave like response, respectively. For intermediate stratification, wave nodes

tilt at an angle from the vertical such that the nodes at the surface are typically further offshore than at depth. Weaker stratification implies a reduced tilt (vertical for barotropic waves). The importance of topographic width, depth, latitude and stratification strength can be captured by the Burger number, which is approximated by the first baroclinic Rossby radius L_d divided by the length scale of the sloping topography L

$$S = \frac{N^2 H^2}{f^2 L^2} \approx \left(\frac{L_d}{L}\right)^2. \tag{2.36}$$

This implies that for strong stratification, steep topography and low latitudes, where $S \gg 1$, the internal Kelvin wave response is approached, and for weak stratification, broad topography and high latitude, where $S \ll 1$, the barotropic Shelf wave response is approached. Very strong stratification can therefore be imagined as the topography being 'seen' as a vertical sidewall. A consequence of moving from a Shelf wave to internal Kelvin wave response is a modulation of wave speed (typically phase speed increases with stratification) with internal Kelvin wave speed of order NH, equivalent to order 1 m/s for a density difference between bottom and surface of 0.001 ρ_0, and depth 100 m. The effect of shelf and slope steepness on the coastal response will be examined more closely in later chapters, however sloping topography can be thought to scatter the boundary response into topographic waves (Johnson, 1990). Note also that the effect of long-shore changes in topography is a scattering of waves into a different decomposition (Howe and Mysak, 1973), this will be seen more clearly from the nature of the solutions derived in Chapter 4.

2.5.3 Other modifying effects

As has been discussed in the steady state case in section 2.2, at low frequencies the ***role of friction*** must also be considered and as will be found in later chapters, frictional dissipation is a key mechanism controlling the distribution of variability at western boundaries. While the waves discussed thus far propagate alongshore, Brink and Allen (1978) and Brink (1982) showed that friction resulted in cross-shore phase shifting and damping of the waves. In essence, as depth decreases, the bottom drag term rv/H becomes more important in the alongshore momentum balance relative to the term $\partial v/\partial t$. As the two terms are out of phase, the phase of the alongshore flow changes with depth, across-shore. Frictional damping of waves also results in decreased propagation speed and decreased decay distance. For example, assuming $r = 3 \times 10^{-4}$ m/s with $H = 100$ m implies a decay distance of 300 km for a wave propagating at 1 m/s (Huthnance et al., 1986). Because wave decay can also imply energy dissipation, the wave response at the boundary is important to discussions

of energy dissipation at western boundaries (Zhai et al., 2010), which can also be due to mechanisms other than friction (e.g., Dewar and Hogg, 2010; Deremble et al., 2017).

The advective effect of a uniform ***mean current*** on wave propagation is thought to be small, though slower high mode waves may have their direction reversed. Inclusion of a strong cross-shore shear in the current on the other hand modifies the background potential vorticity and implies modification of the waves in addition to advection (Mysak, 1980b; Huthnance et al., 1986). In the stratified case, vertical shear of the current is associated with horizontal density gradients and may result in new wave forms and hybrid instabilities (Huthnance et al., 1986). Hence the strong boundary current at western boundaries has the potential to modify wave behaviour, particularly slower, higher mode waves.

A number of linear idealized, yet ***sophisticated numerical solutions*** to models including bottom topography and stratification have been applied to investigate the coastal response to forcing. Huthnance (1987b) found that wind-stress or a horizontal density gradient in an ocean basin produced essentially barotropic currents on the slope and shelf and that the evolution distance corresponded with the lowest mode damped Shelf wave. Ocean sea level features of very large scale (greater than 1000 km) were required to penetrate fully to the coast, though around small islands without broad shelves coastal sea levels do follow ocean levels. Kelly and Chapman (1988) used a steady state model including continuous stratification, vertical and horizontal diffusion and linear bottom friction and found that the penetration of offshore pressure forcing onto the shelf was limited and barotropic. They also found a surface-intensified pressure perturbation forcing, as well as greater stratification, increased penetration onto the upper slope. Diffusion was found to be relatively unimportant. The cross-shore decay scale (typically the dominant baroclinic Rossby radius for a fluctuating response) of the response relative to the slope width was found to be a key indicator of penetration, with a narrow slope promoting greater penetration. Chapman and Brink (1987) found consistent results in a similar model investigating the effect of fluctuating offshore forcing on circulation on the shelf and slope. They found increased stratification inhibited motion up and down the slope, leading to intense bottom trapping which larger friction somewhat counteracted, enabling greater transport in the bottom boundary layer. Using the same model as Chapman and Brink (1987) (code by Brink and Chapman (1985)), Huthnance (2004) investigated the sea-surface elevation response to oceanic forcing. At the coast, elevations were typically 2 orders of magnitude smaller than the oceanic elevation for short scale alongshore forcing, increasing as the length scale of forcing increased relative to the alongshore decay lengthscale of the first mode coastal trapped wave. Increasing friction reduced the decay lengthscale and increased penetration. The elevation response was found

to be relatively insensitive to other parameters (e.g., topography scales, stratification and vertical scale of stratification) implying that the response to oceanic forcing is qualitatively similar to the barotropic case.

A limitation in the above models is the assumption of a ***constant Coriolis parameter***. At low frequencies, Clarke and Shi (1991) showed that by allowing the Coriolis parameter to vary with latitude, Rossby waves could be generated at boundaries. Earlier, Miles (1972) had shown a variable Coriolis parameter to result in the amplitude decay of Kelvin waves with latitude ($\propto \sqrt{f}$) even in an inviscid model. In Clarke and Van Gorder's (1994) frictional, stratified model of the eastern boundary, low frequency sea level signals propagated polewards with decreasing amplitude, and long Rossby waves propagated westward into the interior ocean. In this sense the eastern boundary is dynamically more straightforward, with variability propagating away from the boundary. Variability is expected to be locally generated or be in the form of poleward propagating CTW's, excited by eastward propagating equatorial Kelvin waves. On the western boundary, clearly the situation is different and using a vertical sidewall flat bottomed model, Marshall and Johnson (2013) showed that a low frequency first baroclinic mode short Rossby boundary wave could propagate equatorward along the western boundary as a result of including the β-effect, where $\beta = df/dy$. As we will see in Chapters 3 and 4, the β-effect has an important impact on topographic western boundary waves and by extension the low frequency coastal response to offshore forcing.

2.6 State-of-the-art and objectives of the thesis

From the reviewed literature there is an evident interest in the spatial structure and temporal evolution of sea level along western boundaries. Recent improvements in the quality of observations and advances in numerical models have shown that sea level along the US east coast, for example, appears to be driven by forcing that is local to the shelf, as well as by forcing that originates far away (remotely) at poleward latitudes or in the interior ocean. Within the existing literature, there is a gap in our understanding of this connection between coastal sea level and interior ocean dynamics. Steady state idealizations connecting western boundaries with the interior ocean tend to be expressed in terms of the flow, rather than sea level, and those that are framed explicitly in terms of sea level typically neglect the sloping bathymetry of the continental shelf and slope. A result of these theoretical models has been coastal sea level that is insensitive to the value of the friction parameter, which has implications for considerations of numerical ocean model configuration, but is contrary

to other studies showing boundary sensitivity to friction. Furthermore, modelling studies that do include sloping bottom topography tend to neglect the latitude dependence of the Coriolis parameter, which should also be important at western boundaries when considering large scale, low frequency forcing. The first objective of this thesis therefore is to extend the literature by relating long period western boundary sea level with the interior ocean sea level in an idealized model which retains a continental shelf and slope, and includes friction and the β-effect. By doing so it will be established whether western boundary sea level is sensitive to these parameters. This is the topic addressed in the following chapter.

For higher frequency forcing (annual and longer), the theory of coastally trapped boundary waves has been invoked in a number of diagnostic studies within the reviewed literature as a possible mechanism for explaining fluctuations in sea level along western boundaries. Coastal trapped wave theory, however, has tended to evolve independently, and there is a gap in the literature in terms of explicitly and clearly relating coastal sea level with coastally trapped waves. This is particularly true for western boundary waves generated by large scale, low frequency forcing that originates at poleward latitudes and in the interior ocean. At western boundaries, on these spatial and temporal scales, the effects of the topography, friction and the β-effect have not be thoroughly investigated for a barotropic fluid. This is the topic addressed in chapter 4.

Further to the effects of cross-shore variation in bottom topography, the geometry of a realistic continental shelf and slope can vary significantly alongshore, and a strong current can also exist alongside the slope, particularly at western boundaries. The modifying effects of realistic topography and nonlinear effects due to the mean flow are often neglected in the idealized studies reviewed in order to establish tractable problems. On the other hand, studies using sophisticated numerical models and observations require statistical methods to establish correlation rather than causality. The objective of chapter 5 is to use a model of medium complexity to bridge this gap, with the aim of relating on- and off-shelf sea level variability (that has been established in observations) with theory, while accounting for modification by realistic topography and nonlinear effects due to the mean flow.

Chapter 3

Bathymetric Influence on Coastal Sea Level

Bathymetric Influence on the Coastal Sea Level Response to Ocean Gyres at Western Boundaries

3.1 Preamble

This chapter investigates the relationship between mean dynamic sea level along western boundaries and ocean dynamics using an idealized model that includes a continental shelf and slope, as well as bottom friction and a variable Coriolis parameter. As discussed in the previous chapter, these variables have not been thoroughly investigated in terms of western boundary sea level, and the intention here is to determine whether they might be important.

Publication and Author Contributions

This chapter has been published in the December 2018 edition of the *Journal of Physical Oceanography* (DOI: 10.1175/JPO-D-18-0007.1). The paper has three authors: Myself (Anthony Wise), Christopher W. Hughes and Jeff A. Polton. As primary author, I carried out the research, wrote the paper and managed the publication process. My supervisors Jeff Polton and Christopher Hughes, provided valuable supervision, editorial critique and discussion of ideas. The paper appears in the bibliography under Wise et al. (2018).

3.2 Paper Abstract

It is our aim with this paper to investigate how the presence of a continental shelf and slope alters the relationship between interior ocean dynamics and western boundary (coastal) sea level. The assumption of a flat bottomed basin with vertical sidewall at the coast is shown to hide the role that depth plays in the net force acting on the coast. A linear β-plane theory is then developed describing the transmission of sea level over variable depth bathymetry as analogous to the steady advection-diffusion of a thermal fluid. The parameter $P_a = \beta H L^{(x)}/r$, relating the friction parameter r to the bathymetry depth H and width $L^{(x)}$, is found to determine the contribution of interior sea level to coastal sea level, with small P_a giving maximum penetration and large P_a maximum insulation. In the small P_a (infinite friction) limit the frictional boundary layer extends far off-shore and coastal sea level tends towards the vertical sidewall solution. Adding simple stratification produces exactly the same result, but with reduced effective depth, and hence enhanced penetration. Penetration can be further enhanced by permitting weakly nonlinear variations of thermocline depth. Wider and shallower shelves relative to the overall scales are also shown to maximize penetration for realistic values of P_a (≤ 10). The theory implies that resolution of bathymetry and representation of friction can have a large impact on simulated coastal sea level, calling into question the ability of coarse resolution models to accurately represent processes determining the dynamic coastal sea level.

3.3 Introduction

Improvements in geoid determination enabled Woodworth et al. (2012), Higginson et al. (2015) and Lin et al. (2015) to demonstrate that sea level (SL) along coastal boundaries can differ markedly from the adjacent open ocean (interior). In particular Higginson et al. (2015) showed that between the Florida Keys and Halifax, the approximately 1 m northward drop in SL across the Gulf Stream is missing at the coast, replaced by a smaller 20 cm drop some 10 degrees farther south.

While SL (specifically ocean surface dynamic topography) gradients in the deep ocean are approximately in geostrophic balance, the zero normal-flow condition imposed by continents implies this balance does not describe coastal alongshore SL gradients. The threat of rising global SL has motivated the investigation of the drivers of coastal SL globally and is of particular interest along the North American east coast due to the identification of a SL rise 'hot spot' (Sallenger Jr et al., 2012). Advancing our understanding of the basic processes relating coastal to interior SL, particularly where strong western boundary currents and complex bathymetry are present, is fundamental to building confidence in the predictions of numerical models.

For basins modeled with flat bottoms and vertical sidewalls Stommel (1948) showed that a solution for the circulation could be found by balancing the vorticity added by wind stress with bottom friction. This approach resulted in boundary layers running north-south which Munk (1950) further developed by replacing bottom friction with lateral friction, a more realistic assumption for flows which do not reach the bottom. Charney (1955) also used horizontal momentum advection to balance vorticity resulting in an additional western inertial boundary layer.

More recently Minobe et al. (2017) addressed western boundary (coastal) SL for the Munk or Stommel type solution with vertical sidewalls and found an equatorward displacement and attenuation in coastal SL relative to the interior SL. Their relationship depends on the meridional integral of mass anomalies in the ocean interior, thus building on the idea that mass input into the boundary layer is transmitted equatorward (Godfrey, 1975; Marshall and Johnson, 2013). This relationship allows coastal SL at a chosen latitude to be given by contributions of coastal SL at some poleward latitude and the interior SL between the two latitudes. Notably, their relationship also describes coastal SL as being independent of the details of friction. A missing element however, in this special vertical sidewall case, is the influence of continental shelves and slopes, potentially important given the variable bathymetry along the North American east coast (Pratt, 1968).

Csanady (1978) looked at the effect of a linearly sloping bathymetry in a steady f-plane barotropic model and showed that alongshore pressure gradients prescribed at the edge of the shelf resulted in the same gradient being present at the coast, beyond some initial insulated region. Wang (1982) and Huthnance (1987b) later showed that including a continental slope increased the insulation to thousands of kilometers in scale and in a more complex model employing stratification Huthnance (2004) found results similar to the barotropic case. For the case of modeling large scale SL along western boundaries however, allowing the Coriolis parameter to change and maintaining consistency when applying the boundary condition with the deep ocean are, as will be seen, crucial. This added complexity has contributed to limiting the study of SL in western boundary regions over sloping bathymetry. One notable result comes from Salmon (1998b) in his study of linear ocean circulation where sloping bathymetry was described as 'advecting' pressure along isobaths and the β-effect (due to variable Coriolis parameter) 'advecting' pressure westward. In referring to 'advection' Salmon extended an advection-diffusion analogy that had first been made by Welander (1968), and later Becker and Salmon (1997), regarding the mass transport streamfunction. Although Salmon's model included both bathymetry and stratification, the assumption of linearity in the equation for density advection resulted in a somewhat artificial role for diapycnal diffusivity to balance any vertical velocity.

The inclusion of bathymetry (in this paper we intend bathymetry to mean sloping bottom topography) in these models resulted in solutions depending explicitly on the bottom friction parameter. As we will show, a consequence of using a western boundary vertical sidewall is that the coastal SL solution is independent of the details of friction because geostrophic flow is always distributed over the same depth range. Indeed Minobe et al. (2017) list the effects of bathymetry, alterations to the vertical mode structure and nonlinear advection as areas to explore further. In this paper we study the first two points.

We consider SL along the east coast of North America relative to the adjacent interior SL that originates from a wind-driven double gyre corresponding to a SL depression from the subpolar gyre and elevation from the subtropical gyre. Our focus is the effect of bathymetry on coastal SL for a specified ocean interior SL, we are therefore excluding the more local response to near-coastal wind stress. See e.g. (Hong et al., 2000; Thompson and Mitchum, 2014; Frederikse et al., 2017; Valle-Levinson et al., 2017) for discussions on the importance of interior ocean wind stress to coastal SL. Although the North Atlantic region provided our motivation, this idealized study would apply equally well to other ocean basins with western boundary currents.

The remainder of this paper is as follows. In section 3.4 the result of Minobe et al. (2017)

is derived from an angular momentum argument to explicitly highlight the importance of bathymetry on coastal SL. In section 3.5 we formulate a model that includes bathymetry for a single layer interior and an interior with a decoupled upper layer. In section 3.6 the effects of the continental shelf and slope on SL are presented and in section 3.7 this is extended to a simple stratified case. Section 3.8 summarizes and highlights implications.

3.4 Vertical side wall special case

Minobe et al. (2017) found a relationship between interior SL and coastal SL, for the case of an ocean with vertical sidewalls and linear dynamics. Defining η_w as the coastal (western) SL and η_i as the interior SL near the western boundary, but to the east of any western boundary current, their relationship (Eq. (14) in their paper) in the steady state can be written as

$$\left(\frac{\eta_w}{f}\right)_y = -\frac{\beta}{f^2}\eta_i, \tag{3.1}$$

where x and y are the zonal and meridional coordinates respectively, subscripts x and y denote partial differentiation, f is the Coriolis parameter and $\beta = df/dy$ (note the equation given in their paper is the integral of this with respect to y, multiplied by f).

This can be interpreted as the interior SL at each latitude contributing to a step up in coastal SL toward the south, at that latitude, which then decays to zero at the equator in a manner proportional to sine of latitude. The effect of this at the coast is to smooth and reduce the interior signal, and shift it toward the equator.

In this special case, the solution can be found without specifying the form of the friction in detail. In fact, all that is needed for the derivation are the assumptions of no normal flow at the western boundary, and that friction acts in a western boundary layer. A simpler argument can be made which leads to the same conclusion.

If the active layer has constant thickness H and an applied zonal wind stress τ^x, then a simple angular momentum balance tells us that the zonally-integrated wind stress must be balanced by the east-west pressure difference on vertical sidewalls (the Coriolis force integrates out because, in the steady state, as much water must flow to the north across each latitude as flows to the south). The boundary pressure perturbation p_w is related to boundary SL η_w by hydrostatic balance: $p_w = \rho g \eta_w$, with a similar relationship at the east, so the steady-state zonally integrated zonal momentum balance between the western and eastern coasts, x_w and x_e respectively, gives

$$-\rho g H \eta_w = \int_{x_w}^{x_e} \tau^x \, dx, \tag{3.2}$$

where we have assumed that the eastern boundary SL is a constant, and taken it to be zero.

Consistency with the relationship of Minobe et al. (2017) can be shown by noting that, for this configuration, the interior flow is determined by Sverdrup balance. For illustration purposes we will assume a purely zonal wind stress τ^x (the relationship holds for more general wind stress and a matching eastern boundary SL profile, but the derivation becomes rather more involved). In this case, Sverdrup balance is

$$-\frac{\beta v H \rho}{f} = \left(\frac{\tau^x}{f}\right)_y, \tag{3.3}$$

together with geostrophic balance $v = g\eta_x/f$. Integrating gives

$$\frac{\beta \rho g H}{f^2}\eta_i = \left(\int_{x_w}^{x_e} \frac{\tau^x}{f}\, dx\right)_y, \tag{3.4}$$

and then substitution of the zonal momentum balance, Eq. (3.2), into the integrated Sverdrup balance, Eq. (3.4), gives Eq. (3.1); the steady-state form of the relation found by Minobe et al. (2017).

The simpler determination of the western boundary SL, from Eq. (3.2), illustrates straightforwardly the critical nature of the assumption of vertical sidewalls. The net force on the western boundary is determined by the combination of the SL η_w, and the depth range H over which the resulting pressure anomaly acts. With a bathymetric slope at the boundary, this will come to depend crucially on where currents flow. A western boundary current flowing higher up the continental slope will produce a larger SL signal for the same total transport, as the associated boundary pressure signal becomes concentrated in a shallower region, reducing the effective value of H. Recirculating currents on the slope can complicate things even further. Note that although we have found a simpler way to derive the Minobe et al. (2017) result, this relies on certain assumptions about interior ocean dynamics, for example that there is no interaction with bathymetry within the basin to disturb Sverdrup balance and that there is no outflow along the northern boundary, which would imply a non-zero zonal integral of meridional velocity in Eq. (3.2). By relating coastal SL to nearby interior SL, Minobe et al. (2017) have sidestepped these requirements and produced a valuable result, albeit restricted to the case of a vertical sidewall at the west.

For this reason, it is our aim in this paper to investigate how the presence of a continental shelf and slope alters the relationship between interior ocean dynamics and boundary SL.

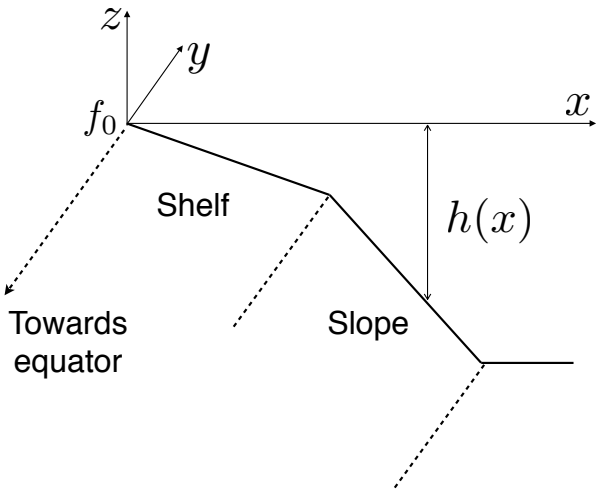

Figure 3.1: *Model coordinates.*

3.5 Model formulation

We begin by introducing the conceptual model. Consider the western boundary region and the interior basin as two separate domains where in the interior, between x_i and x_e, friction and vertical motion at the ocean bottom are assumed small such that Sverdrup balance governs SL for a specific wind stress and eastern boundary SL. For the western domain, between x_w and x_i, which includes bathymetry, SL at the eastern boundary of this region x_i, can simply be specified as equal to the westernmost SL of the interior domain, η_i.

A northern hemisphere coordinate system is oriented with x in the zonal and y in the meridional, as shown by the schematic in Fig. 3.1. Note that though y increases in the poleward direction, a reference latitude, $y = 0$, is set far from the equator. In the derivations that follow it is convenient to express latitude as $-y$ increasing towards the equator. Bathymetry is defined by the function $h(x)$, which tends continuously to zero at the coast, $h \to 0$ as $x \to 0$, and is taken to be uniform alongshore, i.e. independent of y.

For orientation and as an introduction to the general character of the solutions we will find, an example is shown in Fig. 3.2. Figure 3.2a shows SL contours over the combined interior and western domains for a purely zonal wind stress over the interior (producing a double gyre circulation). Figure 3.2b shows only the SL contours for the western domain where bathymetry is present and where there is no wind stress.

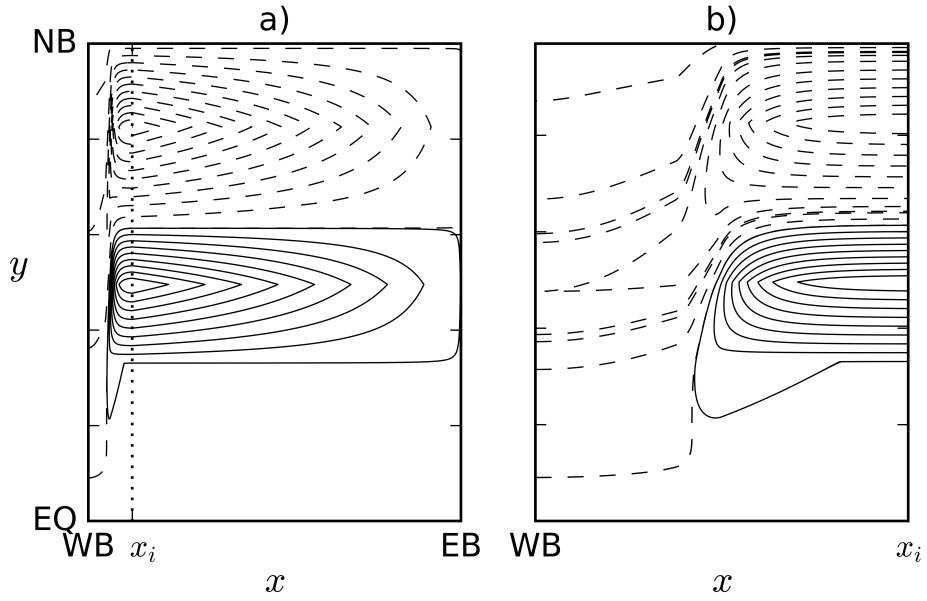

Figure 3.2: *Illustrative SL contours arising from a classic wind-driven double gyre for a single layer ocean basin. Panel a) shows the whole domain. Panel b) shows only the western region. NB, WB and EB denote the Northern ($y = 0$), Western and Eastern boundaries respectively and EQ the Equator ($y = -1$). Walls are assumed along the boundaries, except the western boundary, where a continental slope and shelf allow the depth to tend to zero. The dashed line x_i separates the flat bottomed interior ocean domain (x_i to EB) from the variable depth western domain (WB to x_i). Wind stress $\boldsymbol{\tau} = (\tau^x(y), 0)$ acts in the interior only, with Sverdrup balance assumed. Solid and dashed contours denote positive and negative sea level anomalies respectively. For comparison with later results $P_a = 5$, $S = 0.75$, $H_S = 0.075$ (these parameters are defined later).*

The model for the western domain begins with the steady, linearized, depth-integrated momentum and mass continuity equations

$$f\hat{\mathbf{k}} \times h\mathbf{u} + gh\boldsymbol{\nabla}\eta = \frac{\boldsymbol{\tau}}{\rho}, \tag{3.5}$$

$$\boldsymbol{\nabla} \cdot (h\mathbf{u}) = 0, \tag{3.6}$$

where we define the Coriolis parameter $f = f_0 + \beta y$, density ρ, velocity $\mathbf{u}$, gravity g, inverse barometer corrected SL η, horizontal differential operator $\boldsymbol{\nabla}$ and stress $\boldsymbol{\tau} = \boldsymbol{\tau}_s - \boldsymbol{\tau}_b$ with subscript s for surface stress and b for bottom friction.

Dividing (3.5) by f and then taking the projection of the curl in the z coordinate, $\hat{\mathbf{k}} \cdot \boldsymbol{\nabla} \times$,

gives

$$\boldsymbol{\nabla} \cdot (h\mathbf{u}) + \hat{\mathbf{k}} \cdot \boldsymbol{\nabla} \times \frac{gh}{f} \boldsymbol{\nabla}\eta = \hat{\mathbf{k}} \cdot \boldsymbol{\nabla} \times \left(\frac{\boldsymbol{\tau}}{\rho f} \right), \tag{3.7}$$

which, by making use of the continuity equation to remove the first term on the left and the identity $\hat{\mathbf{k}} \cdot \boldsymbol{\nabla} \times a\boldsymbol{\nabla} q \equiv \hat{\mathbf{k}} \cdot (\boldsymbol{\nabla} a \times \boldsymbol{\nabla} q) \equiv -\mathbf{J}(q, a)$ to rewrite the second term on the left, can be expressed as

$$-\mathbf{J}\left(\eta, \frac{h}{f}\right) = \hat{\mathbf{k}} \cdot \boldsymbol{\nabla} \times \left(\frac{\boldsymbol{\tau}}{f\rho g} \right). \tag{3.8}$$

Equation (3.8) is a form of potential vorticity equation [see (Hughes, 2008) for discussion] and $\mathbf{J}$ is known as the Jacobian operator. Recalling the discussion about friction in section 2.2.2, if now we invoke a linear friction relation for the bottom stress, giving $\boldsymbol{\tau}_b = \rho r \mathbf{u}_g$ with r the friction parameter and $\mathbf{u}_g = (g/f)\hat{\mathbf{k}} \times \boldsymbol{\nabla}\eta$ the geostrophic horizontal velocity, we can expand Eq. (3.8) as

$$\boldsymbol{\nabla} \cdot \left(\frac{r\boldsymbol{\nabla}\eta}{f^2} \right) - \mathbf{J}\left(\eta, \frac{h}{f}\right) = \hat{\mathbf{k}} \cdot \boldsymbol{\nabla} \times \left(\frac{\boldsymbol{\tau}_s}{f\rho g} \right). \tag{3.9}$$

Ignoring wind stress in the western region removes the term on the right of Eq. (3.9) and if also we neglect friction in the zonal momentum equation on the basis that the bathymetrically-steered frictional boundary currents are predominantly meridional, we can simplify Eq. (3.9) to

$$\frac{r}{f^2}\eta_{xx} - \left(\frac{h}{f}\right)_y \eta_x + \left(\frac{h}{f}\right)_x \eta_y = 0. \tag{3.10}$$

Note that while we assume that the western coastline runs meridionally, the results do generalize to the case where the coastline is at an angle ϕ to the meridional. As shown in the appendix of Minobe et al. (2017), a transformation to bathymetry following coordinates, i.e. $y = Y\cos(\phi) + X\sin(\phi)$, allows us to continue neglecting cross-shore friction. A tilted coastline would increase the alongshore path length for a given change in f, so we would expect the main result of such a change to be similar to a latitude-dependent friction coefficient.

Equation (3.10) requires boundary conditions at the coast $x = 0$, along the interface with the interior $x = x_i$, and along the northern boundary $y = 0$. The choice of x_i plays a subtle but important role in how we define the vertical structure of the ocean interior. For example, if we take the geometry considered by Stommel with a flat bottomed basin and vertical sidewall along the western boundary, then bottom friction acts on the single layered ocean and produces a boundary layer of thickness $\delta_s = r/(H\beta)$ (Stommel, 1948) along the vertical sidewall running between the north and south. Outside (east of) this boundary layer, the flow is governed by Sverdrup balance. In this situation the interface

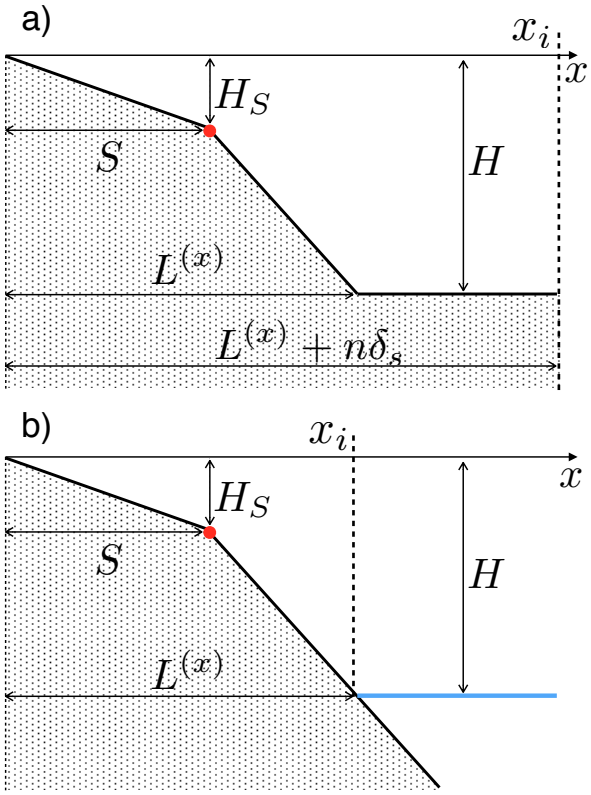

Figure 3.3: *Across-slope section of bathymetry: a) Homogeneous single layer ocean of depth H with $n \gg 1$, and interior boundary located at $x_i = L^{(x)} + n\delta_s$. b) Upper layer ocean of thickness H with $n = 0$ with interior boundary located at $x_i = L^{(x)}$. Red dot denotes shelf break where S is the relative width of shelf and H_S is the relative depth of the shelf break. Throughout this paper S and H_S are normalized by $L^{(x)}$ and H respectively.*

boundary condition at x_i must be farther from the coast than the width of the boundary layer, i.e. $x_i \gg \delta_s$, or $x_i = n\delta_s$ for some large n. If the vertical sidewall is replaced with sloping bathymetry of cross-shore width $L^{(x)}$, we require the interface boundary condition to be located farther from the foot of the slope than the width of the boundary layer, i.e. $x_i = L^{(x)} + n\delta_s$. The schematic in Fig. 3.3a shows a cross section of the western domain for this scenario, with H the maximum ocean depth.

Consider now taking $n = 0$, so that the interface boundary condition is along the foot of the slope. In such a situation we are effectively specifying a boundary layer width of zero, which implies that bottom friction does not act east of the foot of the slope. This can be thought of as specifying the interior ocean as having an upper layer of uniform thickness

H, which makes contact with the bathymetry at a distance $L^{(x)}$ from the coast, and a motionless bottom layer which plays no part in the western domain. The schematic in Fig. 3.3b shows a cross section of the western domain for this scenario. This boundary condition approach is consistent with that used by Csanady (1978) and for our application has the advantage, ostensibly, of allowing the model to capture the effects of basic stratification at sloping bathymetry for an ocean in which most of the flow is confined to the surface layers. Note, however, that this configuration leads to a subtle issue with boundary conditions (discussed later) which can produce difficulties.

We now have two different modeling scenarios. In the single layer case (Fig. 3.3a), the boundary condition is $\eta = \eta_i$ at $x = L^{(x)} + n\delta_s$, which allows space for a frictional boundary layer to the east of the continental slope. In the upper layer case (Fig. 3.3b) we have $\eta = \eta_i$ at $x = L^{(x)}$ (i.e. $n = 0$), as there is no viscosity acting to the east of the topography in the active layer. In both cases, $\eta = 0$ at $y = 0$, i.e. inactivity to the north. Along the coast we have no normal flow, $uh = 0$, however with depth tending to zero at the coast, from Eq. (3.5) we obtain $\boldsymbol{\tau}$ tending to zero at the coast, i.e. a balance between wind and bottom stress. Since we neglect wind stress in the western region, this means bottom stress vr is zero, and hence (since v is zero and in geostrophic balance), $\eta_x = 0$ at $x = 0$.

To better understand the behavior of Eq. (3.10) it is non-dimensionalized, along with the boundary conditions, with the following scales

$$\eta = \Phi\eta^*, \qquad h = Hh^*, \qquad x = L^{(x)}x^*, \qquad y = L^{(y)}y^*, \tag{3.11}$$

where * denotes non-dimensional variables, Φ is the maximum magnitude of the SL along the boundary with the interior ocean, η_i, and the alongshore length scale is given by $L^{(y)} = f_0/\beta$. In the alongshore direction the domain is $-1 < y^* \leq 0$, where $y* = -1$ is the equator, i.e. the solutions presented here do not extend all the way to the equator, $y* = -1$, where the Coriolis parameter vanishes. The non-dimensional variables η^* and h^* are of order unity and the interior boundary is at $x_i^* = 1 + n\delta_s/L^{(x)}$, where $x_i^* = 1$ is the foot of the continental slope.

Until now the derivation has been consistent with bathymetry that changes both along- and cross-shore, i.e. $h = h(x, y)$, we now assume uniformity alongshore, expand the derivatives of $h(x)/f(y)$ and substitute Eqs. (3.11) into Eq. (3.10) to give

$$\left[\frac{r}{(L^{(x)}f_0)^2}\right]\frac{1}{(1+y^*)^2}\eta^*_{xx} + \left[\frac{H\beta}{L^{(x)}f_0^2}\right]\frac{h^*}{(1+y^*)^2}\eta^*_x + \left[\frac{H\beta}{L^{(x)}f_0^2}\right]\frac{h^*_x}{1+y^*}\eta^*_y = 0. \tag{3.12}$$

Dividing through by the coefficient of the first term then gives the final form of the equations,

non-dimensionally, as

$$\eta_{xx} + P_a\, h(x)\eta_x + P_a\, h_x(x)(1+y)\eta_y = 0, \tag{3.13}$$

$$\eta_x = 0 \qquad \text{at} \quad x = 0, \tag{3.14}$$

$$\eta = \eta_i(y) \qquad \text{at} \quad x = x_i = 1 + \frac{n}{P_a}, \tag{3.15}$$

$$\eta = 0 \qquad \text{at} \quad y = 0, \tag{3.16}$$

where the * notation has been dropped and P_a is a non-dimensional parameter given by $P_a = \beta H L^{(x)}/r$. We discuss this parameter in detail below, but to describe how it appears in the boundary condition, Eq. (3.15), we first note its relation to the width of the Stommel boundary layer. Defining the boundary layer width as $\delta_s = r/(H\beta)$ (Stommel, 1948) we obtain $P_a = L^{(x)}/\delta_s$, i.e. P_a is the combined width of shelf and slope divided by the Stommel width. The cross-shore non-dimensional domain width can then be written as $1 + n/P_a$.

To interpret the meaning of the parameter P_a, it is useful to introduce a streamfunction gh/f for a fictitious velocity field

$$U = \left(\frac{gh}{f}\right)_y, \qquad V = -\left(\frac{gh}{f}\right)_x, \tag{3.17}$$

equivalent to $(U, V) = \boldsymbol{\nabla}\,(gh/f) \times \hat{\mathbf{k}}$ which, in flat regions, is simply a westward flow at the long Rossby wave speed. Note this "advection" velocity was described earlier by Tyler and Käse (2000). Equation (3.9) can then be written as an analogue advection-diffusion equation

$$-\boldsymbol{\nabla} \cdot (\kappa \boldsymbol{\nabla}\eta) + \mathbf{U} \cdot \boldsymbol{\nabla}\eta = \hat{\mathbf{k}} \cdot \mathbf{S}, \tag{3.18}$$

with the 'diffusion coefficient' defined as $\kappa = gr/f^2$ and the source term by $\mathbf{S} = -\boldsymbol{\nabla} \times (\boldsymbol{\tau}_s/f\rho)$. Here we interpret SL η to be 'advected' tangentially to the streamlines of gh/f (quotation marks denote analogous diffusion and advection, as opposed to actual advection by the current). This implies that SL is rapidly 'advected' alongshore over steep bathymetry and with an increasing rapidity cross-shore at lower latitudes, where we also note that the 'diffusion coefficient' becomes large. Figure 3.4 shows the contours of gh/f in a western boundary region with bathymetry, along which SL is 'advected' towards a single point at the meeting of equator and zero depth. Note that SL will always be 'advected' towards this point and therefore 'diffusion' (friction) is necessary for coastal SL to be influenced by the interior SL. The non-linear dependence of SL on f (decreasing f allows SL contours to cross isobaths) indicates why constant f-plane models would suggest greater bathymetric

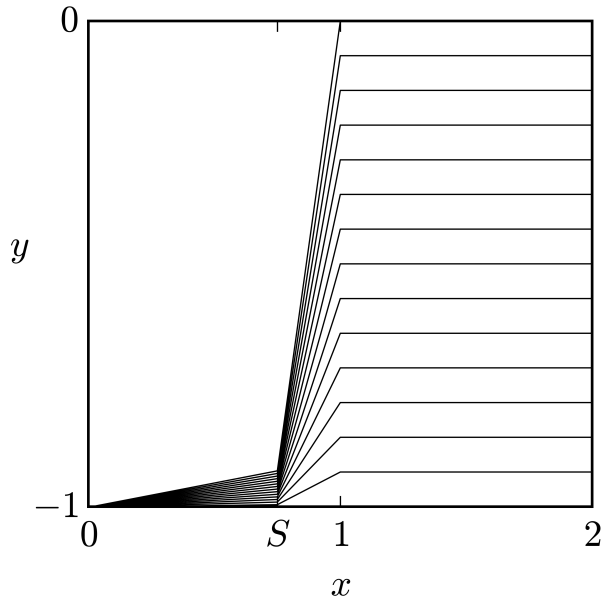

Figure 3.4: *Contours of $gh(x)/f(y)$ for relative shelf width $S = 0.75$ and relative shelf break depth $H_S = 0.075$. Non-dimensional across- and along-shore coordinates are given by x and y respectively.*

insulation between coast and interior, i.e. constant f does not allow the effectiveness of bathymetry to steer SL to change with latitude. Note that, although we are using a beta-plane in order to simplify the geometry as far as possible, Eq. (3.9) and the advection diffusion analogy hold exactly on a sphere, so there will be no qualitative difference in the more general case, although the insulating effect of topography will increase at higher latitudes as β reduces.

In the context of thermal fluids, a non-dimensional Péclet number, Pe, is often defined as a measure of the relative importance of advection and diffusion with respect to unidirectional thermal energy transport; Pe greater than unity implies advection is dominant and Pe less than unity that diffusion is dominant. In our analogy we have defined an analogous 'Péclet number', P_a, as a measure of the relative importance of cross-shore 'advection' and 'diffusion' with respect to the transport of SL. Note that we do not have an alongshore 'Péclet number' due to the omission of zonal friction which implicitly assumes that alongshore 'advection' dominates alongshore 'diffusion'.

In terms of coastal SL, the purely 'advective' part of SL transport is invariant to scale (following gh/f contours). Increasing the importance of cross-shore 'diffusion' therefore, by decreasing P_a, should result in a coastal SL signal that more closely resembles interior SL.

In other words, increasing friction r, and/or decreasing the scales of the bathymetry (H and $L^{(x)}$) should increase interior SL penetration to the coast. Since $P_a = L^{(x)}/\delta_s$, this also implies that decreasing the cross-shore scale of the shelf and slope relative to the Stommel boundary layer width increases SL penetration.

It is important to note that the parameter P_a does not account for the variable coefficients in Eq. (3.13). This means that locally, at any given (x, y), 'advection' and 'diffusion' (and therefore SL penetration) depend on the geometry of the bathymetry $h(x)$, and latitude y.

As will be demonstrated in the next section, the theory suggests two independent controls on the contribution of interior SL to coastal SL; firstly through the parameter P_a, grouping together the effect of overall bathymetric scale and the friction parameter; and secondly the definition of the function $h(x)$ independent of scale, i.e. the relative proportions of the continental shelf and slope.

3.6 Coastal SL parameter study

In this section we present solutions of the advection-diffusion Eqs. (3.13 - 3.16). Subsection a) looks at the effect of the 'Péclet number' P_a without changing the relative proportions of the bathymetry for the single layer model (Fig. 3.3a) where $x_i = 1 + n/P_a$. Subsection b) repeats this investigation now for the upper layer model (Fig. 3.3b) where $x_i = 1$. Subsection c) then looks at the effect of bathymetric configuration by changing the relative width and depth scales of the shelf and slope.

In the following we are concerned only with the western domain, taking the SL along the interior boundary, $\eta_i(y)$, as a given function. For this we assume that wind stress drives subpolar and subtropical gyres in the interior and that along the western edge of the interior at $x_i = 1 + n/P_a$ there is zero net zonal transport. From geostrophic balance this gives the following condition

$$\int_Y \frac{1}{f}\frac{\mathrm{d}\eta_i}{\mathrm{d}y}\,\mathrm{d}y = 0, \tag{3.19}$$

where Y is the latitudinal extent of the domain.

A piecewise linear function is used for η_i with coefficients chosen to satisfy Eq. (3.19). A buffer region of constant SL is used for some distance north of the equator (see black curve in Fig. 3.6).

Bathymetry is defined by a piecewise linear function in x on the basis that it gives the simplest, yet most illustrative means of studying the effects of including a continental shelf and slope. In Figs. 3.3a and 3.3b we define two extra parameters: depth at the shelf break,

H_S, and shelf width S. We take these parameters as non-dimensional ($0 \leq H_S \leq 1$ and $0 \leq S \leq 1$) with scales H and $L^{(x)}$ respectively.

The bathymetry is therefore defined by

$$h(x) = \begin{cases} \alpha_1 x & \text{for} \quad 0 \leq x \leq S, \\ \alpha_1 S + \alpha_2 (x - S) & \text{for} \quad S < x \leq 1, \\ 1 & \text{for} \quad 1 < x \leq 1 + n/P_a, \end{cases} \tag{3.20}$$

where

$$\alpha_1 = \frac{H_S}{S}, \tag{3.21}$$

$$\alpha_2 = \frac{1 - H_S}{1 - S}, \tag{3.22}$$

are the non-dimensionalized shelf and slope gradients. In subsections a) and b) the bathymetric configuration is fixed with $H_S = 0.075$ and $S = 0.75$, which, if we assume an illustrative depth $H = 2000$ m and cross-shore width $L^{(x)} = 130$ km, gives a shelf and slope with drops of 150 m and 1850 m respectively and widths of 97.5 km and 32.5 km respectively. The characteristics of the shelf and slope along the east coast of North America vary considerably, but this configuration captures the basic structure.

Before looking at the dependence of SL on P_a, it is useful to establish a characteristic value for P_a based on $H = 2000$ m, $L^{(x)} = 130$ km, $f_0 = 10^{-4} s^{-1}$, $\beta = 1.667 \times 10^{-11}$ (m s)$^{-1}$ and some value of the friction parameter r, which can be considered as a linear approximation of quadratic friction (Gill, 1982). Two values for r used in the literature: $r = 0.0005$ m s^{-1} (Chapman and Brink, 1987; Xu and Oey, 2011) and $r = 0.001$ m s^{-1} (Csanady, 1978; Huthnance, 2004), give an illustrative parameter value for P_a as 8.67 and 4.33 respectively.

Equations (3.13) to (3.16) will now be solved using a Crank-Nicholson finite difference scheme with non-dimensional resolution $\Delta x = 0.003$ and $\Delta y = 0.00063$, which was found to give resolution independence. We also apply a slight bathymetric gradient over flat bottomed portions of bathymetry for numerical purposes, though it is small enough to be insignificant in terms of the solution.

3.6.1 Sea level dependence on P_a - single layer

In this subsection we use the Stommel type model (Fig. 3.3a) where $x_i = 1 + n/P_a$ and H is the depth scale of the ocean. We take $n \geq 7$ to be large enough that the frictional boundary layer has decayed west of the interior boundary.

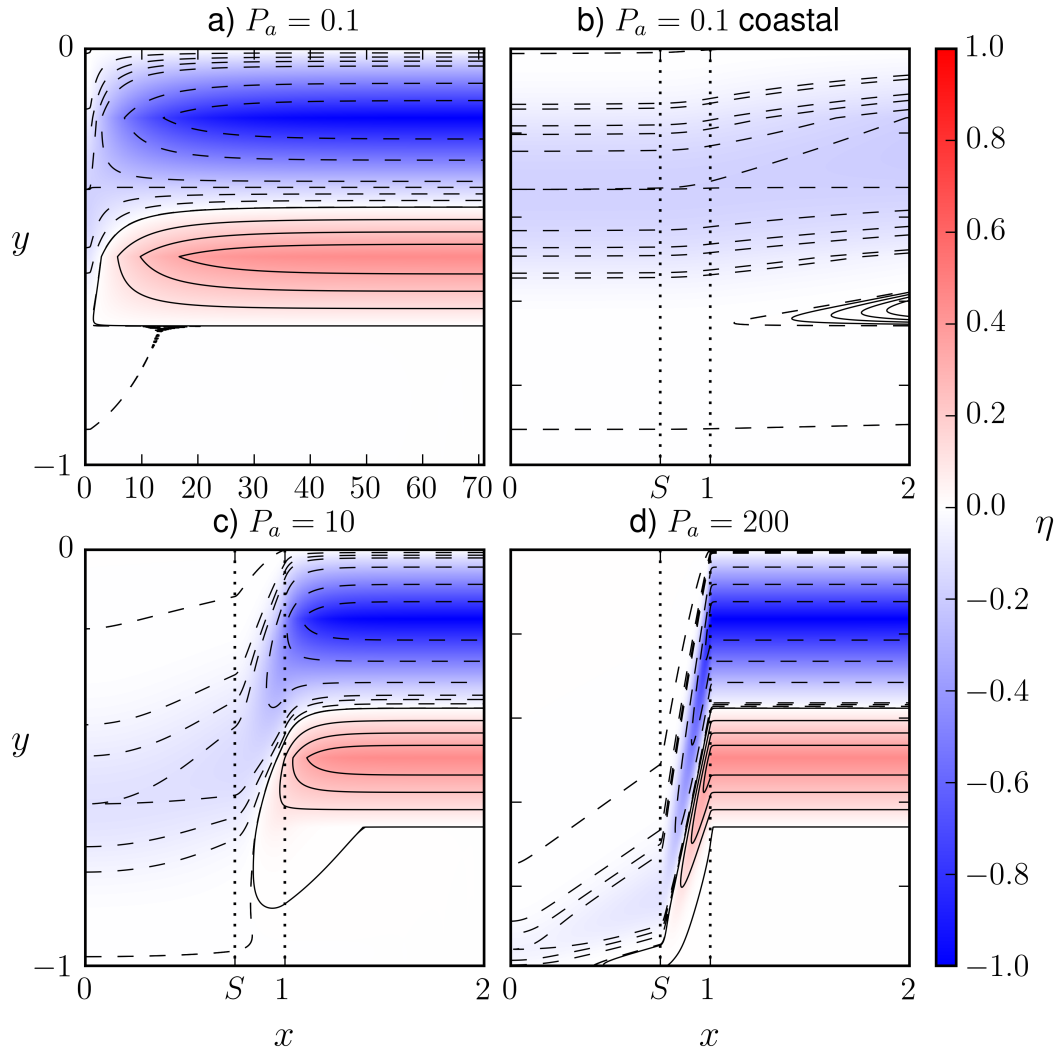

Figure 3.5: *Western domain sea level contours, $\eta(x, y)$ (non-dimensional, dashed negative), for relative shelf width $S = 0.75$ and relative shelf break depth $H_S = 0.075$, where x and y are the non-dimensional across- and along-shore coordinates respectively. Vertical dotted lines indicate shelf break at $x = S$ and slope floor at $x = 1$. a) $P_a = 0.1$, b) $P_a = 0.1$ coastal close up, c) $P_a = 10$ and d) $P_a = 200$.*

Figure 3.5 gives SL in the western domain for three values of $P_a = \beta H L^{(x)}/r$: $0.1, 10$ and 200, where 0.1 is small and 200 large relative to the illustrative characteristic values which are between 4.3 and 8.7. By comparing Figs. 3.5a, 3.5c and 3.5d we see that the frictional 'boundary layer' extends farther offshore when P_a is small, relating to either a large frictional parameter or small scale bathymetry, demonstrating why the cross-shore domain width is dependent on P_a (incorporating δ_s). The solutions in Figs. 3.5b-3.5d also show that smaller values of P_a result in greater penetration of the interior SL to the coast, that is to say, between the interior and the coast, the SL depression and elevation experience less equatorward displacement and less attenuation when P_a is smaller.

From our advection-diffusion analogy, Fig. 3.5d ($P_a = 200$) relates to a highly 'advective' solution where SL contours follow gh/f streamlines closely, resulting in significant equatorward displacement and attenuation of the interior SL. Figure 3.5c ($P_a = 10$) relates to a relatively 'advective' solution and there is less displacement and attenuation of SL. Finally Figs. 3.5a and 3.5b ($P_a = 0.1$) show a relatively 'diffusive' solution with SL experiencing less displacement and attenuation. As suggested by the analogy, increasing the friction parameter and/or decreasing the scale of the overall shelf and slope increases penetration. The implication is that SL within the western domain is sensitive to the representation of bottom friction when continental shelves and slopes are included into the model. Furthermore, it shows that the depth and width scales of the overall bathymetry alter coastal SL, so resolving the continental slope can be important.

Focusing on coastal SL $\eta(x = 0, y)$, Fig. 3.6a shows interior and coastal SL for $P_a = 0.1, 1, 10$ and 100. The coastal SL in each case can be described as a smoothed version of the interior SL with an equatorward displacement and an attenuation that in general increases with displacement, both increase as P_a increases. A comparison of the depression minimum for $P_a = 0.1$ and $P_a = 10$ shows the magnitude reduces by nearly 35% and the alongshore displacement increases by approximately 1600 km (in the case where $\beta = 1.667 \times 10^{-11}$ and $f_0 = 10^{-4}$ s^{-1}). Increasing the friction parameter, and/or decreasing the scale of the combined shelf and slope increases the penetration of SL to the coast.

This result of a displaced and attenuated SL depression supports the result presented by Higginson et al. (2015) of an interior ocean SL tilt (the transition from SL depression to elevation where the Gulf Stream heads off-shore) observed at the coast displaced equatorward by 10 degrees of latitude and attenuated from 1m to 20 cm. The result here suggests that equatorward displacement of the tilt would be reduced in the following circumstances: 1) the combined width of the shelf and slope are reduced, 2) the depth to the foot of the slope is reduced and 3) bottom drag is increased. The same is implied for the magnitude

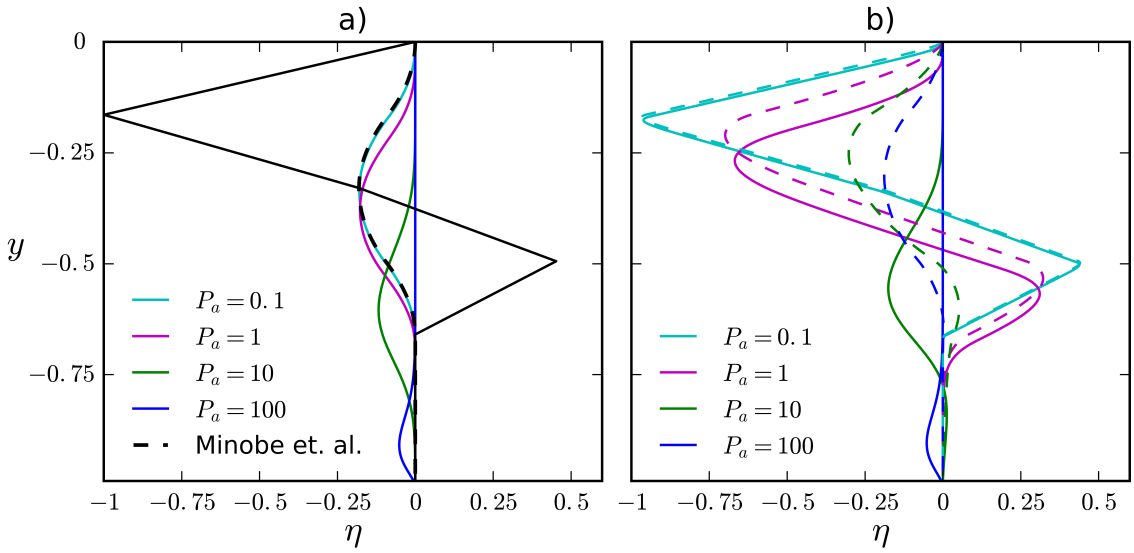

Figure 3.6: *Coastal sea level, $\eta(y)$ (non-dimensional), for $P_a = [0.1, 1, 10, 100]$ with interior sea level, $\eta_i(y)$ (solid black line), where y is the non-dimensional along-shore coordinate (equator at $y = -1$). The relative shelf width is $S = 0.75$ and the relative shelf break depth is $H_S = 0.075$. In panel a) for a single layer homogeneous interior, the black dashed line is the coastal sea level for the case of a vertical sidewall using Minobe et al. (2017) Eq. (14) with our interior sea level, η_i. In panel b) solid lines are coastal sea level $\eta(y)$ for the interior ocean with an active upper layer and motionless lower layer using $\eta_i(y)$ (solid black line) at the interior boundary. Dashed lines are the associated vertical sidewall solution (Minobe et al. (2017) Eq. 14) when using the true interior sea level, Eq. (3.25).*

of the tilt. Note that while Higginson et al. (2015) do not comment on overall bathymetric scale, they do speculate that the width of the continental shelf, i.e. the definition of $h(x)$, plays a role in the latitudinal position of the coastal SL tilt, an issue we cover in subsection c).

An important result can be demonstrated by looking at the limit $P_a \to 0$. This can be interpreted as either the high friction limit or the narrow topography (vertical sidewall) limit ($L^{(x)} \to 0$). In Fig. 3.6a we see that, for low P_a, the solution approaches the friction independent vertical sidewall solution of Minobe et al. (2017). Thus, for a single layer model, the vertical sidewall represents the maximum possible penetration of the interior SL.

3.6.2 Sea level dependence on P_a - upper layer, $n = 0$

In this subsection we model an upper layer of the ocean (Fig. 3.3b) where $x_i = 1$ and H is the scale for the thickness of the upper layer.

The general behavior of SL in this case is qualitatively similar to the single layer case and the 'advection - diffusion' analysis of the previous subsection holds. There is however a distinct quantitative difference in coastal SL. In Fig. 3.6b, the solid lines show coastal SL for $P_a = 0.1, 1, 10$ and 100 (this is the upper layer counterpart to the single layer version Fig. 3.6a) and it is clear that displacement and attenuation of the interior SL is reduced. This is particularly noticeable for $P_a < 10$, where the coastal SL begins to closely resemble interior SL.

This result suggests that, consistent with the results of Csanady (1978), it is possible to have greater penetration of interior ocean SL than the vertical sidewall limit permits. However, there is a subtlety that is being missed in this case: the "interior" SL should be imposed on the ocean side of the boundary where bottom friction is zero, but in using Eq. (3.10) we are effectively imposing a value on the slope side of that boundary.

The subtly and importance of how the boundary between interior ocean and western region is defined can be demonstrated by allowing the bottom friction parameter to decrease as we move away from the coast. Defining friction as $R = R(x)$, requires Eq. (3.10) to be rewritten as

$$\frac{(R\eta_x)_x}{f^2} - \left(\frac{h}{f}\right)_y \eta_x + \left(\frac{h}{f}\right)_x \eta_y = 0. \tag{3.23}$$

We take R to be continuous, constant over the shelf and slope (between $x = 0$ and $x = L^{(x)}$) and decreasing to zero between $x = L^{(x)}$ and x_i, i.e.

$$R = \begin{cases} r & \text{if } x < L^{(x)} \\ rG(x) & \text{if } x \geq L^{(x)}, \end{cases} \tag{3.24}$$

where $G(x) = 1$ at $x = L^{(x)}$ and $G(x) = 0$ at $x = x_i$ (x_i is a point at which the frictional boundary layer has decayed).

The extent to which the frictional boundary layer extends offshore now depends on how $G(x)$ is defined, specifically, where we choose x_i to be ($G(x_i) = 0$ implies geostrophic balance in the depth integrated zonal flow). Moving x_i closer to the slope therefore decreases the width of the frictional boundary layer.

Integrating Eq. (3.23) from $L^{(x)}$ to x_i (a region in which h is constant), and recalling that $\delta_s = r/H\beta$, gives

$$\eta_i = \eta_{L^{(x)}} + \delta_s (\eta_x)_{L^{(x)}}, \tag{3.25}$$

where subscript $L^{(x)}$ denotes evaluation at $x = L^{(x)}$. This relation leads to a surprising result. Equation (3.25) shows that SL on the shelf and slope is independent of the details of offshore friction (east of $L^{(x)}$). We can infer this by noting that if we assume that SL at the edge of the slope, $\eta_{L^{(x)}}$, is known, then SL on the shelf and slope can be found by solving Eq. (3.10) with $\eta_{L^{(x)}}$ as the boundary SL. We can then obtain η_i from Eq. (3.25) without any knowledge of $G(x)$. Surprisingly therefore, this result shows that the details of offshore friction are only important in determining the width of the frictional boundary layer, not SL on the shelf and slope.

This result becomes relevant to the upper layer model, used in this section, if we take the limit of $x_i \to L^{(x)}$, i.e. we take x_i to be infinitesimally close to the edge of the slope at $L^{(x)}$. To denote this we will use a subscript $-$ to represent the shoreward point and subscript $+$ to represent the offshore point. Across these points, the friction parameter drops to zero, so that $R_- = r$ and $R_+ = 0$. Equation (3.23) now becomes

$$\eta_+ = \eta_- + \delta_s(\eta_x)_-. \tag{3.26}$$

This relation shows that despite the distance between η_+ and η_- being infinitesimally small, SL in the ocean interior η_+ is not the same as that on the shoreward side of the boundary η_-. The upper layer model (Fig. 3.3b) therefore fails to specify the true ocean interior SL that is being used in the single layer model (Fig. 3.3a). The degree to which it fails is proportional to δ_s (inversely proportional to P_a) and the result is a jump in SL between western and interior domains, calculated by projecting the slope $(\eta_x)_-$ out to a distance of one Stommel width beyond the boundary.

The jump in SL is required to conserve depth-integrated mass flux. A discontinuity in bottom stress implies a discontinuity in offshore Ekman flux, which therefore implies a discontinuity in the onshore geostrophic flow, and hence a jump in SL. This is also a problem with section 10 of Csanady (1978). In that paper the coastal influence of a linear meridional SL slope is considered with the conclusion that the entire amplitude of the slope penetrates to the coast. There is however no way to connect this solution to a frictionless ocean interior, without invoking a step in sea level.

The upper layer model appears to allow greater penetration of the interior SL signal because it is effectively using a larger amplitude interior SL signal. In fact the upper and single layer models are the same, except that the upper layer model implicitly uses a larger amplitude interior SL. To demonstrate this point, the dashed lines in Fig. 3.6b show the coastal SL for the case with a vertical sidewall when the equivalent interior SL, calculated from Eq. (3.25) or (3.26), is used. The dashed curves show that the vertical sidewall solutions

remain the limit of penetration as in Fig. 3.6a.

3.6.3 Coastal SL and bathymetric configuration

In reality continental shelves and slopes have varied proportions (configurations) and so we look now at the dependence of SL on $h(x)$, i.e. the scales of the shelf and slope relative to each other and independent of P_a.

Changing the relative proportions of the shelf and slope requires the location of the shelf break to change without changing the combined depth and width of the shelf and slope. This simply means keeping P_a fixed and allowing the shelf break parameters H_S and S to vary between zero and one. For example, by increasing H_S from 0.075 to 0.5 the depth scale of the shelf is increased by $(0.5 - 0.075)H$ and that of the slope is decreased by the same amount.

So far we have looked at the penetration of interior SL at the coast for specific values of P_a, S and H_S. In the remainder of this section we explore the parameter space of these three parameters more thoroughly, using the single layer model (Fig. 3.3a) exclusively.

In the following we focus on a single reference point of the coastal SL signal to investigate attenuation and displacement. For this we choose the coastal SL minimum and define it as η_{min}. We are therefore interested in the attenuation of η_{min} and the displacement of η_{min} as shown in Figs. 3.7a and 3.7b. Note that the displacement is measured relative to $y = 0$, whereas the open ocean SL minimum is at $y = -1/6$, meaning that displacements smaller than 0.167 would actually be northward relative to the open ocean SL (though no such displacements occur).

In Figs. 3.7c and 3.7d we plot attenuation and displacement of η_{min} as a function of H_S (the shelfbreak depth relative to the maximum depth H) and P_a with the shelf width S held constant. We use $0.01 \leq H_S \leq 0.99$, $1 \leq P_a \leq 50$ and $S = 0.75$. In Figs. 3.7e and 3.7f we plot attenuation and displacement of η_{min} as a function of S (the shelf width relative to the combined width of shelf and slope $L^{(x)}$) and P_a with the shelfbreak depth H_S held constant. We use $0.05 \leq S \leq 0.95$, $1 \leq P_a \leq 50$ and $H_S = 0.075$. In Figs. 3.7c-3.7f lighter colors denote greater attenuation and displacement (less penetration).

Figures 3.7c and 3.7d show that displacement and attenuation are maximized in the approximate region $0.2 < H_S < 0.7$. As H_S becomes small or large relative to this region, displacement and attenuation decrease. This suggests that geometries where the shelf is quite shallow increases penetration. This appears to hold for the range of P_a considered

Figures 3.7e and 3.7f show that for $P_a < 20$, attenuation and displacement decrease as

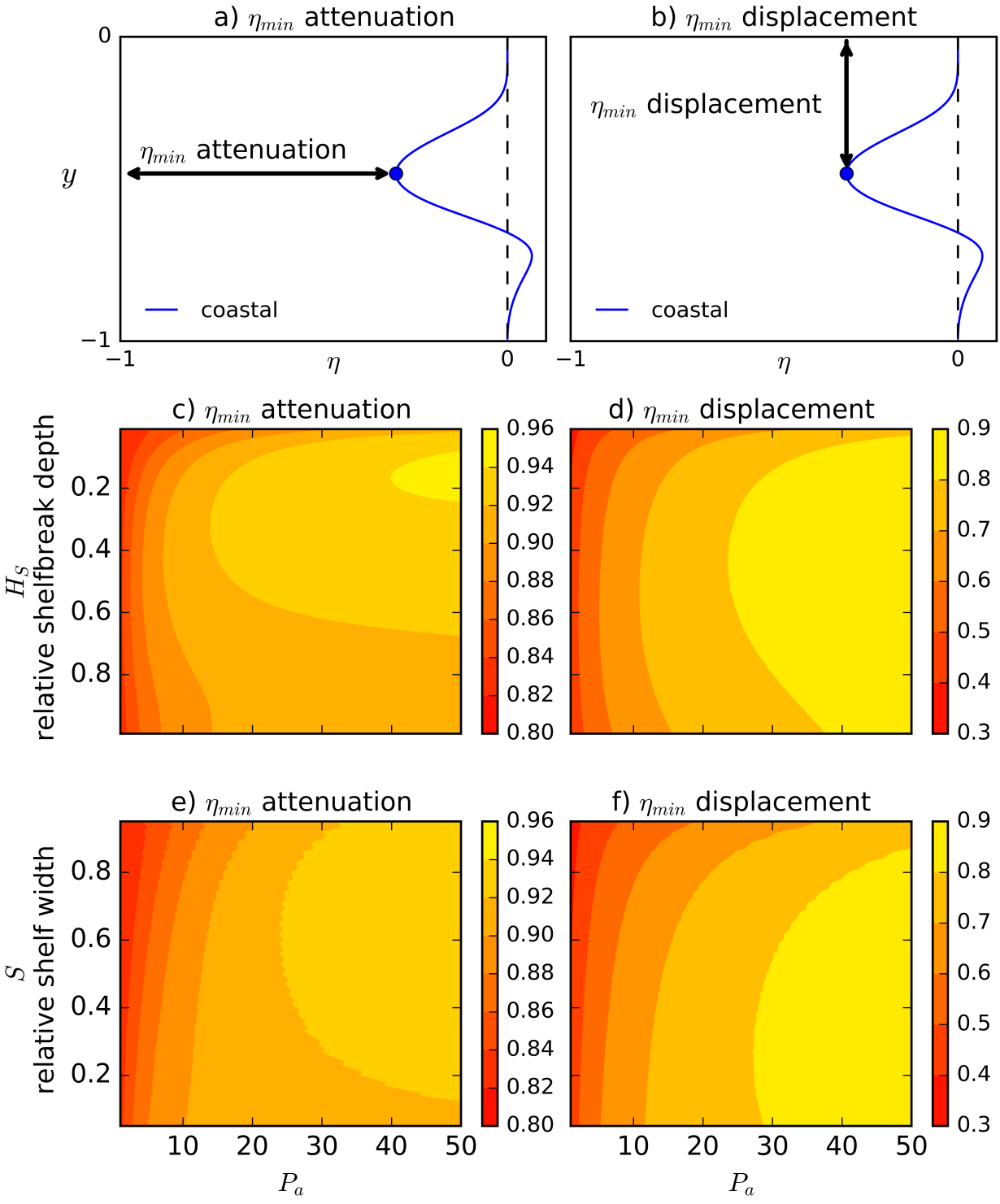

Figure 3.7: *In a) and b) the blue curve represents non-dimensional coastal sea level $\eta(y)$. a) demonstrates how the attenuation of the coastal sea level minimum η_{min} is measured for plots c and e and b) demonstrates how the displacement of the coastal SL minimum η_{min} is measured for plots d and f.*

Figure 3.7: *c) Colormap of attenuation of η_{min} as a function of shelf break depth H_S and P_a with $S = 0.75$. d) Colormap of the displacement η_{min} as a function of shelf break depth H_S and P_a with $S = 0.75$. e) Colormap of the attenuation of η_{min} as a function of shelf width S and P_a with $H_S = 0.075$. d) Colormap of the displacement of η_{min} as a function of shelf width S and P_a with $H_S = 0.075$. In c) to f) lighter colors denote greater attenuation and displacement (less penetration).*

S increases, i.e. as the shelf becomes wider. For $P_a > 20$, smaller values of S also decrease attenuation and displacement

As a whole, the results of Fig. 3.7 show that penetration of interior SL to the coast increases rapidly (non-linearly) as P_a decreases and that this holds for any configuration of shelf and slope. Surprisingly, however, the results also show that wide shallow shelves increase the penetration of interior SL to the coast. More generally the results show that configurations tending towards vertical wall-like geometries have increased penetration. Therefore, while it is true that broader combined shelf and slope, $L^{(x)}$, in comparison to the Stommel boundary layer width (i.e. larger P_a) leads to greater insulation of the coast from the deep ocean, a broader, shallower shelf region for a given overall width has the opposite effect.

The strong dependence of the solution on geometry and scale raises the question of the effect of model resolution on coastal SL; for example a one-degree ocean model has perhaps only one or two grid points on the combined shelf and slope. Assuming for example $P_a = 5$ with a cross-shore width of $L^{(x)} = 130$ km, a shelf width of 97.5 km and a slope width of 32.5 km, we found that a cross-shore resolution of 9 km (3 grid points on the slope) resulted in close to a 15 % decrease in the magnitude of the coastal minimum compared to the high resolution converged solution. In this illustrative example we found 6 grid points on the slope (5.2 km resolution) gave a coastal minimum that deviated from the high resolution solution by only 1 % in magnitude. This indicates that ocean models with resolution coarse compared to the width of the shelf and slope could be distorting coastal SL due to a poor representation of bathymetry.

It is clear that the solutions do depend on the geometry of the shelf and slope, as well as the overall scales and the friction parameter, in the next section we extend the model by considering a 1.5 layer interior. The following analysis will use dimensional quantities.

3.7 Dimensional model with 1.5 layers

It is more realistic to assume background stratification will alter the vertical mode structure and change how the flow interacts with bathymetry. In this section we create a simple stratified model by allowing the upper layer depth along the interior boundary to be non-uniform, i.e. $H = H(y)$.

In contrast to the previous sections, we now directly calculate SL and upper layer thickness in the whole interior for a specified interior-only wind stress using a reduced gravity model with a single active upper layer of constant thickness h_e along the eastern boundary x_e. For this we use a density difference between the two layers of 1.02 kg m^{-3} and apply a zonal wind stress that varies meridionally

$$\tau^x(y) = \begin{cases} \tau_0 \left[1 - \cos\left(\frac{3\pi y}{L^{(y)}}\right)\right] & \text{for} \quad -\frac{2}{3}L^{(y)} < y \leq 0, \\ 0 & \text{for} \quad -L^{(y)} < y \leq -\frac{2}{3}L^{(y)}, \end{cases} \tag{3.27}$$

where τ_0 (N m^{-2}) is the amplitude (see Fig. 3.8 for the wind stress profile). The interior domain is of width 4500 km with constant top layer depth at the eastern boundary of $h_e = 900$ m.

We then take SL along the westernmost edge of the reduced gravity interior model and use it as the interior boundary condition for the western domain η_i (as in previous sections).

For the western domain, we represent an upper layer thickness that changes with latitude by allowing the depth h in the model developed in section 3.5, to vary alongshore, i.e. $h = h(x, y)$. The depth h is defined by projecting the upper layer thickness at the interior boundary, which changes in y, up to the slope. The effect of this change on the theory developed in section 3.5 is that the path along which SL is 'advected' changes to reflect the modified gh/f contours. From Eq. (3.17) we now have a fictitious advecting zonal velocity $U = gh_y/f - gh\beta/f^2$, where the first term is new.

We consider two different cases. In the first case we allow only a slight latitudinal variability in the thermocline thickness. This relates to weak interior gyres (solid lines in Fig. 3.8). In the second case we allow a larger latitudinal variation in the upper layer thickness. This relates to stronger interior gyres (dashed lines in Fig. 3.8). In the latter case, we note that due to the larger latitudinal variation of h, there is a reversal in the direction of U, the zonal 'advecting' velocity, in the northern part of the subpolar gyre. This results in a somewhat artificial frictional boundary layer extending to the northeastern corner (not shown).

Figure 3.9a shows the interior boundary SL, the new coastal SL and the vertical wall

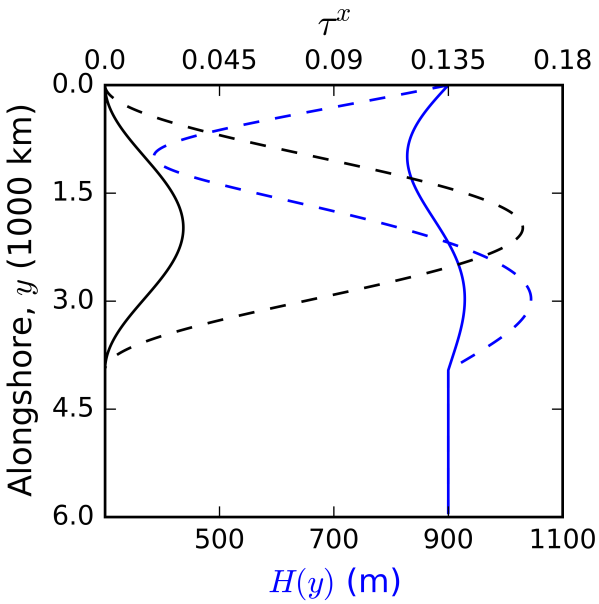

Figure 3.8: *Solid lines are wind stress (black) and resulting upper layer thickness (blue) along the interior boundary x_i for $\tau_0 = 0.015$ $N\ m^{-2}$. Dashed lines are wind stress (black) and resulting upper layer thickness (blue) along the interior boundary x_i for $\tau_0 = 0.082$ $N\ m^{-2}$. Here $y = 0$ is the poleward reference point where $f_0 = 10^{-4}$. The reduced gravity interior has width 4500 km and the eastern boundary upper layer thickness is $h_e = 900$ m.*

solution for the weak interior gyre case. We show in addition the corresponding solution for the single layer model with P_a adjusted for a comparative thickness. The figure shows that slight variability in the upper layer thickness allows for a slight change in the distribution of the coastal SL (the attenuation is slightly smaller). Figure 3.9b repeats Fig. 3.9a for the stronger gyre case. Now we clearly see increased penetration (decreased attenuation) beyond the vertical wall limit.

Vertical mode interaction allows the thickness of the upper layer to be redistributed such that it decreases over a poleward portion of the interior. This decrease enables the interior SL over this poleward portion to penetrate farther towards the coast before making contact with the bathymetry, this can increase penetration of the SL due to the subpolar gyre. On the other hand, the upper layer thickens towards the equator suggesting a decrease in penetration of SL due to the subtropical gyre. In effect our 'Péclet number' is changing with latitude, smallest where the upper layer thickness is thinnest. The reversal of the characteristic direction in the strong gyre case means the validity of this solution is questionable. This raises questions about SL penetration when a linear approximation may

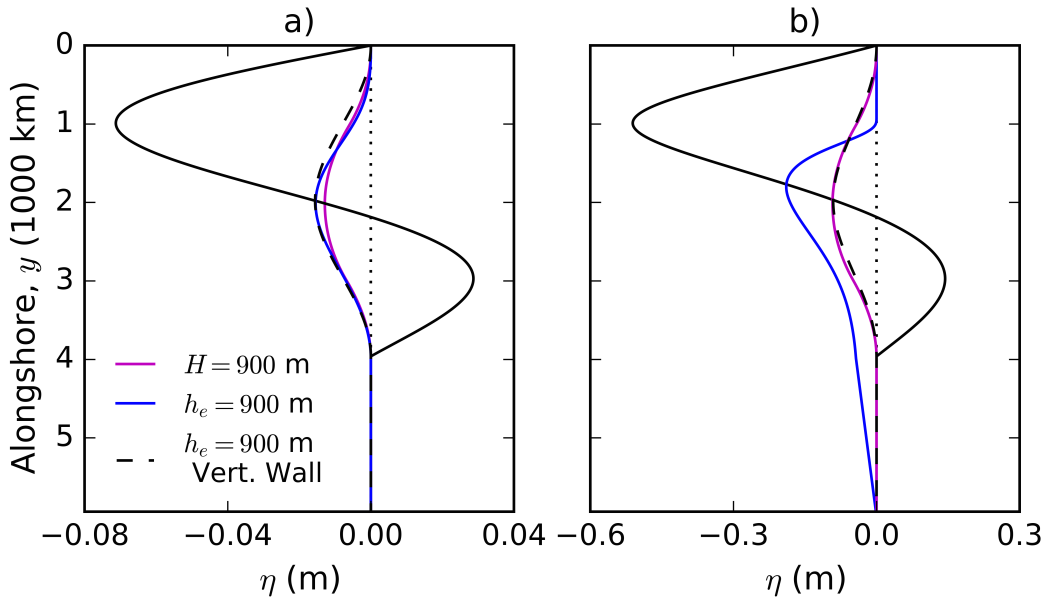

Figure 3.9: *Interior and coastal sea level using a variable thickness upper layer for two wind stress magnitudes: a) $\tau_0 = 0.015$ $N\ m^{-2}$ and b) $\tau_0 = 0.082$ $N\ m^{-2}$ (see Fig. 3.8 wind stress and layer thickness profiles). For both a) and b) the black solid curve is interior sea level η_i, the solid blue line is the resulting coastal sea level, the dashed black line is the resulting 1.5 layer vertical wall coastal sea level and the magenta line is the coastal sea level using the single layer model with a comparable interior sea level. For the non vertical wall coastal sea levels (blue and magenta) we use shelf width 97.5 km, shelfbreak depth 150 m, eastern boundary thickness $h_e = 900$ m, $r = 0.0166$ $m\ s^{-1}$, $H = 900$ m, $L^{(x)} = 113.3$ km, (equivalent $P_a = 0.1$).*

not be appropriate for modeling thermocline depth. We leave this investigation for future studies.

3.8 Discussion and Conclusion

We have shown that the assumption of a vertical sidewall at the coast within a western boundary allows coastal SL to be independent of layer thickness and the friction parameter and that the vertical sidewall solution is a special limit case for the more general problem that includes sloping bathymetry.

A β-plane theory has been developed for a general bathymetry that is uniform alongshore showing that interior SL transmits to the coast analogously to the steady 'advection-

diffusion' of a thermal fluid. For an interior SL originating from a wind-driven double gyre, corresponding to a coastal SL depression from the subpolar gyre and elevation from the subtropical gyre, the theory demonstrates that ocean interior sea level can penetrate to the coast having been attenuated and displaced equatorward. The analogy describes SL as being 'advected' along gh/f contours with sloping bathymetry steering ('advecting') SL contours along isobaths and the β-effect steering ('advecting') contours westward. For bathymetry that tends to zero at the coast and Coriolis parameter that vanishes at the equator, the interior SL does not register at the coast in the limit of no friction (though technically a friction stress is required at the singularity at the coastal equator point). The addition of alongshore friction, however, introduces cross-shore 'diffusion' and allows SL contours to cross gh/f contours such that the interior SL penetrates to the coast, where greater penetration implies less equatorward displacement and attenuation of the depression and elevation signal.

A non-dimensional 'Péclet number', $P_a = HL^{(x)}\beta/r = L^{(x)}/\delta_s$ where δ_s is the Stommel boundary layer thickness, quantifying the relative importance of 'advection' and 'diffusion', is defined to demonstrate how smaller combined shelf-slope width and depth scales and a larger friction parameter increase 'diffusion' relative to 'advection' and increase SL penetration. Increasing the scale of the combined bathymetry and decreasing the friction parameter have the opposite effect. Using this parameter it has been demonstrated that for a single layer interior, increasing the friction parameter towards infinity ($P_a \to 0$), results in coastal SL tending towards the vertical sidewall solution for any bathymetry, implying that the vertical sidewall is the maximum penetration limit for a single layered interior. Since $P_a = L^{(x)}/\delta_s$ is the width of the combined shelf and slope divided by the width of the Stommel boundary layer δ_s, we find that open ocean influence on coastal SL is essentially the same as the vertical sidewall case only in regions where the combined shelf and slope width lie within the Stommel boundary layer, i.e. P_a is small.

A distinction is drawn between a single layer interior and an interior with a decoupled upper layer of uniform thickness that makes contact with the continental slope at a distance $L^{(x)}$ from the coast. In the former the frictional boundary layer extends into the deep ocean but in the latter it is restricted to the shelf and slope region. After noting a subtlety in the boundary condition for this case we find it to be exactly the same as the single layer case, but with the possibility of smaller layer thickness, which results in greater SL penetration. The model is then extended to the case where upper and lower interior layers interact, producing an upper layer thickness that is non-uniform alongshore; thinner where SL is depressed due to the subpolar gyre. It is shown that this can enhance penetration further,

by reducing the steering effect of the continental slope on the poleward SL contours. This can be thought of as the parameter P_a changing meridionally (smaller where the upper layer is thinner).

Independently of the overall scales accounted for in P_a, it is shown that the configuration of shelf and slope can significantly alter how interior SL transmits to the coast. For realistic overall scales giving $P_a \leq 10$, it is found that wider and shallower shelves, relative to the overall scales, maximize SL penetration. This raises questions about the effect of model resolution on coastal SL and in our experiments it was found that fewer than 6 grid points on the slope ($\sim$5 km resolution for a 30 km slope) could produce noticeable error in the coastal SL. Further questions arise, and remain to be investigated, when the stratification leads to characteristics which propagate information away from the western boundary.

The results and analysis presented here have implications for our understanding of the drivers of coastal SL. Higginson et al. (2015) showed that the 1 m difference in interior SL across the location where the Gulf Stream moves into deep water is represented at the coast by an attenuated and equatorward displaced version. They noted that this was not explained by f-plane theoretical models, which suggest that oceanic SL features should not penetrate to the coast over the observed alongshore distance. The β-plane model developed here explains why a displaced and attenuated tilt in coastal SL should be expected and that, for example, an increased interior SL due to a weakened subpolar gyre (decreased tilt) would affect the coast.

Higginson et al. (2015) also suggested that the position of the coastal tilt might be explained by the narrow shelf at the Florida Straits. This study has shown that topography that is well approximated by a vertical wall ($L^{(x)} \ll \delta_s$) should enable greater penetration of the interior signal. More generally, moving northward of 32 degrees along the North American east coast, the combined shelf and slope width decreases significantly and this would suggest a transition to reduced bathymetric insulation. This is important for predictions of coastal SL if we consider that the tilt of interior SL experiences latitudinal variability driven by the North Atlantic Oscillation (NAO) (McCarthy et al., 2015). If the insulating properties of the shelf and slope change meridionally then a northward shift in the interior SL tilt would not necessarily result in a coastal SL tilt shifted by the same distance. This may also have implications for the suggestion that the latitudinal positions of SL rise hotspots along the eastern United States are being determined by the NAO (Valle-Levinson et al., 2017).

The results and analysis presented here suggest that how bathymetry is configured and how finely it is resolved, in addition to the representation of bottom friction, are potentially

quite important to ocean models focusing on SL in western boundaries. While the linear model used here has been intentionally simple, many additions can be made, notably the impact of including momentum advection and including time dependence to explore shorter time scale SL adjustments in a more sophisticated numerical model.

Chapter 4

Leaky Slope Waves and Sea Level

Leaky Slope Waves and Sea Level: Unusual Consequences of the Beta-Effect Along Western Boundaries with Bottom Topography and Dissipation

4.1 Preamble

In the previous chapter, the large scale coastal mean sea level response to deep ocean forcing was found to be modified by the β-effect and depend on the friction parameter and the geometry of the bathymetry. While the parameter space of these dependencies was explored, a natural followup is to explain why the coastal sea level is sensitive to these parameters, leading to the question: *what is the physical mechanism of adjustment at the boundary, and how and why is it sensitive to the parameters?*.

To answer the above question, this chapter explores the relationship between coastal sea level and coastally trapped waves (CTWs), which propagate anomalies in the sea state along coastal zones. The theory of CTWs is developed to include the effects of a variable Coriolis parameter, friction and different configurations of bathymetry, and the evolution of the waves is explored when forced from the interior ocean and from poleward latitudes. By forming an explicit relationship in dynamic sea level between the deep ocean, poleward latitudes, and the coast, for both low frequency variability and the steady state (mean sea level), a physical explanation for the results of Chapter 3 are sought.

Publication and Author Contributions

This chapter has been published in the *Journal of Physical Oceanography* (DOI: 10.1175/JPO-D-19-0084.1). It was published online in November 2019. The paper has four authors: My-

self (Anthony Wise), Christopher W. Hughes, Jeff A. Polton and John M Huthnance. As primary author, I carried out the research, wrote the paper and managed the publication process. My supervisors Jeff Polton, Christopher Hughes and John Huthnance provided valuable supervision, editorial critique and discussion of ideas. The paper appears in the bibliography under Wise et al. (2020).

4.2 Paper Abstract

Coastal Trapped Waves (CTWs) carry the ocean's response to changes in forcing along boundaries, and are important mechanisms in the context of coastal sea level and the meridional overturning circulation. Motivated by the western boundary response to high latitude and open ocean variability, we investigate how the latitude dependence of the Coriolis parameter (β-effect), bottom topography, and bottom friction, modify the evolution of western boundary CTWs and sea level using a linear, barotropic model. For annual and longer period waves, the boundary response is characterized by modified Shelf Waves and a new class of leaky Slope Waves that propagate alongshore, typically at an order slower than Shelf Waves, and radiate short Rossby waves into the interior. Energy is not only transmitted equatorward along the slope, but also eastward into the interior, leading to the dissipation of energy locally and offshore. The β-effect and friction result in Shelf and Slope Waves that decay alongshore in the direction of the equator, decreasing the extent to which high latitude variability affects lower latitudes, and increasing the penetration of open ocean variability onto the shelf - narrower continental shelves and larger friction coefficients increase this penetration. The theory is compared against observations of sea level along the North American east coast and qualitatively reproduces the southward displacement and amplitude attenuation of coastal sea level relative to the open ocean. The implications are that the β-effect, topography, and friction are important in determining where along the coast sea level variability hot spots occur.

4.3 Introduction

The propagation of waves along ocean boundaries occurs as part of the oceanic adjustment to variability in environmental forcing, such as wind stress or buoyancy. Over a period of time, wave propagation enables changes in forcing to be communicated over large distances along boundaries and between the open ocean and coast. The characteristics of these waves, often referred to as Coastally Trapped Waves (CTWs) due to their decaying away from the boundary, are therefore important to oceanic adjustment processes; for instance regional sea level (Hughes and Meredith, 2006) and the Meridional Overturning Circulation (MOC) (Roussenov et al., 2008; Buckley and Marshall, 2016). CTWs are important to the transmission of energy along boundaries and are relevant in the context of energy dissipation at western boundaries and the oceanic energy budget, e.g. as a sink of ocean-eddy energy (Zhai et al., 2010). An improved understanding of the physics at boundaries is also recognized as desirable in order to improve the dynamical justification for sub-gridscale parameterizations in Ocean Circulation Models (OCMs) (Deremble et al., 2017), which can have significant effects on important oceanic features, e.g. Gulf Stream separation sensitivity to viscosity parameterization (Bryan et al., 2007).

At ocean boundaries, where the no normal flow condition holds, variability in the open (interior) ocean or at higher (poleward) latitudes results in an adjustment of potential vorticity that manifests as waves propagating along the boundary. The properties of these waves have been explored in idealized settings for different boundary geometries (vertical sidewall, sloping sidewalls), stratification profiles and frequencies, see: Mysak (1980b), Huthnance et al. (1986) and Hughes et al. (2019). In the following we restrict ourselves to variability at sub-inertial frequencies, $\omega < f$, where f is the Coriolis parameter.

For vertical sidewall boundaries, CTWs are typically a series of barotropic and baroclinic Kelvin waves propagating cyclonically around the ocean (boundary on the right in the northern hemisphere). With the inclusion of sloping sidewalls at the boundary, the modal structure ceases to be separable in the horizontal and vertical. In the barotropic limit, the modes evolve into Shelf waves.

Wajsowicz and Gill (1986) showed friction to attenuate Kelvin waves resulting in the decay of alongshore amplitude. Brink and Allen (1978) applied bottom friction to a barotropic model with a continental shelf and slope and found the wave response to local alongshore forcing to be damped and with a cross-shore phase lag. The amplitude of this boundary response is associated with the energy flux at the boundary and is relevant to energy dissipation and monitoring of the Meridional Overturning Circulation, as discussed in Kanzow

et al. (2009) and Marshall and Johnson (2013). Friction has also been shown to promote the interior ocean contribution to western boundary coastal sea level (Minobe et al., 2017; Wise et al., 2018).

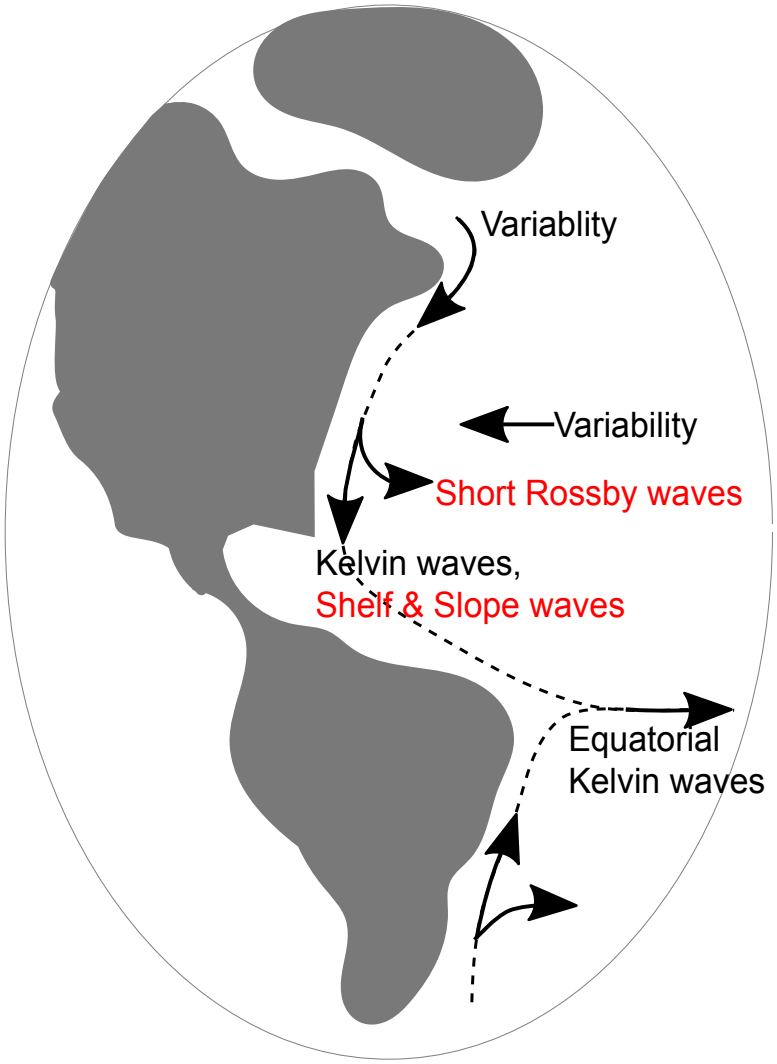

Figure 4.1: *Schematic of the transmission of variability along western boundaries and eastward at the equator. The Shelf, Slope and short Rossby waves (denoted in red) are the subject of this study.*

The theory of CTWs is based primarily on the assumption that the Coriolis parameter is constant (f-plane approximation), particularly for sloping sidewalls. However, Miles (1972) found that the curvature of the Earth and changes in depth over a continental shelf modify wave amplitude and phase speed at inertial frequencies ($\omega \sim f$) (he used an

inviscid barotropic model). He also showed the wave amplitude to decay with latitude, proportionally to $\sqrt{f}$, a result previously obtained by Moore (1968) for equatoral Kelvin waves. Johnson and Marshall (2002) identified the attenuated Kelvin wave amplitude at western boundaries as a key component in an "equatorial buffer" mechanism to describe the transmission of thermohaline variability around the Atlantic, with information transmitted westward from the eastern boundary as long Rossby waves, equatorward along the western boundary and eastward at the equator. Allen and Romea (1980) also showed that equatorial baroclinic disturbances could be carried poleward along eastern boundaries as Kelvin waves that change into barotropic shelf waves at mid-latitudes. Figure 4.1 illustrates the relevant western boundary information pathways, with red denoting the wave types that are the subject of this study.

Using a frictional reduced-gravity model, Marshall and Johnson (2013) extended the vertical sidewall, β-plane theory to wave periods longer than a few months and found that buoyancy anomalies could propagate along western and eastern boundaries as short and long Rossby waves, respectively. They found the western boundary wave to dissipate virtually all its energy during propagation towards the equator, with no dependence on the value of the dissipation coefficient.

While Marshall and Johnson (2013) demonstrated the importance of the β-effect and friction at western boundaries, they noted that the inclusion of more realistic bottom topography would modify the results. It is our intention with this paper to use a simple model to extend their investigation of the western boundary response to the case where the bottom topography includes a continental shelf and slope. As we will see, the boundary response is dependent on the evolution of CTWs that are lost in the vertical sidewall assumption - and the β-effect and friction have interesting effects on their behavior, including the addition of a new class of leaky Slope wave.

The paper is structured as follows. In section 4.4 we formulate the problem and present wave solutions. In section 4.5 we discuss the cross-shore structure of these waves. Section 4.6 discusses the alongshore evolution and energetics of waves excited by high latitude forcing and section 4.7 continues this for forcing from the interior. Section 4.8 applies the results to western boundary sea level and we conclude with implications and a summary of the key points.

4.4 Formulation and solutions

We will be considering throughout a rectangular section of the ocean between a high and low latitude boundary (not reaching the equator) that stretches from a western boundary coastline to a boundary $\mathcal{O}(100)$ km offshore. For a coordinate system with x in the zonal and y in the meridional direction, we consider a straight western boundary coastline, oriented along the y-axis (meridionally) at $x = 0$, with the equator at $y = 0$ and larger y corresponding to higher latitudes. Bottom topography h is taken to be uniform alongshore, i.e. independent of y, but variable in the cross-shore direction, i.e. $h = h(x)$. Figure 4.2a gives a schematic of the bottom topography with $x = x_s$ denoting the shelf break, $x = x_b$ the bottom of the slope and $x = x_{in}$ the boundary with the interior. Note that the boundary forcing (applied at the boundary with the interior) is applied east of where the boundary response has decayed. Depth at the shelf break and bottom of the slope are denoted by H_s and H_b. We assume that depth tends to zero at the coast and increases monotonically away from the coast. For numerical calculations we use 5th order smoother-step functions to define the shelf, slope and off-shore portions of $h(x)$, i.e.

$$h(x) = \begin{cases} H_s \left[6\left(\frac{x}{x_s}\right)^5 - 15\left(\frac{x}{x_s}\right)^4 + 10\left(\frac{x}{x_s}\right)^3 \right] & \text{for} \quad 0 \le x \le x_s, \\ H_s + (H_b - H_s)\left[6\left(\frac{x-x_s}{x_b-x_s}\right)^5 - 15\left(\frac{x-x_s}{x_b-x_s}\right)^4 + 10\left(\frac{x-x_s}{x_b-x_s}\right)^3 \right] & \text{for} \quad x_s < x \le x_b, \end{cases} \tag{4.1}$$

with $h(x) \approx H_b$ east of the slope ($x > x_b$).

In the following we consider solutions of the linearized, depth-integrated shallow water equations for annual-to-decadal variability ($\omega \ll f$). The equatorial β-plane Coriolis parameter, $f = \beta y$, is used for simplicity - the solution method is valid for a general $f(y)$, however. Assuming the flow to be bathymetrically steered alongshore and with $\omega/f \ll 1$, we follow Gill and Schumann (1974) (long wave approximation) and allow the zonal momentum equation to be in geostrophic balance while retaining the (linear) bottom friction (as in Csanady (1978)) in the meridional momentum equation,

$$-fhv + gh\frac{\partial \tilde{\eta}}{\partial x} = 0, \tag{4.2}$$

$$h\frac{\partial v}{\partial t} + fhu + gh\frac{\partial \tilde{\eta}}{\partial y} = -rv, \tag{4.3}$$

with $\mathbf{u} = (u, v)$ the velocity, $\tilde{\eta} = \tilde{\eta}(x, y, t)$ the inverse barometer corrected dynamic topography (dynamic sea level), g gravity and r the linear friction parameter. For the continuity

equation

$$\frac{\partial \tilde{\eta}}{\partial t} + \frac{\partial (uh)}{\partial x} + \frac{\partial (vh)}{\partial y} = 0, \tag{4.4}$$

we begin by retaining the free-surface for discussion but we ultimately follow Buchwald and Adams (1968) and Gill and Schumann (1974) in making the rigid-lid approximation such that the continuity equation becomes $\boldsymbol{\nabla} \cdot (\mathbf{u}h) = 0$.

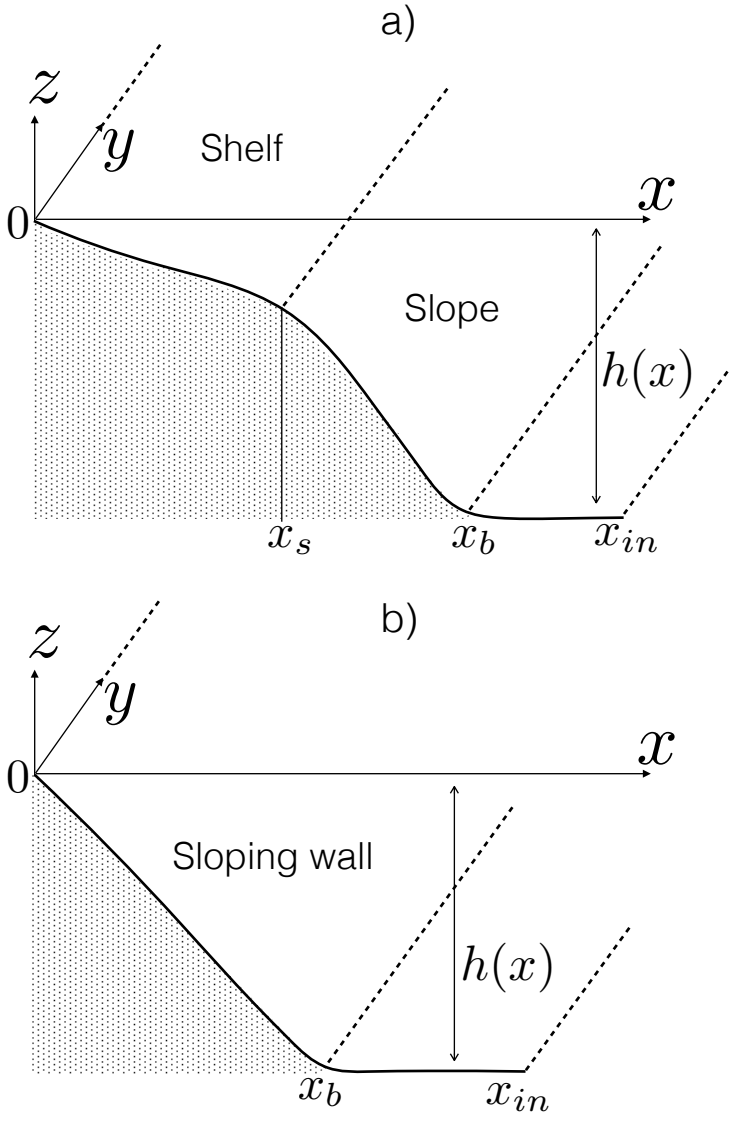

Figure 4.2: *Schematic illustrating the coordinates and bottom topography for a) a continental shelf and slope, b) a sloping sidewall. The shelf break, slope bottom and boundary with the interior ocean are denoted by x_s, x_b and x_{in} respectively.*

Taking the vertical component of the curl of the momentum equations, (4.2)/h and (4.3)/h, and substituting in the continuity equation (4.4) gives the vorticity relation

$$\frac{\partial^2 v}{\partial t \partial x} + \beta v - \frac{f}{h}\left(\frac{\partial \tilde{\eta}}{\partial t} + h'u\right) = -\frac{r}{h^2}\left(\frac{\partial v}{\partial x}h - h'v\right), \tag{4.5}$$

where prime denotes d/dx. On the left hand side, the first term relates to relative vorticity, the second to the advection of planetary vorticity, the third to stretching of vorticity and the term on the right hand side to vorticity induced by bottom friction - a source such as wind-stress or a boundary condition could be included as an additional right hand side term. Alternatively, using (4.2) and (4.3) to rewrite in terms of $\tilde{\eta}$, a more useful quantity in this context, we get

$$\frac{\partial^3 \tilde{\eta}}{\partial t \partial x^2} + \beta \frac{\partial \tilde{\eta}}{\partial x} + \left(\frac{f h'}{h}\frac{\partial \tilde{\eta}}{\partial y} + \frac{h'}{h}\frac{\partial^2 \tilde{\eta}}{\partial t \partial x} - \frac{1}{L_d^2}\frac{\partial \tilde{\eta}}{\partial t}\right) = -\frac{r}{h}\frac{\partial^2 \tilde{\eta}}{\partial x^2} \tag{4.6}$$

where $L_d = \sqrt{gh}/f$ is the external Rossby radius of deformation.

For the flat bottom 1.5 layer vertical sidewall scenario with $f = \beta y$, the terms involving h' disappear and L_d can be considered the internal Rossby radius L_d^{int}. As discussed by Clarke and Shi (1991), below a critical frequency, i.e. for the low frequency variability considered here, the planetary vorticity term can come into balance with the stretching and relative vorticity terms, allowing Rossby waves at the boundary. Using this model Marshall and Johnson (2013) found a buoyancy anomaly to propagate along the boundary towards the equator as a short Rossby wave at the classical Kelvin wave speed $c = \sqrt{gh}$, multiplied by L_d^{int}/δ_s, where $\delta_s = r/\beta$.

Alternatively, for the sloping bottom with constant f scenario, we retain the stretching terms involving h' but lose the β term. The retained stretching terms are the topographic equivalent of β, i.e. the sloping bottom topography establishes a potential vorticity gradient. The balance between relative vorticity and stretching due to the bottom topography gives rise to Shelf waves (topographic Rossby waves) (Salmon, 1998a, p.73).

4.4.1 Wave solutions

In this study we are interested in the effect of retaining the stretching due to bottom topography terms, the advection of planetary vorticity β term and the friction term for annual-to-decadal variability. To this end, we simplify the model by making the rigid-lid approximation. For this, as in Gill and Schumann (1974), we assume that the Rossby radius of deformation L_d is larger than the cross-shore scale of the boundary response L, i.e. $L_d \gg L$ and that the frequency of variability ω is restricted by $\omega \ll \beta L_d^2/L$. This allows

the first term in the continuity equation (4.4), and therefore the third stretching term of the vorticity equation (4.6), to be neglected. This term is also small compared to the first stretching term and the term on the right hand side of (4.6). With this approximation we have effectively filtered out the barotropic Kelvin wave response.

For the boundary conditions, we assume some specified anomaly along the poleward and interior boundaries, i.e. $\tilde{\eta} = \tilde{\eta}_p$ at $y = y_p$ and $\tilde{\eta} = \tilde{\eta}_{in}$ at $x = x_{in}$, where throughout we use sub- and superscripts p and in to refer to poleward and interior respectively. The interior boundary condition is applied far enough away from the coast such that the boundary response has decayed west of it, i.e. $x_{in} > L$. We consider $\tilde{\eta}_{in}$ as forcing due to the dynamics in the interior ocean, where basin-scale Rossby waves dominate the adjustment and hence $\tilde{\eta}_{in}$ can be thought of as describing a long Rossby wave incident on the western boundary. Similarly $\tilde{\eta}_p$ defines the forcing from a poleward (higher latitude) region, see Fig. 4.3. Finally, as the coast is approached, $x \to 0$, we have $h \to 0$, which leads to $rv \to 0$ from (4.3) and then $\partial\tilde{\eta}/\partial x \to 0$ from (4.2). The boundary value problem can then be defined as

$$\frac{\partial^3\tilde{\eta}}{\partial t\partial x^2} + \beta\frac{\partial\tilde{\eta}}{\partial x} + \frac{h'}{h}\left(f\frac{\partial\tilde{\eta}}{\partial y} + \frac{\partial^2\tilde{\eta}}{\partial t\partial x}\right) = -\frac{r}{h}\frac{\partial^2\tilde{\eta}}{\partial x^2}, \tag{4.7}$$

$$\frac{\partial\tilde{\eta}}{\partial x} \to 0 \qquad \text{at} \quad x \to 0, \tag{4.8}$$

$$\tilde{\eta} = \tilde{\eta}_{in}(y,t) \qquad \text{at} \quad x = x_{in}, \tag{4.9}$$

$$\tilde{\eta} = \tilde{\eta}_p(x,t) \qquad \text{at} \quad y = y_p. \tag{4.10}$$

and we seek solutions in the form $\tilde{\eta}(x,y,t) = \eta(x,y)e^{-i\omega t}$.

The equations (4.7) - (4.10) can be solved by first separating variables in x and y to yield an eigenvalue problem in x, see equation (4.17). This eigenvalue problem can then be solved via finite differencing or, for example, by applying a Chebyshev transformation discretization to the eigenvalue problem and solving using a standard eigenvalue package, e.g. see Kaoullas and Johnson (2010). The y dependent part of the equations can then be solved for each eigenvalue. The solution method applied here, which to the authors' knowledge is somewhat novel and potentially useful, is derived in Appendix A. For clarity we simply state the solution below.

The solution of equations (4.7) - (4.10) is

$$\eta(x,y) = \eta_{in}(y) - \sum_{j=1}^{\infty}\gamma_j C_j(x)A_j^{in}(y) + \sum_{j=1}^{\infty}\alpha_j C_j(x)A_j^p(y) \tag{4.11}$$

$$A_j^p(y) = \left(\frac{y}{y_p}\right)^{\lambda_j} \tag{4.12}$$

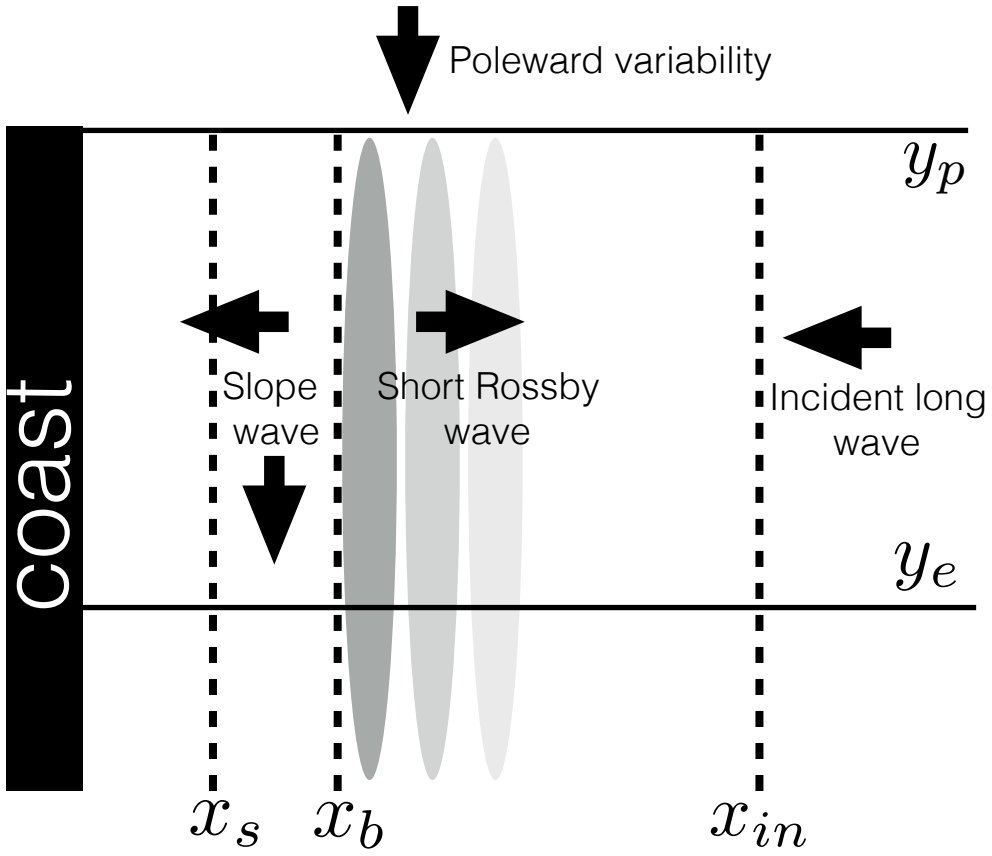

Figure 4.3: *Schematic illustrating the idealized domain, with variability imposed at the poleward boundary y_p and at the interior boundary x_{in} between the latitudes y_p and y_e, where y_e is equatorward of y_p. The shelf break and slope bottom are denoted by x_s and x_b. The arrows indicate the energy fluxes involved.*

$$A_j^{in}(y) = \int_y^{y_p} \frac{d\eta_{in}}{ds} \left(\frac{y}{s}\right)^{\lambda_j} \, ds, \tag{4.13}$$

where γ_j, α_j, λ_j are complex constants, $C_j(x), A_j^p(y)$ and $A_j^{in}(y)$ are complex and s is a dummy integration variable. Recalling that $\tilde{\eta}(x, y, t) = \eta(x, y)e^{-i\omega t}$, the real part of (4.11) describes the adjustment at the boundary as the summation of three sets of waves, with subscript j denoting the wave mode number. Note that throughout, we use $\Re(\cdot)$ and $\Im(\cdot)$ to denote real and imaginary parts of complex numbers, i.e. $z = \Re(z) + i\Im(z)$.

The first term in (4.11) is the incident long wave from the interior, the second term is a set of waves excited by the incident wave from the interior and the third term is a set of waves excited by the poleward forcing. For the second and third terms, $C_j(x)$ defines the j^{th} wave mode's cross-shore structure. Note that the first two terms disappear when

$\eta_{in} = 0$ and the third term disappears when $\eta_p = 0$ (α_j will be zero).

For our purposes it is enough to consider γ_j and α_j as constants that simply scale and phase shift each wave, we do not consider them further. The constants λ_j are the eigenvalues of an eigenvalue problem and are dependent on the topography, friction parameter and frequency of variability.

Each wave mode has a specific alongshore decay rate and phase and we have ordered the modes according to the decay rate, i.e. the magnitude of $\Re(\lambda_j)$ where $1 \leq \Re(\lambda_1) < \Re(\lambda_2) < \Re(\lambda_3) \cdots < \Re(\lambda_n)$, for $n \to \infty$. For waves excited from poleward, this orders the modes according to their alongshore decay rate, such that the first wave mode $j = 1$ propagates farthest. As will be discussed later is section 4.6 the lower bound condition on the real part of the eigenvalues, $\Re(\lambda_i)$, ensures that the rate of dissipation of a wave does not tend to infinity as the equator is tended towards, which would be unreasonable. There would be no guarantee of a convergent solution in that case.

Apart from where specified otherwise, we use the parameter configuration defined in Table (4.1) for calculations. The configuration has been chosen to be somewhat representative of reality and we note the friction parameter is small to investigate weak damping, which helps elucidate the wave structures, though we also explore stronger damping.

ω (s^{-1})	r (m s^{-1})	x_s (km)	x_b (km)	H_s (m)
10^{-7} (24 months)	0.00002	100	130	100
H_b (m)	β (m^{-1} s^{-1})	$\frac{2\pi\omega}{\beta}$ (km)	$\frac{\sqrt{gH_s}}{f}$ (km)	$\frac{\sqrt{gH_b}}{f}$ (km)
4100	1.667×10^{-11}	37.7	310	2000

Table 4.1: *Parameter configuration used throughout unless explicitly stated otherwise. The final three columns are the short Rossby wavelength and the Rossby radius of deformation for shelf and open ocean depths respectively, with* $f = 10^{-4}$ s^{-1}.

Note that our boundary wave assumption fails as we approach the equator, where waves cease to be trapped to the boundary. Context determines how close to the equator this failure occurs. For example, in a purely barotropic ocean we would expect an equatorial barotropic Rossby radius to be the relevant scale (around 2000 km in water 4 km deep). If, instead, we are considering the boundary processes to represent the upper layer of a two-layer system, the situation is less clear. Accordingly, we present results all the way to the equator, but caution that interpretation is uncertain close to the equator.

4.5 Cross-shore wave structure

From (4.11), we note that the cross-shore structures of the wave modes $C_j(x)$, are the same irrespective of whether they are excited by poleward or interior forcing.

In contrast to inviscid f-plane Shelf waves, which only propagate along the shelf, there is now a cross-shore contribution to the phase, denoted by $\varphi_j^x(x) = \arg[C_j(x)]$. The cross-shore component of the wave amplitude is $|C_j(x)|$, where we use $|\cdot|$ to denote the magnitude of a complex number.

Figure 4.4 shows the real and imaginary parts of the first nine wave modes, $\Re(C_j)$ and $\Im(C_j)$, $j = 1, 2, \ldots, 9$, each normalized by maximum amplitude. The waves can be classified into two classes of wave based on their dominant characteristics. Firstly, wave modes 1, 2, 6 and 9 decay on the shelf with little or zero amplitude off-shelf. These waves are akin to topographically trapped f-plane Shelf waves (Robinson, 1964; Huthnance, 1975), where the number of offshore nodes (zero amplitudes) increases with mode number. Here the Shelf waves are subject to modification by the inclusion of bottom friction and the β-effect. We label this group of waves (viscous) β-plane Shelf waves. The second group of waves, modes 3, 4, 5, 7 and 8, are by contrast characterized by a significant off-shore component where the wavenumber is, to a first approximation, that of the inviscid short Rossby wave,

$$\frac{d}{dx}\left[\varphi_j^x\right] \approx -\frac{\beta}{\omega}, \quad \text{for} \quad x > x_b. \tag{4.14}$$

This is approximate because frictional damping will also have a contribution. These waves have a structure on the slope, e.g. for higher mode Slope waves $d\varphi_j^x/dx \sim 10^{-4}$ m^{-1} on the slope, and we label this group: Leaky Slope waves.

Figure 4.4 also shows the imaginary parts of the waves, giving a sense of the zonal phase lag, for example the westward phase propagation of the short Rossby component of the waves, though we do not discuss this further.

For the higher mode number waves not shown, i.e. $j > 9$, we find that each wave fits, with increasing fidelity, into one or the other group, giving essentially two sets of wave types: Beta-plane shelf waves (1,2,6,9) and Leaky slope waves (3,4,5,7,8). With this classification made, we note two points. Firstly, wave modes can be said to exhibit characteristics from both types of wave (particularly lower modes), however for the purposes of exploring boundary adjustment processes, it is helpful to group them by their dominant characteristics. Secondly, we note that while the wave modes shown in Fig. 4.4 are naturally specific to the parameter regime we have chosen, the two wave types, as described above, have been found to be general within the scope of the parameter space used in this study. It is worth

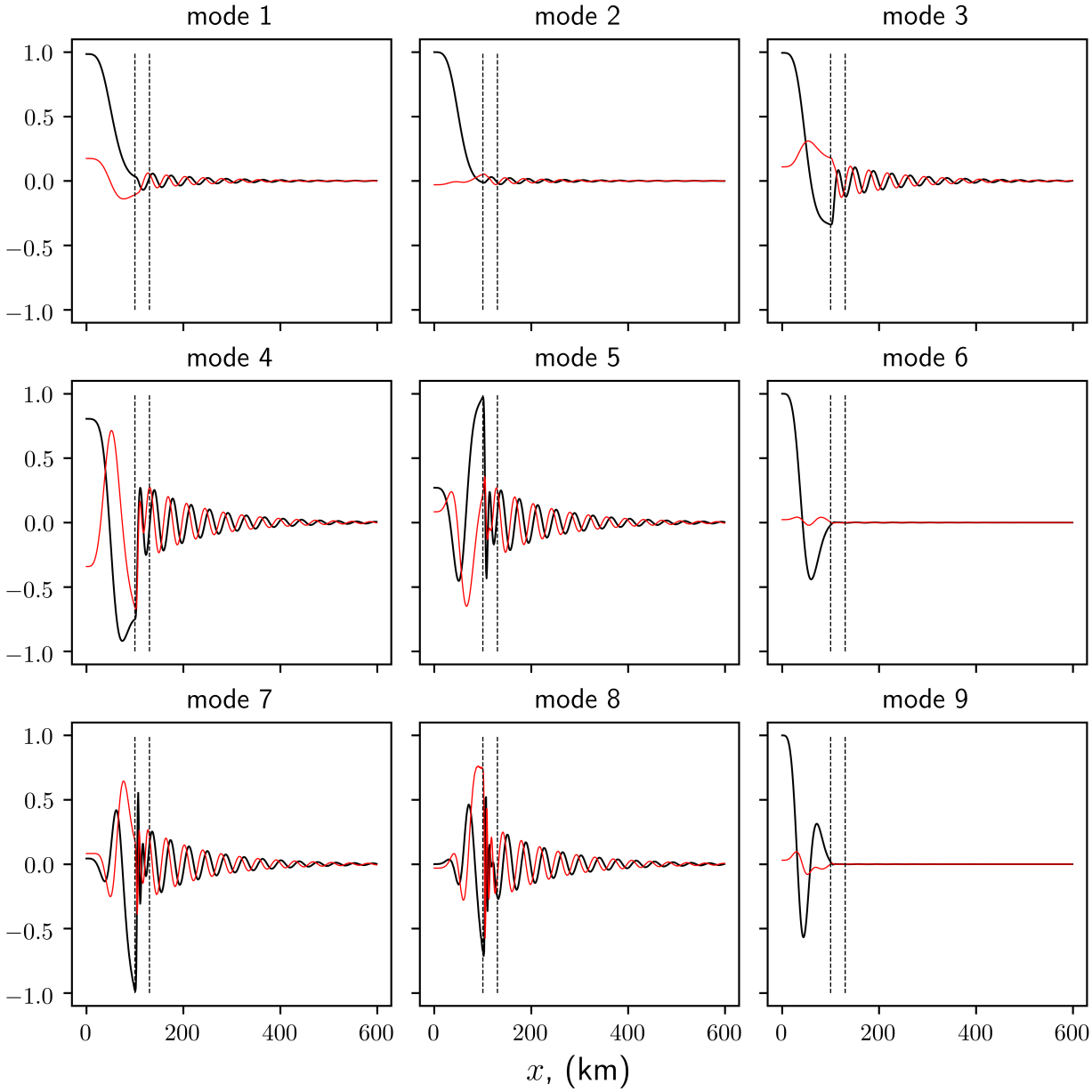

Figure 4.4: *Cross-shore structure of the first nine wave modes, each normalized by its maximum amplitude* $|C_j(x)|_{max}$*. Black corresponds to the real part of the* x *dependent part of the solution,* $\Re[C_j(x)]$*, and red to the imaginary part* $\Im[C_j(x)]$*. The dashed lines denote the shelfbreak at* $x = x_s = 100$ *km and slope bottom at* $x = x_b = 130$ *km.*

noting however that as the friction parameter is increased, the Short Rossby component becomes damped and a Stommel-like frictional boundary layer expands off-shore instead. Beyond the additional scenario of very long time period variability, $\omega \ll r/H$, an exhaustive parameter study is beyond the scope of this paper. From here onward we will use mode 5 to represent the set of leaky Slope waves and mode 6 to represent the set of β-plane Shelf waves; we will also include mode 1 in the discussion as this proves to play a somewhat special role in the overall boundary response.

In the following sections we will look at the alongshore wave evolution and energetics for the cases of poleward and interior variability.

4.6 Forcing from poleward

4.6.1 Alongshore evolution

When the waves are generated by variability from higher latitudes, (4.11) reduces to

$$\tilde{\eta}(x,y,t) = \sum_{j=1}^{\infty} \alpha_j C_j(x) A_j^p(y) e^{-i\omega t}, \tag{4.15}$$

$$A_j^p(y) = \left(\frac{y}{y_p}\right)^{\Re(\lambda_j)} \exp\left[i\,\Im(\lambda_j)\ln(y/y_p)\right], \tag{4.16}$$

where A_j^p gives the alongshore wave evolution and we have separated λ_j into real and imaginary parts to explicitly show the amplitude and phase components.

Pre-emptively assuming, for a moment, that $\Re(\lambda_j) > 0$ for all j, the relation (4.16) describes the wave amplitudes as decaying alongshore in the direction of the equator (note that $(y/y_p) \leq 1$). The physical limitations of the model close to the equator are important avenues for future research, i.e. non-linear effects and stratification should become important, however for the solutions presented here we can make use of the vorticity equation (4.7) to justify the above assumption.

Separating variables in (4.7) by substituting $\tilde{\eta}(x,y,t) = C(x)A^p(y)e^{-i\omega t}$ yields the generalized eigenvalue problem

$$(r - ih\omega)\,C'' + \left(h\beta - ih'\omega\right)C' = -\lambda h' C \tag{4.17}$$

subject to $C' = 0$ at $x = 0$ and $C = 0$ at $x = x_{in}$. For solutions of the form $C_j = |C_j(x)|\exp(i\varphi_j(x))$, substitution into (4.17) and taking the real parts gives

$$-\Re(\lambda_j)h'|C_j| = 2\omega h|C_j|'\varphi_j' + \omega h|C_j|\varphi_j'' + \omega h'|C_j|\varphi_j' + \beta h|C_j|' + r|C_j|'' - r|C_j|(\varphi_j')^2 \tag{4.18}$$

Using integration by parts and the boundary conditions, the right hand side (RHS) of $\int_0^{x_{in}} (4.18)|C_j|\,dx$ is ≤ 0. Given that the left hand side (LHS) of $\int_0^{x_{in}} (4.18)|C_j|\,dx$ must also be ≤ 0 and that $\int_0^{x_{in}} h'|C_j|^2\,dx \geq 0$, it is true that $\Re(\lambda_j) \geq 0$. Hence all wave modes decay in amplitude in the direction of the equator. Later we will argue to further restrict this lower bound to $\Re(\lambda_j) \geq 1$ such that $1 \leq \Re(\lambda_1) < \Re(\lambda_2) < \Re(\lambda_3) \cdots < \Re(\lambda_n)$, for $n \to \infty$. This implies that all modes have decayed to zero at the equator and that, for example, mode 2 will decay farther from the equator than mode 1.

The solid lines in Fig. 4.5 show the alongshore amplitude, $(y/y_p)^{\Re(\lambda_j)}$, for the first nine wave modes, together with the value of $\Re(\lambda_j)$. The first mode decay is approximately linear, $\Re(\lambda_j) \approx 1$, and the decay rate increases as mode number increases. Figure 4.6a shows the solution $\tilde{\eta}(x, y, t)$ at time $t = 0$ between two latitudes y_p and y_e, where subscript e denotes equatorward, for $j = 1, 2, \ldots, 1000$ with the poleward forcing constant on the shelf and slope, $\eta_p = -1$, such that $v = 0$ at y_p on the shelf and slope. Note how the amplitude decays on the slope in the direction of the equator as fewer modes contribute to the boundary response and how this effectively allows the interior amplitude, which in this case is zero, to penetrate onto the slope at lower latitudes (between the dashed lines: it is dark blue at the poleward boundary and pale blue at the equatorward boundary).

We noted previously that λ_j are dependent on the parameters $h(x)$, r and ω. The dashed lines in Fig. 4.5 show the alongshore amplitudes when the shelf width has been decreased to 20 km (solid lines are for a shelf width of 100 km). The alongshore amplitude decay rate (in space not time) increases for all modes except mode 1. A relatively small increase in $\Re(\lambda_j)$ can significantly shorten the lengthscale over which the wave decays. Figure 4.7a compares $\Re(\lambda_j)$ for the first 40 wave modes for shelf widths of 100 km and 20 km. As the shelf width decreases, higher wave modes decay at increasingly high latitudes and in effect become negligible for the overall boundary response. The narrower shelf width acts to filter out higher wave modes from the boundary response. A narrower shelf also tends to decrease wave propagation speed (increasing the magnitudes of $\Im(\lambda_j)$). Hence slower wave propagation, and the decay of the wave amplitude over a shorter alongshore distance, result from a narrower shelf. This is consistent with the results of Huthnance (1987b), where an f-plane is used.

This result implies that a high latitude pressure anomaly propagates farther towards the equator when the shelf is wider. It also suggests, as we will discuss in the following section, that information from the interior ocean will give a relatively larger contribution to the coast when the shelf is narrower. In Fig. 4.6a this would be seen as the shelf and slope amplitudes decaying towards zero farther away from y_e, i.e. greater penetration from

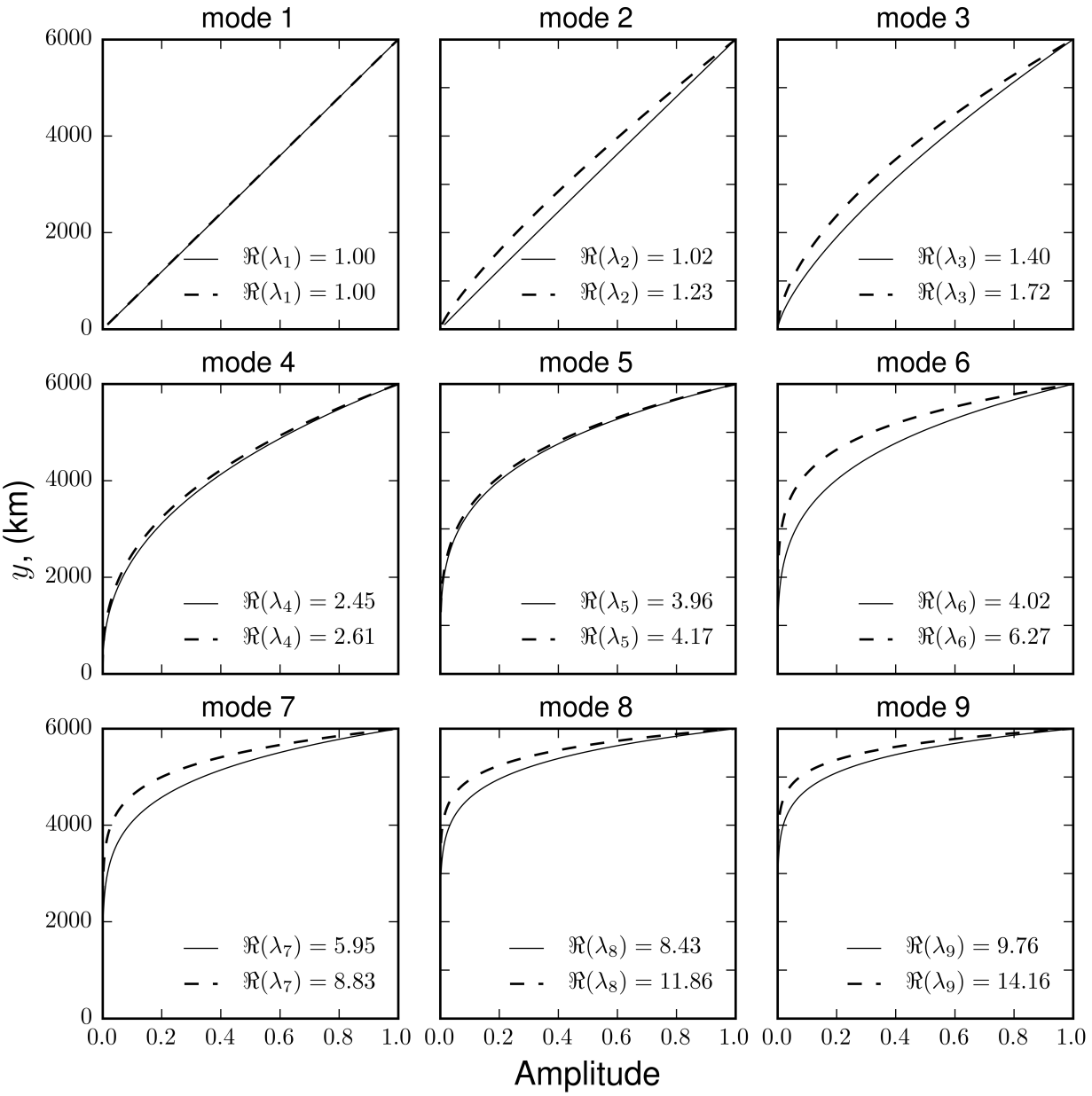

Figure 4.5: *Alongshore amplitude* $(y/y_p)^{\Re(\lambda_j)}$ *of the first nine wave modes,* $j = 1, 2, \ldots, 9$*, where solid lines denote a shelf width of 100 km and dashed lines a shelf width 20 km.* $y = y_p$ *is 6000 km poleward of the equator at* $y = 0$*.*

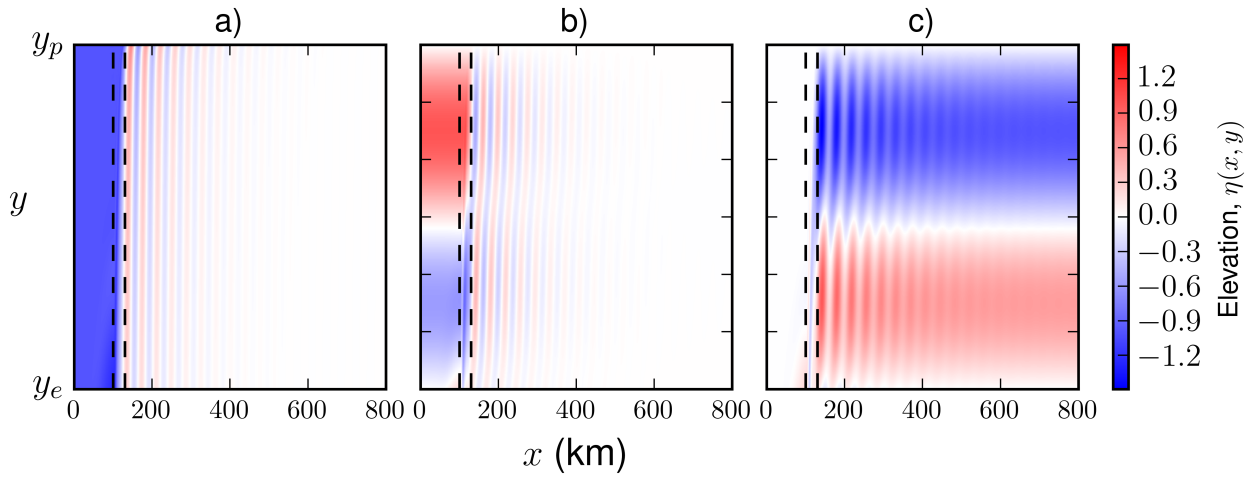

Figure 4.6: *a) Sum of all wave modes $\sum_j^\infty \alpha_j C_j(x) A_j^p(y)$, for a poleward forcing at y_p that is constant on the shelf and slope $\eta_p = -1$, and tends smoothly to zero east of the slope. b) Sum of all wave modes $-\sum_j^\infty \gamma_j C_j(x) A_j^{in}(y)$ when forced by an interior representing a double gyre (see dashed line η_{in} in Fig. 4.10b). c) Incident long wave from the interior plus the sum of waves shown in b), i.e. $\eta_{in} - \sum_j^\infty \gamma_j C_j(x) A_j^{in}(y)$. In all panels: time $t = 0$, dashed lines denote shelfbreak and slope bottom, y_p and y_e are 6000 km and 3000 km poleward of the equator respectively. Panels b) and d) are discussed in section 4.7.1*

the interior. Coastal bathymetry is often represented coarsely in numerical models and with a vertical wall in conceptual models. These results suggest that the representation of bathymetry could be a source of difference between OCM simulations of western boundaries.

The consequences of using a vertical sidewall can be shown more explicitly by considering the decay rate of waves for the case of a sloping sidewall at the boundary (schematic Fig. 4.2b) when the gradient of the sloping sidewall h'_w is increased. Figure 4.7b compares $\Re(\lambda_j)$ for the first 60 wave modes when the sloping sidewall has three different gradients: $h'_w =$ 0.041, 0.137 and 0.41, where a larger gradient equates to a steeper sidewall. As the sloping sidewall steepens, the magnitudes of $\Re(\lambda_j)$ increase and fewer wave modes contribute to the boundary response. Indeed in the steepest case (sidewall depth 4100 m and width 10 km), only the first 5 modes are effectively contributing to the boundary response.

An important exception to this dependency on bottom topography is the mode 1 wave. For all sidewall gradients, $\Re(\lambda_1) \approx 1$. Decreasing the shelf width (steepening) is compensated for by changes in the cross-shore wave structure as frictional effects increase. In the steep slope limit, where the sloping sidewall tends to vertical, all modes except mode one are effectively 'killed off' and a single mode remains. In the absence of topographic effects,

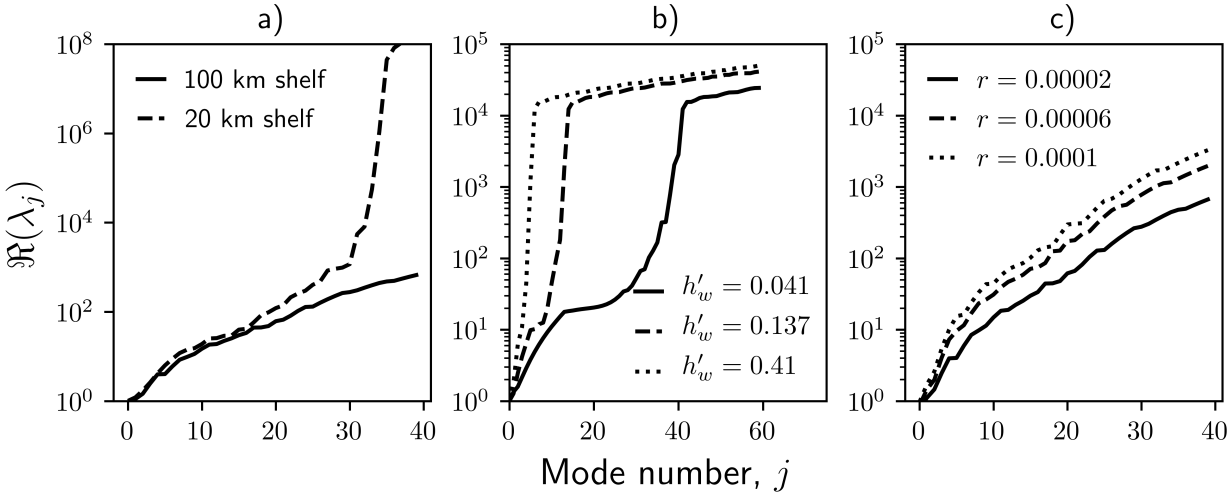

Figure 4.7: *Semi-log plots a) The first 40 $\Re(\lambda_j)$ for two shelf widths. b) The first 60 $\Re(\lambda_j)$ for a sloping sidewall bottom topography (see Fig. 4.2b) for three different sidewall gradients h'_w i.e. $H_b = 4100$ m and $x_b = 100$ km (solid), 30 km (dashed) or 10 km (dotted). c) The first 40 $\Re(\lambda_j)$ for three different values of the friction coefficient r, with the standard shelf and slope configuration.*

this mode decays alongshore proportionally to f such that, as we will see, the zonal energy flux is constant with latitude. This is consistent with Marshall and Johnson (2013) who found only a single wave decaying linearly alongshore in their vertical sidewall model. The reason mode 1 is so similar to the first baroclinic wave of Marshall and Johnson (2013) is that the mode 1 wave is effectively a rigid-lid version of the free-surface wave, maintaining no-horizontal divergence across the domain. For low frequency forcing, the first baroclinic wave is, relatively, very fast (i.e. compared to the forcing time-scale, the boundary adjustment is quick and soon comes into equilibrium), here with the rigid-lid, mode 1 does this effectively instantaneously. Note that this rigid-lid response can be split across multiple modes. The important point is that by filtering out higher wave modes from the boundary response, the vertical sidewall is a limit where the propagation of variability from higher to lower latitudes is minimized.

The choice of friction parameter can affect the boundary response in a similar fashion. Figure 4.7c compares $\Re(\lambda_j)$ for the first 40 modes for three values of the friction parameter r, using the standard shelf configuration. Increasing the friction parameter is found to increase the magnitudes of $\Re(\lambda_j)$ and therefore effectively decreases the number of modes contributing to the boundary response, as described above. Once again mode 1 remains

the exception with $\Re(\lambda_1) \approx 1$. Increasing the friction parameter is compensated for by an increase in the boundary layer width. In the large friction limit, the boundary layer width becomes large compared to the width of the topography and higher modes are 'killed off', leaving a single wave that decays proportionally to f (topographic effects have become small). As has been discussed by Deremble et al. (2017), the dynamical justification for the sub-gridscale parameterization of viscosity in OCMs is somewhat opaque and can be a source of inconsistency between simulations, e.g. Gulf stream separation point (Bryan et al., 2007). The dependency of the waves on the friction parameter r is a plausible mechanism for some of this inconsistency. This issue is somewhat lost in vertical sidewall models, which already filter out the higher wave modes. Indeed Marshall and Johnson (2013) found the wave amplitude to be independent of the friction parameter in their vertical sidewall model. These parameter sensitivities should also broadly apply to the f-plane.

To be clear, the lack of penetration of the interior sea level onto the shelf in Fig. 4.6a (as well as in Fig. 4.6c) compared to the results from Chapter 2 are down to the parameter regime being investigated here. In Chapter 2 the friction parameter is large relative to the frequency of variability, which in that case is in steady state. Here, we are exploring the case where the frequency of variability is larger and the friction parameter is smaller. This results in less penetration from the interior onto the shelf. We have discussed in this section that this occurs because friction is important for determining the lengthscale over which the waves decay (see the values of the $\Re(\lambda_j)$ in Fig. 4.7c). A larger friction parameter results in a smaller wave decay lengthscale, and this allows more of the interior sea level to penetrate onto the shelf. The wave mechanism discussed here and in the following sections, and the parameter sensitivities, is informative for understanding how coastal sea level adjusts to variability. The discussion is brought back to the case of the steady state sea level in section 4.8 where a larger friction parameter is used.

From (4.16) the alongshore phase component of the waves is given by $\varphi_j^y(y) = \Im(\lambda_j)\ln(y/y_p)$, which grows in magnitude in the direction of the equator. For wave number $d\varphi_j^y/dy$, Slope waves are typically shorter than Shelf waves, with the mode 5 Slope wave of order 10^{-6} m^{-1} and the mode 6 Shelf wave of order 10^{-7} m^{-1}, for example. The mode 5 wave speed is therefore ~ 0.01 m/s and the mode 6 wave speed ~ 0.1 m/s. In general, the higher the shelf or slope mode number, the shorter the wave becomes. Given that the amplitude decay distance is of order 10^6 m alongshore and of order 10^5 m cross-shore, the geostrophic assumption in (4.2) appears valid with $(\omega/f)(\partial_y/\partial_x) \ll 1$. Modes 1 and 2 can be very long for weak damping ($\sim 10^{-9}$ to 10^{-10} m^{-1}). Increasing the friction parameter or steepening the topography typically results in slower wave propagation. The exception here is mode 1,

which as we have noted, does not decay over shorter lengthscales as damping or topographic steepness increase. Instead, the mode 1 wavenumber tends to becoming vanishingly small as damping increases and the solution tends to a Stommel-like boundary solution.

An interesting consequence of allowing f to change with latitude is that waves no longer strictly propagate equatorward. This can be shown from the eigenvalue problem introduced in equation (4.17). For solutions of the form $C_j = |C_j(x)| \exp(i\varphi_j(x))$, substitution into (4.17) and taking the imaginary parts gives

$$-\Im(\lambda_j)h'|C_j| = 2r|C_j|'\varphi_j' + r|C_j|\varphi_j'' - h'\omega|C_j|' + h\omega|C_j|(\varphi_j')^2 - h\omega|C_j|'' + \beta h|C_j|\varphi_j'. \quad (4.19)$$

Multiplying through by $|C_j|$ and integrating over x then gives

$$-\Im(\lambda_j)\int_0^{x_{in}} h'|C_j|^2\,dx = \omega\int_0^{x_{in}} h\left(|C_j|'\right)^2\,dx + \omega\int_0^{x_{in}} h|C_j|^2(\varphi_j')^2\,dx + \beta\int_0^{x_{in}} h|C_j|^2\varphi_j'\,dx, \quad (4.20)$$

where we have used integration by parts and the boundary conditions to simplify. The first and second terms on the RHS of (4.20) are ≥ 0 but the sign of the third term depends on φ_j'. Given that the integral on the LHS is ≥ 0, the sign of $\Im(\lambda_j)$ will depend on φ_j'. Hence wave propagation is strictly poleward ($\Im(\lambda_j) \geq 0$) if (i) $\varphi_j' \leq 0$ for all x (westward phase propagation) and (ii) the third term on the RHS is larger in magnitude than the sum of the first and second terms on the RHS. We have found these conditions can be met for modes 1 and 2 when damping is weak, though this may be a spurious artifact of the rigid-lid approximation, as noted above.

An important consequence of the latitude dependence and parameter sensitivity of alongshore amplitude and phase, is that phase speed is a potentially poor measure of information propagation; amplifying a similar conclusion by Marshall and Johnson (2013).

4.6.2 Energetics

The velocity at which energy flows at the boundary can be considered as the velocity at which information flows. We are therefore interested in the energy flux of the boundary response. Multiplying the momentum and continuity equations (4.2), (4.3) and (4.4) by ρu, ρv and $\rho g\eta$, respectively, and adding together the three resulting equations gives the energy equation

$$h\frac{\partial}{\partial t}\left(\frac{\rho v^2}{2}\right) + \nabla\cdot\rho g h\tilde{\eta}\mathbf{u} = -\rho r v^2. \quad (4.21)$$

In the steady state the divergence of the energy flux $\nabla\cdot\rho g h\tilde{\eta}\mathbf{u}$ balances dissipation $-\rho r v^2$ and we denote the time averaged energy flux as $\rho g h\overline{\tilde{\eta}\mathbf{u}} = (\tilde{F}^x, \tilde{F}^y)$.

Using geostrophic balance for v and (4.3) and (4.15) for u and $\tilde{\eta}$ respectively, the divergent time averaged energy flux is

$$(F^x, F^y) = -\frac{\rho g^2}{4}\left\{\left[\frac{r}{f^2}\frac{\partial}{\partial x}\left(|\eta|^2\right) + \frac{2h\omega}{f^2}|\eta|^2\frac{\partial\varphi}{\partial x}\right]\hat{\mathbf{i}} + |\eta|^2\hat{\mathbf{k}}\times\nabla\left(\frac{h}{f}\right)\right\}, \tag{4.22}$$

where a non-divergent part, $\hat{\mathbf{k}}\times\nabla\left(|\eta|^2 h/f\right)$, has been excluded (Longuet-Higgins, 1964). Written in this way the flux consists of a purely zonal component and a component along h/f contours that is directed towards the west and equator. The meridional component, which is always directed equatorward, is

$$F^y = -\frac{\rho g^2 h'}{4f}|\eta|^2. \tag{4.23}$$

Figure 4.8a shows the meridional flux at each longitude as a fraction of the total equatorward flux per meter of latitude for the boundary response presented in Fig. 4.6a, i.e. for the sum of all wave modes. The energy flows as a jet along the slope towards the equator - the steep topographic gradient on the slope supports the strong alongshore velocity and hence kinetic energy.

The zonal component of the flux is

$$F^x = -\frac{\rho g^2}{4f^2}\left[r\frac{\partial}{\partial x}\left(|\eta|^2\right) + 2h\omega|\eta|^2\frac{\partial\varphi}{\partial x} + h\beta|\eta|^2\right] \tag{4.24}$$

and Fig. 4.8b shows the fraction of total equatorward flux at y_p that is fluxed zonally across each longitude (m^{-1} of longitude). On the slope, the energy flows towards the shelf break, whereas off-shore of the slope, the energy flow is towards the interior. The primary energy flow can therefore be described as an equatorward jet along the slope, which leaks out eastward into the interior. This is quite different from the meridional energy flow expected of an f-plane, inviscid solution, where the Shelf waves propagate along-shelf without decaying.

In general, the energy flux cannot be separated into contributions from the individual wave modes because of the interactions between waves. However, with each mode satisfying the governing equations, it remains insightful to consider the fluxes of the individual waves, recalling that mode 6 represents β-plane Shelf waves and mode 5 represents leaky Slope waves. Figures 4.9a-c show the meridional fraction of total equatorward flux (m^{-1}) for wave modes 1, 5 and 6 respectively. Panels a) and c) show that the Shelf waves transmit energy equatorward along the shelf, whereas panel b) shows that Slope waves transmit energy equatorward along the slope. Figures 4.9d-f show, for the same three modes, the fraction of total equatorward flux at y_p that is fluxed zonally across each longitude (m^{-1})

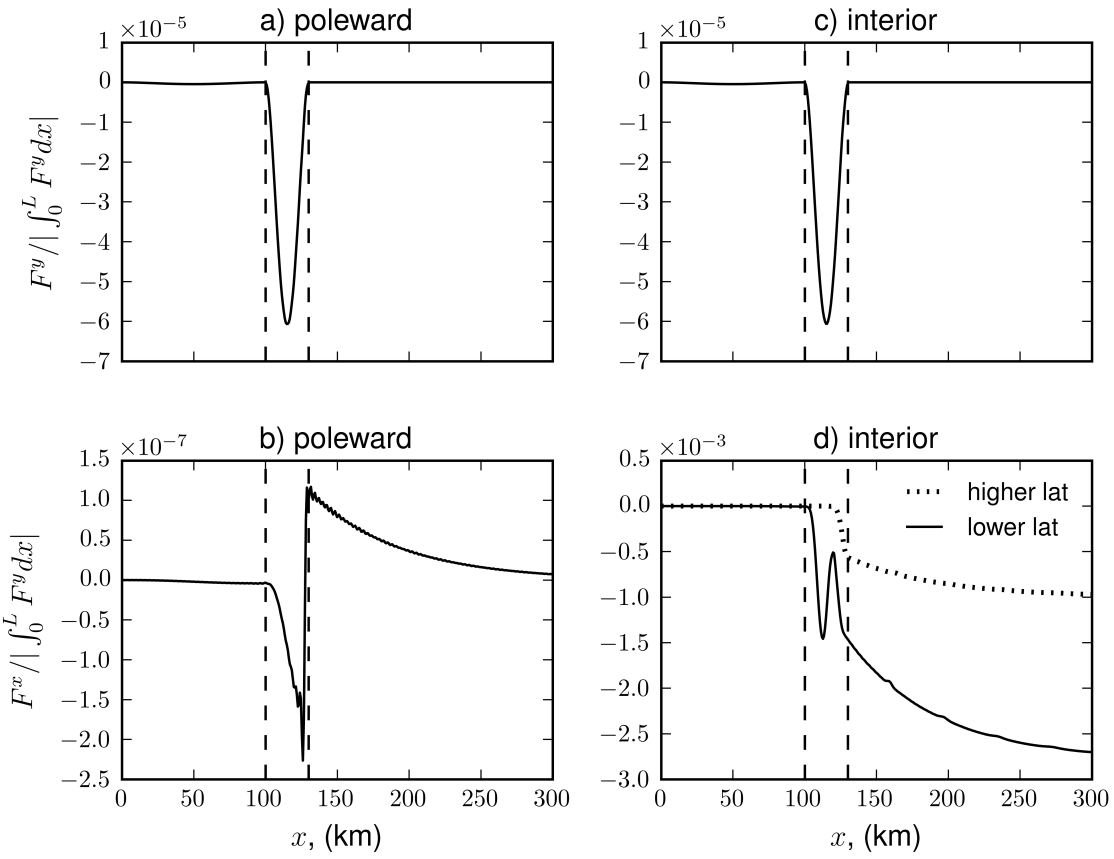

Figure 4.8: *Energy fluxes for the full solutions shown in panels a and c of Fig. 4.6. a) Meridional flux as a fraction of total equatorward flux (m^{-1} of latitude) for the case of poleward variability. b) Zonal flux as a fraction of total equatorward flux (m^{-1} of longitude) at $y \to y_p$ for the case of poleward variability. c) Meridional flux as a fraction of total equatorward flux (m^{-1} of latitude) for the case of interior variability. d) Zonal flux at two different latitudes as a fraction of total equatorward flux at $y \to y_p$ (m^{-1} of longitude) for the case of interior variability. In d) the zonal fluxes are taken at a high latitude (dotted) and lower latitude (solid) where $|\eta_{in}| = 0.5$.*

at two different latitudes, y_p and y_e, where e denotes a latitude equatorward of y_p. Panels d) and f) show that the Shelf waves transmit energy across the shelf, whereas panel e) shows that the leaky Slope waves transmit energy from the slope onto the shelf and into the interior. The dashed lines show that the zonal flux decreases at lower latitudes for modes 5 and 6. With the amplitude of the Shelf waves decaying on the shelf, it is the Leaky Slope waves that are responsible for the main energy pathway, shown as a schematic in Fig. 4.3.

Clearly the leaky Slope waves are not topographically trapped but instead radiate Rossby waves offshore, which then decay due to dissipation. In the limit of small dissipation the open ocean energy flux becomes the product of energy density and the group speed of Short Rossby waves.

The fluxes of the individual waves decrease at lower latitudes according to

$$(F^x, F^y) \propto \left[(y/y_p)^{2\Re(\lambda_j)-2}, (y/y_p)^{2\Re(\lambda_j)-1} \right]. \tag{4.25}$$

For mode 1, assuming $\Re(\lambda_1) \approx 1$, the zonal flux is approximately constant through all latitudes and the meridional flux decreases approximately linearly to zero at the equator. As mode number increases, the zonal and meridional fluxes both decay at lower latitudes at a higher, non-linear, rate. These rates increase when the friction parameter is increased or when the width of the shelf is decreased.

Energy is lost to dissipation at an alongshore rate

$$\int_0^L rv^2 \, dx = \left(\int_{shelf} + \int_{slope} + \int_{off-slope} \right) \nabla \cdot gh\tilde{\eta}\mathbf{u} \, dx, \tag{4.26}$$

where the zonal integral has been split into the shelf, slope and east of slope components. For Shelf waves, the integrals across the slope and offshore are small. The Slope waves, by contrast, dissipate energy on the slope as well as off-slope. Hence along western boundaries the β-effect and friction enable an additional energy pathway and an increased dissipation rate, with the effect that high latitude variability has a reduced footprint at lower latitudes. Compared to a vertical sidewall model, more energy is fluxed equatorward and there is less dissipation at higher latitudes, however as the shelf width decreases, or friction parameter increases, more energy is dissipated at higher latitudes.

Finally, to readdress the issue of the lower bound of $\Re(\lambda_j)$, we note that the alongshore dissipation rate of an individual mode is $\propto (y/y_p)^{2\Re(\lambda_j)-2}$. In which case allowing $\Re(\lambda_j) < 1$ implies that the rate of energy lost to dissipation increases as latitude decreases, tending to infinity at the equator. This would imply that effectively all energy is lost precisely at the equator, which appears unreasonable. While not a formal proof, taken together with

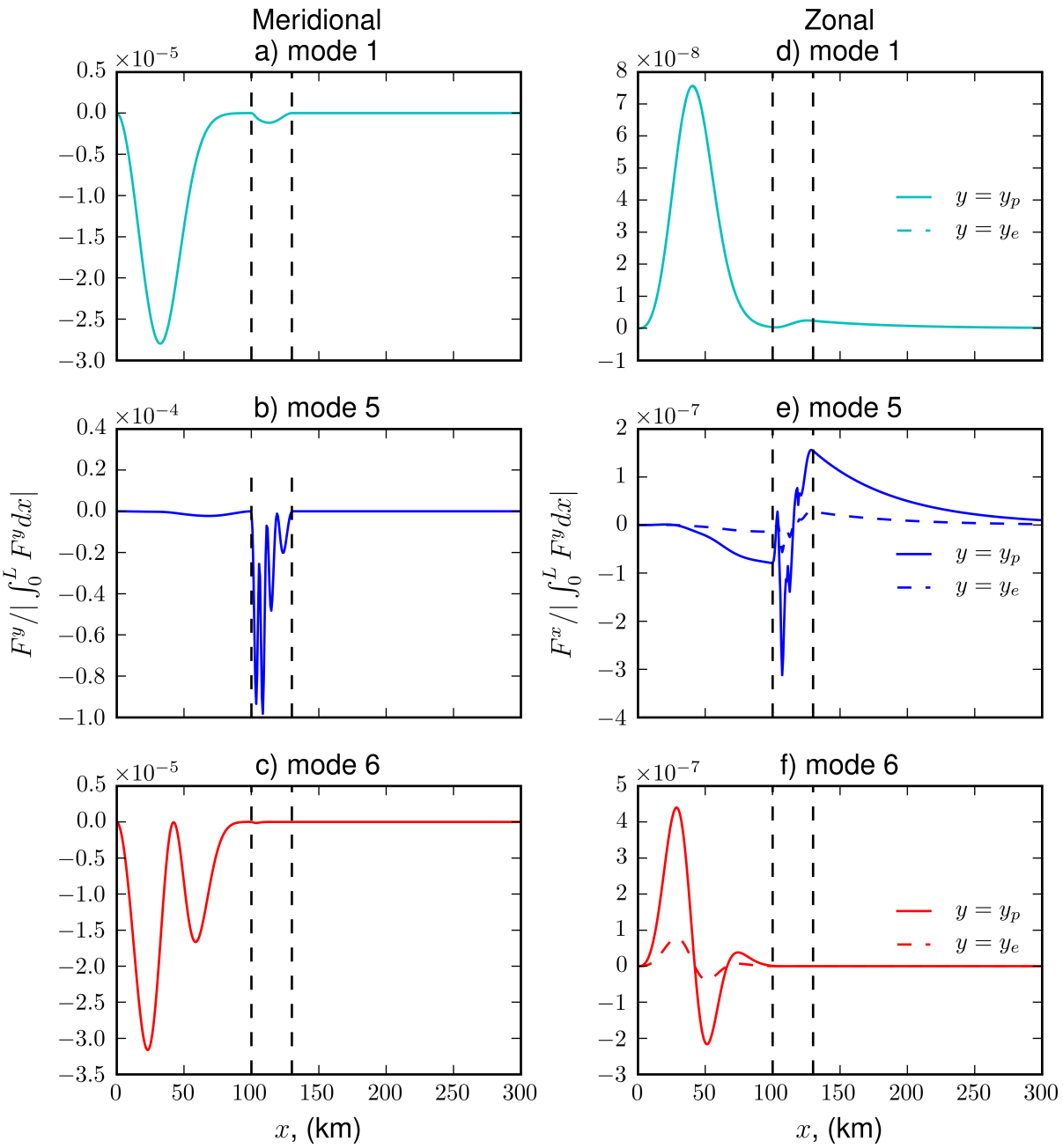

Figure 4.9: *a), b) and c) show, for the poleward forcing case, the meridional flux as a fraction of total equatorward flux (m^{-1} of latitude) for wave modes 1, 5 and 6 respectively. d), e) and f) show the Zonal flux at two different latitudes as a fraction of total equatorward flux at $y \to y_p$ (m^{-1} of longitude). For d), e) and f) the zonal fluxes are taken at a high latitude (solid) and mid latitude (dashed). Black dashed lines denote shelfbreak and slope bottom.*

numerous calculations, we assume it reasonable to take $\Re(\lambda_j) \geq 1$. As previously noted, our assumption of wave trapping breaks down as f becomes small, and we expect energy to leak into the equatorial wave guide and propagate eastward.

4.7 Forcing from the interior ocean

4.7.1 Alongshore evolution

When the boundary waves are excited by variability in the interior ocean, solution (4.11) reduces to

$$\tilde{\eta}(x,y,t) = \left[\eta_{in}(y) - \sum_{j=1}^{\infty} \gamma_j C_j(x) A_j^{in}(y)\right] e^{-i\omega t}, \tag{4.27}$$

$$A_j^{in}(y) = \int_y^{y_p} \frac{d\eta_{in}}{ds} \left(\frac{y}{s}\right)^{\Re(\lambda_j)} e^{[i\Im(\lambda_j)\ln(y/s)]}\, ds, \tag{4.28}$$

where s is a dummy integration variable. Here $\tilde{\eta}$ is the net response at the western boundary where the excited boundary waves are added to the incident long wave η_{in}. The coast will be insulated from variability in the interior when the excited waves destructively interfere with the incident long wave, i.e. when the sum of the excited waves cancels out the long wave on the shelf. Figure 4.6b shows the sum of excited waves when forced by a double gyre interior (see Fig. 4.10b) and 4.6c shows the net response. The shelf is clearly insulated, particularly at higher latitudes, but the alongshore wave amplitudes are important in determining the extent to which the coastline is insulated.

Consider first the case where the interior amplitude $\eta_{in}(y)$ increases linearly from latitude y_e to latitude y_p such that $\eta_{in}(y_e) < \eta_{in}(y_p) = 0$ and $d\eta_{in}/ds$ is constant and can be taken outside the integral in (4.28). At each latitude y between y_e and y_p, the excited wave amplitudes result from a summation (integral) of the effects poleward of y. For mode 1 this gives an alongshore amplitude very roughly proportional to η_{in}. For higher modes, where $\Re(\lambda_j)$ is larger, the amplitude is reduced and concentrated farther poleward. Figure 4.10 shows this clearly with the alongshore amplitudes for modes 1, 5, 6 and 12 for two interior scenarios: a) linear, b) double gyre. In this manner, drawing on our previous analysis, we can see that increasing $\Re(\lambda_j)$, via a decreased shelf width or increased friction parameter, will lead to greater penetration of interior variability at the coast (and at higher latitudes) because the amplitude of the excited waves is reduced and concentrated farther poleward and thus will interfere less with the incident long wave.

Interestingly, unlike the amplitude of waves generated by poleward variability, the alongshore amplitude of waves excited by the interior depend on both $\Re(\lambda_j)$ and $\Im(\lambda_j)$. The

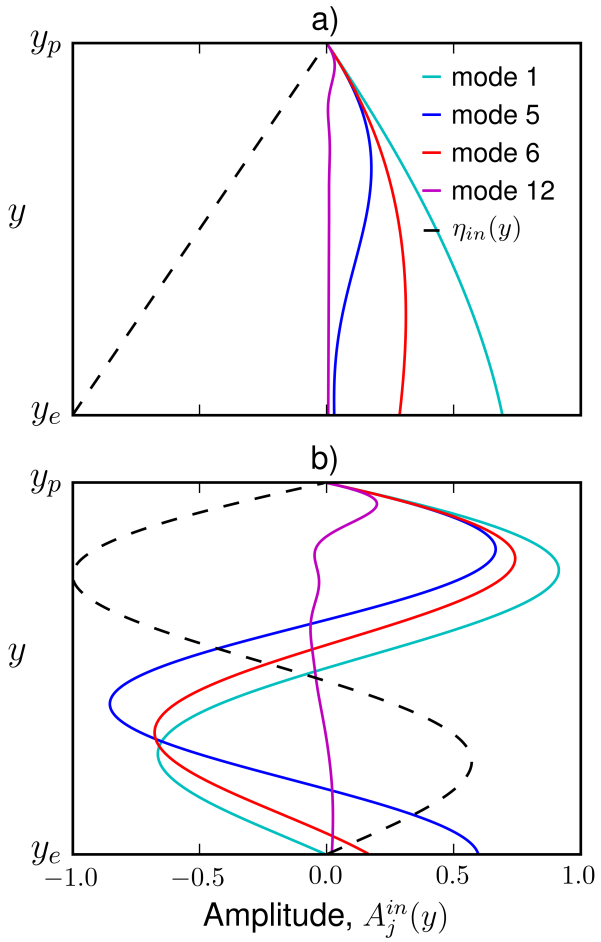

Figure 4.10: *Alongshore amplitude of waves excited by interior variability for modes 1, 5, 6 and 12, i.e.* $A_j^{in}(y)$ *for* $j = 1, 5, 6, 12$ *for two different interior amplitude profiles, a) linear, b) double gyre.*

important point being that the complex exponential cannot be taken outside the integral in (4.28) so that at each latitude s, poleward of y, the alongshore phase of the wave contributes to the equatorward amplitude. The smaller phase speed (larger $\Im(\lambda_j)$) of the Slope waves compared to the Shelf waves results in their decaying relatively farther poleward, e.g. see modes 5 and 6 in Fig. 4.10.

4.7.2 Energetics with interior forcing

The energy flux of the net boundary response will now include interactions between the excited waves and the incident interior long wave. The long wave, by assumption, has no

meridional velocity and therefore does not affect the longitudinal distribution of meridional flux as a fraction of the total equatorward flux, i.e see Fig. 4.8c. The situation is different for the zonal fraction of the energy flux, where the incident wave contributes a westward flux. Fig. 4.8d shows the zonal fraction of the equatorward flux at y_p for two different latitudes: a high latitude where $\eta_{in} = -0.5$ (dotted line) and a lower latitude where $\eta_{in} = 0.5$ (solid line). Clearly the energy due to the incident wave penetrates on-shore to a greater extent at lower latitudes, though the excited wave contribution is clearly visible.

The zonal and meridional fluxes of the individual excited waves remains as given by (4.24) and (4.23) and the energy pathways of the waves remain as shown in Fig. 4.9.

The latitude dependency of the fluxes now becomes

$$(F^x, F^y) \propto \left(|A_j^{in}|^2/f^2, |A_j^{in}|^2/f\right), \tag{4.29}$$

implying that the alongshore decay rate of the energy fluxes increases with mode number. Increasing the friction parameter or decreasing the width of the bottom topography will increase the alongshore decay rate of the fluxes of all modes, except mode 1.

The dissipation of Shelf and Slope waves excited by forcing in the interior ocean is a mechanism by which western boundaries can act as a sink of energy in the ocean energy budget, and is consistent with the Rossby 'graveyard' idea (Zhai et al., 2010). Energy incident from the interior results in an equatorward jet of energy on the slope and leakage of energy back towards the interior as radiating short Rossby waves and also onto the shelf (see schematic Fig. 4.3). Decreasing the width of the shelf or increasing the friction parameter reduces the equatorward flux and increases dissipation at high latitudes as the higher wave modes decay at higher latitudes. While section 4.6 showed energy to be dissipated poleward of the equator, it is quite clear from the alongshore evolution of the waves that at the lowest latitude of the latitude band of forcing (y_e), a proportion of the energy from the interior will remain. At y_e, the interior forcing has produced an anomaly η_e, concentrated on the slope, that acts as a source of variability for latitudes equatorward of y_e; the dynamics equatorward of y_e are as discussed in section 4.6.

4.8 Application to western boundary sea level

Hong et al. (2000) and Minobe et al. (2017) have shown that western boundary sea level fluctuations can be described in terms of interior forcing with surprising skill using relatively simple models, e.g. Hong et al. (2000) showed the first long Rossby wave generated by decadal period wind stress curl variability in the open ocean to contribute significantly to

on-shelf variability along the US East Coast. Aspects of this interior to coastal sea level relationship have been highlighted recently, see (e.g. Sallenger Jr et al., 2012; Ezer et al., 2013; Thompson and Mitchum, 2014; Higginson et al., 2015; Ezer, 2017; Calafat et al., 2018). Despite this success, the physics remains less clear. The roles of topography and friction are often hidden in complex numerical models, statistical descriptions or idealizations. We consider the coastal effect of long period sea level change in the interior by considering $\omega \ll r/H$. In the steady state limit the boundary adjustment is assumed fast relative to the variability in the interior, i.e. following the initial propagating boundary wave adjustment, the interior sea level is represented at the boundary as a series of 'arrested' waves, as in Csanady (1978) (note that all imaginary parts of the solution become zero and we are interested in the wave amplitudes).

Physically, for long period variability, friction acts as a sink in the conservation of potential vorticity relation. The effect of this in terms of sea level is made clearer by extending Csanady's (1978) heat conduction analogy (to the beta-plane). Here we write the vorticity relation (4.7) in terms of sea level in the form of an advection-diffusion equation

$$-\frac{\partial}{\partial x}\left[\left(\frac{r}{f^2}\right)\frac{\partial \eta}{\partial x}\right]+\frac{\partial}{\partial y}\left(\frac{h}{f}\right)\frac{\partial \eta}{\partial x}-\frac{\partial}{\partial x}\left(\frac{h}{f}\right)\frac{\partial \eta}{\partial y}=0, \tag{4.30}$$

where r/f^2 represents the analogous 'diffusion' coefficient and h/f the analogous stream function of an 'advecting velocity' (which is the Long Rossby wave speed if we multiply through by g). From this transport equation, we know that in the limit of small friction, $r \to 0$ (first term vanishes), the conservation of potential vorticity must result in sea level contours following h/f contours. For non-zero r, the compensating effect of friction enables sea level contours to deviate from the h/f contours and 'bend' towards a zonal orientation. This 'bending' is more pronounced at lower latitudes where f is smaller (r/f^2 grows), but otherwise is not spatially uniform because the frictional compensation depends on how the flow interacts with the topography. For further discussion of this analogy see Wise et al. (2018) or for the transport streamfunction version (Welander, 1968; Becker and Salmon, 1997).

4.8.1 Influence of interior sea level

Western boundary sea level is related to interior sea level by

$$\eta(x,y)=\eta_{in}(y)-\sum_{j=1}^{\infty}\gamma_j C_j(x)\int_y^{y_p}\frac{d\eta_{in}}{ds}\left(\frac{y}{y_p}\right)^{\lambda_j}\,ds, \tag{4.31}$$

implying that boundary sea level is the interior sea level modified by a series of (arrested) waves. Steeper topography increases alongshore flow and increases the frictional compensation, bending the sea level contours zonally. Increasing the friction parameter also increases frictional compensation and widens the frictional boundary layer. In other words, there is an increased dissipation of energy at higher latitudes and a reduced equatorward flux of energy at lower latitudes relative to the westward flux of energy. This is represented by a reduction in magnitude of the 2nd term in (4.31) (higher mode waves have been killed off), which implies that coastal sea level tends towards interior sea level at lower latitudes.

Integrating the second term of (4.31) by parts gives

$$\eta(x,y) = \sum_{j=1}^{\infty} \gamma_j C_j(x) \int_y^{y_p} \eta_{in}(s) \frac{d}{ds} \left[\left(\frac{y}{s} \right)^{\lambda_j} \right] ds, \tag{4.32}$$

where we have used $\sum_j^{\infty} \gamma_j C_j = -1$ (see Appendix B). At $x = 0$, this relation describes sea level at the western boundary as a summation of weighted integrals of the interior sea level. The weighting function (the derivative part) acts to attenuate the interior sea level and displace it equatorward.

The coastal sea level for a vertical sidewall boundary, found by Minobe et al. (2017) (second term in their Eq. 14), can be written as

$$\eta(y) = -\int_y^{y_p} \eta_{in}(s) \frac{d}{ds} \left(\frac{y}{s} \right) ds. \tag{4.33}$$

Assuming that in the steep topography limit $\lambda_1 \to 1$ and $\lambda_j \gg 1$ for $j > 1$ then the first (arrested) wave mode of (4.32) differs from (4.33) only by a factor $\gamma_1 C_1(0)$, i.e. if $\gamma_1 C_1(0) = -1$ they are equivalent. Note that (4.33) is also closely related to equation (9) in Hong et al. (2000); in that case the topographic effect, and indeed friction, are represented, implicitly, by tuning parameters (their α_N and α_S). In Fig. 4.11a we show the vertical sidewall coastal sea level solution, the first mode solution from (4.32) at $x = 0$ and the full solution of (4.32) at $x = 0$, in each case for the same interior sea level anomaly, which is representative of subtropical and subpolar gyres. The vertical sidewall and mode 1 solutions differ by some factor, but the full solution shows a coastal sea level that has been displaced farther equatorward with greater attenuation. Consider now Fig. 4.11b, where we have significantly increased the friction parameter r. The solutions are now all equivalent, which implies that the vertical wall solution is the large friction / small topographic width limit of (4.32). In practical terms this suggests that an open ocean sea level anomaly, offshore of the North American east coast for example, will be felt at the coast with a reduced southward displacement and a reduced attenuation when the topography is steeper (e.g. a narrow shelf and upper slope).

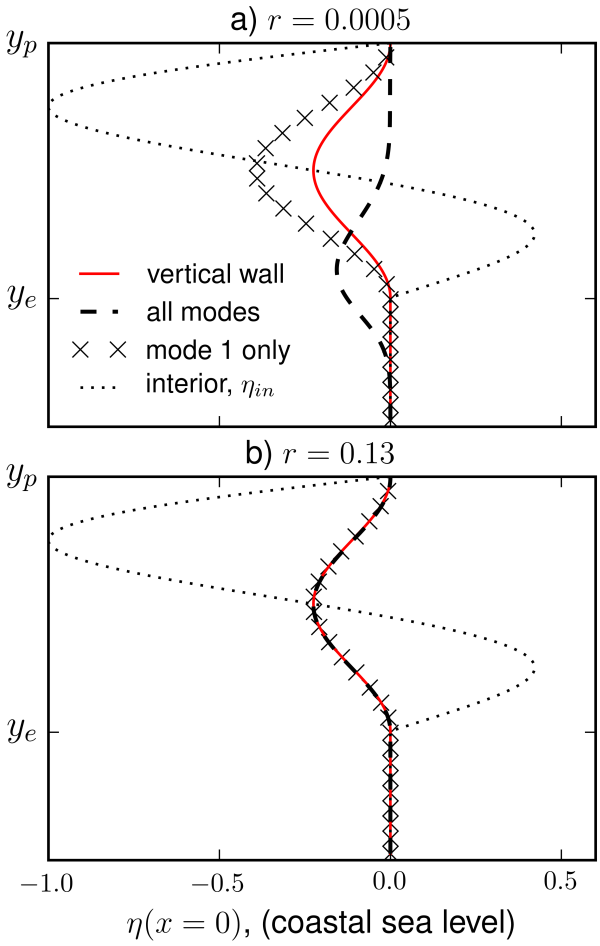

Figure 4.11: *Coastal sea level at the coast, $x = 0$, in response to an imposed interior sea level, η_{in}, that represents a double gyre interior. The model including a shelf and slope (full solution and first wave mode only) is compared with the vertical sidewall model for two friction coefficients, a) $r = 0.0005$, b) $r = 0.13$. Here y_p and y_e are 6000 km and 2000 km poleward of the equator.*

4.8.2 Influence of interior and poleward sea level

From (4.15 and 4.16) western boundary sea level is related to poleward sea level by

$$\eta(x, y) = \sum_{j=1}^{\infty} \alpha_j C_j(x) \left(\frac{y}{y_p}\right)^{\lambda_j}, \tag{4.34}$$

where the poleward sea level specifics are contained within α_j. Figure 4.12a shows sea level at the coast ($x = 0$) when sea level is imposed on the poleward boundary for two different shelf widths: 20 km and 100 km respectively, as well as for a larger friction parameter (with

100 km width shelf). The imposed poleward boundary represents a sea level anomaly, poleward of the domain, which is negative on the shelf relative to the interior ocean. As expected from the previous subsection, Fig. 4.12a shows the negative sea level on the shelf has a reduced influence on lower latitude sea level when friction is increased or when the topography is steepened.

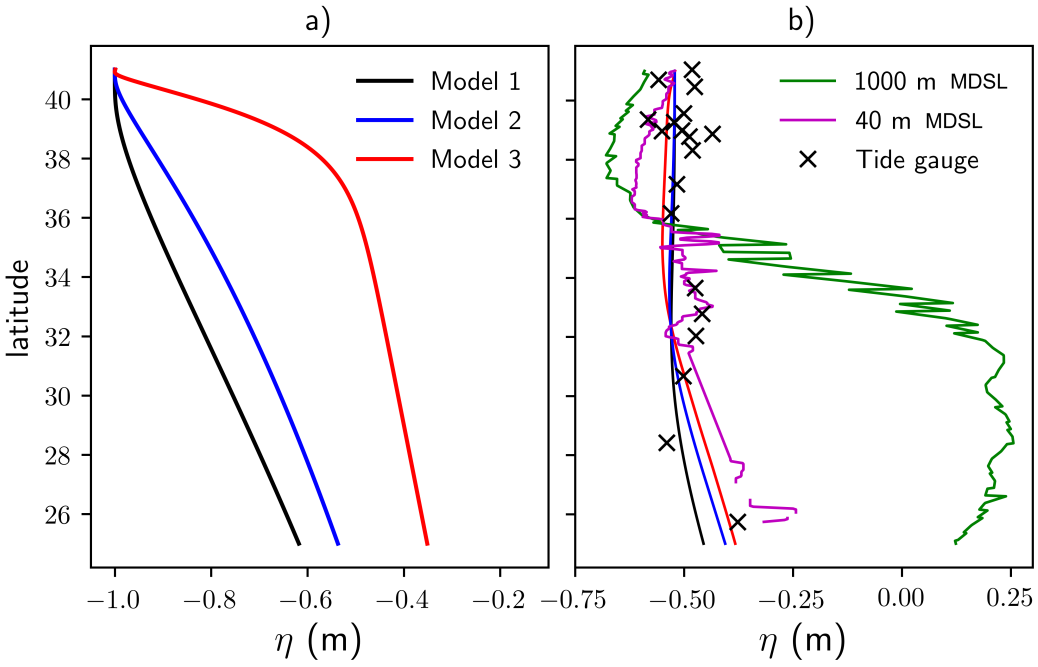

Figure 4.12: *a) Modeled coastal sea level, $\eta(x = 0, y)$, when forced by a 1 m negative sea level anomaly on the shelf at 41 deg latitude (anomaly relative to the deep ocean, $\eta_{in} = 0$). Shelf geometry and friction control the equatorward propagation of information. The colors denote 3 model scenarios: black for shelf width 100 km and friction $r = 0.0005$, blue for shelf width 20 km and friction $r = 0.0005$, red for shelf width 100 km and friction $r = 0.005$. Other parameters are as in Table 4.1. b) Modeled coastal sea level, $\eta(x = 0, y)$, (black, blue and red) along the US east coast when forced by altimetry derived Mean Dynamic Sea Level (MDSL) at the northern and offshore (green) boundaries. The model parameters are as in panel a) but now with max depth 1000 m and slope width 6766 m. MDSL along 40 m and 1000 m depth contours are 22-year means from altimetry (AVISO). Model and observations qualitatively agree.*

The above explanations are well demonstrated by looking at the combined effect of poleward (4.34) and interior sea level (4.31 or 4.32) on coastal sea level using altimetry and tide gauge data along the US east coast. For the forcing data, we use a 22-year

mean (1993-2014 inclusive), AVISO altimeter-derived, dynamic sea level (MDSL) (i.e. sea level relative to the geoid - the Ssalto/Duacs, delayed mode, gridded absolute dynamic topography product using all available satellites - note that the satellite community refers to dynamic sea level as "dynamic topography", although Gregory et al. (2019) recommend limiting this usage to refer to a calculation based on hydrographic density measurements). To force the model we use this MDSL along the 1000 m depth contour between 41N and 25N for our interior sea level, η_{in}, and the MDSL at 40 m, 41N, for the poleward sea level (which is relaxed smoothly to the interior sea level). Figure 4.12b shows the model coastal sea level ($\eta(x = 0, y)$) compared to the altimetry MDSL along the 40 m depth contour and tide gauges. Mean dynamic topography at tide gauges is taken from Andersen et al. (2018), using the EIGEN-6C4 geoid (Förste et al., 2014). Andersen et al. (2018) compared the difference in the tide gauge derived MDSL with 8 different global MDSL from ocean model output and altimetry across 302 points. They found a height (m) standard deviation ranging between 0.123 and 0.163 with the percentage of errors below 9 cm ranging between 68 % and 42 %. They noted that the point values at tide gauges could show scatter due to limited knowledge of the geoid at fine scales. The offset between tide gauge and satellite MDSL data is removed from the tide gauges by subtracting the absolute difference in the means of the 40 m MDSL and the tide gauges. The model compares well with observations. The southward increase in interior sea level across 36N drives a smaller increase at lower latitudes along the Florida coastline. This penetration may be experiencing an amplification due to the narrowing of the shelf along Florida, boosting the frictional compensation and bending sea level contours zonally, across h/f contours.

4.9 Conclusion

Waves at western boundaries are fundamental to how the ocean adjusts to changes in wind and buoyancy forcing. At low frequencies, we find that the β-effect, friction, and bottom topography, result in modified Shelf waves and the appearance of a new class of leaky Slope wave. Slope waves propagate along the continental slope and radiate damped short Rossby waves into the interior, and without friction are not trapped. Waves propagate alongshore typically at orders of 0.1 - 0.01 m/s and amplitudes decay over 1000s km (shorter distances and slower for higher modes). The latitude dependence and parameter sensitivity of alongshore amplitude and phase make phase speed a potentially poor measure of information propagation.

The leaky Slope waves are responsible for transmitting energy (information) as a jet

along the slope and eastward into the interior as damped short Rossby waves. This additional energy pathway due to the inclusion of the β-effect is crucial to shortening the alongshore distance that the waves propagate. The waves decay alongshore (equatorward) as energy is dissipated at a rate that depends on latitude, the friction parameter and the bottom topography. As the friction parameter increases or the width of the shelf decreases, dissipation increases and the waves decay farther poleward. Pressure information due to high latitude variability therefore propagates farther equatorward when the friction parameter is small and the shelf is wide. Conversely, interior variability penetrates onto the shelf to a greater extent (and at higher latitudes) when the friction parameter is large and the shelf is narrow. The limit of large friction is found to be equivalent to a vertical sidewall boundary, where all but the first wave mode become negligible, implying that representing the bottom topography in this way maximizes high latitude dissipation, minimizes the equatorward energy flux and maximizes penetration from the interior. These results follow naturally to long time period variability where the waves become arrested and represent the dynamic interior contribution to coastal sea level, which can be represented by a weighted integral of interior sea level values poleward of the target latitude, as in Minobe et al. (2017).

The simple model and analytic wave solutions provide a physical description for the adjustment process at western boundaries and the sensitivity of these waves to parameter configuration is a plausible explanation for some of the variation found between Ocean Circulation Models in western boundary simulations. We note however that a number of important issues are not accounted for and should be considered for context.

Firstly, a more sophisticated model involving stratification, mean flow and non-linearities will modify the boundary response. For example, medium and strong stratification have been shown to induce a transition in shelf waves towards internal Kelvin waves (Huthnance, 1978) and we expect that stratification effects become more important below the upper slope, complicating the response e.g. (Huthnance, 2004; Kelly and Chapman, 1988; Chapman and Brink, 1987). First indications are that stratification can increase penetration (Wise et al., 2018), but more complete calculations are required to understand the effect in more realistic cases.

Another consideration is the western boundary mean flow. As discussed by Mysak (1980b), a laterally sheared alongshore mean flow will modify the background potential vorticity, and waves (particularly short, slow waves), can be advected by the current and potentially amplified. Where the shear is comparable to f, a divergence of sea level contours from h/f contours is expected.

There are also number of ways to represent friction. One consideration is whether the

friction parameter varies with depth, i.e. $r = r(x)$. In that case the 'advection'-'diffusion' transport equation (4.30) remains the same, implying that frictional compensation simply increases where r is larger. Other alternatives include non-linear bottom friction or lateral friction. In these cases the frictional compensation takes on higher order forms and might amplify effects on the slope.

Finally, it is useful to make a few distinctions with respect to eastern boundaries. Unlike the radiation of short Rossby waves into the interior at western boundaries, Clarke and Van Gorder (1994) show that friction and topography (in a stratified model) allow low frequency sea level signals to propagate polewards with decreasing amplitude, while the cross-shore sea level gradient is small at low latitudes and increases away from the coast at higher latitudes. Clearly friction and topography have an important influence at eastern boundaries, where information propagates along the boundary away from the equator, and into the ocean interior as long Rossby waves.

Topography and friction can be seen to modify the coastal sea level signals associated with waves at both eastern and western boundaries and accounting for these effects at the western boundary leads to some surprising results. Nonetheless, the western boundary waves can be interpreted as a means of propagating energy equatorward along the boundary, with part of that energy being dissipated by a combination of local friction and radiation of short Rossby waves into the interior.

4.10 Appendix A

The solution method below draws upon the integral transform method for solving heat conduction problems detailed by Ozisik (1993) applied to a problem with non-constant coefficients, extending the approach of (Do, 1984; Johnston and Do, 1987; Johnston, 1994).

Substituting $\tilde{\eta}(x, y, t) = \eta(x, y)e^{-i\omega t}$ into (4.7) yields

$$\frac{\partial^2 \eta}{\partial x^2} + b(x)\frac{\partial \eta}{\partial x} + f(y)a(x)\frac{\partial \eta}{\partial y} = 0, \tag{4.35}$$

$$a(x) = \frac{h'}{r - ih\omega}, \tag{4.36}$$

$$b(x) = \frac{h\beta - ih'\omega}{r - ih\omega}. \tag{4.37}$$

and $f(y) = \beta y$. This problem can alternatively be solved by first separating variables and solving the eigenvalue problem in x (via a number of methods). The method used below is particularly direct, obtaining the eigenvalues and eigenfunctions simultaneously,

for a given frequency, from an explicitly defined matrix without finite differencing or special differentiation matrices. Other spectral methods, i.e. Kaoullas and Johnson (2010), may have greater efficiency and accuracy.

We first substitute $\eta(x,y) = \phi(x,y) + \eta_{in}(y)$ to make the boundary conditions at $x = 0$ and $x = x_{in}$ homogeneous and (4.35) becomes

$$\frac{\partial^2\phi}{\partial x^2} + b(x)\frac{\partial\phi}{\partial x} + f(y)a(x)\frac{\partial\phi}{\partial y} + f(y)a(x)\frac{d\eta_{in}}{dy} = 0, \tag{4.38}$$

subject to $\partial\phi/\partial x \to 0$ at $x \to 0$, $\phi = 0$ at $x = x_{in}$ and $\phi = \eta_p(x) - \eta_{in}$ at $y = y_p$.

Defining an eigenvalue problem in Sturm-Liouville form consistent with the x boundary conditions

$$\frac{d^2\psi}{dx^2} + k^2\psi(x) = 0, \tag{4.39}$$

subject to $d\psi/dx = 0$ at $x = 0$ and $\psi = 0$ at $x = x_{in}$. The eigenfunction solutions (in our case considered in the main text $\psi_j = \cos(k_j x)$, with $k_j = (j - 1/2)\pi/x_{in}$ for $j = 1, 2, \dots$) form a complete set of basis functions with the orthogonality condition

$$\int_0^{x_{in}} \psi_i(x)\psi_j(x)\,dx = \psi^N\delta_{i,j}, \tag{4.40}$$

where $\delta_{i,j}$ is the kronecker delta ($\psi^N = x_{in}/2$ in our case). A function on $[0, x_{in}]$ satisfying the boundary conditions can be represented by

$$\phi(x,y) = \sum_j^{\infty} \widehat{\phi}_j(y)\psi_j(x), \tag{4.41}$$

$$\widehat{\phi}_j(y) = \frac{1}{\psi^N}\int_0^{x_{in}} \phi(x,y)\psi_j(x)\,dx. \tag{4.42}$$

Substituting (4.41) into the second and third terms of (4.38) gives

$$\frac{\partial^2\phi}{\partial x^2} + b(x)\sum_{j=1}^{\infty}\frac{d\psi_j}{dx}\widehat{\phi}_j + f(y)a(x)\sum_{j=1}^{\infty}\psi_j\frac{d\widehat{\phi}_j}{dy} + f(y)a(x)\frac{d\eta_{in}}{dy} = 0, \tag{4.43}$$

and taking the transform of (4.43) with respect to $\psi_i(x)$ (multiply through by ψ_i, integrate over x and divide by ψ^N) yields a set of equations dependent on y only

$$\begin{aligned}\frac{1}{\psi^N}\int_0^{x_{in}} a(x)\psi_i\sum_{j=1}^{\infty}\psi_j\,dx\,\frac{\partial\widehat{\phi}_j}{\partial y} + \left(-k_i^2\delta_{i,j} + \frac{1}{\psi^N}\int_0^{x_{in}} b(x)\psi_i\sum_{j=1}^{\infty}\frac{d\psi_j}{dx}\,dx\right)\frac{1}{f(y)}\widehat{\phi}_j \\ = -\frac{1}{\psi^N}\int_0^{x_{in}} a(x)\psi_i\,dx\,\frac{d\eta_{in}}{dy},\end{aligned} \tag{4.44}$$

where we have made use of Green's theorem (see (Ozisik, 1993, p.526)) to get

$$\frac{1}{\psi^N}\int_0^{x_{in}} \psi_i \frac{\partial^2 \phi}{\partial x^2}\, dx = -k_i^2 \widehat{\phi}_i. \tag{4.45}$$

Equation (4.44) is more usefully written as a matrix equation

$$\mathbf{A}\frac{d\widehat{\boldsymbol{\phi}}}{dy} + \mathbf{B}\frac{1}{f(y)}\widehat{\boldsymbol{\phi}} = \mathbf{b}\frac{d\eta_{in}}{dy}, \tag{4.46}$$

where bold capital denotes a matrix and bold lower case a vector and where

$$\mathbf{A}_{i,j} = \frac{1}{\psi^N}\int_0^{x_{in}} a(x)\psi_i\psi_j\, dx, \tag{4.47}$$

$$\mathbf{B}_{i,j} = \operatorname{diag}\left(-k_j^2\right) + \frac{1}{\psi^N}\int_0^{x_{in}} b(x)\psi_i\frac{d\psi_j}{dx}\, dx, \tag{4.48}$$

$$\mathbf{b}_i = -\frac{1}{\psi^N}\int_0^{x_{in}} a(x)\psi_i\, dx, \tag{4.49}$$

with diag denoting a diagonal matrix. For matrices the first subscript index denotes the row and the second the column. The boundary condition for (4.46) is

$$\widehat{\boldsymbol{\phi}}_p = \frac{1}{\psi^N}\int_0^{x_{in}} \psi_i\left[\eta_p(x) - \eta_{in}\right]\, dx \tag{4.50}$$

and solving with the integrating factor

$$\mathbf{P}(y) = \exp\left(-\mathbf{T}\int_y^{y_p}\frac{1}{f(s)}\, ds\right), \tag{4.51}$$

where $\mathbf{T} = \mathbf{A}^{-1}\mathbf{B}$ gives the solution

$$\widehat{\boldsymbol{\phi}} = \mathbf{P}^{-1}\widehat{\boldsymbol{\phi}}_p - \mathbf{P}^{-1}\int_y^{y_p}\mathbf{P}(s)\frac{d\eta_{in}(s)}{ds}ds\,\mathbf{A}^{-1}\mathbf{b}. \tag{4.52}$$

We recover ϕ by substituting (4.52) into (4.41), and recover η by adding η_{in}, giving

$$\eta(x,y) = \eta_{in} + \boldsymbol{\psi}\cdot\left[\mathbf{P}^{-1}\widehat{\boldsymbol{\phi}}_p - \mathbf{P}^{-1}\int_y^{y_p}\mathbf{P}(s)\frac{d\eta_{in}(s)}{ds}ds\,\mathbf{A}^{-1}\mathbf{b}.\right], \tag{4.53}$$

where $\boldsymbol{\psi} = [\psi_1, \psi_2, \dots]$. The solution can be written as a series. For a diagonalizable $\mathbf{T}$, we have the eigendecomposition $\mathbf{T} = \mathbf{Q}\boldsymbol{\Lambda}\mathbf{Q}^{-1}$, where $\boldsymbol{\Lambda}$ is diagonal with each element λ_j an eigenvalue of $\mathbf{T}$ and the columns $\mathbf{q}_j$ of $\mathbf{Q}$ the corresponding eigenvectors of $\mathbf{T}$. Then using the identity $\exp(\mathbf{T}) = \exp(\mathbf{Q}\boldsymbol{\Lambda}\mathbf{Q}^{-1}) = \mathbf{Q}\operatorname{diag}(e^{\lambda_j})\mathbf{Q}^{-1}$ and ordering the terms in the series by λ_j, the solution is

$$\eta(x,y) = \eta_{in}(y) - \sum_{j=1}^{\infty}\gamma_j C_j(x)A_j^{in}(y) + \sum_{j=1}^{\infty}\alpha_j C_j(x)A_j^{p}(y) \tag{4.54}$$

$$C_j(x) = \boldsymbol{\psi}(x) \cdot \mathbf{q}_j \tag{4.55}$$

$$A_j^{in}(y) = \exp\left[-\lambda_j \int_y^{y_p} 1/f(s)\, ds\right] \int_y^{y_p} \frac{d\eta_{in}}{ds} \exp\left[\lambda_j \int_s^{y_p} 1/f(\hat{s})\, d\hat{s}\right] ds \tag{4.56}$$

$$A_j^{p}(y) = \exp\left[-\lambda_j \int_y^{y_p} 1/f(s)\, ds\right] \tag{4.57}$$

where $\gamma_j = \left(\mathbf{Q}^{-1}\mathbf{A}^{-1}\mathbf{b}\right)_j$ and $\alpha_j = \left(\mathbf{Q}^{-1}\widehat{\boldsymbol{\phi}}_p\right)_j$ are constants and s and $\hat{s}$ are dummy integration variables.

4.11 Appendix B

Left multiplying (4.46) by $\boldsymbol{\psi} \cdot \mathbf{A}^{-1}$ gives

$$\boldsymbol{\psi} \cdot \frac{d\widehat{\boldsymbol{\phi}}}{dy} + \boldsymbol{\psi} \cdot \mathbf{A}^{-1}\mathbf{B}\frac{1}{f(y)}\widehat{\boldsymbol{\phi}} = \boldsymbol{\psi} \cdot \mathbf{A}^{-1}\mathbf{b}\frac{d\eta_{in}}{dy}. \tag{4.58}$$

Dividing (4.43) through by $f(y)a(x)$ gives an expression for $\boldsymbol{\psi} \cdot d\widehat{\boldsymbol{\phi}}/dy$ which substituting (4.58) into gives

$$\frac{1}{f(y)a(x)}\left(\frac{\partial^2\phi}{\partial x^2} + b(x)\sum_{j=1}^{\infty}\frac{d\psi_j}{dx}\widehat{\phi}_j\right) + \frac{d\eta_{in}}{dy} = \boldsymbol{\psi} \cdot \mathbf{A}^{-1}\mathbf{B}\frac{1}{f(y)}\widehat{\boldsymbol{\phi}} - \boldsymbol{\psi} \cdot \mathbf{A}^{-1}\mathbf{b}\frac{d\eta_{in}}{dy}. \tag{4.59}$$

If at $y = y_p$ we take ϕ to be zero, then $\hat{\phi}_j$ are also zero and the first terms on both sides of (4.59) become zero. This implies that $\boldsymbol{\psi} \cdot \mathbf{A}^{-1}\mathbf{b} = -1$. Finally, we have

$$\sum_j^{\infty} \gamma_j C_j = \boldsymbol{\psi} \cdot \mathbf{Q}\mathbf{Q}^{-1}\mathbf{A}^{-1}\mathbf{b} = \boldsymbol{\psi} \cdot \mathbf{A}^{-1}\mathbf{b} = -1. \tag{4.60}$$

Chapter 5

Hot Spots Along the North American East Coast

Modelling offshore-forced sea level hot spots and boundary waves along the North American east coast

5.1 Preamble

In the previous chapter the relationship between sea level along a western boundary and linear coastally trapped wave theory has been explored. For the barotropic case, Shelf and Slope waves are found to mediate the influence of open ocean variability on the coast by propagating information equatorward along the shelf. The beta-effect and friction are found to be important drivers of dissipation and wave decay, and thereby influence the extent to which off-slope variability can penetrate onto the shelf. The direction of information propagation, with the coast on the right, implies control from poleward latitudes over the coastal sea level along a western boundary.

The previous chapters have been based on linear dynamics with idealized coastal bathymetry. In this chapter we extend the study to a more realistic regional general ocean circulation model that includes realistic bathymetry and a mean current, which allows for advection by the mean flow to be accounted for. The coastal sea level and adjustment process are investigated along the North American east coast, in the context of observed hot spots of coastal sea level variability, and the extent to which linear idealized dynamics remains valid is explored.

Publication and Author Contributions

This chapter has been prepared for submission to Ocean Modelling. The paper has four authors: Myself (Anthony Wise), Jeff A. Polton, Christopher W. Hughes and John M. Huthnance. As primary author, I carried out the research and wrote the paper. My supervisors Jeff Polton, Christopher Hughes and John Huthnance, provided valuable supervision, editorial critique and discussion of ideas.

5.2 Paper Abstract

Sea level rise hot spots along the North American east coast have been shown to shift in latitude repeatedly over the past 95 years, and they have been linked with a number of forcing phenomena including the North Atlantic Oscillation (NAO) and the Atlantic Meridional Overturning Circulation (AMOC). Using model output we show on-shelf sea level variability to be highly consistent with linear barotropic trapped wave theory and use this to explain how coastal sea level rise at a given latitude can be driven by on and off-shore SSH anomalies many degrees of latitude ($\sim$100s km) further north. Using a barotropic 1/12 $^\circ$ NEMO model of the North American east coast, we show that the character of the coastal sea level response to remote SSH variability on the upper slope is well represented by barotropic dynamics. Hilbert transform Complex EOF analysis reveals the propagation and amplitudes of two modes of variability that have been generated by off-slope SSH anomalies representative of those described in observational studies. The first mode of variability describes in-phase coherence along the entire coastline and is driven by a SSH anomaly in the subpolar gyre. The second mode of variability describes in-phase coherence along the coast south of Cape Hatteras and is driven by an off-slope SSH anomaly that is consistent with the NAO or fluctuations in meridional heat divergence in the sub tropical band of the Atlantic.

5.3 Introduction

In recent years a spotlight has been cast over the local and remote drivers of coastal sea level variability along the North American east coast. Most recently, Volkov et al. (2019) drew attention to a basin scale tripole Sea Surface Height (SSH) pattern of variability linked to the Atlantic Meridional Overturning Circulation (AMOC) and North Atlantic Oscillation (NAO) that was a source of interannual-to-decadal SSH variability along the southeast coast of the United States. As in a number of studies looking at these processes, barotropic waves trapped against the western boundary are invoked as a possible mechanism for the actual adjustment that occurs between the coast and interior ocean (or elsewhere on the shelf). The objective of this study is to use a medium complexity numerical model, including realistic bathymetry and nonlinear terms, with analysis methods that reveal the propagation of variability, to more thoroughly connect the processes identified by observational studies with the theory of coastally trapped boundary waves.

The term "hot spot" has been used to describe areas of accelerated sea level rise. Coastal hot spots of sea level rise have the potential to increase the background sea level making the adjacent coast vulnerable to shorter time scale events that can cause flooding, for example storm surges. The mechanisms that govern these hot spots are of particular interest, therefore, when they are located along densely populated coastlines. Sallenger Jr et al. (2012) identified, from observations, a "hot spot" along 1000 km of the North American coastline north of Cape Hatteras where the rate of increase of sea level rise was of order 3-4 times larger than the global average during 1980-2009. While it remains debated, they suggested the sea level rise might be associated with a slowdown of the AMOC. In addition to the AMOC, a number of processes, both local and remote, have been investigated as drivers of this "hot spot", and assigning causality between sea level anomalies and forcing, more generally, has been shown to be complex due to the coupling of driving phenomena. Kenigson et al. (2018) suggest that changes in the local wind stress (particularly alongshore), linked to the NAO, are strongly related with sea level anomalies north of Cape Hatteras. Similarly, Piecuch et al. (2016) show annual coastal sea level changes North of Cape Hatteras to be driven by wind stress over the continental shelf and slope, and highlight the apparent dominance of barotropic dynamics in the adjustment of coastal sea level to forcing. Furthermore, the anticorrelation between coastal sea level north of the Cape, and overturning circulation at 26N, is suggested by Piecuch et al. (2019) not to be causal, but instead driven by temporally coherent, but different, forcing mechanisms. In the case of the former, local alongshore wind and air surface pressure are responsible, and in the latter, zonal wind stress

along 26 N is responsible - though they note the potential role of large-scale atmospheric modes of variation linking them, such as the NAO. In terms of remote drivers, over a 50 year period of observations (1965-2014) Frederikse et al. (2017) found a strong correlation between coastal sea level north of the Cape and decadal steric variability in the Subpolar Gyre. The steric signal showed an upward sea level trend and acceleration, which is also found along the coast. They suggest the variability likely originates in the Labrador sea, from where it propagates southward. The linkage between coastal sea level and the Labrador Sea is also noted by Andres et al. (2013), with a similar correlation map, though they note the mechanism of propagation onto the shelf is not clear.

Sea level variability along the North American east coast is subject to regional differences north and south of Cape Hatteras, where the Gulf Stream separates from the western boundary. This has led to investigations into the connection between the Gulf Stream and coastal sea level. In particular Ezer et al. (2013); Ezer (2019) suggest that changes in the strength of the Gulf Stream and its position relative to the mid-Atlantic Bight, north of Cape Hatteras, affects sea level gradients. They conclude that a strong Gulf Stream leads to lower coastal sea level in the mid-Atlantic Bight, while the effect is reduced south of the Cape.

Variability in the strength of the Gulf Stream can itself, of course, be a consequence of large scale forcing variability. Valle-Levinson et al. (2017) show that between 2011 and 2015, sea level rise actually decelerated north of Cape Hatteras, while accelerating to 3 times the global mean south of the Cape - the latter phenomenon also being reported by Park and Sweet (2015). Valle-Levinson et al. (2017) show this sea level rise "hot spot" to be active over the past 95 years with a shifting latitude. They go on to suggest that the existence of the "hot spot" is conditional upon the cumulative effects of El Niño and that the latitudinal position depends on the cumulative effects of the NAO. The acceleration of sea level rise south of the Cape has also been attributed to a 0.2 °C per year warming of the Florida Current and the deceleration north of the Cape to a combination of increased atmospheric surface pressure, changing wind patterns and cooling (Domingues et al., 2018). Volkov et al. (2019) suggest that sea level south of the Cape is largely driven by large-scale meridional heat divergence influenced by the AMOC. Stronger mean heat transport by the Florida Current leads to higher thermosteric sea level in the interior ocean at mid latitudes, which is then coherent with coastal sea level. They also point to the large scale atmospheric forcing, with a positive NAO also leading to higher interior sea level across the same latitude band. Indeed while they show the very large scale first mode of variability of SSH, steric and thermosteric sea levels to have a similar tripole spatial pattern, one suspects a similar

pattern could also be shown for the wind stress curl, with the NAO acting to shift the zero wind stress-curl latitudinally. For example, the NAO+ shifts the zero wind stress-curl line northward and increases its zonal tilt, i.e. the eastern portion of the zero wind stress-curl is shifted farther northward. The NAO- results in a more zonal zero wind stress-curl. This feature of the NAO in terms of ocean circulation has been discussed by Marshall et al. (2001). In terms of sea level, the resulting increase or decrease in interior SSH near Cape Hatteras appears to influence the SSH on the shelf along the Florida coastline. Remote forcing from the interior ocean has also been put forward as an explanation for large inter-annual to decadal variability in the amplitude of the sea level annual cycle south of Cape Hatteras (Calafat et al., 2018). They suggest that larger amplitudes in the annual cycle, coherent along much of the coast from Cape Hatteras into the Gulf of Mexico, are the result of density anomalies in the interior ocean travelling westward towards the western boundary. They note that larger annual cycle amplitudes correspond with larger annual upper mid-ocean transport, which would be explained by a larger pressure gradient between eastern and western boundaries of the Atlantic. This latter point clearly brings into focus the connection between western boundary sea level and the AMOC - discussed in detail by Bingham and Hughes (2009); Little et al. (2019) - with consequences for meridional heat transport (Zhai et al., 2011), and thereby also the climate.

Clearly there are a number of forcing phenomena that are correlated with coastal sea level variability, however in order to explain the spatial distribution of coastal sea level variability we must also consider the actual process of adjustment between the coast and off-slope (or elsewhere on the shelf). Linear theory with idealized geometry and bathymetry suggests that western boundary sea level is determined by what occurs poleward of the point being considered (Wise et al., 2018, 2020; Minobe et al., 2017), but this neglects any possible role of advection by a boundary current. This work takes the next step by considering realistic bathymetry, and allowing nonlinear terms so that advection of potential vorticity is accounted for. We will find that this does not substantially affect the poleward control of sea level.

In the following section we introduce the theoretical concepts of how the open ocean is connected to the coast. We then describe the model and method of analysis used in this study, present results, and conclude with a discussion and summary.

5.4 Theory

Because the western boundary acts like a wall, the flow must diverge as it approaches, implying that the dynamics at the coast are not as they are in the interior ocean. This has important consequence for how sea level variability is spatially distributed along the coastline and draws attention to the role of the continental slope in separating the shelf (coast) from the interior ocean. While variability can spread relatively slowly via advection by the current, here we look at the quicker mechanism of signal propagation by waves trapped to the coast (boundary) (Huthnance, 1975, 1978).

Huthnance (1987b); Chapman and Brink (1987); Huthnance (2004) show that in idealized experiments with stratification, forcing in the interior ocean due to wind stress or density gradients elicit an essentially barotropic response along the shelf, which propagates over long distances with the boundary on the right. For eastern boundaries, Clarke and Van Gorder (1994) show that at typical El Niño-Southern Oscillation (ENSO) frequencies, on-shelf sea level signals travel poleward with a reduction in amplitude as latitude increases. Using isopycnal models validated with altimetry, Roussenov et al. (2008) find that changes in high-latitude forcing are communicated along the continental slope by boundary waves over several thousand kilometers. The result is coherent signals in SSH and bottom pressure variability over large distances - see also (Hughes and Meredith, 2006; Hughes et al., 2018).

The body of literature investigating coastally trapped waves (CTW) in various settings is extensive, see Hughes et al. (2019), Brink (1991), Huthnance et al. (1986) and Mysak (1980b) for reviews. Here, by assuming that the response on the shelf and upper slope is dominated by barotropic dynamics, as studies noted above suggest, we focus specifically on barotropic waves, which can also be thought of as waves in a homogeneous upper layer of the ocean that is grounded on the sea floor between the upper slope and coast (i.e. lower surface in contact with shelf and upper slope). Offshore, the layer is considered to be the upper layer only, with a motionless layer beneath. This simplification allows us to model the adjustment mechanism at the coast to a SSH anomaly, regardless of which specific forcing phenomenon produced it, i.e. wind or density induced SSH anomaly. We simply relate coastal sea level to the off-slope sea level (remote forcing) and to the sea level at a specific latitude (local forcing). For example fluctuations in wind stress in the open ocean (remote forcing) produce a SSH anomaly adjacent to the slope and wind stress fluctuations on the shelf produce local forcing.

In terms of what we expect from theory, for annual to decadal forcing periods, Wise et al. (2020) showed that when the forcing originates in the north, the western boundary

response consists of a set of Shelf and Slope waves that carry the sea level anomaly southward, and decay due to dissipation of energy as a result of bottom friction and through the radiation of short Rossby waves. When the forcing was from off-slope, Shelf and Slope waves were generated that cancelled the interior signal, which can be thought of as a long Rossby wave incident on the boundary. As the excited waves propagated equatorward they decayed, allowing the interior signal to penetrate onto the shelf at lower latitudes. Marshall and Johnson (2013) showed a similar mechanism involving the first baroclinic mode wave for the case where the boundary is a vertical sidewall in a reduced gravity model. Physically, off-slope SSH anomalies (possibly carried westward by long Rossby waves) modify the amplitude (and speed) of southward propagating boundary waves (generated by local and remote forcing farther northward). As the southward propagating boundary waves dissipate energy, they reduce in amplitude and the incident long Rossby waves from off-slope modify the amplitude of the boundary waves to a greater extent, thereby allowing greater penetration of interior SSH variability. Importantly, the rate of dissipation is shown to depend on a number of factors: steepness and width of the bottom topography, friction parameter, as well as latitude (Wise et al., 2020, 2018; Huthnance, 2004; Chapman and Brink, 1987; Brink and Allen, 1978). Note that while we do not explicitly cover the case of local forcing on the shelf, on-shelf alongshore wind stress forcing also produces shelf and slope waves that propagate with the coast on the right.

5.5 Model and analysis method

5.5.1 Model setup

The model is based on a 2d configuration [1] of the NEMO 4.0 (Gurvan Madec and NEMO System Team, 2019) General Ocean Circulation model that we have modified to create a barotropic North Atlantic western boundary. The model has one active layer using the terrain following s-coordinate, and the horizontal grid is a 1/12 of a degree grid using the NEMO ORCA_R12 grid as the parent grid.

The nonlinear equations solved by NEMO are (2.1) - (2.4) introduced in Chapter 2 with the density perturbation set to zero, $\rho = 0$. The free surface η is calculated from

$$\frac{\partial \eta}{\partial t} = -\boldsymbol{\nabla} \cdot [(H + \eta)\, \boldsymbol{u}]\,, \tag{5.1}$$

where $\boldsymbol{u}$ is the horizontal velocity. The impermeability kinematic boundary condition at

[1] http://forge.ipsl.jussieu.fr/nemo/svn/branches/UKMO/dev_r8814_surge_modelling_Nemo4

the bottom ($z = -H$), where $H(x, y)$ is the depth of the ocean bottom, is

$$w = -\boldsymbol{u} \cdot \boldsymbol{\nabla} H, \tag{5.2}$$

and the free surface kinematic boundary condition, where the water interacts with the atmosphere ($z = \eta$), is

$$w = \frac{\partial \eta}{\partial t} + \boldsymbol{u} \cdot \boldsymbol{\nabla} \eta. \tag{5.3}$$

For the dynamic conditions, wind stress is exerted at the sea surface

$$A_V \frac{\partial \boldsymbol{u}}{\partial z} = \frac{1}{\rho_0}(\tau^x, \tau^y), \tag{5.4}$$

and the bottom friction is applied at the ocean bottom

$$A_V \frac{\partial \boldsymbol{u}}{\partial z} = C_d \sqrt{u^2 + v^2}\, \boldsymbol{u}, \tag{5.5}$$

where C_d is a frictional drag coefficient. Note that throughout we take the meridional wind stress τ^y to be zero and there is no atmospheric pressure gradient included.

The lateral boundaries are closed with no normal flow, except for the northern and southern boundaries, which have Flather (1994) radiation conditions imposed on the velocity normal to the boundary, which allows gravity waves to exit the domain (external field variables are taken to be zero) i.e. the normal velocity is $u^{norm} = (\sqrt{gH}/H)\eta$ at the boundary. The purpose of the Flather condition is to minimize any artificial leakage of the interior ocean signal onto the shelf close to the boundary. For land boundaries partial slip is imposed.

While the bottom topography at the western boundary is realistic - we use the 15 arc-second GEBCO 2019 gridded data set (https://www.gebco.net/) - we modify it in two ways. Firstly, we set the maximum depth for the entire domain to a constant H_c, i.e. any depth $H(x, y)$ greater than H_c is set equal to H_c. This allows us to represent an idealized upper ocean layer between the upper slope and coast. Secondly, we truncate the eastern extent of the domain to roughly follow the Mid Atlantic Ridge. This reduces computational expense while retaining an adequate interior ocean for subpolar and subtropical gyres to form and set up the SSH off-slope of the western boundary.

For bottom friction, which is non-linear, it is sensible to assume that there is a reduced frictional effect on the upper layer of the flow in the interior ocean, and we therefore use two different friction coefficients; one for the shelf and slope C_D^S, and another smaller value, C_D^{in}, for greater depths (i.e. where $H = H_c$). The main effect of this is to create a more realistic boundary current since a large friction parameter in the interior ocean was found

H_c	C_D^s	C_D^{in}	B_h	Partial slip parameter
500 m	2.3×10^{-3}	4×10^{-4}	-5 $\times$ 10^9 m^4 s^{-1}	1

Table 5.1: *Values of the parameters used in the model: max depth H_c, friction coefficient on shelf and slope C_D^s, friction coefficient over flat bottom interior ocean region C_D^{in}, bilaplacian horizontal diffusion coefficient B_h and the partial slip mask parameter value where 0 is free slip and 2 is no slip.*

to create an unrealistically wide boundary layer in preliminary experiments (to some extent the quadratic friction formulation used will also reduce bottom friction effects in the deeper open ocean). Ultimately we are concerned with creating a more realistic off-slope SSH to relate to the on-shelf SSH. Finally, the model is set up to use a lateral bilaplacian diffusive operator and a free surface. All parameter values are listed in Table 5.1.

5.5.2 Forcing

Forcing of the model is provided exclusively via an idealized zonal wind stress, τ_u. All other forcing mechanisms are turned off. As previously noted, from an analysis point of view, it is unimportant how the interior ocean SSH is set up, however using wind stress allows us to maintain extremely simple boundary conditions while selecting a wind stress magnitude that results in quite realistic SSH gradients. The wind stress magnitude applied is unrealistically large, i.e. approximately double observed values, however this is physically reasonable given the reduced domain width.

The model experiments have two forcing stages, a "spin-up" stage, and a stage where the wind stress changes in time and space. During the spin-up, a quasi steady state is established using a time independent zonal wind stress, which we consider as the time mean wind stress $\tau_u^M(x, y)$, as shown in Fig. 5.1a. The structure of this wind stress profile is chosen to be representative of the long period time-mean zonal wind stress, i.e. see Hellerman and Rosenstein (1983). Note that a key feature of the wind profile is the intersection of the zero wind-stress curl contour with the western boundary, and also its basin scale characteristics, i.e. the zero curl line (where τ_u is maximal or minimal) is not zonal. In Fig. 5.1a the zero wind stress curl corresponds to the contours emanating from 35 ° N and 20° N. The latitude of the zero wind-stress curl, relative to Cape Hatteras plays an important role in how the Gulf Stream separates from the boundary and this has been discussed in detail for a barotropic ocean e.g. (Dengo, 1993; Munday and Marshall, 2005) and for more complex

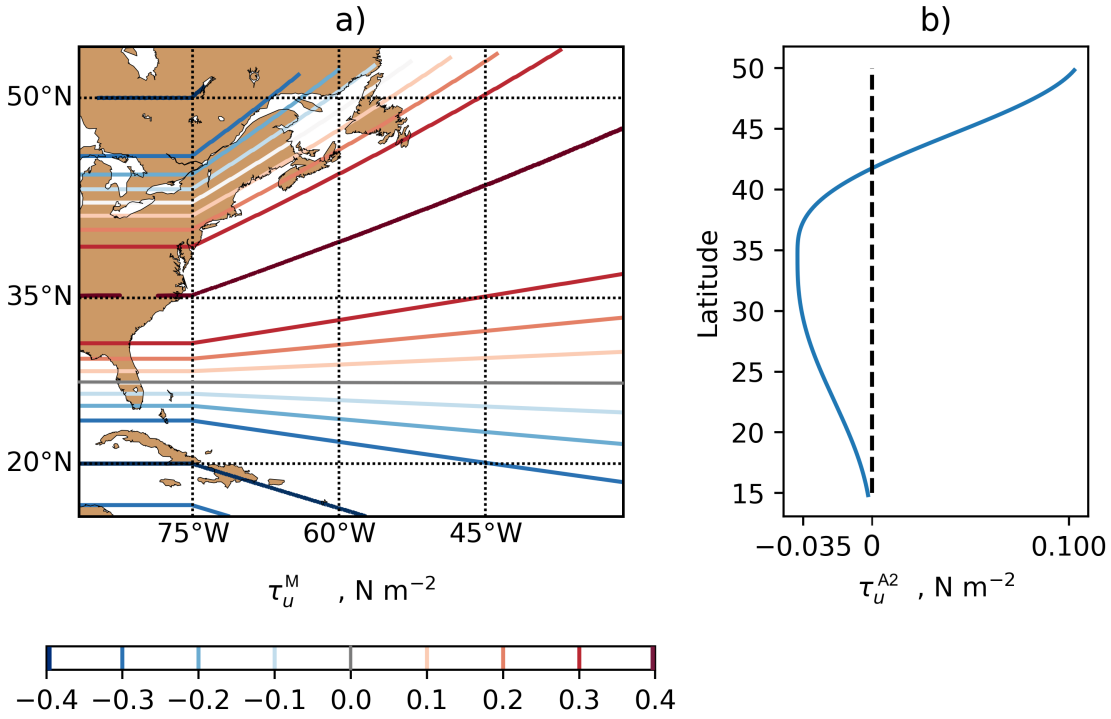

Figure 5.1: *a) Contours of τ_u^M: the steady, purely zonal wind stress applied to establish a mean circulation. b) The additional zonal wind stress τ_u^{A2} which is applied at all deep water longitudes with a time-dependent amplitude, to simulate NAO variations, following Zhai et al. (2014).*

settings e.g.(Chassignet and Marshall, 2008; Bryan et al., 2007). In terms of off-slope SSH, this is important for creating a realistic "step-up" in SSH where the Gulf Stream separates. Using a spin-up period of 3 years, Fig. 5.2a shows the model SSH across the entire domain, and Fig. 5.2b shows the model SSH along the 800 m and 40 m depth contours as well as the Mean Dynamic Topography (MDT) derived from altimetry along the same contours - note that the contours are denoted in Fig. 5.2a (magenta and green contours respectively). The MDT is the 22-year mean (1993-2014 inclusive) from AVISO (the Ssalto/Duacs, delayed mode, gridded absolute dynamic topography product using all available satellites). The Ssalto/Duacs altimeter products were produced and distributed by the Copernicus Marine and Environment Monitoring Service (CMEMS) (http://www.marine.copernicus.eu). Note that in coastal regions the coarse resolution of satellite observations and geoid models can introduce errors to the coastal signal. Here comparisons are made along the 40 m depth contour rather than at the coast to help compensate for this. Having said this, as shown

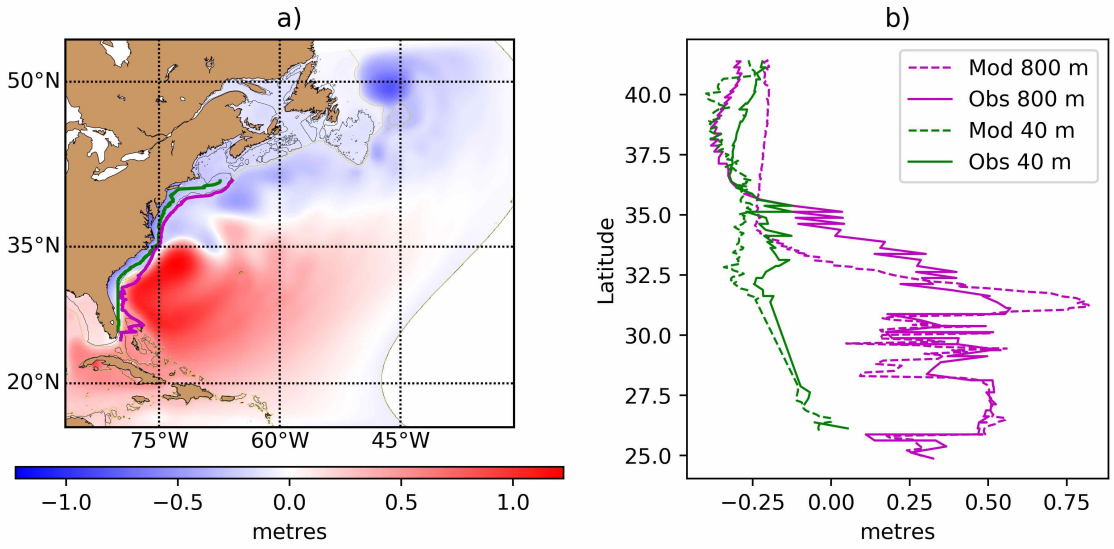

Figure 5.2: *a) Quasi-steady state Sea Surface Height (SSH) from the model after a three-year spin up. b) Model Sea Surface Height (Mod) after the 3-year spin up and satellite derived Mean Dynamic Topography (MDT) (Obs) along the 40 and 800 metre depth contours as a function of latitude. The contours are shown in panel a). The difference between the latitude mean of the 800 m SSH and 800 m MDT has been removed from the 40 m and 800 m MDT.*

by Andersen et al. (2018), the satellite derived dynamic coastal sea levels are comparable to those from tide gauges and a range of numerical ocean models.

While the model is not intended to be realistic, given the simplicity of the forcing and vertical structure, it is surprising how well the model captures the observed SSH. The main differences to note are that the model Gulf Stream separates slightly too far southward and some on-shelf processes are obviously missing. The sub polar SSH low is also slightly under represented, which is probably due to the missing eddy-driven recirculation gyre just north of the Gulf Stream, between approximately 36 and 41 N (See Fig 3 of Liu et al. (2018)).

Following the 'spin-up', a wind stress anomaly $\tau_u^A(x, y, t)$ that varies in space and time is added to the mean field

$$\tau_u(x, y, t) = \tau_u^M(x, y) + \tau_u^A(x, y, t). \tag{5.6}$$

To isolate the relationship between interior and coastal SSH, the wind stress anomaly is damped close to the shelf and slope of the North American mainland and zero on the shelf and slope. This ensures that variability on the shelf and slope is due to interior ocean

dynamics only. Defining the wind stress in this way does have the drawback of introducing an artificial wind stress curl between the interior and coast, however with adequate damping, i.e. avoiding large $\partial\tau_u/\partial y$, this contribution is found to only moderately affect the zonal integral of the wind stress curl (not shown) and does not materially affect the results and discussion presented. Specifically, the wind stress anomaly, τ_u^A, is set to zero on the shelf and slope of the North American mainland (i.e. not the various islands in the domain) and a linear ramp up is applied over approximately 2 degrees of latitude from the foot of the continental slope.

The wind stress anomaly is defined to induce two general effects on the off-slope SSH, representative of the off-slope forcing suggested by observational studies. Firstly, we wish to fluctuate the magnitudes of the SSH low and high north and south, respectively, of the Gulf Stream separation latitude. This is achieved by simply adding a wind stress contribution, $\tau_u^{A1}(x, y, t)$, that modulates the mean wind stress amplitude in time, but with the same spatial pattern as the mean, i.e. as shown in Fig. 5.1a. This contribution to the anomaly is periodic with a period of 4 years and amplitude 0.1 N m^{-2} - the mean field amplitude is 0.4 N m^{-2}. In addition, we wish to fluctuate in time the magnitude and latitude of the off-slope SSH low north of, and high south of, the Gulf Stream separation latitude. This is achieved by adding another wind stress contribution, $\tau_u^{A2}(y, t)$, which is zonally uniform (excepting for the damping) and differs from the mean field in its latitudinal structure, see Fig. 5.1b. Again, this contribution to the anomaly is periodic, but with only a 2 year period. Note that $\tau_u^{A2}(y, t)$ is based on the wind anomaly due to the NAO. Specifically, we have approximately represented the meridional NAO profile used by Zhai et al. (2014), where they have regressed monthly reanalysis zonal wind stress onto the NAO index for the period 1950-2010 and then zonally averaged (i.e. multiplying this wind stress by the monthly NAO index gives a zonal-mean wind stress anomaly that fluctuates in time with the NAO index).

In order to efficiently use computer time we apply both fluctuating fields simultaneously (over a 4 year model run) and separate out the responses in post processing. The fluctuating wind stress anomaly is therefore defined as

$$\tau_u^A(x, y, t) = D(x, y) \left[\tau_u^{A1}(x, y, t) + \tau_u^{A2}(y, t)\right], \tag{5.7}$$

where $D(x, y)$ is the damping. This fluctuating forcing is used to set up SSH variability that represents the off-slope SSH variability described in the various observational studies discussed in the introduction.

5.5.3 Data Analysis

To determine the connection between the interior ocean and coastal sea level, we apply a Hilbert transformed Complex Empirical Orthogonal Function (CEOF) analysis to the model SSH output. Unlike with correlation maps or standard EOFs, this approach allows us to investigate the spatial and temporal phase and amplitude of the domain wide response.

Following Navarra and Simoncini (2010), for the de-meaned time series $\boldsymbol{d}_i$ (at discrete points in time), where $i = 1, 2, \ldots, m$ and m is the number of points at which there are time series data (in this case the number of grid points) we have the data matrix $\boldsymbol{D} = [\boldsymbol{d}_1, \boldsymbol{d}_2, \ldots, \boldsymbol{d}_m]^T$. A conventional EOF analysis will return linearly independent modes of variability of the data as spatial maps, they are the EOFs, and can be defined as the eigenvectors of the covariance matrix

$$\boldsymbol{S} = \frac{1}{m-1}\boldsymbol{D}\boldsymbol{D}^T. \tag{5.8}$$

Each EOF is accompanied by a function describing the amplitude of the variability as a function of time, and the eigenvalues of $\boldsymbol{S}$ provide the variance explained by each mode (each EOF). In practise the EOFs are calculated by computing the Singular Value Decomposition of $\boldsymbol{D}$

$$\boldsymbol{D} = \boldsymbol{U}\boldsymbol{\Sigma}\boldsymbol{V}^T, \tag{5.9}$$

Where the EOFs are the left singular vectors, the amplitude of the EOFs in time, the Principle Components (PCs) are the corresponding right singular vectors scaled by the corresponding singular value and the variance explained is given by the square of the singular value divided by the sum of all the squared singular values so that at time t the original signal at each point is given as a sum of the modes

$$\boldsymbol{D}_t = \sum_k \boldsymbol{u}_k \sigma_k \boldsymbol{v}_k(t). \tag{5.10}$$

In order to obtain information about the propagation properties of the variability, the EOF method can be extended into complex space and Complex EOF analysis used to obtain information about the phase of the variability. Such data analysis methods are described by Navarra and Simoncini (2010) and Hannachi et al. (2007) and have been used to study propagating signals connected to the Monsoon (Barnett, 1983), for example. The method is described as follows.

For the time series of data at a single point described by the function $d(t)$, with t time, the complex Fourier series can be written as

$$d(t) = \sum_{n=-\infty}^{\infty} C_n e^{i\omega_n t}, \tag{5.11}$$

where C_n are the complex coefficients $C_n = A_n + iB_n$, and ω_n the angular frequencies. The Hilbert transform of a continuous function is formally

$$\mathcal{H}(d(t)) = \frac{1}{\pi} \int \frac{d(s)}{t-s} ds, \tag{5.12}$$

where the integral is the Cauchy principal value. In the Fourier representation, the Hilbert transform introduces a $-\pi/2$ phase shift to each positive frequency and a $\pi/2$ phase shift to each negative frequency. As a clear example, for the time series containing only two frequencies

$$\begin{aligned} d(t) &= 2\cos(\omega t) + 2\cos(2\omega t) && (5.13)\\ &= e^{i\omega t} + e^{-i\omega t} + e^{i2\omega t} + e^{-i2\omega t}, && (5.14) \end{aligned}$$

the Hilbert transform is

$$\begin{aligned} \mathcal{H}(d(t)) &= e^{i\omega t - i\pi/2} + e^{-i\omega t + i\pi/2} + e^{i2\omega t - i\pi/2} + e^{-i2\omega t + i\pi/2} && (5.15)\\ &= 2\sin(\omega t) + 2\sin(2\omega t). && (5.16) \end{aligned}$$

A new complex time series can therefore be defined as

$$\widehat{d}(t) = d(t) + i\mathcal{H}(d(t)), \tag{5.17}$$

where the negative frequency components are removed and which contains information about the rate of change of the data $d(t)$ with respect to time, for the example above it is

$$\begin{aligned} \widehat{d}(t) &= 2\cos(\omega t) + 2\cos(2\omega t) + i\left[2\sin(\omega t) + 2\sin(2\omega t)\right] && (5.18)\\ &= 2e^{i\omega t} + 2e^{i2\omega t}. && (5.19) \end{aligned}$$

For the case of m grid points each with a discrete, $t = 1, 2, \ldots, n$ time series of data $\boldsymbol{d}$, the complex time series is

$$\widehat{\boldsymbol{D}} = \boldsymbol{D} + i\mathcal{H}(\boldsymbol{D}), \tag{5.20}$$

where $\boldsymbol{D} = [\boldsymbol{d}_1, \boldsymbol{d}_2, \ldots, \boldsymbol{d}_m]$. All computations use Python's (programming language) built in Hilbert transform routine and the complex time series $\widehat{\boldsymbol{D}}$ is calculated by taking the discrete Fourier transform of the time series at each point, replacing the Fourier coefficients corresponding to negative frequencies with zeros and doubling the positive coefficients, and then calculating the inverse discrete Fourier transform on the result.

As previously described, the Singular Value Decomposition can then be used to obtain the CEOFs of $\widehat{\boldsymbol{D}}$ (with transposition replaced by complex transposition), where the kth

CEOF is $\boldsymbol{u}_k$, and the kth time dependent Complex PC is $\sigma_k \boldsymbol{v}_k$. For the kth mode of variability, the spatial amplitude is given by $|\boldsymbol{u}_k|$, where $|\cdot|$ denotes the component-wise absolute values and the spatial phase is given by $\arg(\boldsymbol{u}_k)$, where $\arg(\cdot)$ denotes the component-wise arguments. Similarly, the temporal amplitude is $\sigma_k|\boldsymbol{v}_k|$ and the kth temporal phase is $\arg(\boldsymbol{v}_k)$. By stressing the phase relation in the data the Complex EOFs therefore obtain patterns of variance that optimise to include propagation, making it a suitable method for identifying propagating anomalies along the continental shelf and slope.

5.6 Results and Discussion

In this section we will present and discuss the CEOFs in context with the theory of coastal trapped waves as well as observations of sea level correlations.

5.6.1 CEOFs & Modes of Variability

The CEOF analysis of the model SSH output reveals two dominant modes of variability, accounting for ∼95% of the variability, with each mode associated with a component of the wind stress anomaly. Note that the relative variance explained by each could be somewhat misleading, given that it will depend on the amplitudes we have chosen for the two wind stress contributions. With that said, the two different wind stress amplitudes are comparable and it is interesting to note the similarity of the variance explained with that found for the two dominant EOF modes by Valle-Levinson et al. (2017), which were related to ENSO and the NAO.

Panels a) and c) in Fig. 5.3 show the spatial amplitude and phase, respectively, of the first CEOF, which accounts for 71% of the variability. The temporal phase and amplitude are not shown, but the first mode of variability is approximately in temporal phase with the windstress forcing, τ_u^{A1}. Panel a) shows the amplitude of SSH variability in the interior ocean (white contour denotes 500 m isobath) resulting from strengthening and weakening of the subpolar and subtropical gyres as the magnitude of the zonal windstress increases and decreases. Along the coast there is clear leakage of the off-slope SSH variability onto the shelf, with amplitudes substantially reduced. The largest coastal variability is seen between 32N and 38N, around Cape Hatteras. Panel c) shows the propagation of the coastal variability along the entire North American east coast, down to 25 degrees north, to be coherent (relative to the long 4-year period of the mode). Generally speaking, this coastal signal is in phase with the interior signal north of 37N and mostly out of phase with the interior signal south of 37N (although the signal immediately off-slope is also in

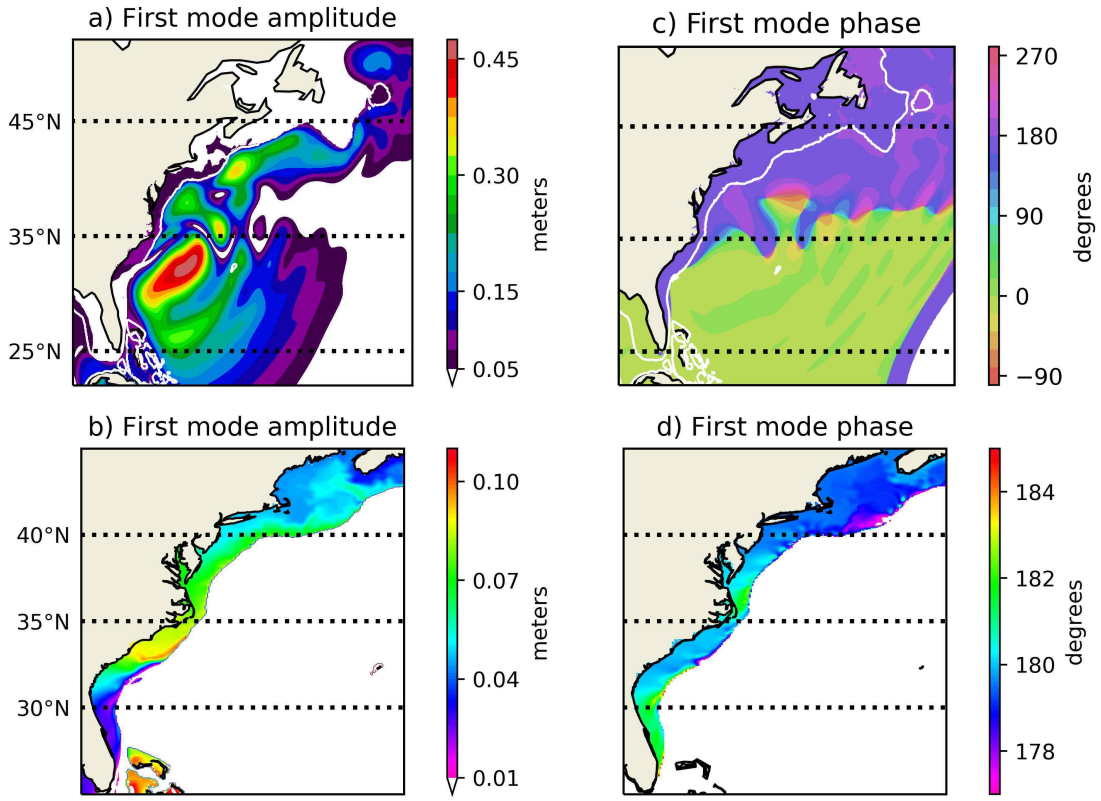

Figure 5.3: *Panels a) and c) are the spatial amplitude and phase of the first Complex EOF of Sea Surface Height from the model experiment, where the interior ocean only has been forced with a zonal wind stress anomaly. Panels b) and d) are the same but focused on the shelf and slope using a high resolution colourmap. The white contour is the 500 m isobath.*

phase with the shelf down to about 33N). The mode 1 coastal SSH anomaly is therefore of reduced magnitude compared to the interior (it is attenuated) and there is a southward displacement, i.e. the anomaly at the coast appears to be farther south than in the interior.

Panels a) and c) in Fig. 5.4 show the spatial amplitude and phase for the second CEOF, accounting for 22% of the variability. Again the temporal components are not shown but this mode of variability is closely in phase with the windstress forcing τ_u^{A2}. Together they show NAO+ (NAO-) forcing a positive (negative) SSH anomaly across much of the interior which penetrates in phase onto the shelf, most notably below 33N (the amplitude of shelf

variability above 33 degrees is very small). The interior ocean variability captured by mode two is in many respects a northward shifted version of mode one, this can be seen by comparing the two phase plots of Figs. 5.3c and 5.4c. The on-shelf variability appears, on first inspection, to be quite different however, with the on-shelf variability of mode 2 being almost entirely in phase with the interior.

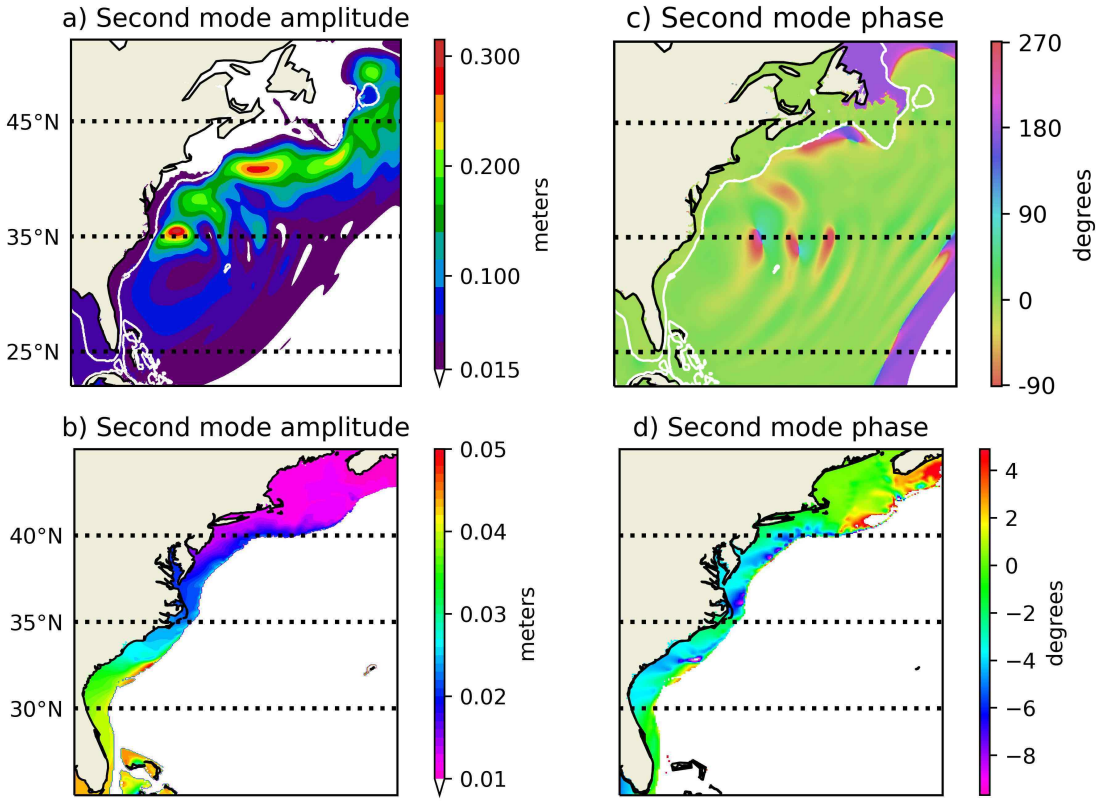

Figure 5.4: *Panels a) and c) are the spatial amplitude and phase of the second Complex EOF of Sea Surface Height from the model experiment, where the interior ocean only has been forced with a zonal wind stress anomaly. Panels b) and d) are the same but focused on the shelf and slope with a high resolution colourmap. The white contour is the 500 m isobath.*

With no direct forcing on the shelf and slope, the immediate implication from the two modes of variability is that phenomena increasing the off-slope SSH will drive a smaller increase in coastal SSH variability that is displaced southward along the coast relative to

the off-slope signal. In the first mode case, the amplitude initially grows in the southward direction, with increasing influence of the subpolar gyre, then it starts to decrease as the subtropical gyre influence penetrates, which is out of phase. In the second mode case, interior sea level is in phase everywhere, so the coastal sea level signal keeps increasing all the way to the tip of Florida This is consistent with observational studies, which we discuss in the following subsection as well as theory, which we discuss later.

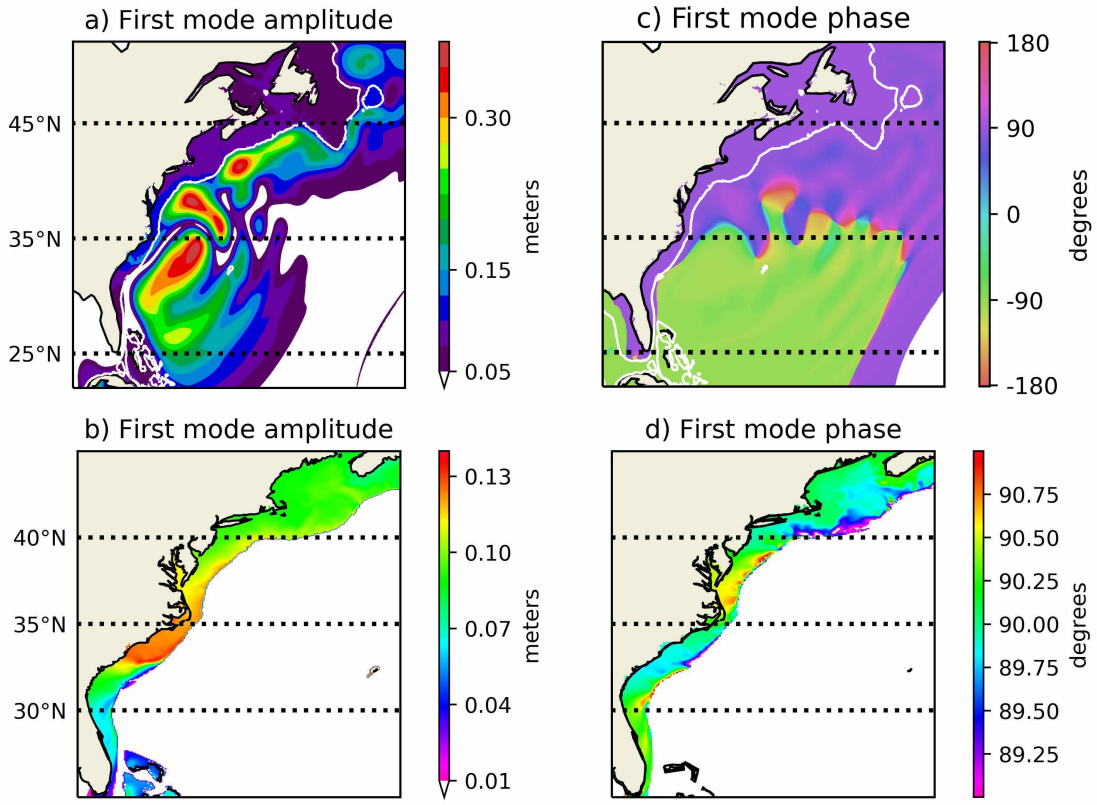

Figure 5.5: *As in Fig. 5.3 but for closed northern and southern boundaries.*

Before discussing observations, it should be noted that the radiative boundary conditions at the northern and southern boundaries of the domain can have an impact on the character of the modes of variability. For example, a large portion of the variability in the second mode (Fig. 5.4 a and b) is in phase, which implies that the majority of the surface elevation tends to rise and fall coherently across the domain. This suggests that mass is not conserved and implies that the Flather boundary conditions are playing a large role in leaking mass

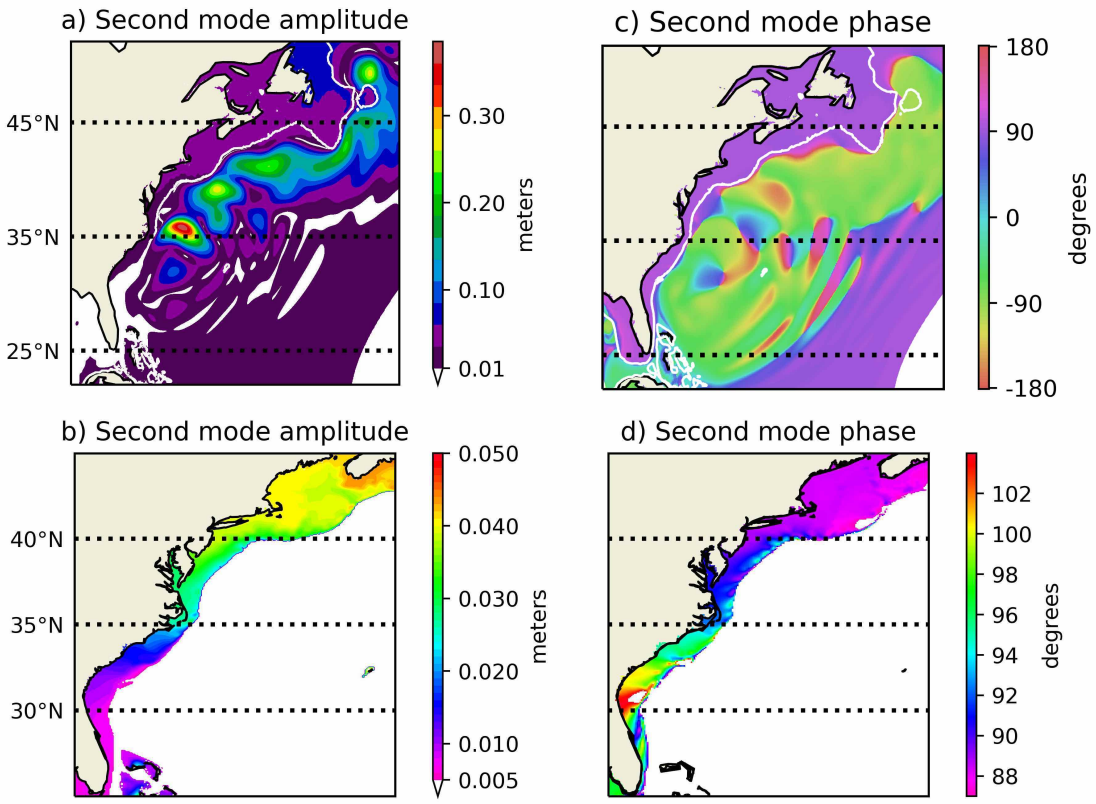

Figure 5.6: *As in Fig. 5.4 but for closed northern and southern boundaries.*

in and out of the domain. In the real ocean, mass would be able to spread north and south of the domain being modelled, as occurs here, but here the dynamics that are occurring in these unmodelled regions is being lost.

To demonstrate this issue more clearly, figures 5.5 and 5.6 show the same experiment with closed northern and southern boundaries. It is clear from panels a and c in Fig. 5.6 that the second mode of variability is indeed strongly influenced by the boundary conditions, with the on-shelf response significantly altered. This can be explained as follows. With mass unable to leak from the domain, the surface elevation in the northern and southern portions of the domain is out of phase with the central band of the domain due to conservation. This does not occur in the Flather experiment. This ultimately results in a very different on-shelf response, because variability on the shelf is strongly controlled by variability at higher latitudes (than the point of interest on the shelf). In fact the contrast between the two

experiments highlights this point quite clearly.

Clearly the choice of boundary conditions is an important concern. Here we suspect that the reality is somewhere between the two cases (Flather and Closed). This is because some spreading of mass northward and southward of the domain should be expected in reality, and this would be compensated for at other locations in the interior ocean that have also not been included in the domain (but that are not necessarily adjacent to the continental slope, as is the case in the Closed experiment).

5.6.2 Consistency with observations

Most strikingly, the results of mode two are consistent with coherent variability on the shelf, south of Cape Hatteras, being forced remotely by warming/cooling of the Florida current, as found by Domingues et al. (2018); Volkov et al. (2019), and the NAO (Valle-Levinson et al., 2017; Volkov et al., 2019). Similarly, the results are also consistent with off-slope anomalies modulating the amplitude of the sea level annual cycle, as described by Calafat et al. (2018). Mode one is also consistent with the correlation maps in Frederikse et al. (2017) and Andres et al. (2013) depicting coherence between the coastal sea level variability north of Cape Hatteras and off-slope, farther northward - though their correlation maps do not show coherence extending significantly south of Cape Hatteras. Perhaps most interestingly, the EOF modes of coastal 5 yr rates of sea level change depicted in figure 3 of Valle-Levinson et al. (2017) bear a remarkable resemblance to the two modes presented here. They show the first mode as being responsible for in-phase variability along the entire coastline whereas the second mode is responsible for variability also along the entire coastline, but in anti-phase, roughly about Cape Hatteras. The combination of the two modes results in a hot spot which is highly latitudinally mobile. This raises an interesting point: typically correlation maps show a certain degree of decoupling north and south of the cape, however, the modes of variability found here, together with the EOF analysis by Valle-Levinson et al. (2017), does raise the possibility that this perhaps conceals the various modes of variability at work, in combination. An interpretation of observations together with our modelling results are as follows:

- A mode of variability acts coherently and in phase along the coastal zones both north and south of Cape Hatteras. This is potentially related to La Niña and El Niño events modulating the high latitude open ocean SSH.
- A second mode of variability also acts coherently along the entire coastline. This can be related to the effect of the NAO+(-) (and in reality also to warming (cooling) of

the Florida current) creating off-shelf SSH highs (lows) in the sub tropical band of the ocean and on-shelf highs (lows) south of Cape Hatters. While this mode acts coherently along the entire shelf, observational studies discussed in the introduction, i.e. Piecuch et al. (2019), suggest that the NAO can also modulate on-shelf winds north of Cape Hatteras, which we have not included, that could modify the phase of the response north of the Cape.

5.6.3 Relating hot spots to boundary waves

The results can be explained using the theory of coastally trapped waves. The coherence of the signal along the shelf suggests that off-slope variability generates a long barotropic trapped wave response at the boundary, which rapidly transmits SSH information southward along the coast. This wave response is composed of Shelf and Slope waves of different speeds that decay over different lengthscales. With the southward propagation of SSH information along the shelf and slope, it is typically difficult to determine the pathways of variability from ocean-to-coast, i.e which sections of off-slope variability are driving sea level variability along specific sections of coastline?

Figure panels 5.3d and 5.4d show the spatial phases of the CEOFs on the shelf in very fine resolution. The temporal phase of both modes of variability is positive, and in phase with the two wind forcing components. An approximate local wave number can be obtained from the spatial phase plots and the sign of the local wavenumber can be estimated by noting the direction of the phase lag. For example, decreasing spatial phase with increasing latitude implies a negative meridional wavenumber. Southward propagation on the shelf can be identified in both figures 5.3d and 5.4d. Interior variability penetrates onto the slope, which is relatively coherent in phase along large distances, as noted from observations by Hughes and Meredith (2006) and Roussenov et al. (2008), and appears to leak onto the shelf at lower latitudes, i.e. the amplitude of the boundary wave response is modulated by off-slope variability at higher latitudes. This is evident from the fine resolution first mode amplitude plot Fig. 5.3 b. In this case, peak variability in the off-slope SSH penetrates onto the slope at 42N and 38N, and peak variability appears on the shelf at around 33N.

On-shelf variability at a given latitude is determined by:

1. The response on the shelf northward of the given latitude,

2. The response on the slope northward of the given latitude,

3. The off-slope signal at the given latitude, which will modify the response on the slope,

4. Local forcing on the shelf, which we do not cover.

Consider then the SSH variability due to mode 1 south of 33 N. On first inspection it appears as though the SSH variability off-slope of the Florida coastline does not influence coastal SSH, however this is simply because the on-shelf and off-slope variability are in anti-phase, hence the off-slope mode 1 variability simply acts to reduce the amplitude of the on-shelf variability.

The fine resolution amplitude and phase for mode 2, shown in Figs. 5.4b and 5.4d, again demonstrate the interior ocean signal running southward along the slope and appearing to leak onto the shelf at lower latitudes. The SSH signal off-slope of Florida is now increasing (rather than decreasing) the amplitude of the on-shelf SSH variability because it is in phase with the boundary waves rather than being in anti-phase.

The picture presented by the fine resolution plots is instructive. Physically, interior SSH anomalies carried towards the slope, for example as westward propagating long Rossby waves, modify the amplitude and speed of southward propagating Shelf and Slope waves (generated by local and remote forcing farther northward). As the southward propagating waves dissipate energy, they reduce in amplitude and speed, and the long Rossby waves from the interior modify the amplitude of the boundary waves to a greater extent, effectively allowing greater penetration of interior SSH variability onto the shelf.

An appreciation of how the boundary wave mechanism adjusts coastal sea level is important. For example, when considering modulation of sea level south of Cape Hatteras, part of the variability will ultimately originate a number of degrees farther northward (off-slope and on-shelf). Because the interior ocean signal may be correlated (i.e. the variability in the interior ocean may be coherent over many degrees of latitude), and the boundary adjustment so rapid, this can be difficult to spot without knowing the phase of the variability, for example compare again the phase of CEOF mode 2 in low resolution and high resolution. Furthermore, because trapped waves are sensitive to bottom topography, this could be particularly problematic when using coarse resolution models around areas such as the Florida straits, where variability on the shelf, partially or largely originating from further north, appears to originate east of the Bahamas, or in the strait.

On timescales where the variability of forcing is slow relative to the adjustment at the boundary, Wise et al. (2020) showed that the western boundary coastal sea level anomaly η becomes related to the off-slope sea level anomaly η_{in} - for a meridionally uniform coastline with a shelf and slope on the beta-plane with bottom friction - by a weighted integral of the interior sea level anomaly over the entire latitudinal extent of the off-slope anomaly

poleward of the point in question

$$\eta(y) = \int_{y}^{y_p} \eta_{in}(s) W(s, y)\, ds, \tag{5.21}$$

where y is the latitude coordinate, y_p a poleward latitude and s a dummy variable for integration, and the weighting function $W(s, y)$ depends explicitly on the characteristics of the shelf and slope and the friction parameter. The relation was shown to give good qualitative agreement with observations. Equation (5.21) is consistent with relations derived by Hong et al. (2000) and Minobe et al. (2017), which have been validated with observations and model output. The weighted integral over the entire latitudinal extent of the anomaly underscores the importance of poleward variability on lower latitudes.

Friction at the boundary results in dissipation and this has been shown in linear models to accelerate the alongshore decay of boundary waves, enabling off-slope variability to leak onto the shelf. This remains important in the nonlinear case where advection of potential vorticity is allowed by a mean flow.

Neglecting horizontal diffusion, the role of friction in the barotropic vorticity equation can be related to the potential vorticity as

$$\frac{D}{Dt}\left(\frac{\zeta + f}{h}\right) = -\frac{1}{h}\boldsymbol{\nabla} \times \left(\frac{\boldsymbol{\tau_b}}{h}\right), \tag{5.22}$$

where $D/Dt = \partial/\partial t + \boldsymbol{u} \cdot \boldsymbol{\nabla}$, $\boldsymbol{\nabla}$ is the horizontal derivative, f is the Coriolis parameter, h is the depth H plus free surface and $\boldsymbol{\tau_b}$ is bottom friction. Without friction, and with no mean flow, potential vorticity $(\zeta + f)/h$ is conserved and the flow follows f/H contours (Salmon, 1998a), with dynamic sea level η following H/f contours (Wise et al., 2018). The inclusion of friction enables the flow to deviate and in the linear case has been shown to enable sea level to penetrate from the interior onto the shelf, crossing H/f contours. The inclusion of a mean flow, clearly a consideration at western boundaries, will modify the background potential vorticity, for example $\zeta = \partial v/\partial x - \partial u/\partial y + V'(x)$, where V' is the shear of a meridional mean flow. As noted by Mysak (1980b), suggestions are that when the shear is comparable to f, shelf waves can be significantly advected by the current. It is not clear however, to what extent this affects sea level penetration onto the shelf.

For the case without fluctuating forcing, with the model in a quasi-steady state such that $\partial/\partial t \approx 0$, Fig. 5.7a shows the frictional contribution to (5.22), i.e. the term on the right. The figure shows large friction on the slope and shelf, in particular it fits the pattern of leakage shown in the CEOF plots from the slope onto the shelf. Note also the enhanced off-shelf friction contribution between 31 N and 34 N where the upper slope widens and

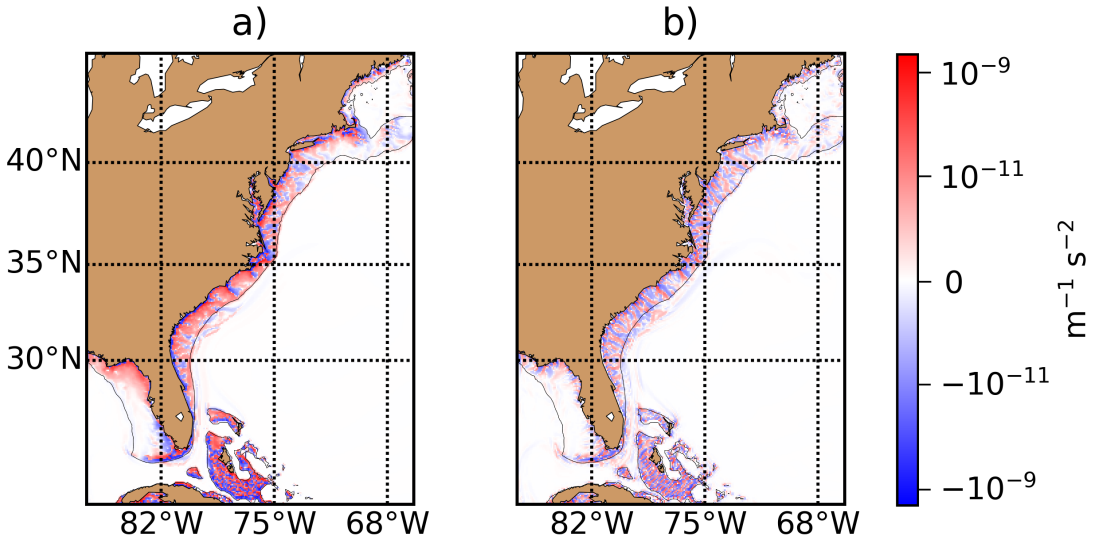

Figure 5.7: *Panel a) shows the friction contribution to the time rate of change of the potential vorticity, i.e. right hand side of equation (5.22). b) shows* $\boldsymbol{u} \cdot \boldsymbol{\nabla}(\zeta/h)$*, where* ζ *is the relative vorticity and* h *the depth plus free surface. c) shows the difference between the fields shown in a) and b) (friction term minus relative vorticity term). The black line denotes to 200 m depth contour.*

narrows, i.e. as the slope becomes narrow, friction increases and penetration increases - see (Hill, 1995) for a linear discussion of leakage due to a narrowing slope. Figure 5.7b shows the non-linear relative vorticity contribution $\boldsymbol{u} \cdot \boldsymbol{\nabla}(\zeta/h)$. While it clearly plays a role on the shelf and slope, this term is typically an order of magnitude smaller than the friction contribution. This suggests that even a strong mean flow does not change the character of the frictional balance found in the linear case and therefore it does not prevent the low frequency on-shelf sea level being determined by the on- and off-shelf dynamics poleward of the point in question, i.e. the waves are not completely arrested by the mean current.

The consistency of the results with observation and theory is convincing. Nevertheless by assuming a barotropic ocean we have neglected certain processes that could modify our results. For example, Février et al. (2007) showed that variation in the thickness of an active mid ocean layer as a result of Kelvin wave propagation, could induce a negative feedback on the upper layer. This forcing is proportional to the mean vorticity gradient and therefore can be large at the Gulf Stream separation area. This forcing on the upper layer does not prevent the Kelvin wave from propagating southward but does result in the appearance of a new coastal sea level anomaly with opposite sign in the vicinity of the Gulf

Stream separation point. In addition, Dewar and Hogg (2010) and Deremble et al. (2017) discuss the role of non-viscous energy dissipation from the mesoscale at boundaries. They show that in a stratified flow, Kelvin and topographic waves trapped at the boundary can be "arrested" by an opposing balanced flow - potentially important along the US east coast where the Gulf Stream could arrest trapped boundary waves. It is worth speculating that the combined effects of stratification, topography and mean flow could, for example, be an alternative explanation for greater de-coherence between the regions north and south of Cape Hatteras than our results suggest.

Furthermore, it should be noted that the adjustment in the interior ocean will be slower and more latitude dependent in reality than in our model, this is due to the fact that adjustment will take place via baroclinic Rossby waves rather than the faster barotropic, Rossby waves (even in a 500 m depth layer). This implies that the decoupling between deep ocean and coastal zone is more pronounced than our results suggest - our results should be interpreted as the coastal response to the nearby ocean. Finally, the choice of a 500 m layer depth was chosen partly to generate a realistic Gulf Stream, however this will not be the best choice for all latitudes.

5.7 Summary

Observations have shown that sea level rise hot spots along the North American east coast are correlated with a number of forcing phenomena and can appear at different latitudes. Understanding the mechanisms of how the coast adjusts to forcing is important when explaining how hot spots are distributed along the coast. Using a barotropic general circulation model of the North American east coast, we have shown that the coastal sea level response to SSH variability on the upper slope is well represented by barotropic dynamics. Using a Hilbert transform Complex EOF method, we examine the propagation and amplitude of two modes of variability generated by off-slope SSH anomalies that are characteristic of the remote SSH anomalies described by observational studies. The first mode of variability describes in-phase coherence along the entire coastline and is driven by a SSH anomaly in the subpolar gyre. The second mode of variability describes in-phase coherence along the coast south of Cape Hatteras and is driven by an off-slope SSH anomaly consistent with the NAO and temperature fluctuations in the sub tropical band of the Atlantic. Observations suggest that NAO-linked on-shelf wind and pressure forcing would drive an anomaly of opposite phase north of Cape Hatteras, though we have not tested this here. The results presented are shown to be consistent with linear barotropic trapped wave theory such

that Shelf and Slope waves propagate with the coast on the right, carrying SSH anomaly information equatorward along the shelf and slope. The role of boundary waves in the adjustment process is used to explain how a sea level rise hot spot at a given latitude on the shelf is driven by an offshore SSH anomaly 3 or 4 degrees of latitude farther north. Finally, the decay of topographic waves due to bottom friction, as described by linear theory, appears to be the key barotropic process enabling off-slope anomalies to penetrate on to the shelf. The inclusion of non-linear effects that enable advection of potential vorticity does not appear to significantly alter the dependence of coastal sea level on higher latitudes, and this ultimately suggests that the Gulf Stream does not stop coastally trapped waves from propagating (acknowledging the limits of the barotropic assumption).

The analysis presented here fits in with the view that baroclinic variability is strongly suppressed on western boundary shelves due to the rapid decay of higher wave modes as a result of the sloping topography and friction. Furthermore, it better ties in coastal sea level variability with the growing theory of how anomalies propagate about ocean basins with relevance also for studies of the overturning circulation.

Chapter 6

Conclusions

Western boundaries are special places, where the latitudinal variation of the Coriolis parameter, friction and sloping ocean depth have defining effects on ocean circulation. The effect of these parameters on the influence of the open ocean on coastal sea level has typically not been well understood, with conceptual models often representing the boundary as a vertical sidewall and sophisticated ocean models suffering from poorly resolved bottom topography and output that is difficult to diagnose.

The research in this thesis aims to increase our understanding of how the continental shelf and slope affects the relationship between coastal sea level and ocean dynamics along western boundaries. In Chapter 3 the parameter sensitivities of western boundary long period dynamic sea level, when forced from the interior ocean, are explored for a homogeneous ocean layer. In Chapter 4, sea level is related to the behaviour of barotropic boundary waves that are dependent on the β-effect, friction, and sloping bottom topography. In Chapter 5 the model is extended to include non-linear effects and realistic bottom topography with the use of a sophisticated numerical model. The evolution of coastal variability when forced from the open ocean is explored with reference to observations and theory.

Effects of topography on western boundary sea level

The initial result of the thesis is to demonstrate that the net force acting on the western boundary depends on depth (or upper layer thickness). The implication is that neglecting the continental shelf and slope, as in a vertical sidewall model, assumes the depth to be uniform, distorting the resulting dynamic sea level along the coast. Using an idealized single layered model including friction, the β-effect and a continental shelf and slope, it is demonstrated that long period dynamic sea level on the shelf and slope is qualitatively

governed by a familiar transport equation, where sea level is transported analogously to the advection and diffusion of a thermal fluid. In the analogy, sea level is "advected" southwestward along h/f contours and "diffused" cross-shore as a result of bottom friction. As seen in observations, this simple analogy can describe the penetration of high latitude, open ocean, sea level lows onto the continental slope and shelf at lower latitudes, wedging between the coast and the open ocean sea level high in the subtropical gyre. The open ocean sea level penetrates to the coast having been attenuated and displaced equatorward. These results are consistent with a downward tilt (with increasing latitude) in mean sea level along the US east coast that is being driven by the gyre circulation in the open ocean.

Critically, the analogy highlights the importance of the β-effect and friction in transporting the sea level signal westward and the importance of sloping topography in transporting the sea level signal equatorward. Stronger friction implies greater penetration from ocean to coast. A measure of the ocean-to-coast penetration is given by a scaling argument using an analogous non-dimensional Péclet number, $P_a = HL\beta/r = L/\delta_s$. Small P_a implies greater penetration - hence a narrower combined shelf and slope, relative to the Stommel boundary layer thickness δ_s, implies greater penetration of the ocean signal to the coast. The sensitivity to the representation of bottom topography and friction is a plausible explanation for part of the inconsistency between numerical model simulations of the sea level tilt along the US east coast - as in (Woodworth et al., 2012; Higginson et al., 2015).

The non-dimensional relationship also implies that the vertical sidewall limit, $L \to 0$, and large friction limit, $r \to \infty$, converge towards equivalence, $P_a \to 0$. This is demonstrated by comparison with Minobe et al.'s (2017) vertical sidewall model solution and explains why the vertical sidewall model relating coastal sea level to open ocean sea level is invariant to the friction parameter r. The effectiveness of friction, and thereby the role of ocean dynamics as a driver of the amplitude and distribution of coastal sea level at a western boundary, is clearly related to the geometry of the bottom topography, with vertical sidewall geometry underestimating the attenuation and equatorward displacement of the open ocean sea level signal as it penetrates to the coast.

While the model uses a homogeneous active layer over the bottom topography, the effect of stratification to decouple the ocean column is shown to be comparable to a modification of the layer thickness with latitude. In the case of a deep ocean buoyancy anomaly decreasing the thickness of the upper ocean layer, topographic steering is reduced, and penetration to the coast is enhanced. Outcropped layers have been shown to behave consistently with the upper-layer (in the outcropped region) (Huang, 1984) and therefore, while stratification will alter the above results, it may not change the general conclusions. On the other hand,

effects due to interaction of layers over the sloping bottom topography associated with the temperature structure, of relevance to Gulf Stream separation, is not considered, and this is a research area worth pursuing further.

Western boundary sea level and boundary waves

The results in Chapter 3 demonstrate the importance of a varying Coriolis parameter, friction and bottom topography, but they do not explain the adjustment mechanism that takes place at the boundary. In Chapter 4, Shelf wave theory is developed to include these factors and it is shown how barotropic off-shore and on-shore annual (and longer) period variability elicits a western boundary response composed of Shelf and Slope waves.

Slope waves are found to propagate along the continental slope and radiate damped short Rossby waves into the interior ocean, and are a direct consequence of the β-effect. The amplitude of the generated waves decays in the direction of the equator as energy is transmitted offshore by the short Rossby waves and dissipated on the shelf and slope due to friction. Steeper topography and a larger friction parameter increase dissipation, resulting in wave decay further poleward. By relating CTWs to the equatorward propagation of on-shelf sea level variability, it is demonstrated how the decay lengthscale of the waves determines how far towards the equator that higher latitude variability will extend. By the same mechanism, the decay lengthscale determines the degree of penetration of open ocean sea level variability onto the shelf. As the decay lengthscale decreases (greater dissipation) more of the energy carried westward by the long Rossby wave penetrates on to the shelf, producing greater penetration of interior ocean variability onto the shelf and at higher latitudes.

The equatorward displacement and attenuation of open ocean sea level variability as it penetrates onto the shelf, demonstrated in Chapter 3, and shown by observations, is a direct result of the equatorward propagation of CTWs. Increasing dissipation via an increase in the friction parameter or steepening of the topography decreases the CTW decay lengthscale and results in less equatorward displacement and attenuation of open ocean sea level variability as it penetrates onto the shelf. Ultimately, increasing the steepness of the topography to the vertical sidewall limit "kills off" all but the lowest CTW, akin to the hybrid Kelvin-short Rossby wave found by Marshall and Johnson (2013), and therefore explains the maximum penetration limit found in Chapter 3, i.e. a minimum of energy is transmitted to lower latitudes.

The explicit relationship found between western boundary variability and interior ocean

variability is extended to the steady state (long period sea level) giving an explicit relationship between coastal sea level and interior ocean sea level (and poleward sea level). The relationship is a generalization of the parametrised and vertical sidewall relationships found by Hong et al. (2000) and Minobe et al. (2017) to the case of an arbitrary shelf and slope geometry (that is uniform alongshore). The qualitative agreement between these analytic relationships and observations implies that different representations of topography and friction in ocean models is a plausible source of quantitative inconsistency in simulations of western boundary sea level.

Decoupling of the water column due to stratification will modify the evolution of the boundary waves discussed in Chapter 4, for example the upper layer thickness will vary with latitude, as discussed in Chapter 3. Nevertheless, this effect can qualitatively be interpreted as a modulation of depth with latitude, which is effectively a modulation of the friction parameter with latitude (thicker layer - smaller friction). Waves may, therefore, experience enhanced decay where the layer thins. On the other hand, continuous stratification has been shown to result in hybrid internal Kelvin-Shelf waves and it is not clear exactly how the effect of bottom friction will be modified in this situation, and much may depend on the vertical structure of the open ocean forcing. Where the vertical structure of the low frequency forcing is concentrated towards the surface and the horizontal scale is large ($\sim$ 1000 km), one might expect qualitatively similar results to a reduced depth barotropic model, because the lowest modes, with the largest alongshore decay scale, should be similar in the stratified and barotropic cases. This would be consistent with Huthnance (2004) and Hughes et al. (2018), and is a subject in need of further research with the use of more sophisticated numerical models.

Another important issue at western boundaries is the effect of the mean flow, which can be strong. In the case where the shear of the mean flow is strong, it is to be expected that higher modes, which are slower, will be modified. Along the US southeast coast, for example, the strong northward current may arrest higher wave modes. As has been discussed in Chapter 4, CTWs carry variability equatorward and an arresting of these waves would be expected to promote the transmission of long wave variability from the interior ocean onto the shelf. This again is an area which can be explored further with more sophisticated numerical models.

Sea level hot spots, realistic bathymetry & nonlinear effects

Chapter 5 demonstrates that the idealized dynamics discussed in Chapters 3 and 4 continue to be important when the constraints of linearity and idealized bathymetry are relaxed. Despite being barotropic, when the model is spun-up to a quasi steady state it can reproduce the on-shelf and off-slope altimetry derived Mean Dynamic Sea Level along the US east coast with surprising skill. The implication is that the long period relationship between the upper slope and coastal zone is well represented by barotropic dynamics.

Low frequency fluctuations in the upper-slope sea level, north of Cape Hatteras, are found to induce a coherent fluctuation in the sea level on the shelf extending all the way south to the tip of the Florida Straits. This is consistent with the identification from observations of a common mode of variability along the US east coast that has been linked to the El Niño-Southern Oscillation and to a meridional convergence of Sverdrup transport in the interior ocean. The implication is that increasing (decreasing) the amplitude of the sea level signal in the sub-polar band of the North Atlantic will induce sea level rise (fall) along the entire US coastline. The consistency of these results with the steady linear barotropic dynamics investigated in Chapter 3 suggests that the identified roles of the β-effect, friction and sloping bathymetry hold in more complex settings.

Latitudinal variation of the off-shore sea level, attributed in observational studies to variability via the North Atlantic Oscillation (NAO) and fluctuations in heat transport via the Florida current, produces latitudinal variation in the on-shelf variability. A northward shift in the off-shore sea level signal (NAO+, increased heat transport) raises the sea level along the US east coast south of Cape Hatteras. A mode of variability along the coast consistent with this result has also been identified in observational studies (Valle-Levinson et al., 2017; Volkov et al., 2019; Domingues et al., 2018).

A combination of these two modes of variability is a plausible explanation for the time varying latitude of sea level rise hotspots along the US east coast, which is an active area of research.

The role of CTWs in the dependence of coastal sea level on poleward latitudes, and the distribution of variability along the shelf and slope is clearly evident when the phase of the simulated response is examined in fine resolution. The dynamics on the shelf are characterised by a long wave response that is rapid relative to the low frequency of the mode of variability. There is also a decoupling of the shelf and slope region from the interior ocean (recalling also that adjustment in the interior here is far more rapid than in reality, due to the response being barotropic rather than baroclinic). From the results

in Chapter 4 regarding the sensitivity of wave decay to bathymetry, it should be expected that under-resolving the continental shelf and slope, which can result in representing the topography as being less steep, is likely to overestimate the equatorward shift in variability at the coast because the decay of Shelf and Slope waves (dissipation) is underestimated. On the other hand, under-resolving can create steps which may require increased friction to maintain stability.

Consistent with the simplified linear dynamics, the crossing of the flow over f/h contours appears to be enabled primarily by bottom friction, which is large compared to the non-linear advection of relative vorticity term. The mean flow does not appear to halt the dominant equatorward propagation of Shelf and Slope waves, for example there is no clear decoupling of the response at Cape Hatteras. It is of course important to note that vertical decomposition of the waves due to stratification could increase the relative importance of the mean flow in terms of arresting wave propagation at Cape Hatteras. This is clearly an avenue for future research.

The results discussed here have developed the theoretical framework for how open ocean dynamics influence the western boundary response via equatorward propagating topographic boundary waves that are modified by friction, the latitude dependence of the Coriolis parameter, and the geometry of the shelf and slope. By investigating the sensitivity of the boundary adjustment mechanism to these factors, it is shown why numerical models that have different representations of bathymetry and friction can produce different results at the western boundary. The important role of bottom friction in determining the boundary response also highlights the critical role played by this parametrisation.

Future work

With more time there are a number of steps that could be taken to develop the barotropic model established in chapter 5. Given the results of chapters 3 and 4 regarding sensitivity to friction, one obvious avenue would be to explore the effects of different friction configurations on sea level and boundary waves. This could include variation of the coefficient value (including spatial variation), as well as different parametrisations. Another option would be to include some form of stratification effect. This could be included into the barotropic model directly as a forcing term or by adding a number of vertical layers and allowing temperature and salinity to vary. While this increases the level of complexity in the model, it would open up a number of interesting possibilities. For example, it would be interesting to investigate the effects of the stratification when the 'wind-only' forcing is

applied, directly comparing with the barotropic model, and it would be interesting to exchange wind forcing for thermal forcing. Other opportunities would be to vary the strength of the mean flow, extend the domain of the model latitudinally and to investigate both lower and higher frequency forcing. The combined effect of baroclinicity and topography on sea level penetration, similar to JEBAR, could then be explored. The above extensions to the model would be intermediate steps towards a realistic ocean model, while maintaining some of the benefits of being able to isolate specific mechanisms of interest.

Appendix A

Sea level and the role of coastal trapped waves in mediating the influence of the open ocean on the coast

A.1 Preamble

While the focus in this thesis has been on western boundary sea level and barotropic boundary waves, it has been noted that there is an extensive body of literature examining the theory of - and observational evidence for - coastally trapped waves. This appendix consists of a published article (of which I am a co-author) that takes a broader perspective in reviewing the current understanding of the role of coastally trapped waves as mediators of the relationship between the open ocean and coastal sea level. It forms part of a special issue in the November 2019 edition of *Surveys in Geophysics*: "Relationships Between Coastal Sea Level and Large Scale Ocean Circulation".

Publication and Author Contributions

This appendix has been published in the November 2019 edition of *Surveys in Geophysics* (DOI: 10.1007/s10712-019-09535-x) (first online in May 2019) and is presented here unmodified. The paper has eight authors: Chris W. Hughes, Ichiro Fukumori, Stephen M. Griffies, John M. Huthnance, Shoshiro Minobe, Paul Spence, Keith R. Thompson and Anthony Wise (Myself). Chris W. Hughes is the primary and corresponding author. As co-author

I contributed discussion of ideas, editorial critique and figures. The paper appears in the bibliography under Hughes et al. (2019).

A.2 Abstract

The fact that ocean currents must flow parallel to the coast leads to the dynamics of coastal sea level being quite different to the dynamics in the open ocean. The coastal influence of open-ocean dynamics (dynamics associated with forcing which occurs in deep water, beyond the continental slope) therefore involves a hand-over between the predominantly geostrophic dynamics of the interior ocean and the ageostrophic dynamics which must occur at the coast. An understanding of how this hand-over occurs can be obtained by considering the combined role of coastal trapped waves and bottom friction. We here review understanding of coastal trapped waves, which propagate cyclonically around ocean basins along the continental shelf and slope, at speeds which are fast compared to those of baroclinic planetary waves and currents in the open ocean (excluding the large-scale barotropic mode). We show that this results in coastal sea level signals on western boundaries which, compared to the nearby open ocean signals, are spatially smoothed, reduced in amplitude, and displaced along the coast in the direction of propagation of coastal trapped waves. The open ocean influence on eastern boundaries is limited to signals propagating polewards from the equatorial waveguide (although a large scale diffusive influence may also play a role). This body of work is based on linearised equations, but we also discuss the nonlinear case. We suggest that a proper consideration of nonlinear terms may be very important on western boundaries, as the competition between advection by western boundary currents and a counter-propagating influence of coastal trapped waves has the potential to lead to sharp gradients in coastal sea level where the two effects come into balance.

A.3 Introduction

In the open ocean, sea level gradients (strictly, dynamic sea level gradients as defined in Gregory et al. (2019)) are, to first order, in geostrophic balance with currents near the surface, with wind stress adding an additional flow in the surface Ekman layer. This implies a geostrophic flow perpendicular to the sea-level gradient. The mean ocean currents sustain sea-level differences of around 3 m between the North Pacific subtropical gyre and the Weddell Sea near Antarctica (Rio et al., 2014).

If sea level slopes along the coast, the implied geostrophic flow is toward or away from the coast, inconsistent with the coastal boundary condition of no normal flow. Thus, as the coast is approached, a different dynamical balance must come into play. This change in dynamical balance has, in many cases, the effect of reducing the size of the signal, so that

sea level changes at the coast can be smaller than nearby open-ocean changes.

When a change of forcing occurs on the ocean, the oceanic response to that change can be felt at distant locations after some time. This information transfer happens in part because of advection by ocean currents, but usually the fastest response is mediated by waves. Thus waves, and in particular those in the coastal waveguide, known as Coastal Trapped Waves (CTWs), play an important role in setting up the coastal sea-level response to open-ocean changes. In this paper, we focus on the way in which an understanding of CTWs informs the interpretation of this coastal response. We will find that, for continental boundaries, the strong mesoscale variability in the ocean interior is strongly damped at the coast, meaning the basin-scale signals are the main consideration. We start here by summarizing elements of wave phenomenology, identifying salient features to be described in more detail later in this paper.

A.3.1 Waves in a flat-bottom ocean

In idealised models of the ocean with a flat bottom and vertical sidewalls, linear ocean waves can be sorted into orthogonal vertical modes with different vertical structures. These modes are enumerated by the number of vertical nodes (i.e., depths at which the amplitude is zero). For each mode of subinertial frequency (wave frequency σ less than f or periods longer than the inertial period of $2\pi/f$, where f is the Coriolis parameter), the waves can be classified as Rossby waves in the interior (arising from meridional gradients in the Coriolis parameter), and Kelvin waves at the boundary. Rossby waves have westward phase speeds, yet only long Rossby waves (whose wavelength is longer than 2π times the Rossby deformation radius) have westward group velocity whereas shorter Rossby waves have eastward group velocity. Superinertial waves (waves with frequencies greater than f and periods less than $2\pi/f$) are characterized differently. For this review we focus on the subinertial regime for which coastal trapping is possible.

Kelvin waves are a form of CTW, with the Rossby deformation radius acting as an exponential decay scale away from the vertical side boundary. Kelvin waves propagate cyclonically around an ocean basin with the boundary on the right (facing in the direction of propagation) in the northern hemisphere and on the left in the southern hemisphere. They also generally move much faster than Rossby waves of the corresponding mode. In particular, Rossby waves travel fastest at the equator, at one third of the equatorial Kelvin wave speed, and they slow dramatically with increasing latitude whereas Kelvin waves do not. This contrast is illustrated for the first baroclinic mode (mode-1) in Figure A.1.

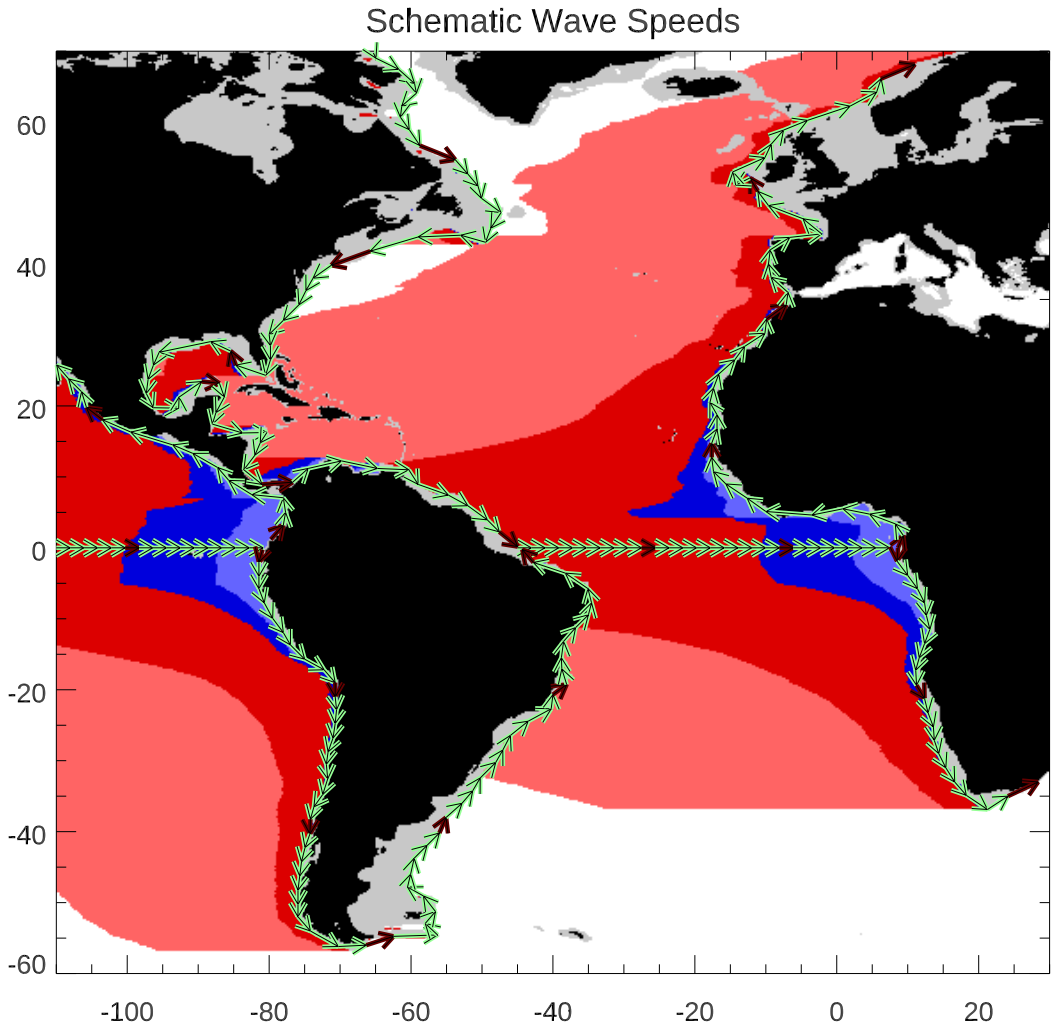

Figure A.1: *Illustration of subinertial wave speeds in a flat-bottomed ocean, showing the fastest (long wavelength) mode-1 waves, and assuming a spatially uniform typical Kelvin wave speed of 2.5 ms^{-1}. Arrows show the distance covered per day by Kelvin waves, with every tenth day highlighted. Colours show the westward distance covered by Rossby waves from the eastern boundary in ten days (pale blue), one month (dark blue), one year (red) and ten years (light red). For each, the boundary of the ocean is taken as the 500 m isobath (shallower regions are grey). In a more realistic ocean with variable stratification and bathymetry, the Rossby wave speeds would be reduced, and the boundary wave speeds increased, at high latitudes.*

Mode-0 waves (the barotropic mode) adjust rapidly, with the Kelvin wave speed being of order 200 m s^{-1} and the Rossby radius of order 2000 km. Consequently, Mode-0 Kelvin waves transfer forcing change information globally in just a few days (Lorbacher et al., 2012). For higher wave modes the adjustment time scale can be much longer. The Mode-1 (first baroclinic) equatorial Kelvin wave speed is typically 2.5 m s^{-1}. Furthermore, the corresponding Mode-1 Rossby wave speed drops below 10 cm s^{-1} poleward of about 20°, with theoretical speeds below 1 cm s^{-1} poleward of about 60° (Chelton and Schlax, 1996). The ocean, of course, does not have a flat bottom. Away from the continental slopes, even the relatively weakly sloping seafloor has an influence on the structure of Rossby waves, strongly reducing the amplitude of the Mode-1 Rossby wave at the seafloor and slightly altering its dispersion relation, but otherwise the general results from flat-bottom theory remain valuable (Lacasce, 2017).

A.3.2 The disparity between coastal and open ocean wave speeds

There is a great disparity in wave speeds and length scales between coastal signals and open ocean signals. The open ocean adjustment process is dominated by basin-scale Rossby waves, whereas boundary waves are trapped to the continental slope over a length scale that is the larger of the Rossby radius (in the case of a Kelvin wave) and the width of the slope itself (as we will see for other kinds of coastal trapped waves). This length scale is typically tens of kilometres outside the tropics, and a maximum of about 250 km near the equator (excluding the rapidly-adjusting mode-0, which is basin scale). Within a few equatorial Rossby radii of the equator, equatorial Kelvin waves and Yanai waves (mixed Rossby-gravity waves) carry signals rapidly to the east, thus removing the coastal trapping found away from the equator. The above dynamics is standard and is described in oceanography textbooks such as Gill (1982).

The disparity in wave properties means that the coast is a special place, with communication of signals along the coastal boundary moving rapidly compared to the ocean interior. There is hence the possibility of a decoupling between coastal and open ocean sea level signals. Such a decoupling is seen in observations and ocean models, which show quite different spectra of sea level between the coast and the open ocean in many regions, though most dramatically away from the equatorial and eastern boundary regions (Hughes and Williams, 2010; Bingham and Hughes, 2012; Hughes et al., 2018).

The effect of rapid propagation of coastal trapped waves is seen in the coastal sea level response to El Niño events along the eastern boundary of the Pacific (Enfield and Allen,

1980; Kurapov et al., 2017). It has also been noted indirectly via the uniformity of sea level signals around Antarctica as discussed by Hughes et al. (2014) and references therein, and by an analogous mode in the Arctic (see Fukumori et al. (2015) and references therein). These polar modes are manifestations of the response to near-coastal winds being trapped and rapidly propagated along the coast, a phenomenon also seen in the eastern North Atlantic (Calafat et al., 2012, 2013), and discussed in more detail elsewhere in this volume. Further indirect evidence of the influence of CTWs is seen in the coherence of sea level signals above long stretches of the global continental slope (Hughes and Meredith, 2006). Recent model-based analysis suggests that much of the shelf coherence results from the strong suppression of mesoscale variability over the continental slope, thus permitting the large scale barotropic mode to be seen in the resulting quiet regions (Hughes et al., 2018), thus representing an indirect manifestation of CTW effects.

A.3.3 Importance of the continental slope

The influence of the continental slope on the results described above highlights an important aspect of the real ocean; namely, it does not have vertical sidewalls. Instead, as illustrated in Figure A.2, typical off-shore bathymetry at the coast consists of a gently sloping shelf region, followed by a steeply-sloping continental slope down to the abyssal plain of the open ocean. In the presence of a sloping sidewall, CTWs are no longer pure Kelvin waves. Given that the rapid propagation of CTWs appears to be responsible for the above mentioned decoupling between the coast and open ocean, we assume that physical characteristics of CTWs play an important role in mediating the influence of the open ocean on the coastal region. The purpose of this paper is to review the extent to which this assumption offers a valuable framework for understanding how the open ocean communicates with the coast. We begin by considering properties of CTWs when sloping topography is present. The complementary question of how CTWs act to trap and propagate sea level signals that are themselves generated close to the coast, rather than in the open ocean, is considered elsewhere in this volume.

At subinertial frequencies, and assuming f to be constant (the f-plane approximation is almost ubiquitous in the theory of CTWs; this is a significant issue which we will pick up later on), it remains the case even with nontrivial topography that plane waves cannot propagate away from the shore. There are still waves that travel along-shelf with an off-shelf decay. Hence, the concept of CTWs remains valid. However, the presence of topography breaks the decomposition into vertical modes. Typically, these CTWs form a sequence with

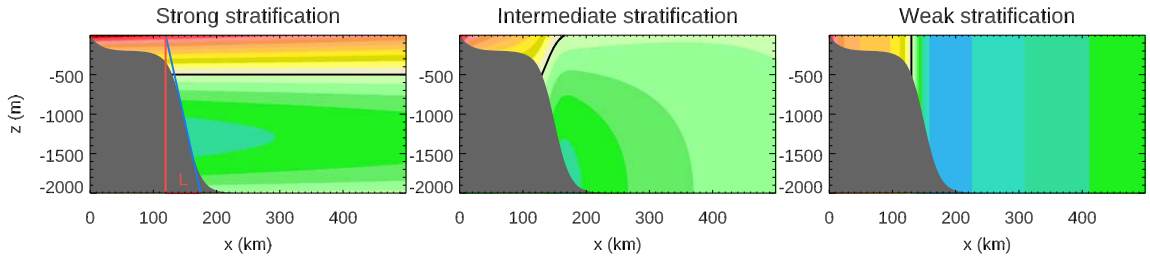

Figure A.2: *Schematic showing the typical configuration of topography, coordinate system, and mode-1 CTW characteristics for various strengths of stratification as defined by the Burger number (see text). The y direction is into the page, and would be to the north if the boundary is on the west of the ocean. Grey shading represents topography, with a typical gently sloping shelf region, followed by a steeply-sloping continental slope. The topographic length scale L corresponding to a particular position (where the blue line is tangent to the slope) is illustrated in the first panel. Shading represents the perturbation pressure associated with the mode, with the node (zero value) marked with a black contour. In the northern hemisphere, the wave would be propagating out of the page (the opposite in the southern hemisphere). The offshore decay in the strong stratification case is exaggerated, to make it more visible.*

an increasing number of nodes in bottom pressure, spaced down the slope, as we see in baroclinic Kevin waves for the vertical sidewall case. What is different is that the nodes reach the sea floor at different distances from the shore, because of the finite slope, and their extension away from the sea floor is no longer horizontal as it is in baroclinic Kelvin waves, but at some angle, becoming vertical in the barotropic limit (Huthnance, 1978), as seen in Figure A.2.

For a given along-shelf wavelength, higher modes (with more offshore nodes) have lower frequency and propagate more slowly. Mode-0, which depends on the surface of the ocean being free to move (i.e., not rigid) is termed a (barotropic) Kelvin wave. Even in the presence of topography, the mode-0 Kelvin wave usually has maximum elevation at the coast and offshore decay with no change of sign, and is much like the barotropic Kelvin wave in the flat bottom case. Typically mode-1 also has maximum elevation at the coast and a node near the shelf break. As the forms with simplest and largest-scale spatial structure (shelf-width scale for mode-1) modes 0 and 1 are most naturally generated by large-scale forcing (from atmosphere, deep ocean or tides) with resulting maximal effects of elevation at the coast. Along-shelf phase propagation remains cyclonic around an ocean basin with typical speeds of hundreds of metres per second for a mode-0 Kelvin wave and several metres per

second for mode-1. The speeds other than mode-0 tend to be similar to, or faster than, the corresponding pure (i.e., vertical sidewall) baroclinic Kelvin wave speeds.

A.4 Properties of f-plane coastal trapped waves

CTWs are subinertial waves (wave frequency σ less than the magnitude of the inertial frequency $|f|$), with along-shelf propagation and off-shelf decay. We here present a summary of their properties on the f-plane. Far more details, including mathematical derivations, can be found in the review papers by Huthnance (1978); Mysak (1980b,a); Huthnance et al. (1986); Huthnance (2001) and references therein. We follow the usual convention whereby the waves are described using a coordinate system with $\hat{\mathbf{x}}$ (the unit vector along the x-axis) pointing in the off-shelf direction into the ocean interior (as in Figure A.2) and the y-axis direction, $\hat{\mathbf{y}}$, directed along the coast (pointing into the page in Figure A.2). Hence, northern hemisphere waves propagate in the $-\hat{\mathbf{y}}$ direction for a right-handed coordinate system in which $\hat{\mathbf{z}}$ points upwards (note that $\hat{\mathbf{y}}$ points approximately to the north on western ocean boundaries, and to the south on eastern boundaries).

We are concerned with the following restoring mechanisms leading to ocean wave propagation: gravity (tending to level the sea surface and interior isopycnals; the Kelvin wave mechanism) and potential vorticity conservation (tending to constrain any bottom-reaching flow to be along depth contours in the f-plane limit). The latter is analogous to the Rossby-wave mechanism that gives westward phase propagation in the open ocean due to the meridional gradient of the Coriolis parameter. We thus refer to "topographic Rossby waves" when the potential vorticity gradient is predominantly due to gradients in water depth (i.e., topographic β), rather than gradients in the Coriolis parameter (planetary β). In this manner, cyclonic around an ocean basin corresponds to the westward phase propagation of Rossby waves. Another common term for CTWs, especially in the unstratified case, is "continental shelf waves".

The two relevant length scales are the cross-shelf scale of the topography, L, and the first baroclinic Rossby deformation radius, L_d. The cross-shelf length scale is given by $L = h/|s|$, where $z = -h(x, y)$ is the vertical position of the ocean bottom topography and $s = \partial h/\partial x$ is its offshore slope. The deformation radius L_d scales approximately as $NH/|f|$ where H is the vertical scale and N is the buoyancy frequency measuring the strength of stratification: $N^2 \equiv -(g/\rho_0)d\rho/dz$ where z is the vertical coordinate (positive upward), g is acceleration due to gravity, $\rho(z)$ is the background vertical structure of potential density at rest and ρ_0 is a reference background density. When stratification is strong, i.e., the Rossby radius

of deformation exceeds the cross-shelf topographic scale, the continental slope and shelf may be "seen" by the wave as a near-vertical sidewall. Wave-forms in this limit are modes of vertical structure with off-shelf decay on the scale of the Rossby radius of deformation; i.e., they act like "Kelvin waves". Strong stratification corresponds to a narrow shelf slope compared to the Rossby radius: $(L_d/L)^2 \gg 1$. Here, $(L_d/L)^2$ is approximately equivalent to the Burger number

$$S \equiv N^2 H^2 / f^2 L^2 \approx (L_d/L)^2. \tag{A.1}$$

The spatial structure of a wave mode changes as stratification, topography and/or latitude changes. Nodal lines of perturbation pressure typically tilt upward toward the surface, from horizontal (strong stratification/steep topography/low latitude, $S \gg 1$) in the Kelvin wave limit to vertical (weak stratification/broad topography/high latitude, $S \ll 1$) in the barotropic topographic Rossby wave limit. Figure A.2 schematically illustrates the progression from strong to weak stratification for mode-1, with the nodal lines marked in black. In the Kelvin wave limit, the modes have the same offshore structure as the corresponding open ocean vertical modes. As stratification weakens, the slope becomes less steep, or $|f|$ increases, the CTW modes evolve more complex structures which no longer match the interior modes, and are not separable in the vertical coordinate, until they become simply barotropic in the low S limit. A clear example of this transformation of modal structure from equator to high latitude is given by Allen and Romea (1980), who also explain how (in the absence of scattering by small scale topography) energy is retained within a particular mode even as its structure changes with latitude.

A.4.1 Characteristic properties in various limits

For mode-1 in the relatively weak stratification limit (i.e. a topographic Rossby wave or "continental shelf wave"), the cross-shelf scale tends to match the shelf width L. At low frequencies the waves become non-dispersive with a propagation speed of order Lf, which is $\mathcal{O}(10\ \mathrm{m\ s^{-1}})$ for $f = 10^{-4}\ \mathrm{s^{-1}}$, $L = 100$ km. Hence, long period implies long wavelength. Mode-1 tends to have a maximum (sub-inertial) frequency at which the along-shelf scale is comparable with the shelf width. Shorter waves then have lower frequency so that energy propagation at the group velocity is reversed (phase propagation remains cyclonic around the deep ocean). This behaviour is again analogous to Rossby waves: the frequency maximum for Rossby waves is at a length scale (wavelength divided by 2π) which is comparable to the smaller of the Rossby radius and the meridional length scale, whereas for CTWs the frequency maximum is at a length scale comparable to the shelf width. As

the stratification increases, the waves transition towards (internal) Kelvin waves with a propagation speed of order NH, which is $\mathcal{O}(1\ \mathrm{m\ s^{-1}})$ for a bottom-top density difference $0.001\rho_0$ in depth 100 m. Correspondingly, for stratification-dominated waves (the Kelvin wave limit) the dispersion relation for frequency σ as a function of along-slope wavenumber k can approach and even pass smoothly through the inertial frequency as k increases (Dale et al., 2001).

For short along-slope wavelengths (large k), the general coastal trapped wave form is bottom trapped. Bottom-trapped waves (Rhines, 1970) are a limiting case in simple geometry, with uniform stratification N^2 and motion everywhere parallel to a plane sloping seafloor; they decay away from the seafloor. They can propagate up or down the slope, but always with a component along the slope cyclonically around the deeper water. In more general geometries, CTWs in the large k limit become bottom-trapped waves confined near the seafloor where Ns is maximum, with frequency given by $\sigma = Ns$ (Huthnance, 1978).

With increasing distance from the equator, the inertial frequency f increases from zero in proportion to the sine of latitude. Oceanic stratification also generally decreases. For any given off-shore profile of coastal bathymetry, these changes imply a poleward trend from more to less stratification (decreasing Rossby radius of deformation or decreasing Burger number). This transition of the Burger number thus leads to a transition from (internal) Kelvin waves towards topographic Rossby waves. An implicit assumption is that changes in f, the stratification, and the continental shelf form are small over one wavelength, so that local wave forms are roughly as for a uniform shelf. Then also individual wave modes conserve along-shelf energy flux. However, in realistic cases the shelf-depth profile can vary relatively rapidly, thus causing scattering between wave modes.

The shelf width may be the most important factor in determining whether stratification is "strong", i.e. if the Rossby radius of deformation exceeds the cross-shelf scale L so that the Burger number is larger than unity. With a bottom-top density difference of $0.001\rho_0$, $f = 10^{-4}\mathrm{s}^{-1}$ and $L = 100$ km, the Burger number is $S = 10^{-4}H$ where H is the water depth measured in metres. For this case with a fairly wide shelf, stratification is weak, especially over the shelf where H is small. For a narrower shelf of $L = 10$ km, then $S = 10^{-2}H$ (again, with H in metres). In this case stratification is strong especially over the adjacent slope. At a latitude of about 12.5° the factor f^{-2} in S becomes ten times larger than the typical midlatitude value of f assumed above, thus making stratification ten times more effective than in the above scalings.

A.4.2 The long-wave limit

The long-wave limit is (as we will show below) the most relevant to open-ocean interaction with the coast at periods longer than a few days. At very low frequencies and negligible bottom friction, with correspondingly small along-shelf wavenumber, and with shelf width scales much smaller than the barotropic Rossby radius ($gH/f^2L^2 \gg 1$), we use the linear, inviscid boundary equations:

$$\rho_0 f v' = \frac{\partial p'}{\partial x}, \tag{A.2}$$

$$\rho_0 \frac{\partial v'}{\partial t} + \rho_0 f u' = -\frac{\partial p'}{\partial y}, \tag{A.3}$$

$$\rho_0 \frac{\partial \rho'}{\partial t} + \rho_0 \frac{N^2}{g} w' = 0, \tag{A.4}$$

where primes represent perturbations about a stably-stratified state of rest. Assuming a wave-like form travelling along the boundary, with $(u', v', w', \rho', p') = (u, v, w, \rho, p)e^{i(ky-\sigma t)}$, and substituting into the momentum equations, we find that velocity components are related to pressure p by

$$\rho_0 f^2 (u, v) = \left(-ik \left[-c\frac{\partial p}{\partial x} + fp \right], f\frac{\partial p}{\partial x} \right). \tag{A.5}$$

Here we are assuming a wave propagating in the y direction (along-slope). This means that the wave phase speed is $c = \sigma/k$ (we will find that c takes the opposite sign to f), and imaginary quantities are 90° out of phase with real quantities. Thus along-shelf flow v is in phase with the pressure field, but cross-shelf flow u lags it by 90°. Within equation (A.5), the pressure p obeys

$$\frac{\partial^2 p}{\partial x^2} + \frac{f^2}{N^2}\frac{\partial^2 p}{\partial z^2} = 0. \tag{A.6}$$

The boundary condition of no normal flow through the seafloor $w = -udh/dx$ at $z = -h(x)$ means that at the bottom we have

$$\frac{\partial h}{\partial x}\left(\frac{\partial p}{\partial z} - \frac{fp}{c} \right) + \frac{f^2}{N^2}\frac{\partial p}{\partial z} = 0. \tag{A.7}$$

Assuming a rigid lid boundary condition, which is usually a good approximation for modes 1 and higher, but not the mode-0 Kelvin wave, the equivalent boundary condition at the top is

$$\frac{\partial p}{\partial z} = 0. \tag{A.8}$$

Since only c appears in equation (A.7), rather than σ and k separately, the eigenmodes that satisfy equation (A.6) and its boundary condition all have the same speed c for all

wavelengths in this long wavelength limit. This means that long waves are nondispersive and characterised by a single propagation speed for each mode.

Given speeds measured in metres per second (hundreds of kilometres per day), these long waves are clearly the appropriate limit for considering the coastal influence of open ocean currents with natural time scales of more than a few days. However, as time scales become longer, it becomes important to consider the role of friction.

Friction causes cross-shelf phase shifts, altered amplitude distributions, and significant damping of CTWs (e.g. Brink (1982, 1991)). Qualitatively, this effect can be understood by thinking in terms of how the ocean responds to an externally imposed along-shelf wind stress τ rather than the along-shelf pressure gradient which is a part of the wave itself. For idealized uniform conditions (no along-shelf pressure gradient and no on-offshore transport) the depth-integrated alongshore momentum balance is

$$\partial v/\partial t + rv/h = \tau/\rho_0 h. \tag{A.9}$$

In this equation, v is the along-shelf component of flow and r is a bottom friction coefficient with units of speed. This friction coefficient expresses a linear drag law proportional to bottom velocity, based on an assumed quadratic drag linearised around a background, usually tidal velocity u_0. The momentum equation (A.9) means that the along-shelf flow is in phase with the forcing wind stress τ if the frequency of oscillation of the stress is much smaller than r/h (in which case the time tendency term can be dropped). In contrast, the flow lags more as the frequency increases to approach r/h. Since drag becomes important more rapidly (i.e. at higher frequency) in shallower water, its effect is to bias v to greater amplitude in deeper water, which in turn mitigates the damping effect (Huthnance, 2001). For example, nearshore currents lag the wind less than currents in deeper water offshore. Within damped CTWs it is found that v shifts from being in a geostrophic balance $v \propto \partial p/\partial x$ offshore (where h is large) to a frictional balance in which flow is down the slope of sea level $v \propto \partial p/\partial y$ in shallow water.

Damping rates may be estimated as $r/h = \mathcal{O}(0.003\, u_0\, h^{-1})$, where the value 0.003 is a standard non-dimensional quadratic drag coefficient. This leads to a decay time less than 4 days for a typical current with $u_0 = 0.1$ m s^{-1} and depth $h = 100$ m. This decay time converts to a decay distance $c_g h/r$ for a wave with energy propagation speed c_g. Such decay distances are largest (hundreds to a thousand kilometres or more) for long waves with 'forward' energy propagation; much less for (short) waves with slow 'backward' energy propagation.

Thus, although CTWs are an important factor in regulating the link between the ocean

and coast, for time scales of days and longer it is important to include the role of friction. In order to understand this effect in more detail, we reintroduce bottom drag, and consider the low frequency limit for which the coastal adjustment to open ocean changes may be considered to be complete, and a steady state has been reached.

A.4.3 The low frequency limit

We now examine how variability on the middle and outer shelf can influence coastal sea level as $\sigma \to 0$, remaining on an f-plane, showing that the effect of the continental slope is to smooth the open-ocean sea level signal, and shift it in the direction of CTWs before it reaches the coast.

To simplify the discussion we follow Csanady (1982) and references therein, and assume a straight coast at $x = 0$ and a "wedge" depth profile of the form $h = sx$ defined over a coastal strip of width l. The flow is assumed to be steady, linear and barotropic and the wind stress is zero. A further simplification (which results from the along-shelf currents being much larger than the cross-shelf currents) is the neglect of bottom stress in the cross-shelf direction leaving a geostrophically balanced alongshore flow.

Under the above assumptions the sea level distribution over the coastal strip ($0 < x < l$) satisfies

$$\frac{\partial \eta}{\partial y} = -\frac{r}{fs}\frac{\partial^2 \eta}{\partial x^2}. \tag{A.10}$$

As noted by Csanady (1978), this is a diffusion equation with alongshore distance in the direction of CTW propagation playing the role of time. The coastal boundary condition of no normal flow, combined with the alongshore momentum balance as depth tends to zero, leads to a boundary condition $\partial\eta/\partial x = 0$ under the present assumptions. The offshore boundary condition specifies $\eta(l, y)$.

This highly idealized model illustrates two important consequences of the coastal boundary condition. First, spatial variations of mean sea level "diffuse" along the coastal strip in the same direction as CTW propagation, i.e. cyclonically. This feature explains the use of "Arrested Topographic Wave" to describe Csanady's model. Second, this diffusive effect leads to coastal sea level being smoother than the variability offshore. More specifically, if the sea level at the offshore boundary of the coastal strip is taken to be $\eta(l, y) = \cos(ky)$ then sea level at the coast is given by $A(k)\cos(ky + \phi)$ where the gain $A(k) \to 1$ from below as $k \to 0$; only infinite wavelengths diffuse completely to the coast (Figure A.3).

A more complete analysis includes the effect of stratification (Huthnance, 2004). Consistent with the above discussion it is concluded that coastal tide gauges can only monitor

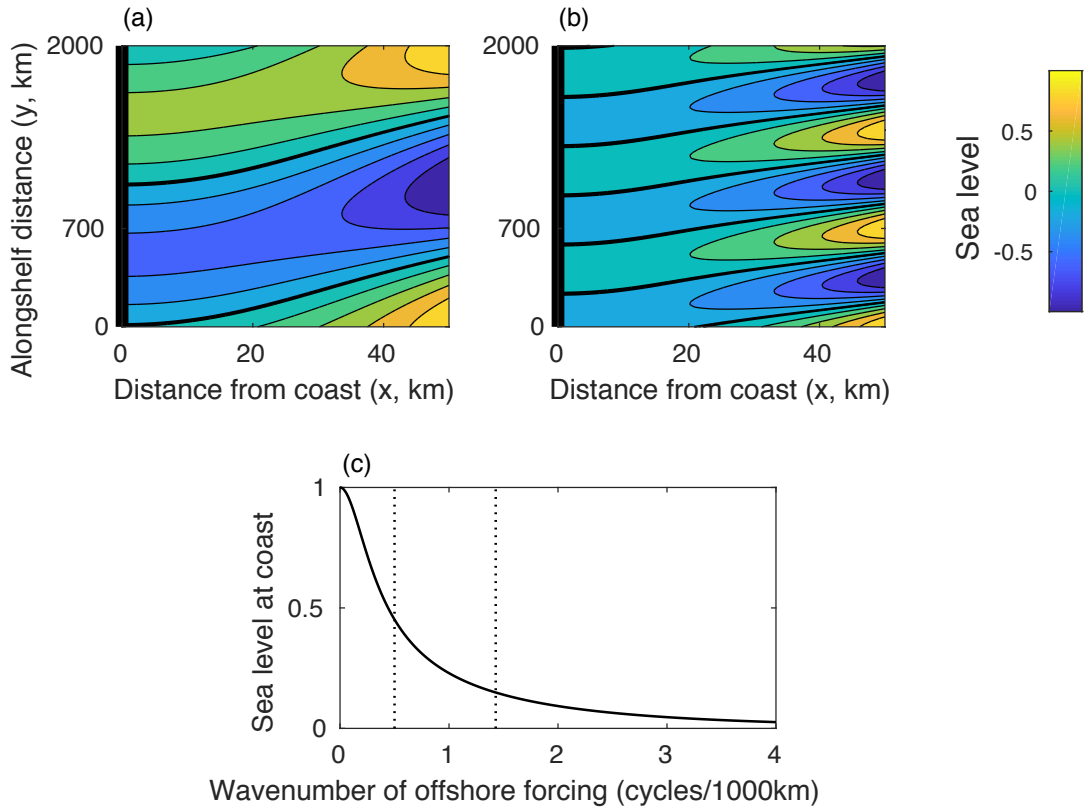

Figure A.3: *Response of coastal sea level to steady sinusoidal forcing specified at the offshore boundary of a narrow coastal strip, calculated using Csanady's Arrested Topographic Wave model (see text for details). Panels (a) and (b) show sea level as a function of cross (x) and along (y) shore distance. The coast is at x=0 and marked by the thick black vertical line. The offshore boundary is at x=50 km where sea level is assumed to be sinusoidal with unit amplitude and alongshore wavelength of (a) 2000 km and (b) 700 km. Zero contours are shown by the thicker black lines. Panel (c) shows the amplitude of coastal sea level as a function of the wavenumber of the offshore forcing. The wavenumbers used in (a) and (b) are indicated by the dotted lines. The linear friction coefficient is* 5×10^{-4} *m* s^{-1}*, the Coriolis parameter is* 10^{-4} s^{-1} *and the slope of the wedge-shaped bathymetry is* 3×10^{-3} *(implying a depth of 150 m at the offshore boundary).*

large-scale oceanic motion with scales of thousands of kilometers. Lin et al. (2015) provide observational evidence for the smoothness of mean sea level along extended coastlines exposed to the open ocean. Based on an analysis of mean sea level observed by 31 tide gauges along west coast of North America, and a realistic model of the geoid, they showed that changes of coastal mean sea level have a range of about 0.3 m between 30 and 60°N. They then used the Arrested Topographic Wave model to show that the primary driver of this alongshore variability was wind forcing over the shelf rather than the open ocean, consistent with simulations by realistic ocean models.

On other coastlines, however, different dynamics apply. Tide gauge data, satellite altimetry, and ocean model simulations agree on the general features of the global coastal mean dynamic topography (Woodworth et al., 2012; Andersen et al., 2018), which shows smooth variations on eastern boundaries (except at the Strait of Gibraltar where the Mediterranean inflow allows for a step Hughes et al. (2015)), but larger and sharper steps in places along western boundaries, with different models in particular showing significant differences in the latter case. The sharp steps appear to be associated with western boundary currents, the Gulf Stream in particular being a clear example (Higginson et al., 2015), but the steps are smaller than those across the western boundary currents and occur equatorward of the main open ocean step as if displaced in the direction of CTW propagation.

In summary, the coastal boundary condition of no normal flow has a profound influence on the way signals originating in the open ocean are transmitted across the shelf to the coast: spatially smoothing the ocean signal and diffusing it along the shelf in the same direction as CTW propagation. It is important to note however that the Arrested Topographic Wave model is only relevant on the inner shelf and describes how sea level variability on the middle to outer shelf is transmitted to the coast. It is not meant to model the transmission of signals across slope to the open ocean. We return to this more complicated problem in Section A.5.

Given the apparent importance of bottom friction in allowing the ocean sea level signal to "diffuse" toward the coast, we now consider the possibility of dynamical effects that may reduce the role of bottom friction.

A.4.4 Slippery bottom boundaries

It has been pointed out (MacCready and Rhines (1993) and references therein) that the presence of stratification can have an important effect on the operation of bottom friction. Friction induced by a bottom current along isobaths will result in an Ekman flux perpendic-

ular to those isobaths, advecting buoyancy up or down the slope. The resulting upwelling or downwelling leads to horizontal density gradients near the bottom which in turn produce a change in the bottom geostrophic flow, as a result of the associated change in thermal wind balance. The result is always a tendency to reduce the near-bottom geostrophic flow, and hence reduce the friction, thus making the bottom effectively more "slippery" than might initially be thought (although the flow near the bottom has been reduced, this Ekman flux induced adjustment means the frictional interaction of the flow with the bottom is subsequently reduced). In fact, a similar process applies over a flat bottom, as a result of the convergence or divergence of the Ekman flux, but the presence of a slope can accelerate the process as it does not require the Ekman flux to be divergent.

The logical extreme of this idea is that, after some time, the bottom geostrophic flow tends to zero and bottom friction ceases to act at all. It is important to put this interpretation into a broader context to see why it cannot be correct in general, though there are circumstances in which it may be a useful concept.

First, in the context set out by MacCready and Rhines (1993), the bottom geostrophic flow does not decay to zero, but to a particular value determined by a balance between vertical diffusion and upslope Ekman flux of density. It could only approach zero in the absence of diffusivity. Furthermore, diffusion is the only form of forcing in this scenario, as the problem considered involves no wind stress and no influence from the open ocean (which we will discuss below in terms of the addition of varying Coriolis parameter) other than the establishment of a background stratification.

Second, if we consider the steady, linear, along-slope, depth-integrated momentum budget, as there is no variation in depth in the along-slope direction, bottom form stress does not appear and the budget can be written as

$$fU = -\frac{\partial P}{\partial y} + \tau_s - \tau_b, \tag{A.11}$$

where U is the depth-integrated offshore mass transport, P is the depth-integrated pressure, τ_s is the alongshore surface wind stress, and τ_b is the alongshore stress on the bottom. The terms on the right hand side represent the offshore geostrophic, wind-driven Ekman, and bottom Ekman flows respectively. As the depth approaches zero at the coast, both U and P must approach zero, being depth integrals of finite quantities, so the balance becomes one between wind stress and bottom stress, meaning that bottom friction cannot reduce to zero. This is consistent with the steady state form of equation (A.10) in Section A.4.3 describing the Arrested Topographic Wave: in the absence of wind stress, the bottom stress must decay to zero at the coast, but balance the depth-integrated pressure gradient offshore.

Third, if we take the curl of the steady, depth-integrated linear momentum equations (e.g. substitute constant f, $H = h(x)$, $Q = 0$ and $\partial/\partial t = 0$ into equation 20 of Hughes (2008)), then we obtain

$$\frac{\partial p_b}{\partial y}\frac{dh}{dx} = \hat{\boldsymbol{k}} \cdot \boldsymbol{\nabla} \times \boldsymbol{\tau}, \tag{A.12}$$

where p_b is the bottom pressure and $\boldsymbol{\tau}$ is the vector surface minus bottom stress. In this equation, we have ignored nonlinear terms in the momentum equation and the very small effect of stress due to atmospheric pressure acting on the free surface slope of the ocean, but otherwise the equation is general and applies in either stratified or unstratified oceans. Integrating along characteristics (contours of h in this case) shows that, in the absence of any bottom stress, bottom pressure must vary along the contours in a manner determined by wind stress. The resulting bottom pressure field will in general imply the presence of geostrophic flows at the bottom, which is inconsistent with the slippery boundary assumption. This aspect of the analysis leads us to consider the connection to distant forcing, and hence to open ocean dynamics, for which we must abandon the assumption of constant f. This scenario will be considered further in the next section.

Finally, the assumption that the bottom flow can be shut down relies on there being sufficient stratification. Advection of denser water up or down the slope will tend to reduce the alongshore bottom velocity, but by an amount which depends on the density contrast. For strong currents in weak stratification, it may be impossible to generate sufficient density contrast to shut down the bottom flow. This is the likely to be the case on the inner shelf.

In summary, while the bottom Ekman layer produces an adjustment which tends to reduce the bottom geostrophic flow, there are fundamental reasons why this bottom flow cannot generally shut down. It is required in order to balance the (wind or buoyancy) forcing.

A.5 The influence of ocean dynamics at the coast

We have seen above that CTWs propagate rapidly compared to the typical speeds associated with baroclinic open ocean dynamics. Mode-0 is sufficiently fast that a large-scale adjustment can occur globally in a matter of a few days. Furthermore, low modes also typically propagate at speeds measured in metres per second, and are trapped to the coast with a length scale which is (outside the equatorial waveguide) small compared to ocean basin scales. This disparity in length scales and propagation speeds requires special consideration in both theoretical and numerical models of ocean circulation. A common approach is to

use a framework in which the shelf response is assumed to be in a steady equilibrium with the instantaneous ocean interior, effectively assigning an infinite speed to the CTWs.

An example is the quasigeostrophic (QG) approximation, in which sidewalls must be vertical and the CTWs become an infinitely fast series of Kelvin waves. This introduces some subtleties into the boundary conditions, which are resolved by considering volume conservation in each of the ocean's density layers. Once the correct boundary conditions are applied, a boundary-trapped mode is added to the equations enabling the evolution of the ocean circulation to mimic the case with explicitly-resolved Kelvin waves (Milliff and McWilliams, 1994). This is an unusual case in which the boundary signal has been explicitly considered. It is more usual in idealised ocean circulation studies (such as Stommel (1948); Munk (1950) and their descendants) to solve for the interior circulation plus a western boundary current in a manner which eliminates pressure from the equations, and not to explicitly consider the boundary pressure or sea level values. Although this is simply a choice of solution method, it does have the effect of obscuring the physics associated with sea level and boundary pressures.

Something similar occurs in the linear shallow water equation approximation used by Johnson and Marshall (2002) to describe the overturning circulation. Again, vertical sidewalls are assumed, with boundary (and equatorial) Kelvin waves travelling fast compared to other time scales. And again, a volume integral constraint is needed to determine the boundary pressure values. By allowing the waves to travel rapidly, causality is obscured, and the entire boundary appears to "know" about the interior ocean simultaneously.

Another system which exhibits similar behaviour is the linear planetary geostrophic equations with topography. Here, wherever the topography is steep enough to produce closed contours of f/h (or, equivalently, of gh/f which we will later show to be a more useful quantity in the sea level context), it is found that baroclinic signals impinging on the topography can effectively "jump" zonally across the topography, disappearing from one side and appearing more rapidly than expected on the other side, a phenomenon termed a "Rossby wormhole" (Marshall, 2011). When the disturbance originates outside the topography, it jumps across from east to west. When it originates inside the topography, as in a basin configuration, the jump is back from west to east, enabling resonant basin modes to occur (as Kelvin waves would do in a vertical sidewall basin). The hidden mechanism involved here is the implicit (infinitely fast) propagation of barotropic topographic Rossby waves around the closed gh/f contours, thus setting up a bottom pressure signal which absorbs the baroclinic disturbance at one side and re-radiates it on the other side of the topography. Here, the implied boundary waves are barotropic (a limitation of the planetary

geostrophic approximation which cannot support Kelvin waves, in which relative vorticity is significant), complementing the baroclinic Kelvin waves of the vertical sidewall case to represent the opposite extreme of the family of CTWs: topographic Rossby waves. Between the quasigeostrophic and planetary geostrophic approximations we have two illustrations of how CTWs can have a profound effect on ocean adjustment processes, in the baroclinic Kelvin wave limit and the barotropic continental shelf wave limit respectively.

A.5.1 Implications of rapidly-propagating waves: smoothing

The implication of these idealised systems is that the continental slope should act as a smoother, taking signals which impinge on it and propagating them rapidly around the boundary. A similar conclusion can be drawn from a scaling argument based on vorticity balance (Hughes et al., 2018). Essentially, if a mesoscale eddy interacts with the sloping seafloor, the lack of flow through the boundary means that horizontal velocities induce vertical velocities at the bottom. However, using the same mesoscale eddy velocity in the vorticity balance results in a much smaller scaling for vertical velocity at the bottom; the vorticity constraint means that the large vertical velocity required by the bottom boundary condition cannot, in fact, be supplied.

As a result, the bottom velocities must be much smaller than typical mesoscale velocities, and the mesoscale is not strongly represented in bottom pressure on the continental slope. In effect, the eddies are "fended off" by the continental slope, although some fluid exchange occurs at scales smaller than the mesoscale; see e.g. Cherian and Brink (2016) for an illustration of this process. Bottom pressures on the slope should therefore be coherent over large distances, in contrast to sea level in the ocean interior which decorrelates rapidly over the mesoscale. The scaling involved here is a reflection of the rapid propagation of CTWs compared to Rossby waves. A related argument can be made in the case of vertical sidewalls as described by Kanzow et al. (2009).

The latest ocean models can now be run with sufficient resolution that it is no longer necessary to artificially smooth the topography to avoid a vertical sidewall, although even at $1/12^\circ$ resolution, which is still considered high resolution for a global ocean model, the slope remains only marginally resolved in some regions of very steep topography, and details on the slope are certainly not resolved. As a result, it is becoming possible to test these theoretical ideas. It is found that, in a model with realistic mesoscale energy and spectra, the bottom pressure on continental slopes does indeed display coherence over distances measured in tens of thousands of kilometres (Hughes et al., 2018). Using this coherence

it is possible to identify the circuit times for mode-1 and mode-2 CTWs in the (model) North Atlantic as 115 and 205 days respectively. This defines a time scale with respect to which the system evolution must be "slow" to justify the assumption that CTWs are in equilibrium with the interior (the mode-0 adjustment time is too fast to clearly resolve). The mode-1 time is equivalent to an average CTW speed of around 4–5 m s^{-1}, significantly faster than the corresponding Kelvin wave speed anywhere in the North Atlantic (Chelton et al., 1998). The fact that the speed is faster than a Kelvin wave speed shows that the finite inclination of the continental slope is an important factor in this boundary adjustment process, so the planetary geostrophic limit (implied barotropic topographic Rossby waves) may be more applicable than the QG limit (implied baroclinic Kelvin waves) over much of the domain.

The model results also confirm the strong suppression of bottom pressure variability amplitude on the continental slope, compared to the mesoscale, and show that the mesoscale spectrum does not penetrate strongly into coastal regions (with the exception of a resonant basin mode in the Caribbean Sea, where the coastal signal has a strong 120-day period excited by mesoscale variability Hughes et al. (2016)). This lack of penetration to the coast is consistent with what is seen in satellite altimetry: sea level spectra near western boundaries differ strongly between the coast and open ocean, the two regions being typically separated by a minimum of variability near the top of the continental slope (Hughes and Williams, 2010; Zhai et al., 2010).

It is worth remarking in this context that small islands are a rather special case. The continental slope smoothing effect is rather ineffective because the slope is closed over relatively small distances, so the mesoscale is only averaged over distances smaller than the mesoscale length scale. For this reason, model diagnostics show little difference between the open ocean sea level and island coastal sea level, unless the length scales in the open ocean are smaller than the island scale (Williams and Hughes, 2013). Thus, the special dynamics at boundaries do not upset the traditional interpretation of island gauges as good sites for monitoring ocean sea level variations (Woodworth, 1991), which is why they have proved so useful for satellite altimeter validation, e.g. Mitchum (1994).

A.5.2 Oceans with vertical sidewalls

Having established that most of the mesoscale variability is filtered out by the continental slope, we are left with the question of the basin scale variability and how that affects coastal sea level. For many idealised studies the pressure field (and hence sea level) is implicit in

the solution, but is not explicitly shown.

It is helpful first to consider a simple case, for which an explicit solution can easily be found: the linear Munk (1950) or Stommel (1948) two-gyre ocean with vertical sidewalls and constant layer thickness H. Here, we would typically have an eastward wind stress which is maximum at some middle latitude and decays to zero to the north and south. The wind stress curl then excites a cyclonic subpolar gyre on the poleward side (here, sea level falls from east to west, before rising rapidly again across the western boundary current), and an anticyclonic subtropical gyre on the equatorward side (where sea level rises from east to west, before falling across the boundary current). We can sidestep all the vorticity balance arguments, retaining only the information that friction acts dominantly in the western boundary (it is western boundary current friction that balances the alongshore sea level slope in these models, so this assumption locates that slope on the western rather than eastern boundary), and calculate the coastal sea level simply from the wind stress. Since, when integrating over longitude and depth, there is no net northward transport across any closed section, the effect of the Coriolis force integrates out and the steady, linear, zonal momentum balance (or, strictly, angular momentum about the Earth's axis) becomes a balance between the wind stress and the pressure difference between eastern and western sidewalls:

$$\int_W^E \tau_s^{(x)} = \int_{-H}^0 (p_E - p_W)\, dz, \tag{A.13}$$

where subscripts E and W refer to the eastern and western boundary, and $\tau_s^{(x)}$ is the eastward wind stress (we have neglected sea level in comparison to total open-ocean depth H in the pressure integral). Using the fact that the boundary current is on the west, so pressure on the east is independent of latitude (Hughes and De Cuevas, 2001; Hughes et al., 2018), we can subtract off a function of depth only which represents the eastern pressure at any latitude, giving

$$\int_W^E \tau_s^{(x)}\, dx = -H p'_W, \tag{A.14}$$

where p'_W is the western boundary pressure minus the reference value at the east. Finally, we can use hydrostatic balance to write $p'_W = \rho_0 g \eta_W$, giving

$$\eta_W = -\frac{1}{\rho_0 g H} \int_W^E \tau_s^{(x)}\, dx, \tag{A.15}$$

for sea level at the western boundary relative to an assumed constant eastern boundary sea level. The western boundary sea level is therefore lowest between the gyres, at the latitude where the zonally-integrated wind stress is strongest.

This pattern can alternatively be understood as the effect of friction in the western boundary currents, which must be flowing down the pressure gradient as they converge toward the intergyre boundary. However, the angular momentum argument is insensitive to details of friction, and can even be extended to include nonlinear terms which only become important where there is curvature of the boundary current (Hughes and De Cuevas, 2001). In terms of sea level, the final pattern in this simple Munk or Stommel model looks as if the low sea levels of the subpolar gyre are being "advected" toward the equator by CTWs and leaking through to the coast in a diluted form somewhat further south (see the middle panels of Figure A.4). This is in fact a good analogy, as we will see.

A simple thermohaline circulation can also be added to this model by assuming that the dynamics discussed above refer to an active layer above a deep, passive abyssal layer. The thermohaline flow is then represented by adding a net northward flow into the active layer, and imagining it to be returned to the south in the abyssal layer. The constant poleward mass transport then does induce a (negative) western sea level signal via the Coriolis force, and this signal is proportional to f, so it grows in size at higher latitudes.

While the angular momentum argument is pedagogically useful, the real ocean is not in perfect Sverdrup balance and the ocean circulation near to the western boundary can produce more complex patterns than the simple two-gyre solution. However, it has been shown (Minobe et al., 2017) that the linkage between western boundary sea level and sea level at the western end of ocean interior or eastern end of western boundary layer can be understood in the linear limit, by mass conservation, to be given by

$$\eta[x_W(y), y, t] = \frac{f(y)}{f(y_p)}\eta[x_W(y_p), y_p, t] + f(y)\int_y^{y_p} \frac{\beta}{f^2}\eta[x_I(y'), y', t]dy', \tag{A.16}$$

where, x_W and x_I are the zonal positions of the western boundary and western end of the ocean interior, respectively, y_p is a reference meridional position that is located poleward of the position y, and $\beta = df/dy$. This equation indicates that the western boundary sea level at a particular latitudinal position y is determined by the coastal sea level at a reference position y_p poleward of y, and cumulative effects of ocean interior sea level between y and y_p. The physical mechanism is that the mass flux to the western boundary layer due to incident Rossby waves from the ocean interior must be carried by CTWs equatorward. The corresponding meridional transport is well approximated by a current in geostrophic balance, accompanied by a sea level difference between the western boundary and the ocean interior. The first term on the right hand side reduces in amplitude in proportion to f on approaching the equator, reflecting the smaller sea level signal needed for the same transport to occur at lower latitudes.

The relation (A.16) is derived for a single layer linear model, but based on a decomposition into vertical modes, and given the absence of ocean depth in (A.16), it is suggested that the relation can be used for sea level itself without knowing the detailed vertical mode structures. An important feature of (A.16) is that the relative importance between the first and second terms are strongly dependent on latitude, because of the aforementioned latitudinal dependency of the Rossby wave speed. In lower latitudes, where Rossby waves are fast, interior sea level contributes more strongly than in higher latitudes, and vice versa. That is, the insulation of coastal sea level from the ocean interior sea level is stronger in higher latitudes than in lower latitudes. Hence, in mid-latitudes and high-latitudes, the contributions of western boundary sea level at a higher latitude propagating equatorward due to CTWs are generally important. Consistently with this, it is suggested that the projected future sea level rise seen in coupled climate models between the end of the 20th century and the end of the 21st century in northeast North America, known as a sea-level rise hot spot, is strongly related to the sea level rise in the Labrador Sea (Minobe et al., 2017).

The results of Minobe et al. (2017) as summarised by equation (A.16) are entirely compatible with the angular momentum argument expressed in equation ($A.15$). The same western boundary sea level can be derived directly from some assumed wind stress, and the interior sea level can also be so calculated if it is considered to be determined by Sverdrup balance from the same wind stress. These interior and boundary sea levels are then found to be consistent with equation (A.16) (Wise et al., 2018).

A.5.3 Oceans with topography

The above results for the vertical sidewall ocean are a rather special case, as can be seen from the dependence of equation (A.15) on the constant depth H. The angular momentum balance relies on knowing the vertical extent of the pressure perturbation on the "sidewalls" of the ocean. When there is a continental slope, currents can flow in different directions over different ocean depths leading to a distribution of "sidewall pressure" which can no longer be calculated based on independent vertical modes, and thus complicating the relationship between the open ocean circulation and the coastal sea level. At the simplest level, the more surface-intensified the circulation becomes, the smaller the effective H, and hence the larger the associated coastal sea level signal. However, reversals in the flow can complicate the relationship further, making it questionable whether a meaningful value of H can be determined.

A.5.4 A linear, barotropic case.

An investigation of the simplest (linear, single layer) version of the problem with topography (Wise et al., 2018) has proved revealing. The problem can be reduced to an analogous "advection-diffusion" problem in which a source of water (either a literal source, or the convergence of the Ekman flux due to wind stress) causes a rise in sea level which then behaves as if it is "advected" along characteristics (we use quotation marks to denote words used to describe the analogous problem, it is not a literal advection), while being "diffused" (blurred) by the action of bottom friction. The characteristics in this case are contours of gh/f as shown in Fig. A.4b for the bathymetry illustrated in Fig. A.4a. These contours can be thought of as the streamfunction responsible for the "advection", so the speed of "advection" is given by the size of the gradient of gh/f, and directed perpendicular to that gradient (along the contours at a speed inversely proportional to their spacing). This "advection" speed was first described by Tyler and Käse (2000) who coined the term "string function" for gh/f to avoid confusion with a true stream function associated with currents. In the constant-slope, f-plane case this "advection" becomes simply a constant speed along the coast, leading to the Arrested Topographic Wave interpretation in which diffusion to the coast happens over "time", but "time" is actually distance along the coast in the direction of CTW propagation. A similar analogy, expressed in terms of streamfunction rather than bottom pressure or sea level, was exploited by Welander (1968) and Becker and Salmon (1997) giving similar results, although it is much harder to extract information about coastal sea level from this formulation.

In this interpretation, sea level is "advected" westwards in the flat-bottomed ocean interior (at the long Rossby wave speed) until it encounters the continental slope, whereupon the "advection" turns equatorward and accelerates, due to the convergence of characteristics (string function contours), carrying the sea level pattern with it. This is a natural extension of the Arrested Topographic Wave concept which allows for a dynamical connection between the open ocean and the coast to be made. Note that, although we are here considering a steady state, this only implies that variation in time is slow compared to the relatively short time taken to establish the coastal response by propagation of CTWs.

In the small friction limit, this "advection-diffusion" balance results in all the diffusion occurring close to the equator, where all gh/f contours converge at the western coast, and no sea level signal penetrates to the coast. Figure A.4f shows a case approaching this limit. This is an unrealistic limit: not only does it assume unrealistically small friction, it also assumes the flow can remain barotropic and coastally trapped right to the equator, which

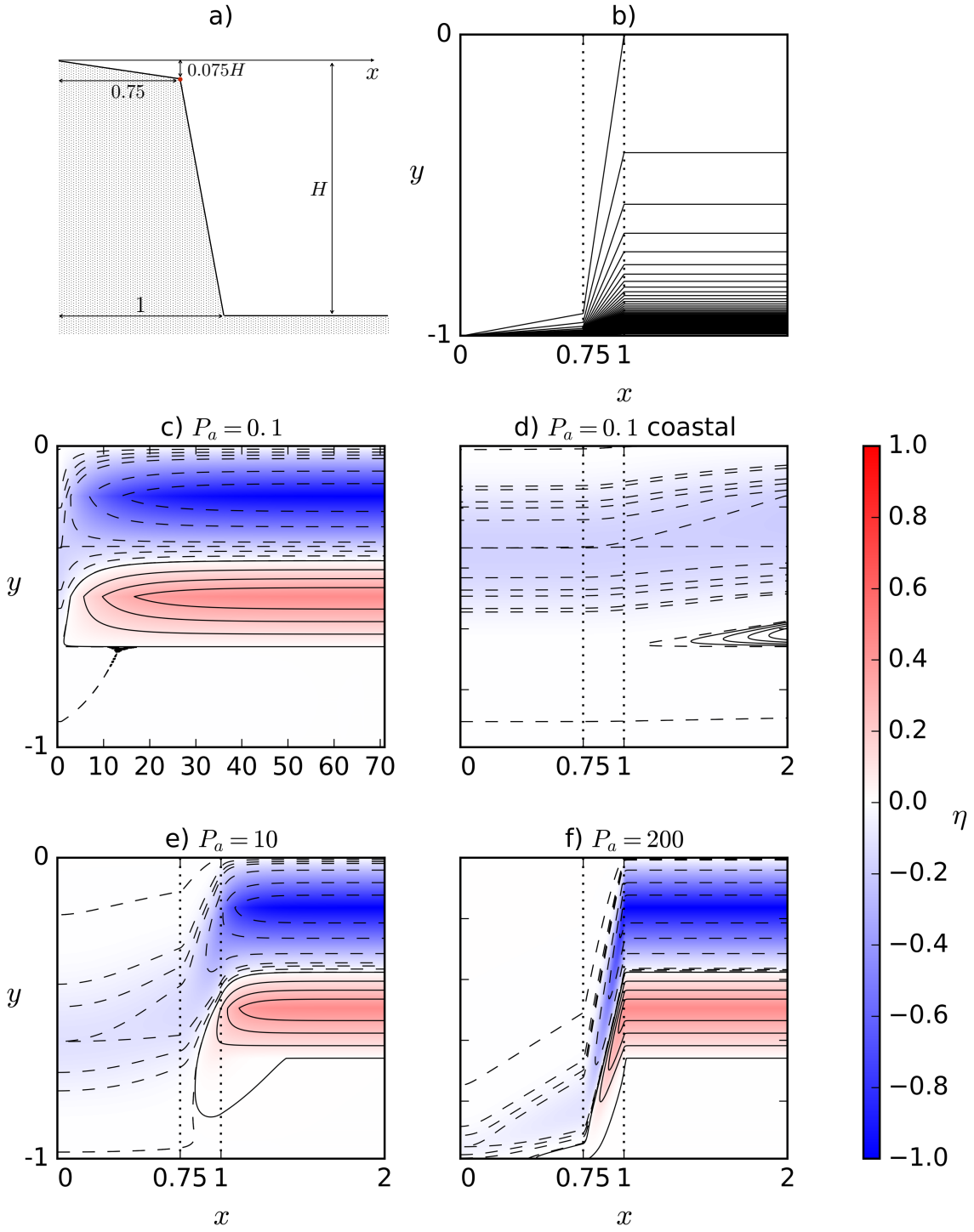
a)
0.075H
x
0.75
H
1
b)
0
y
-1
0
0.75 1
x
c) $P_a = 0.1$
d) $P_a = 0.1$ coastal
e) $P_a = 10$
f) $P_a = 200$
0 10 20 30 40 50 60 70
0.75 1
2
1.0
0.8
0.6
0.4
0.2
0.0
−0.2
−0.4
−0.6
−0.8
−1.0
η

Figure A.4

Figure A.4: *Western ocean sea level in a barotropic model with topography, adapted from figures 3,4 and 5 of [50]. a) Geometry of the western boundary topography, with x measured in units such that the foot of the continental slope is at $x = 1$. b) Corresponding contours of the string function gh/f, with equal spacing (values increase to the south). The y axis represents a range of 6000 km from the equator at $y = -1$ to the northern boundary at $y = 0$, on this constant-beta geometry. c) High friction solution, similar to the vertical sidewall case, resolving the full width of the Stommel boundary layer (P_a is the width of the topography measured in units of Stommel boundary layer width). d) Blow-up of c), focusing on the region with topography. e) and f) similar to d), but with lower friction (narrower Stommel boundary layers).*

is far from the case with realistic stratification. However, as friction increases (other panels in Figure A.4), penetration of the interior signal to the coast increases, and occurs further from the equator. The largest and most rapid penetration (meaning with least southward deflection) occurs in the limit of high friction or narrow continental shelf and slope (these are equivalent limits), and coincides with the vertical sidewall result of Minobe et al. (2017).

The physics of these solutions can be usefully considered in terms of the balance (A.11). Far offshore, the bottom stress term can be neglected (we ignore local wind stress in this boundary problem), and the alongshore pressure gradient is balanced by a depth-integrated onshore (say) geostrophic flow. Close to the coast, the depth-integrated flow becomes negligible and the balance is between the pressure gradient and the bottom stress. This is the same switch from geostrophic to frictional balance that occurs in damped CTWs. Between these two limits, either the bottom stress must build up to provide an offshore Ekman flux which balances the onshore geostrophic flow, or the pressure gradient must reduce as the geostrophic flow is deflected along the slope. In the former case, there is "diffusion" of the sea level signal across gh/f contours, and a coastal response appears. In the latter case, there is no "diffusion", and no coastal response. This interpretation explains an apparent contradiction with Csanady (1978), who found that all the open ocean signal would eventually make it to the coast for long enough wavelengths. In that study (with constant f), the depth-integrated onshore flow was always taken to be zero (consistent with the design of the Arrested Topographic Wave to model circulation over the inner shelf), meaning that the geostrophic onshore flow was always balanced by an offshore flow in the bottom Ekman layer, and a connection with the open ocean (where the pressure gradient is not balanced by bottom stress) was not truly made.

Thus, the size and position of the coastal signal depend on both friction and the shape of the boundary topography. This conclusion is consistent with Higginson et al. (2015), who found that the northward drop in U.S. Atlantic coastal sea level was much smaller and further south than the interior ocean signal, as the above discussion would suggest. They also found that different ocean models disagreed as to the extent of this southward deflection, with some showing much more of a step near Cape Hatteras than would be suggested by the observations, which show almost all the step in south Florida. This is suggestive of the kind of sensitivity to details of topography and friction that the linear barotropic model indicates should be expected.

Further analytical work on the linear barotropic model (Wise et al., 2020) has shown that certain features are robust. The western boundary coastal signal can always be computed as a weighted integral of the open ocean signal from poleward of the point in question just as in the vertical sidewall case as expressed in equation (A.16), but the weightings of the interior and poleward sea level signals become different from those in (A.16). The weighted integral can also still be interpreted as a series of damped boundary modes which propagate information toward the equator. The idea that the interior signal is carried equatorward by CTWs while being leaked across the slope by bottom friction (Huthnance, 1987a, 2004), is therefore a useful interpretation of the dynamics.

It should be noted, however, that the coastal modes in this interpretation can become somewhat more complicated than conventional f-plane CTWs. If f is allowed to vary, a new time scale is introduced, which is the shortest period at which Rossby waves can exist. This period is given by $4\pi/\beta L_d$. Using $L_d = c/|f|$ where c is the gravity wave speed for the same vertical mode, and approximating c as about 2.5 m s^{-1} for the first baroclinic mode (Chelton et al., 1998), this can be approximated as $T \approx |\tan\phi|$ where T is measured in years and ϕ is latitude (although near the poles, the separation of variables used to derive the standard Rossby wave dispersion relation no longer applies). For a truly barotropic mode, taking $c \approx 200$ m s^{-1}, the critical period T is 80 times shorter. The few early studies of CTWs which allowed for variations in f, e.g. Allen and Romea (1980), Grimshaw (1977), limited the frequency range to exclude Rossby waves. When Rossby waves are possible, energy can leak away from the boundaries as short Rossby waves from the west, or long Rossby waves from the east. As shown in the vertical sidewall case by Marshall and Johnson (2013), this results in the boundary signals transitioning from Kelvin to Rossby waves, or to Munk Munk (1950) or Stommel Stommel (1948) boundary layers as friction becomes important. More work is needed to understand the implications of this, but initial work (Wise et al., 2020) suggests that the general conclusions carry over to the case

with topography, suggesting that great care needs to be exercised in the interpretation of measurement of signals propagating along boundaries, as phase speeds can be quite different from those seen in f-plane or higher frequency CTWs.

Nonetheless, the linear barotropic model does show that signals generated in the interior are "advected" to the west at the long Rossby wave speed, and then along gh/f countours along the boundary at a speed which can be considered to be the relevant CTW speed, while being "diffused" by bottom friction.

A.5.5 Considerations of nonlinearity.

The model considered above remains highly simplified, being linear and with only rudimentary stratification (although barotropic, the open ocean part of this model can also be thought of as a model with a single active layer above a passive abyss) There are hints that nonlinear effects may produce a richer array of behaviours on western boundaries, including the formation of fronts in boundary pressure, and hence in sea level. The essential mechanism is the overwhelming of CTW propagation by the flow itself, leading to a reversal of the characteristic velocity along part of the boundary (such reversals of characteristic velocity also lie at the heart of longstanding questions of the extent to which western boundary currents can be considered to be passive in ocean thermocline theory). The flow must oppose the wave propagation to achieve this reversal, implying that the reversal is in the subtropical gyre region (the Gulf Stream in the North Atlantic). In a vertical sidewall case, the relevant waves are Kelvin waves which, at least for high enough modes, can certainly be halted by realistic boundary currents. Loss of balance (generation of small-scale gravity waves which remove energy from the "balanced" part of the flow which can be determined from the potential vorticity equation) is found to occur at the point of convergence of opposing characteristic velocities at the boundary, leading to formation of fronts there (Dewar and Hogg, 2010; Deremble et al., 2017). This mechanism was sketched out (in a case with sloping topography modelled on the Gulf Stream geometry) by Stern Stern (1998), and has gained qualitative support from model sensitivity studies (Schoonover et al., 2017), in which CTW speeds are compared with current speeds to suggest the plausibility of this mechanism as an explanation of Gulf Stream separation.

Nonlinear behaviour may, in fact, arise even without the nonlinear terms in the momentum equations. It has proved possible to solve a variety of special cases of the planetary geostrophic equations with sloping boundaries, and these also show a rich variety of behaviours with formation of fronts, and recirculations either side of the boundary current

extension (Salmon, 1994; Ford, 2000). Again, these solutions can be considered in terms of characteristic "velocities", "advecting" the dynamical quantities, coupled with a form of "diffusion". These "velocities" are compounded of a westward component associated with the baroclinic Rossby wave speed, a component along the topography in the direction of CTW propagation, a genuine advection by the flow, and a modification of the Rossby wave speed due to finite deformation of the stratification (particularly strong in the subpolar gyre). In several cases, the characteristic "velocity" at the western boundary is found to be polewards in the equatorward part of the subtropical gyre, converging with an equatorward velocity from the subpolar gyre, and forming a front at the convergence (a little further offshore the front is found much further polwards, see figures 5–7 of Salmon (1994)). This suggests the possibility of sharp steps in coastal sea level mediated by this competition between advection by the flow and "advection" by CTWs, although the "advected" quantity in these more complex solutions is no longer as simple as the bottom pressure. This is an area ripe for further exploration, with potentially important consequences for understanding and predicting coastal sea level.

A.5.6 Eastern boundaries

The above has focused on western boundaries, where the dynamics are rather complicated. At eastern boundaries things are more straightforward. The open ocean characteristic "velocities" near to eastern boundaries are dominated by the westward Rossby wave speed except at the equator where the influence of the eastward-propagating equatorial Kelvin and Yanai waves is felt. Along the boundary, the CTWs propagate away from the equator, so all coastal signals should either propagate from the equator, or be generated by local forcing close to the coast. The vertical sidewall analytical models suggest that the signal propagating from the equator would, on time scales longer than the basin circuit time, be determined by the layerwise mass balance constraint.

Model diagnostics are consistent with this interpretation (Hughes et al., 2018). They show that, below about 200 m, the bottom pressure variations propagate away from the equator at speeds typical of CTWs, becoming at interannual time scales almost uniform along the entire eastern boundary, and very small (less than 1 cm of water). Variations in sea level along the eastern boundary (and they do occur) must therefore be generated either from equatorial sources or by shelf sea dynamics, with some of the effects radiating out into the open ocean. Illustrating this, it is found that regional model simulations of the US Pacific coast perform better when using "clamped" boundary conditions to the south,

directly importing the observed properties at that boundary via a data assimilating global model, as opposed to the "radiation plus nudging" conditions applied at other boundaries (Durski et al., 2015). Both boundary wave propagation and local winds play important roles in the coastal sea level in this region (Kurapov et al., 2017). The radiation of Rossby waves has been suggested as a mechanism for the formation of poleward-flowing undercurrents below the equatorward winds on certain boundaries (Samelson, 2017), an example of the coastal variability influencing the open ocean rather than vice versa.

A.6 Conclusions

The interaction between open ocean and the coast is a subtle issue, especially at western boundaries. We have found that it is possible to think of CTWs as effectively advecting sea level (or bottom pressure) signals rapidly along the continental slope, in the direction of CTW propagation, with bottom friction acting to diffuse the signal slowly across the slope. Thus the coastal sea level signal emerges from the balance between these two processes, and can become very small when bottom friction is small. The sea level signals reach the continental slope as a result of a similar Rossby wave "advection" from east to west in much of the ocean, or a Kelvin wave "advection" to the east at the equator. Thus eastern boundary coastal sea level signals are only influenced by the equatorial open ocean, as well as near-coastal direct forcing. The western boundary coastal sea level, on the other hand, is influenced by the open ocean from all latitudes.

The conventional vertical sidewall case appears to produce the largest western boundary coastal signals, which are still significantly smaller than the associated open ocean signals, and displaced toward the equator. More realistic topography and lower bottom friction act to reduce the size of these signals further, and push them further toward the equator. Thus, it is expected that western boundary coastal signals should be smaller than interior ocean signals, and should smooth those interior signals over long distances (greatly reducing the influence of mesoscale variability). In the linear limit, western boundary coastal sea level should only be affected by ocean signals poleward of the latitude being considered.

Nonlinear effects, however, may be very important, permitting an advective influence of open-ocean sea level from equatorward of the coastal point, associated with poleward-flowing western boundary currents. Sharp steps along western boundaries may be a manifestation of the convergence of this propagation of influence from poleward (by CTWs) and equatorward (by western boundary currents). More work is needed to clarify these issues.

The smoothing and the equatorward "advection" of open-ocean sea level signals, both

of which act to reduce the magnitude of the signal, only apply when the continental slope is long and spans a wide latitude range. In the case of small islands, the smoothing is limited to the length of the depth contours which close around the island, and the equatorward displacement is similarly limited. This means that the open-ocean influence is felt much more strongly at small islands, increasing the risks from sea level change, but also meaning that measurements from tide gauges on small islands are representative of the surrounding ocean, in contrast to the case for, especially extratropical, continental tide gauges.

For all cases it should be stressed that we have here considered only the dynamical component of sea level change, which results in the sea surface not being level. On top of this component, any increase in the volume of water in the ocean will transmit freely to the coast, with a distribution depending purely on the response of the solid earth and its gravity field to the redistribution of mass, as considered elsewhere in this volume. In addition, we have ignored the inverse barometer response to atmospheric pressure changes, which would also be felt at the coast just as strongly as in the open ocean.

Bibliography

Allen, J. (1975). Coastal trapped waves in a stratified ocean. *Journal of Physical Oceanography*, 5(2):300–325.

Allen, J. (1980). Models of wind-driven currents on the continental shelf. *Annual Review of Fluid Mechanics*, 12(1):389–433.

Allen, J. and Romea, R. (1980). On coastal trapped waves at low latitudes in a stratified ocean. *Journal of Fluid Mechanics*, 98(3):555–585.

Andersen, O. B., Nielsen, K., Knudsen, P., Hughes, C. W., Bingham, R., Fenoglio-Marc, L., Gravelle, M., Kern, M., and Polo, S. P. (2018). Improving the coastal mean dynamic topography by geodetic combination of tide gauge and satellite altimetry. *Marine Geodesy*, 41(6):517–545.

Andres, M., Gawarkiewicz, G. G., and Toole, J. M. (2013). Interannual sea level variability in the western North Atlantic: Regional forcing and remote response. *Geophysical Research Letters*, 40(22):5915–5919.

Barnett, T. (1983). Interaction of the monsoon and Pacific trade wind system at interannual time scales Part I: The equatorial zone. *Monthly weather review*, 111(4):756–773.

Beardsley, R. and Winant, C. (1979). On the mean circulation in the Mid-Atlantic Bight. *Journal of Physical Oceanography*, 9(3):612–619.

Becker, J. M. and Salmon, R. (1997). Eddy formation on a continental slope. *Journal of marine research*, 55(2):181–200.

Bingham, R. and Hughes, C. (2012). Local diagnostics to estimate density-induced sea level variations over topography and along coastlines. *Journal of Geophysical Research: Oceans*, 117(C1).

Bingham, R., Knudsen, P., Andersen, O., and Pail, R. (2011). An initial estimate of the North Atlantic steady-state geostrophic circulation from GOCE. *Geophysical Research Letters*, 38(1).

Bingham, R. J. and Hughes, C. W. (2009). Signature of the Atlantic meridional overturning circulation in sea level along the east coast of North America. *Geophysical Research Letters*, 36(2).

Boon, J. D. (2012). Evidence of sea level acceleration at US and Canadian tide stations, Atlantic Coast, North America. *Journal of Coastal Research*, 28(6):1437–1445.

Bowie, W. (1927). Tilting of mean sea level. *Gerlands Beitraege zur Geophysik*, 23:97–98.

Brink, K. (1982). The effect of bottom friction on low-frequency coastal trapped waves. *Journal of Physical Oceanography*, 12(2):127–133.

Brink, K. (1991). Coastal-trapped waves and wind-driven currents over the continental shelf. *Annual Review of Fluid Mechanics*, 23(1):389–412.

Brink, K. H. and Allen, J. (1978). On the effect of bottom friction on barotropic motion over the continental shelf. *Journal of Physical Oceanography*, 8(5):919–922.

Brink, K. H. and Chapman, D. C. (1985). Programs for computing properties of coastal-trapped waves and wind-driven motions over the continental shelf and slope. Technical report, Woods Hole Oceanographic Institution.

Bryan, F. O., Hecht, M. W., and Smith, R. D. (2007). Resolution convergence and sensitivity studies with North Atlantic circulation models. Part I: The western boundary current system. *Ocean Modelling*, 16(3-4):141–159.

Buchwald, V. and Adams, J. (1968). The propagation of continental shelf waves. *Proceedings of the Royal Society of London. Series A. Mathematical and Physical Sciences*, 305(1481):235–250.

Buckley, M. W. and Marshall, J. (2016). Observations, inferences, and mechanisms of the Atlantic Meridional Overturning Circulation: A review. *Reviews of Geophysics*, 54(1):5–63.

Calafat, F., Chambers, D., and Tsimplis, M. (2012). Mechanisms of decadal sea level variability in the eastern North Atlantic and the Mediterranean Sea. *Journal of Geophysical Research: Oceans*, 117(C9).

Calafat, F., Chambers, D., and Tsimplis, M. (2013). Inter-annual to decadal sea-level variability in the coastal zones of the Norwegian and Siberian Seas: The role of atmospheric forcing. *Journal of Geophysical Research: Oceans*, 118(3):1287–1301.

Calafat, F. M., Wahl, T., Lindsten, F., Williams, J., and Frajka-Williams, E. (2018). Coherent modulation of the sea-level annual cycle in the United States by Atlantic Rossby waves. *Nature communications*, 9(1):2571.

Cane, M. A., Kamenkovich, V. M., and Krupitsky, A. (1998). On the utility and disutility of JEBAR. *Journal of Physical Oceanography*, 28(3):519–526.

Chapman, D. C., Barth, J. A., Beardsley, R. C., and Fairbanks, R. G. (1986). On the continuity of mean flow between the Scotian Shelf and the Middle Atlantic Bight. *Journal of Physical Oceanography*, 16(4):758–772.

Chapman, D. C. and Brink, K. H. (1987). Shelf and slope circulation induced by fluctuating offshore forcing. *Journal of Geophysical Research: Oceans*, 92(C11):11741–11759.

Charney, J. G. (1955). The Gulf Stream as an inertial boundary layer. *Proceedings of the National Academy of Sciences*, 41(10):731–740.

Chassignet, E. P. and Marshall, D. P. (2008). Gulf Stream separation in numerical ocean models. *Geophysical Monograph Series*, 177.

Chelton, D. B., DeSzoeke, R. A., Schlax, M. G., El Naggar, K., and Siwertz, N. (1998). Geographical variability of the first baroclinic rossby radius of deformation. *Journal of Physical Oceanography*, 28(3):433–460.

Chelton, D. B. and Schlax, M. G. (1996). Global observations of oceanic rossby waves. *Science*, 272(5259):234–238.

Cherian, D. A. and Brink, K. H. (2016). Offshore transport of shelf water by deep-ocean eddies. *Journal of Physical Oceanography*, 46(12):3599–3621.

Clarke, A. J. and Shi, C. (1991). Critical frequencies at ocean boundaries. *Journal of Geophysical Research: Oceans*, 96(C6):10731–10738.

Clarke, A. J. and Van Gorder, S. (1994). On ENSO coastal currents and sea levels. *Journal of Physical Oceanography*, 24(3):661–680.

Csanady, G. and Shaw, P. T. (1983). The insulating effect of a steep continental slope. *Journal of Geophysical Research: Oceans*, 88(C12):7519–7524.

Csanady, G. T. (1978). The Arrested Topographic Wave. *Journal of Physical Oceanography*, 8(1):47–62.

Csanady, G. T. (1982). *Circulation in the Coastal Ocean*. Springer.

Dale, A. C., Huthnance, J. M., and Sherwin, T. J. (2001). Coastal-trapped waves and tides at near-inertial frequencies. *Journal of physical oceanography*, 31(10):2958–2970.

Dengo, J. (1993). The problem of Gulf Stream separation: A barotropic approach. *Journal of Physical oceanography*, 23(10):2182–2200.

Deremble, B., Johnson, E., and Dewar, W. (2017). A coupled model of interior balanced and boundary flow. *Ocean Modelling*, 119:1–12.

Dewar, W. K. and Hogg, A. M. (2010). Topographic inviscid dissipation of balanced flow. *Ocean Modelling*, 32(1-2):1–13.

Do, D. (1984). A method for solving diffusion and reaction problems with nonuniform activity catalysts. *Chemical engineering science*, 39(10):1519–1522.

Domingues, R., Goni, G., Baringer, M., and Volkov, D. (2018). What caused the accelerated sea level changes along the US East Coast during 2010–2015? *Geophysical Research Letters*, 45(24):13–367.

Durski, S. M., Kurapov, A. L., Allen, J. S., Kosro, P. M., Egbert, G. D., Shearman, R. K., and Barth, J. A. (2015). Coastal ocean variability in the US Pacific Northwest region: seasonal patterns, winter circulation, and the influence of the 2009–2010 El Niño. *Ocean Dynamics*, 65(12):1643–1663.

Enfield, D. B. and Allen, J. (1980). On the structure and dynamics of monthly mean sea level anomalies along the Pacific coast of North and South America. *Journal of Physical Oceanography*, 10(4):557–578.

Ezer, T. (2017). A modeling study of the role that bottom topography plays in Gulf Stream dynamics and in influencing the tilt of mean sea level along the US East Coast. *Ocean Dynamics*, 67(5):651–664.

Ezer, T. (2019). Regional differences in sea level rise between the Mid-Atlantic Bight and the South Atlantic Bight: Is the Gulf Stream to blame? *Earth's Future*.

Ezer, T., Atkinson, L. P., Corlett, W. B., and Blanco, J. L. (2013). Gulf Stream's induced sea level rise and variability along the US mid-Atlantic coast. *Journal of Geophysical Research: Oceans*, 118(2):685–697.

Février, S., Sirven, J., and Herbaut, C. (2007). Interaction of a coastal Kelvin wave with the mean state in the Gulf Stream separation area. *Journal of physical oceanography*, 37(6):1429–1444.

Flather, R. A. (1994). A storm surge prediction model for the northern Bay of Bengal with application to the cyclone disaster in April 1991. *Journal of Physical Oceanography*, 24(1):172–190.

Ford, R. (2000). A baroclinic western boundary current over a continental slope. *Journal of marine research*, 58(3):327–373.

Förste, C., Bruinsma, S. L., Abrikosov, O., Lemoine, J.-M., Marty, J. C., Flechtner, F., Balmino, G., Barthelmes, F., and Biancale, R. (2014). EIGEN-6C4 the latest combined global gravity field model including GOCE data up to degree and order 2190 of GFZ potsdam and GRGS toulouse.

Frederikse, T., Simon, K., Katsman, C. A., and Riva, R. (2017). The sea-level budget along the Northwest Atlantic coast: GIA, mass changes, and large-scale ocean dynamics. *Journal of Geophysical Research: Oceans*, 122(7):5486–5501.

Fukumori, I., Wang, O., Llovel, W., Fenty, I., and Forget, G. (2015). A near-uniform fluctuation of ocean bottom pressure and sea level across the deep ocean basins of the Arctic Ocean and the Nordic Seas. *Progress in Oceanography*, 134:152–172.

Gill, A. and Clarke, A. (1974). Wind-induced upwelling, coastal currents and sea-level changes. In *Deep Sea Research and Oceanographic Abstracts*, volume 21, pages 325–345. Elsevier.

Gill, A. and Schumann, E. (1974). The generation of long shelf waves by the wind. *Journal of Physical Oceanography*, 4(1):83–90.

Gill, A. E. (1982). *Atmosphere-Ocean Dynamics*, volume 30. Academic Press.

Godfrey, J. (1975). On ocean spindown I: A linear experiment. *Journal of Physical Oceanography*, 5(3):399–409.

Gregory, J. M., Griffies, S. M., Hughes, C. W., Lowe, J. A., Church, J. A., Fukimori, I., Gomez, N., Kopp, R. E., Landerer, F., Le Cozannet, G., et al. (2019). Concepts and terminology for sea level: mean, variability and change, both local and global. *Surveys in Geophysics*, pages 1–39.

Grimshaw, R. (1977). The effects of a variable coriolis parameter, coastline curvature and variable bottom topography on continental shelf waves. *Journal of Physical Oceanography*, 7(4):547–554.

Gurvan Madec and NEMO System Team (2019). Nemo ocean engine. Scientific notes of climate modelling center.

Hannachi, A., Jolliffe, I., and Stephenson, D. (2007). Empirical orthogonal functions and related techniques in atmospheric science: A review. *International Journal of Climatology: A Journal of the Royal Meteorological Society*, 27(9):1119–1152.

Hellerman, S. and Rosenstein, M. (1983). Normal monthly wind stress over the world ocean with error estimates. *Journal of Physical Oceanography*, 13(7):1093–1104.

Higginson, S., Thompson, K. R., Woodworth, P. L., and Hughes, C. W. (2015). The tilt of mean sea level along the east coast of North America. *Geophysical Research Letters*, 42(5):1471–1479.

Hill, A. E. (1995). Leakage of barotropic slope currents onto the continental shelf. *Journal of Physical Oceanography*, 25(7):1617–1621.

Hong, B., Sturges, W., and Clarke, A. J. (2000). Sea level on the US East Coast: decadal variability caused by open ocean wind-curl forcing. *Journal of Physical Oceanography*, 30(8):2088–2098.

Howe, M. and Mysak, L. (1973). Scattering of poincaré waves by an irregular coastline. *Journal of Fluid Mechanics*, 57(1):111–128.

Huang, R. X. (1984). *The thermocline and current structure in subtropical/subpolar basins*. PhD thesis, Massachusetts Institute of Technology.

Hughes, C. W. (2008). A form of potential vorticity equation for depth-integrated flow with a free surface. *Journal of Physical Oceanography*, 38(5):1131–1136.

Hughes, C. W., Bingham, R. J., Roussenov, V., Williams, J., and Woodworth, P. L. (2015). The effect of Mediterranean exchange flow on European time mean sea level. *Geophysical Research Letters*, 42(2):466–474.

Hughes, C. W. and De Cuevas, B. A. (2001). Why western boundary currents in realistic oceans are inviscid: A link between form stress and bottom pressure torques. *Journal of Physical Oceanography*, 31(10):2871–2885.

Hughes, C. W., Fukumori, I., Griffies, S. M., Huthnance, J. M., Minobe, S., Spence, P., Thompson, K. R., and Wise, A. (2019). Sea level and the role of coastal trapped waves in mediating the influence of the open ocean on the coast. *Surveys in Geophysics*, pages 1–26.

Hughes, C. W. and Meredith, M. P. (2006). Coherent sea-level fluctuations along the global continental slope. *Philosophical Transactions of the Royal Society A: Mathematical, Physical and Engineering Sciences*, 364(1841):885–901.

Hughes, C. W., Williams, J., Blaker, A., Coward, A., and Stepanov, V. (2018). A window on the deep ocean: the special value of ocean bottom pressure for monitoring the large-scale, deep-ocean circulation. *Progress in oceanography*, 161:19–46.

Hughes, C. W., Williams, J., Coward, A. C., and de Cuevas, B. A. (2014). Antarctic circumpolar transport and the southern mode: a model investigation of interannual to decadal timescales. *Ocean Science*, 10(2):215–225.

Hughes, C. W., Williams, J., Hibbert, A., Boening, C., and Oram, J. (2016). A Rossby whistle: A resonant basin mode observed in the Caribbean Sea. *Geophysical Research Letters*, 43(13):7036–7043.

Hughes, C. W. and Williams, S. D. (2010). The color of sea level: Importance of spatial variations in spectral shape for assessing the significance of trends. *Journal of Geophysical Research: Oceans*, 115(C10).

Huthnance, J. (1984). Slope currents and JEBAR. *Journal of Physical Oceanography*, 14(4):795–810.

Huthnance, J. (1987a). Effects of longshore shelf variations on barotropic continental shelf waves, slope currents and ocean modes. *Progress in Oceanography*, 19(2):177–220.

Huthnance, J. (2001). Coastal trapped waves. In *Encyclopedia of Ocean Sciences*. Academic Press, San Diego.

Huthnance, J., Mysak, L., and Wang, D.-P. (1986). Coastal trapped waves. *Baroclinic processes on continental shelves*, 3:1–18.

Huthnance, J. M. (1975). On trapped waves over a continental shelf. *Journal of fluid mechanics*, 69(4):689–704.

Huthnance, J. M. (1978). On coastal trapped waves: Analysis and numerical calculation by inverse iteration. *Journal of Physical Oceanography*, 8(1):74–92.

Huthnance, J. M. (1987b). Along-shelf evolution and sea levels across the continental slope. *Cont. Shelf Res.*, 7(8):957–974.

Huthnance, J. M. (2004). Ocean-to-shelf signal transmission: A parameter study. *Journal of Geophysical Research: Oceans*, 109(C12).

Jackson, L. C., Peterson, K. A., Roberts, C. D., and Wood, R. A. (2016). Recent slowing of Atlantic overturning circulation as a recovery from earlier strengthening. *Nature Geoscience*, 9(7):518.

Johnson, E. (1990). The low-frequency scattering of kelvin waves by stepped topography. *Journal of Fluid Mechanics*, 215:23–44.

Johnson, H. L., Cessi, P., Marshall, D. P., Schloesser, F., and Spall, M. A. (2019). Recent contributions of theory to our understanding of the Atlantic Meridional Overturning Circulation. *Journal of Geophysical Research: Oceans*, 124(8):5376–5399.

Johnson, H. L. and Marshall, D. P. (2002). A theory for the surface Atlantic response to thermohaline variability. *Journal of Physical Oceanography*, 32(4):1121–1132.

Johnston, P. (1994). A solution method for the graetz problem for non-newtonian fluids with dirichlet and neumann boundary conditions. *Mathematical and computer modelling*, 19(2):1–19.

Johnston, P. and Do, D. (1987). A new method for solving a large class of heat and mass transfer problems. *Chemical Engineering Communications*, 49(4-6):247–271.

Kajiura, K. (1974). Effect of stratification on long period trapped waves on the shelf. *Journal of the Oceanographical Society of Japan*, 30(6):271–281.

Kanzow, T., Johnson, H., Marshall, D., Cunningham, S., Hirschi, J.-M., Mujahid, A., Bryden, H., and Johns, W. (2009). Basinwide integrated volume transports in an eddy-filled ocean. *Journal of Physical Oceanography*, 39(12):3091–3110.

Kaoullas, G. and Johnson, E. (2010). Fast accurate computation of shelf waves for arbitrary depth profiles. *Continental Shelf Research*, 30(7):833–836.

Kelly, K. A. and Chapman, D. C. (1988). The response of stratified shelf and slope waters to steady offshore forcing. *Journal of physical oceanography*, 18(6):906–925.

Kenigson, J. S., Han, W., Rajagopalan, B., Yanto, and Jasinski, M. (2018). Decadal shift of NAO-linked interannual sea level variability along the US northeast coast. *Journal of Climate*, 31(13):4981–4989.

Kurapov, A. L., Erofeeva, S. Y., and Myers, E. (2017). Coastal sea level variability in the US West Coast Ocean forecast system (WCOFS). *Ocean Dynamics*, 67(1):23–36.

Lacasce, J. H. (2017). The prevalence of oceanic surface modes. *Geophysical Research Letters*, 44(21):11–097.

Lentz, S. J. (2008). Observations and a model of the mean circulation over the Middle Atlantic Bight continental shelf. *Journal of Physical Oceanography*, 38(6):1203–1221.

Lin, H., Thompson, K. R., Huang, J., and Véronneau, M. (2015). Tilt of mean sea level along the Pacific coasts of North America and Japan. *Journal of Geophysical Research: Oceans*, 120(10):6815–6828.

Little, C. M., Horton, R. M., Kopp, R. E., Oppenheimer, M., Vecchi, G. A., and Villarini, G. (2015). Joint projections of US East Coast sea level and storm surge. *Nature Climate Change*, 5(12):1114.

Little, C. M., Hu, A., Hughes, C. W., McCarthy, G. D., Piecuch, C. G., Ponte, R. M., and Thomas, M. D. (2019). The relationship between US east coast sea level and the Atlantic meridional overturning circulation: A review. *Journal of Geophysical Research: Oceans*, 124(9):6435–6458.

Liu, Y., Wilson, C., Green, M. A., and Hughes, C. W. (2018). Gulf stream transport and mixing processes via coherent structure dynamics. *Journal of Geophysical Research: Oceans*, 123(4):3014–3037.

Longuet-Higgins, M. S. (1964). On group velocity and energy flux in planetary wave motions. In *Deep Sea Research and Oceanographic Abstracts*, volume 11, pages 35–42. Elsevier.

Lorbacher, K., Marsland, S., Church, J., Griffies, S., and Stammer, D. (2012). Rapid barotropic sea level rise from ice sheet melting. *Journal of Geophysical Research: Oceans*, 117(C6).

MacCready, P. and Rhines, P. B. (1993). Slippery bottom boundary layers on a slope. *Journal of Physical Oceanography*, 23(1):5–22.

Marshall, D. P. (2011). Rossby wormholes. *Journal of Marine Research*, 69(2-3):309–330.

Marshall, D. P. and Johnson, H. L. (2013). Propagation of meridional circulation anomalies along western and eastern boundaries. *Journal of Physical Oceanography*, 43(12):2699–2717.

Marshall, J., Johnson, H., and Goodman, J. (2001). A study of the interaction of the North Atlantic Oscillation with ocean circulation. *Journal of Climate*, 14(7):1399–1421.

McCarthy, G. D., Haigh, I. D., Hirschi, J. J.-M., Grist, J. P., and Smeed, D. A. (2015). Ocean impact on decadal Atlantic climate variability revealed by sea-level observations. *Nature*, 521(7553):508–510.

Mertz, G. and Wright, D. G. (1992). Interpretations of the JEBAR term. *Journal of Physical Oceanography*, 22(3):301–305.

Miles, J. W. (1972). Kelvin waves on oceanic boundaries. *Journal of Fluid Mechanics*, 55(1):113–127.

Milliff, R. F. and McWilliams, J. C. (1994). The evolution of boundary pressure in ocean basins. *Journal of physical oceanography*, 24(6):1317–1338.

Minobe, S., Terada, M., Qiu, B., and Schneider, N. (2017). Western boundary sea level: A theory, rule of thumb, and application to climate models. *Journal of physical oceanography*, 47(5):957–977.

Mitchum, G. T. (1994). Comparison of TOPEX sea surface heights and tide gauge sea levels. *Journal of Geophysical Research: Oceans*, 99(C12):24541–24553.

Moore, D. W. (1968). *Planetary-gravity waves in an equatorial ocean.* PhD thesis, Harvard University.

Munday, D. R. and Marshall, D. P. (2005). On the separation of a barotropic western boundary current from a cape. *Journal of physical oceanography*, 35(10):1726–1743.

Munk, W. H. (1950). On the wind-driven ocean circulation. *Journal of meteorology*, 7(2):80–93.

Mysak, L. A. (1980a). Recent advances in shelf wave dynamics. *Reviews of Geophysics*, 18(1):211–241.

Mysak, L. A. (1980b). Topographically trapped waves. *Annual Review of Fluid Mechanics*, 12(1):45–76.

Navarra, A. and Simoncini, V. (2010). *A guide to empirical orthogonal functions for climate data analysis*. Springer Science & Business Media.

Nurser, A. G. and Williams, R. G. (1990). Cooling Parsons model of the separated Gulf Stream. *Journal of physical oceanography*, 20(12):1974–1979.

Ozisik, M. N. (1993). *Heat conduction*. John Wiley & Sons.

Park, J. and Sweet, W. (2015). Accelerated sea level rise and Florida Current transport. *Ocean Science*, 11(4):607–615.

Parsons, A. (1969). A two-layer model of Gulf Stream separation. *Journal of Fluid Mechanics*, 39(3):511–528.

Piecuch, C. G., Dangendorf, S., Gawarkiewicz, G. G., Little, C. M., Ponte, R. M., and Yang, J. (2019). How is New England coastal sea level related to the Atlantic Meridional Overturning Circulation at 26 N? *Geophysical Research Letters*, 46(10):5351–5360.

Piecuch, C. G., Dangendorf, S., Ponte, R. M., and Marcos, M. (2016). Annual sea level changes on the North American northeast coast: Influence of local winds and barotropic motions. *Journal of Climate*, 29(13):4801–4816.

Pratt, R. M. (1968). Atlantic continental shelf and slope of the United States-physiography and sediments of the deep-sea basin.

Rhines, P. (1970). Edge-, bottom-, and rossby waves in a rotating stratified fluid. *Geophysical and Astrophysical Fluid Dynamics*, 1(3-4):273–302.

Rio, M.-H., Mulet, S., and Picot, N. (2014). Beyond GOCE for the ocean circulation estimate: Synergetic use of altimetry, gravimetry, and in situ data provides new insight into geostrophic and Ekman currents. *Geophysical Research Letters*, 41(24):8918–8925.

Robinson, A. (1964). Continental shelf waves and the response of sea level to weather systems. *Journal of Geophysical Research*, 69(2):367–368.

Roussenov, V. M., Williams, R. G., Hughes, C. W., and Bingham, R. J. (2008). Boundary wave communication of bottom pressure and overturning changes for the North Atlantic. *Journal of Geophysical Research: Oceans*, 113(C8).

Sallenger Jr, A. H., Doran, K. S., and Howd, P. A. (2012). Hotspot of accelerated sea-level rise on the Atlantic coast of North America. *Nature Climate Change*, 2(12):884–888.

Salmon, R. (1994). Generalized two-layer models of ocean circulation. *Journal of marine research*, 52(5):865–908.

Salmon, R. (1998a). *Lectures on geophysical fluid dynamics*. Oxford University Press.

Salmon, R. (1998b). Linear ocean circulation theory with realistic bathymetry. *Journal of Marine Research*, 56(4):833–884.

Samelson, R. (2017). Time-dependent linear theory for the generation of poleward undercurrents on eastern boundaries. *Journal of Physical Oceanography*, 47(12):3037–3059.

Schoonover, J., Dewar, W. K., Wienders, N., and Deremble, B. (2017). Local sensitivities of the Gulf Stream separation. *Journal of Physical Oceanography*, 47(2):353–373.

Scott, J. and Csanady, G. (1976). Nearshore currents off Long Island. *Journal of Geophysical Research*, 81(30):5401–5409.

Siemes, C. (2012). GOCE gradiometer calibration and Level 1b data processing. Technical report, Tech. rep., ESA Working Paper EWP-2384.

Smeed, D., Josey, S., Beaulieu, C., Johns, W. E., Moat, B., Frajka-Williams, E., Rayner, D., Meinen, C., Baringer, M., Bryden, H., et al. (2018). The North Atlantic Ocean is in a state of reduced overturning. *Geophysical Research Letters*, 45(3):1527–1533.

Speer, K., Tziperman, E., and Feliks, Y. (1993). Topography and grounding in a simple bottom layer model. *Journal of Geophysical Research: Oceans*, 98(C5):8547–8558.

Stern, M. E. (1998). Separation of a density current from the bottom of a continental slope. *Journal of physical oceanography*, 28(10):2040–2049.

Stommel, H. (1948). The westward intensification of wind-driven ocean currents. *Transactions, American Geophysical Union*, 29(2):202.

Sturges, W. (1974). Sea level slope along continental boundaries. *Journal of Geophysical Research*, 79(6):825–830.

Sturges, W. (1977). Comment on nearshore currents off Long Island by JT Scott and GT Csanady. *Journal of Geophysical Research*, 82(9):1451–1452.

Sverdrup, H. U. (1947). Wind-driven currents in a baroclinic ocean; with application to the equatorial currents of the eastern Pacific. *Proceedings of the National Academy of Sciences of the United States of America*, 33(11):318.

Thompson, P. and Mitchum, G. (2014). Coherent sea level variability on the North Atlantic western boundary. *Journal of Geophysical Research: Oceans*, 119(9):5676–5689.

Tyler, R. H. and Käse, R. (2000). A string functionfor describing the propagation of large-scale potential energy anomalies in a rotating fluid. *Geophysical & Astrophysical Fluid Dynamics*, 92(1-2):31–64.

Valle-Levinson, A., Dutton, A., and Martin, J. B. (2017). Spatial and temporal variability of sea-level rise hotspots over the eastern United States. *Geophysical Research Letters*.

Veronis, G. (1973). Model of world ocean circulation. 1. wind-driven, 2-layer. *Journal of Marine Research*, 31(3):228–288.

Veronis, G. et al. (1976). Model of world ocean circulation. ii. thermally driven, two-layer.

Volkov, D. L., Lee, S.-K., Domingues, R., Zhang, H., and Goes, M. (2019). Interannual sea level variability along the southeastern seaboard of the United States in relation to the gyre-scale heat divergence in the North Atlantic. *Geophysical Research Letters*.

Von Schwind, J. J. (1980). *Geophysical fluid dynamics for oceanographers*. Prentice Hall.

Wajsowicz, R. C. and Gill, A. (1986). Adjustment of the ocean under buoyancy forces. Part I: The role of Kelvin waves. *Journal of Physical Oceanography*, 16(12):2097–2114.

Wang, D.-P. (1975). Coastal trapped waves in a baroclinic ocean. *Journal of Physical Oceanography*, 5(2):326–333.

Wang, D.-P. (1982). Effects of continental slope on the mean shelf circulation. *Journal of Physical Oceanography*, 12(12):1524–1526.

Wang, D.-P. and Mooers, C. N. (1976). Coastal-trapped waves in a continuously stratified ocean. *Journal of Physical Oceanography*, 6(6):853–863.

Welander, P. (1968). Wind-driven circulation in one- and two-layer oceans of variable depth. *Tellus*, 20(1):1–16.

Welander, P. (1971). Some exact solutions to the equations describing an ideal-fluid thermocline. *J. mar. Res*, 29(2):60–68.

Williams, J. and Hughes, C. W. (2013). The coherence of small island sea level with the wider ocean: a model study. *Ocean Science*, 9(1):111–119.

Wise, A., Hughes, C. W., and Polton, J. A. (2018). Bathymetric influence on the coastal sea level response to ocean gyres at western boundaries. *Journal of Physical Oceanography*, 48(12):2949–2964.

Wise, A., Hughes, C. W., Polton, J. A., and Huthnance, J. M. (2020). Leaky slope waves and sea level: Unusual consequences of the beta effect along western boundaries with bottom topography and dissipation. *Journal of Physical Oceanography*, 50(1):217–237.

Woodworth, P. (1991). The permanent service for mean sea level and the global sea level observing system. *Journal of Coastal Research*, pages 699–710.

Woodworth, P., Hughes, C., Bingham, R., and Gruber, T. (2012). Towards worldwide height system unification using ocean information. *Journal of Geodetic Science*, 2(4):11–15.

Woodworth, P. L., Maqueda, M. Á. M., Roussenov, V. M., Williams, R. G., and Hughes, C. W. (2014). Mean sea-level variability along the northeast American Atlantic coast and the roles of the wind and the overturning circulation. *Journal of Geophysical Research: Oceans*, 119(12):8916–8935.

Xu, F.-H. and Oey, L.-Y. (2011). The origin of along-shelf pressure gradient in the Middle Atlantic Bight. *Journal of Physical Oceanography*, 41(9):1720–1740.

Zhai, X., Johnson, H. L., and Marshall, D. P. (2010). Significant sink of ocean-eddy energy near western boundaries. *Nature Geoscience*, 3(9):608.

Zhai, X., Johnson, H. L., and Marshall, D. P. (2011). A model of Atlantic heat content and sea level change in response to thermohaline forcing. *Journal of Climate*, 24(21):5619–5632.

Zhai, X., Johnson, H. L., and Marshall, D. P. (2014). A simple model of the response of the Atlantic to the North Atlantic Oscillation. *Journal of Climate*, 27(11):4052–4069.

Zhang, W. G. and Gawarkiewicz, G. G. (2015). Dynamics of the direct intrusion of Gulf Stream ring water onto the Mid-Atlantic Bight shelf. *Geophysical Research Letters*, 42(18):7687–7695.